# VELOCITY STRUCTURE OF THE GARHWAL HIMALAYA FROM INVERSION OF TRAVEL TIME DATA

**Ph.D. THESIS**

*by*

**JYOTIMA KANAUJIA**

**DEPARTMENT OF EARTHQUAKE ENGINEERING**
**INDIAN INSTITUTE OF TECHNOLOGY ROORKEE**
**ROORKEE – 247 667 (INDIA)**
**APRIL, 2016**

# VELOCITY STRUCTURE OF THE GARHWAL HIMALAYA FROM INVERSION OF TRAVEL TIME DATA

A THESIS

*Submitted in partial fulfilment of the*
*requirements for the award of the degree*

*of*

DOCTOR OF PHILOSOPHY

*in*

EARTHQUAKE ENGINEERING

*by*

JYOTIMA KANAUJIA

DEPARTMENT OF EARTHQUAKE ENGINEERING
INDIAN INSTITUTE OF TECHNOLOGY ROORKEE
ROORKEE – 247 667 (INDIA)
APRIL, 2016

# INDIAN INSTITUTE OF TECHNOLOGY ROORKEE
# ROORKEE

## CANDIDATE'S DECLARATION

I hereby certify that the work which is being presented in the thesis, entitled **"VELOCITY STRUCTURE OF THE GARHWAL HIMALAYA FROM INVERSION OF TRAVEL TIME DATA"** in partial fulfilment of the requirements for the award of the Degree of Doctor of Philosophy and submitted in the Department of Earthquake Engineering of the Indian Institute of Technology Roorkee, Roorkee is an authentic record of my own work carried out during a period from July, 2011 to April, 2016 under the supervision of Dr. Ashwani Kumar, Emeritus Fellow, and Dr. S. C. Gupta, Scientific Officer, Department of Earthquake Engineering, Indian Institute of Technology Roorkee, Roorkee.

The matter presented in the thesis has not been submitted by me for the award of any other degree of this or any other Institute.

**(JYOTIMA KANAUJIA)**

This is to certify that the above statement made by the candidate is correct to the best of our knowledge.

| | |
|---|---|
| (Ashwani Kumar)<br>Supervisor | (S.C. Gupta)<br>Supervisor |

Dated:

# ABSTRACT

The knowledge of crustal velocity structure of the seismically active regions at local and regional scale is a key requirement to study the relationship between seismicity and geological structure, and to advance understanding of the seismotectonics and geodynamical processes operative in a region. The velocity structure allows studying the variations in physical properties within and along the fault zones to a scale of a few kilometers and provides valuable information on the segmentation of the fault zones, the nature and distribution of fault zone materials, and the locations and extent of possible asperities or nucleation zones (e.g., *Michelini and Mcevilly*, 1991). Travel time data of seismic phases have been extensively used to estimate the seismic velocity structure of the crust and upper mantle of the earth. For modeling of local velocity structure accurate travel time data are required. Significant improvements have been made in the estimation of velocity models due to advancement in instrumentation, digital data acquisition, and improved capabilities of data processing employing various types of computer softwares. Microearthquakes, because of their high rate of occurrence, provide large amounts of phase data within a short time interval. This phase data is of immense value for estimating the local velocity structure.

The Garhwal Himalaya is one of the most seismically active regions of the Himalayan orogen, and has experienced many moderate and large earthquakes. The region has undergone tectonic deformations that resulted in the formation of several thrusts and faults mapped in and around the study region. The Main Central thrust (MCT) and the Main Boundary thrust (MBT) are the two major intracontinental thrusts of Himalayan orogon. The Garhwal Himalaya lies in the postulated central seismic gap between the 1905 Kangra earthquake and 1934 Bihar-Nepal earthquake. The region has a potential threat for great earthquake(s). Since 1991 three gap-filling earthquakes that include, the 1991 Uttarkashi earthquake ($M$w 6.8), the 1999 Chamoli earthquake ($M$w 6.6), and the 2015 Nepal earthquake ($M$w 7.8) have occurred in the central gap. Therefore, the physio chemical mapping of the crustal material beneath the Garhwal Himalaya is useful for evaluating in areas that lie in the seismic gap.

The aim of the present study is to estimate 1-D and 3-D velocity models primarily for the region around Tehri in the Garhwal Himalaya using local earthquake data, to

relocate local earthquakes using these models, and to interpret the distribution of local seismicity and propose a seismotectonic model for the region. This study has a great relevance because a 260.5 m high Tehri dam—the highest earth and rock-fill dam in southeast Asia, lies in the study region. The study area lies between latitudes 29°50' N–31°50' N and longitudes 77°E–80°E. The data set used in the study consists of the arrival times of the P and S phases of the local events acquired through the 12-station digital telemetered network deployed around the Tehri region in the Garhwal Himalaya. The network covers an area of about 100 km x 80 km around Tehri dam, with inter-station spacing of 10 -20 km. Each remote station houses a triaxial short-period seismometer (Model: CMG 40T-1(natural period 1 s)) to sense the three components of ground motion. The digital data is collected at a rate of 100 sample/s, the phase picking errors are estimated to be less than 0.05 s and 0.1 s for *P* and *S* waves respectively. The data of 2079 local events ($0 \leq M_L \leq 4$) occurred in the study area from January 2008 to December 2012 has been used in the study. The SEISAN software (*Ottemoller et al.*, 2011) is used for earthquake analysis and preliminary event location.

An optimum 1D velocity model for the study region has been estimated using travel-time data of 145 local earthquakes with azimuthal gap ≤ 180°. Simultaneous inversion of travel time data allowed obtaining 1-D velocity model parameters, together with revised hypocenter coordinates and station corrections (Kissling et al., 1994 and Kissling, 1988). The travel-time curves of crustal phases are used to constrain the Moho depth. The model consists of six layers with P- and S-wave velocities ranging from 4.42 to 6.78 km/s and 2.41 to 3.71 km/s, respectively, up to a depth of 24 km. The Moho discontinuity seems to be at a depth of about 46 km, with P- and S-wave velocities of 8.34 and 4.86 km/s, respectively. A 2-km-thick low-velocity layer has been deciphered between a depth of 12 and 14 km. The existence of the low-velocity layer possibly can be attributed to the fractured basement thrust because of weakening of the crustal material at the interface between the overriding Himalayan block and the upper part of the underthrusting Indian plate. This is also supported by the large number of local events occurring in the vicinity of the MCT in the Garhwal Inner Lesser Himalaya.

To study the local seismicity, more than 1400 events are relocated using the optimum 1-D velocity model, with the method of joint hypocenter determination technique (JHD). The spatial distribution of the relocated events shows that about 70% of the seismic activity occurred in the Inner Lesser Himalaya between the MCT and the Srinagar thrust (SNT).

The majority of the locatable events defined about 300-km-long northwest–southeast-trending seismicity zone that follows the trace of the MCT. The depth section drawn along the MCT delineates the geometry of the seismically active Main Himalayan thrust (MHT) below a 300-km-long segment of the MCT. It is found that the MHT is composed of two shallow-dipping fracture zones that seem to represent seismically active thrust zones dipping in opposite directions. The depth section of seismicity across the MCT showed two seismicity zones, at 10 and 15 km depth with a 5 km vertical separation. These zones clearly defined a flat-ramp-flat structure of the MHT in the vicinity of the MCT. The postulated front of the underthrusting Indian plate lies at a depth of about 15–18 km. The lower-flat seismicity zone bifurcates into two, indicating further slicing of the lower-flat zone. The postulated thickness of the brittle part of the underthrusting Indian crust is about 20 km in the vicinity of the MCT.

Local Earthquake Tomography has been carried out using the algorithm LOTOS. The method of simultaneous inversion of P- and S-velocity structure with local earthquake data has been used. A total of 25,030 phase readings (12,794 *P* phase and 12,236 *S* phases) of the 1368 local earthquakes recorded from 2008 to 2012 have been used for the inversion. Horizontal tomographic images of the study area are shown as slices at depths of 1, 3, 5, 10, 12, 15 and 18 km. The horizontal sections of the P- and S- velocity anomalies include several interesting features. The near-surface and sub-surface images of high velocity regions identified in the Sub Himalaya and the Lesser Himalaya seems to indicate the trend and configuration of the postulated Delhi-Haridwar-ridge (DHR) beneath the IGP, the Sub Himalaya and the Lesser Himalaya. From the tomographic images we infer that the DHR continues up to the MCT with a lateral offset in the vicinity of the SNT. In the region around Chamoli in GHH, a high S-wave anomaly with a low P-wave anomaly was found. This area is located near the aftershock zone of the moderate magnitude Chamoli earthquake, and we infer that the subsurface area is highly fractured due to the after effects of the Chamoli earthquake. Subsurface geological structure defined by distributed velocity anomalies indicates the depth of sedimentary rocks is up to about 4 km. This sedimentary layer has relatively low VP and Vs velocity, low VP/Vs value and the Poisson's ratio range from 0.14- 0.18.

The Relationship between seismicity distribution and 3D velocity structure has been studied from the revised hypocenters of events, obtained simultaneously with 3D inversion. From the pattern of distributed seismicity in the tomograms, it is found that most of the seismicity in the investigated area is concentrated on the transition boundaries of high and low velocity anomalies. The transition boundaries define the contact zones of the high velocity material and low velocity material. Seismicity along such zones occur because of stress amplification. These zones of high rigidity contrast, are the areas of high energy accumulation and prone to fracture because of stress failure and probable cause of the seismic events. The flat-ramp-flat type subsurface geometry of the underthrusting Indian plate below the Garhwal Himalaya has been outlined from the velocity distribution and depth distribution of more than 800 relocated hypocenters. This subsurface structure of the Indian plate is in conformity with the current understanding of the Indian crust. The subsurface low velocity anomalies indicated the thickness of sedimentary rocks is about 4 km. An area of the geometrical asperity has been found in the northwestern part, which is located on the basement thrust in the vicinity of MCT. The asperity region is defined by the high strength material with capacity to accumulate high strain energy that can be released in the future in the form of moderate earthquake. The narrow zone of concentrated seismic activity between the Uttarkashi thrust and the MCT seems to be the nucleation zone of future earthquake. This earthquake might nucleate at a depth of about 15 km.

# ACKNOWLEDGEMENTS

I wish to express my sincere appreciation and gratitude to my supervisor, **Prof. Ashwani Kumar**, for the excellent and insightful guidance he provided throughout the course of my study. He patiently provided the vision, encouragement and advice necessary for me to proceed through the PhD program and complete my thesis. I wish to express my sincere regards to my co-supervisor, **Dr. S.C. Gupta**, whose constant support and encouragement keeps me motivated, throughout these four years of my PhD course. It has been truly a pleasure and honour to work under both of my supervisors. I am grateful for all their contributions of time and ideas to make my Ph.D. experience productive and stimulating.

I am grateful to **Prof. M. L. Sharma**, Head, and **Prof. H. R. Wasson** ex Head, Department of Earthquake Engineering, IIT Roorkee for extending all the departmental facilities during my study.

I am thankful to **Dr. J. P. Narayan**, **Dr. J. Das** Department of Earthquake Engineering, and **Dr. Anand Joshi**, Department of Earth sciences, IIT Roorkee for their guidance, constructive comments and inventive suggestions during this work.

Thanks to **Dr. J. R. Kayal**, Jadavpur University, Kolkata, for his support, guidance and helpful suggestions and discussions during my conference and workshop visits. I am Thankful to **Prof. Ivan Koulakov**, Institute of Petroleum Geology and Geophysics, SB RAS for his quick replies over emails for suggestions and discussion over the tomographic program at an early stage of my research work. The use of his tomography program, namely **LOTOS,** is greatly acknowledged.

I would like to thank Tehri Hydro Development Corporation (THDC) India Limited for sponsoring the project under which the dataset of the present work was collected. I am grateful to all the team members of the telemetery project who contributed to the recording, collection, and preliminary processing of data.

I express my gratitude to my fellow researchers, seniors and colleagues for their sincere support and help during the process of this research work. Special thanks is due to my friends as they played the role of my support system to survive my PhD tenure here at IITR Roorkee and I believe they will continue to support me in my all future endevours.

I acknowledge my thank to the non teaching staff and other staff members who had helped a during my entire tenure at the department

In a venture like the present one so many people contribute in so many ways that is quite impossible to list their names, not to mention the extent of their contribution. I would like to thanks all the people who so ever helped me directly and indirectly during my PhD.

No words are adequate to express my indebtedness towards my parents and my loving younger sister whose blessings and unconditional love have always shadowed me. These pages wouldn’t be sufficient to mention their enormous support, encouragement and especially invaluable untiring patience displayed. I owe my whole life to them and would like to dedicate this thesis to my parents.

Last but not least I express my gratitude to the Almighty for this divine favour, whose blessings helped me in working for this thesis and giving it the present shape.

**(Jyotima Kanaujia)**

# PUBLICATIONS FROM THIS THESIS

**Journal Publications**

1. Kanaujia, J., A. Kumar, and S. C. Gupta (2015), 1D Velocity Structure and Characteristics of Contemporary Local Seismicity around the Tehri Region, Garhwal Himalaya, ***Bull. Seismol. Soc. Am.***, 105(4), 1852–1869.

2. Kanaujia, J., A. Kumar, and S.C. Gupta (2016), 3-D velocity structure around tehri region of the garhwal lesser himalaya: constraints on geometry of the underthrusting indian plate. ***Geophys. J. Int.***, 205(2), 900-914.

**Conference Publications**

1. Jyotima Kanaujia, A. Kumar, S. C. Gupta, (2014), Charectoristics of Local seismicity in Garhwal Lesser Himalaya, Abstract in ***10th Asian Seismological commission General assembly, Philippines***.

2. Jyotima Kanaujia, A. Kumar, S. C. Gupta, (2014), "Vp/Vs ratio and Poisson's ratio of the parts of Garhwal Himalaya", Abstract published in Proceedings at ***International Workshop and 3rd Annual convention Advances in Earthquake Sciences-2014***, Indian Seismological Research Institute (ISR), Gandhinagar, Gujarat, India.

3. Kanaujia, , Aswani Kumar, S .C. Gupta, (2 012), 1-D Crustal Model of the Garhwal Lesser Himalaya from Local Earthquake Observations, Proceedings at ***Golden Jubilee Symposium, Indian Institute of Technology Roorkee, Roorkee, India***.

**Poster Published**

1. Jyotima Kanaujia, A. Kumar, S. C. Gupta, (2014), Characteristics of Local seismicity in Garhwal Lesser Himalaya, ***Workshop on Megathrust and Tsunami, International Center for Theoretical Physics (ICTP), Italy***.

# List of Contents

# List of Figures

# LIST OF TABLES

# List of Abbreviations

| | |
|---|---|
| $\sigma$ | Poission's ratio |
| AT | Algar Thrust |
| DHR | Delhi-Haridwar ridge |
| DT | Dunda Thrust |
| MBT | Main Boundary Thrust |
| MCT | Main Central thrust |
| MHT | Main Himalayan Thrust |
| Moho | Mohorovicic discontinuity |
| P | Longitudinal or primary seismic wave |
| P* | Longitudinal or primary seismic wave reflected from the Moho |
| Pn | Longitudinal or primary seismic wave (head wave) refracted on the Mohorovicic discontinuity |
| ST | Siriguri Thrust |
| TT | Tons Thrust |
| UT | Uttarkashi Thrust |
| $V_P$ | Velocity of the longitudinal or primary seismic wave |
| $V_S$ | Velocity of the transverse or secondary seismic wave |
| $V_P/V_S$ | Ratio of P-wave with S-wave |
| S | Transverse or secondary seismic wave |
| S* | Transverse or secondary seismic wave reflected from Moho |
| Sn | Transverse or secondary seismic wave (head wave) refracted on the Mohorovicic discontinuity |
| SNT | Srinagar Thrust |

# Chapter 1

# Introduction

## 1.1 General

The planet Earth forms part of the solar system and resembles like a spherical body, but when viewed from closer distances, detailed structures on its surface become evident. On the magnified scale, many major features such as oceans, mountains, valleys, plains and rivers are visible, and eventually one can see small grains of sand lying on the beach. To comprehend the internal structure of the Earth, one need to dive into the Earth's interior. There, one will experience a complex structure, comprised of zones of various materials with varying physical properties and chemical compositions. As it is difficult to drill beyond 10-12 km, only by the geophysical methods, one can explore the internal structure of the earth. One of the promising ways to study the structure and composition of the earth is from the seismic waves generated by earthquakes. From the study of arrivaltimes of seismic phases and amplitudes of seismic waves, the seismic properties of the Earth's structure at various depths, can be inferred. Many passive and active seismic experiments have been conducted in the last about 100-years to study the earth structure on various scales. These experiments were carried out for the purpose of recording the seismic waves, generated from either natural or artificial seismic sources. These waves propagate through the Earth's interior, and are recorded by a network of seismographs placed normally on the surface of the Earth. By knowing the traveltimes of seismic waves, the velocity structure of the earth along the path travelled by the ray can be determined, by a procedure called seismic inversion. The final goal of seismic inversion is to determine the three-dimensional structure of the interior of the Earth's from a set of 2-D seismic observations at its surface. In spite of last ten decades of seismological research, the work in the area of "seismic tomography", still needs advancement. It's not just because of its intrinsic challenging mathematical and computational necessity, but also because the observed seismic signals often elude a precise and complete analysis and make it difficult to extract the maximum information hidden in the seismic signals. In the present work an attempt is made to carry out seismic tomography around the Tehri region of the Garhwal Himalaya from local earthquake data collected employing a telemetered array.

## 1.2 Historical Development of Seismological Methods

The principal goal of seismology is to measure and interpret the traveltimes of seismic waves produced by earthquakes, nuclear explosions and other artificial sources of energy, and to propose seismological models to describe these arrival times. Tomographic methods using data from teleseismic earthquakes and local earthquakes are powerful means to compute these models. Since 1910, Wiechert introduced the inversion methodology and its application by Aki and Lee (1976) to geophysical problems in teleseismics, there has been significant developments of these techniques, both in terms of computational efficiency and application areas. In this regards the works of Koch (1983a, 1985); Tarantola and Valette (1982a, b); Thurber and Aki (1987), Koch and Kalata (1992), Eberhart-Phillips (1995), Tarantola (1987), Kissling (1988), among others has led to advancements in the tomographic methodology. A brief history of the development of seismic methods and inversion to probe the Earth's interior is given in table 1.1.

The principal goal of geophysical inversion procedures is to acquire a realistic model of a particular physical property of the Earth's interior from the measurement of geophysical data at the Earth's surface. In seismology, from the recorded seismic waves, the seismic arrivaltimes at distinct stations, are measured and used to estimate the seismic structure that provides seismic properties of the earth structure in terms of properties of rocks, magmas, subduction zones, rift zones, volcanoes, etc.

One of the major components of seismological research deals with the study of the near surface structure of the Earth, which is commonly called crust and upper mantle. Near surface is known as the continental crust, whose depth ranges from surface to about 30−40 km, sometimes deeper to about 70 km, and the oceanic crust with a thickness of about 5 − 20 km only and extends upto the first few km of the upper mantle.

The boundary between the crust and the upper mantle is marked by a distinct discontinuity called the Mohorovıcic discontinuity (Moho). This boundary is characterized by a sharp change of physical and chemical properties of the subsurface material that causes a sudden increase in the speed of the seismic waves. Moreover, the sudden change in seismic wave speed at the Moho discontinuity results in the refraction and reflection of the seismic waves which indicate strong vertical seismic inhomogeneity.

**Table 1.1:** Historical development of seismic probing

| Year | Description | Citations |
|---|---|---|
| 1967 | HYPOLAYER: Determine hypocenter of local earthquake in an earth consisting of uniform flat layer over a half space | Eaton, J. P. (1969) |
| 1971 | HYPO71: to estimate the earthquake locations, | Lee et al. (1972) |
| 1972 | Bois, Porte, Lavergne and Thomas deduced 2D velocity structure using cross hole source seismic imaging: well to well seismic measurements. | Bois et al. (1971) |
| 1976 | Aki, and Lee introduced a simple method to infer three dimensional (3D) seismic velocity heterogeneities using body wave arrival times from local earthquakes | Aki and Lee (1976) |
| 1976 | HYPO2D for seismic tomography studies | Ellsworth (1977) and Roecker (1977) |
| 1977 | Spherical harmonic parameterization for mapping of velocity structure of the Earth's mantle by Aki and Dziewinski | Aki and Dziewinski (1977) |
| 1980 | HYPOELLIPSE by Lahr | Lahr (1980) |
| 1981 | Ray-tracing in theoretical Layered-model (Thurber, 1981, 1983; Thurber and Aki, 1987) | Thurber (1981), (1983); Thurber and Aki (1987) |
| 1984 | Estimation of minimum 1-D Model | Kissling et al. (1994) |
| 1985 | SSH Program for simultaneous inversion of hypocenter parameters and velocity model, including a non-linear ray tracing | Koch (1983b) |
| 1985 | Introduction of a non-linear ray tracing for an Improvement in the ACH-method by | (Koch, 1985) |
| 1986 | HYPOCENTER location program using centered, scaled, and adaptively least squares. | Lienert et al., 1986 |
| 1987 | Three dimensional seismic imaging by local earthquake data | Thurber (1981) and Thurber and Aki (1987) |
| 1996 | Joint inversion of reflection and wide angle travel times | Wang and Braile (1996) |
| 1997 | 1997 Joint inversion of travel times and seismic amplitudes (wang and Pratt, 1997; Wang et al., 2000) | Wang and Pratt (1997); Wang et al. (2000) |
| 2000 | Full waveform Tomography | Tarantola (1986), Akçelik *et al.* (2003) |
| 2003 | TomoDD Double Difference tomography by Zhang and Thurber aims to significantly improve hypocenter relocations | Zhang and Thurber (2003) |
| 2009 | LOTOS Simplified Iterative Tomography algorithm for the simultaneous inversion of P and S velocity structure and source coordinates | Kuolakov (2009b) |

## 1.3 Statement of the Problem

The essential goal of this work is to investigate the crustal structure under the Garhawal Lesser Himalaya with a recently developed tomographic inversion method LOTOS of Local Seismic Tomography. Seismological investigations of the Garhwal Himalaya, lies immediately east to the river Yamuna, have attracted the attention of many researchers. This region assumes special importance because many major hydroelectric and other developmental projects have been either commissioned in the region or in the investigation and planning stage. As the region is seismically active, efforts have been made by various research groups to continuously monitor the local seismicity of the region (Khattri et at., 1987; Kumar et al., 1994; Kumar et al., 2012; Wasson and Sharma 2000). The need for an accurate model of the 3-D P- and S-wave velocity structure at Garhwal Himalaya is fundamental to most of the studies underway as part of the monitoring program there. Hypocenter locations, focal mechanisms, source moment tensors, inversion for velocity, attenuation or anisotropy, analysis of controlled-source data, and any other calculations relying on the geometry of seismic wave ray paths within or near the fault zone, all depend critically for their accuracy on a realistic 3D velocity model for P and S waves. Additionally, inference on the variations in physical properties within and along the fault zone to a scale of a few kilometers may provide valuable details on the segmentation of the fault zone, on the nature and distribution of fault zone materials, and on the locations and extent of possible asperities or nucleation zones.

## 1.4 Objective and Goals of the Thesis

According to the statement of the problem mentioned above, the major goal of this thesis is to estimate an improved 1-D and the 3-D velocity structure of the Garhwal Lesser Himalaya and to study the contemporary seismicity of the region. The improvement consists of the application of the recently developed tomographic algorithm of simultaneous inversion and the data set collected through the local seismological network deployed in the study region. The broad objectives of the thesis are listed out as follows:

- Estimation of 1-D velocity model for the Garhwal Himalaya region using local earthquake data.
- Characteristics of local seismicity based on the 1-D velocity model.
- Estimation of 3-D velocity model for the region along with travel time tomography using local earthquake data
- Inversion results and their discussion
- Revisit of seismicity based on estimated 3-D velocity model

## 1.5 Plan of Thesis

The thesis comprises seven chapters. *Chapter 2* contains a brief description of the various methods employed to model 1-D and 3-D velocity structure (seismic tomography) and mathematical background to solve the travel time tomography problem. This chapter also provides brief overview of new ways that have been evolved to exploit seismic traveltime information and to solve tomographic problems and review of the various velocity model developed for the northwestern Himalaya.

*Chapter 3* deals with the estimation of a one-dimensional (1-D) velocity model around the Tehri region of the Garhwal Himalaya from the simultaneous inversion of traveltimes data of local earthquakes. The study of the characteristics of local seismicity based on the spatial and depth distribution of events located using the 1-D velocity model is described in *Chapter 4.*

The inversion of the three-dimensional crustal velocity structure beneath the Tehri region of Garhwal Himalaya from local earthquake data, and description of anomalies observed on the tomograms is a subject matter of *Chapter 5.*

The relationship of the 3-D velocity structure with the local seismicity and tectonics of the region has been described in the *chapter 6*. Chapter 7 includes the summary of results, limitation and scope for future work.

# Chapter 2

# Travel Time Inversion: Theory and Literature Review

## 2.1 Introduction

Seismic data represent one of the most valuable resources to study the structure and composition of the Earth's interior. A. Mohorovicic, a Serbian seismologist, was the first to deduce earth structure from seismic records, in 1909. He noticed two branches on the traveltime graph from an earthquake occurring at a regional distance, and interpreted that one of the branch represents arrivaltimes of direct wave and the other branch represents arrivaltimes of refracted wave from a discontinuity. This discontinuity marked the sharp change in the elastic properties between the crust and upper mantle, and is called the Mohorovicic discontinuity. The technique of Herglotz and Wiechart (see, for example, Gubbins, 1992) was the first to be used in 1910 to construct a one-dimensional model of the whole earth. The method uses the relationship between angular distance and ray parameter to determine velocity as a function of radius within the earth (e.g., Rawlinson & Sambridge 2003).

Now days, a large number of methods are available to determine earth structure from seismic waves. These methods make use of different components of the seismic records which includes: arrival times of seismic phases, amplitudes of seismic waves, spectra of P-, S- and surface waves, and full waveform of the recorded signal. Source-receiver geometry, type of sources and scale of study also differ. For example the layout of network stations may be 1-D, 2-D and 3-D, sources may be located near or far from the stations, sources of seismic waves may be natural or man-made, and the scale may vary from few meters to thousands of kilometres. Finally, there are multitudes of ways of translating the data extracted from the seismograms to a representation of seismic structure.

In this chapter a brief review of seismic traveltime tomography to image earth structure has been presented. This technique is based on inverting traveltimes of seismic waves to determine 2-D and 3-D structure of the Earth. The word *tomography* literally means *slice picture* (from the Greek word *tomos* meaning *slice*). This term was first used in medical imaging to describe the process of mapping the internal density distribution of the human body using x-rays (Lee & Pereyra, 1993) (CT-scan). The term was later adopted by the seismological community to describe a similar process to map the earth structure using seismic waves. Seismologists now routinely use *tomography* to refer to the three dimensional model of the earth; however, the word was originally designed to describe the imaging of 2-D horizontal slices of the Earth only. Although, the basic theory behind seismic tomography and CT-scan is similar, but these techniques differ in their technical details. The CT-scan allows measuring data at large number of points because locations of these points can be controlled and thus high-resolution image of the human body can be obtained (e.g., Carlson, 2006; Zhao, 2015). However, in seismic tomography we do not have any control on sources and receivers, because about 90% of earthquakes occur along the plate boundaries. Further, there is a huge cost involved in the installation and maintenance of seismic stations. In view of this it is difficult to image the subsurface Earth's structure from seismic tomography as precisely and accurately as the CT-scan of the human body.

## 2.2 Classification of Seismic velocity Modelling

For the last about four decades the area of velocity modelling has witnessed a rapid progress. Currently, it is a vast field that covers various aspects of solid earth sciences. An extensive research has been carried out with an aim to seek solutions for different tomographic problems. Different types of terms are used to classify tomography in terms of data used, the lateral extent of the study region, depth range of modelling space, and relative distance between the seismic-station network and the seismic events used.

Based on seismic data used, tomography can be classified into two types: body wave tomography (BWT) and surface wave tomography (SWT). BWT (Fig. 2.1) is the most widely used tomography, and when it is based on inversion of P- and/or S- wave travel time data it is called travel-time tomography. Fig. 2.1 shows the paths of seismic rays in four cases of BWT. SWT makes use of dispersion data of Rayleigh waves or Love waves to estimate the 3-D crustal velocity structure. Waveforms of seismic waves have also been used to conduct waveform tomography.

According to the scale of study areas there are three types of tomography: local, regional and global (Fig. 2.1). In case of local tomography the study area is small and normally varies from a few kilometers to hundreds of kilometres. In regional tomography the study area varies from about few hundered kilometers to a few thousands of kilometers. In global tomography (Fig. 1 (d)) the area encompasses the entire mantle or whole Earth (e.g., Inoue et al., 1990; Vasco et al., 1995; Zhao, 2001).

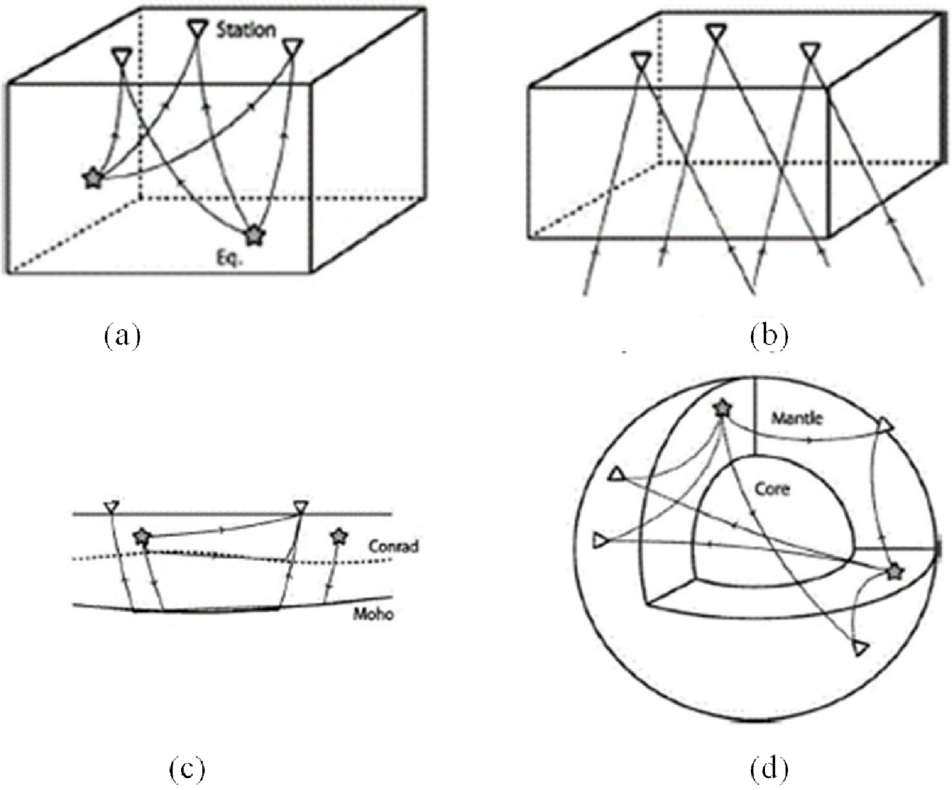

**Figure 2.1:** Various approaches of body-wave tomography. (a) Local earthquake tomography; (b) teleseismic tomography; (c) determining the Conrad and Moho geometry; (d) global tomography (Zhao 2009)

Based on the depth-range of modelling space there are crustal, mantle and core tomography. Depth range of crustal tomography varies from surface to Moho depth or upto the upper mantle, and carried out from the travel times of crustal phases. Depth range of mantle tomography extends upto the upper and lower mantle. Crustal tomography usually involves local earthquake tomography and its range depends upon the diving depth of P- and S- waves, and epicenteral distances. The tomography for depths upto 670 km discontinuity is called upper mantle tomography and for depths upto core mantle boundary is called mantle tomography. Core tomography is Global in nature and makes use of core phases to estimate the velocity structure of the Earth’s core. (e.g., Lei and Zhao 2006).

Based on the distance between seismic network and seismic events, tomography can be divided into two types: local earthquake tomography (LET) and teleseismic earthquake tomography (TET). In the LET (Fig. 2.1 (a)), seismic stations and events considered fall within the study area (e.g., Aki and Lee, 1976; Thurber, 1983; Zhao et al., 1992). LET is carried out from the inversion of traveltimes direct crustal phases (e.g., P- and S- waves). In TET (Fig. 2.1 (b)) 3-D velocity structure beneath a seismic network is estimated from P- or/and S- wave data from teleseismic earthquakes and/or artificial explosions. In the TET the seismic events are located far away from the seismic-network. These are called teleseismic events (with epicenter distance 30°-100°) and their travel times can be used to estimate velocity structure up to lower mantle.

## 2.3 Overview of Various Methodologies used to Study Velocity Structure

The estimation of velocity structure involves finding the information about the Earth structure in terms of velocities and thickness of the various layers. Accurate velocity structure is important, in locating earthquakes, determining the composition and origin of the outer layers of the earth, interpreting large-scale tectonics, and estimating strong ground shaking. Several methods are available to estimate velocity structures, and each method has advantages as well as shortcomings in specific applications. These methods can be classified based on various factors, such type of data available/used and the scale of study (local/regional/global). Some of the methods include: explosion seismology, surface wave dispersion, use of crustal phases and teleseismic phases, receiver function/crustal transfer function, waveform modelling, and use of reflection phases. A brief overview of these methods is given below:

**Explosion Seismology:** Explosion seismology has been used to map the velocity structure of both continental and oceanic regions. Most of the work done using explosion seismology is based on measurements of arrival-times of direct and refracted seismic phases. Some of the difficulties and limitations in the interpretation of the explosion generated data are well known (e.g., Carpenter 1965; Kosminskaya 1969). For example, Initial arrivals may fail to indicate transitional layering and unable to detect low-velocity-layers. The incorporation of arrival-times of refracted and reflected phases and their amplitudes as well as wide-angle-reflections have been attempted to overcome these shortcomings (e.g., Landisman et al., 1971; Mueller and landisman, 1966). However, substantial difficulties were encountered while assessing the reliability of different type of dataset (Healy, 1971).

**Reflection Measurements:** Measurements of timings of reflections from explosions have been used to determine shallow layering, but it has been recognized that to improve the interpretation of sub-surface structure additional information of velocities is normally required. Deep crustal reflection measurements became more common with the increased sophistication of recording equipment (e.g., Perkins and Phinney, 1971). Drill-hole data provides detailed knowledge about the shallow velocity structure (e.g., sonic velocity log), but such investigations are restricted in scope because they provide only localized information from very shallow depths.

**Dispersion of Surface Waves**: In the period range from 1 to 30 sec, dispersion of surface waves has been used to study the crustal structure (e.g., Bucher and Smith, 1971; Ewing and Press, 1959). Theoretically surface waves are sensitive to low-velocity zones, but in practice, these waves are unable to map detailed crustal structure. However, studies based on P wave delay times from teleseismic earthquakes in conjunction with gravity or surface wave data may provide additional constraints on average crustal velocity and layer-thickness (Press and Biehler, 1964)

**Waveform Inversion Tomography:** These techniques make use of the original waveforms and wave equation modeling to obtain the high resolution images. The Full waveform inversion technique involves constructing earthquake source and earth structure models from the analysis of the complex waveforms recorded by modern broadband seismographs. Techniques dealing with waveform inversion can be broadly divided into two categories: (a) direct waveform fitting techniques that map waveform mismatches directly to model parameter perturbations (Tarantola, 1986; Nolet, 1990; Akçelik *et al.*, 2003; Tromp *et al.*, 2005), and (b) data functional techniques that isolate the waveform-fitting step, which is nonlinear, from the inversion step, which is linear or can be linearized. The data functionals are estimated from seismograms that on one hand can quantify waveform misfit and on the other hand can be used as linear constraints on the model parameters (Gee & Jordan 1992; Gaherty *et al.*, 1996; Katzman *et al.*, 1998).

**Travel Time Inversion:** This is the most popular and robust technique that depends on the Ray theory and Fermat's principle. This has been widely used to image subsurface structure at all scales (Global, local and regional) from the inversion of source-receiver traveltimes of seismic waves. For imaging crustal and lithospheric structure this method was introduced in the mid 1970s (Aki, 1976) which is now widely known as travel time tomography. Travel time tomography seeks to estimate the velocity of propagation of seismic waves from the first arrival times. The inverse problem is formulated in the terms of the difference between observed and estimated traveltimes from known sources (earthquake events) to the location of seismic receivers (recording stations).

**Finite-Frequency Traveltime Tomography**: These methods aim at obtaining a higher resolution, and their mathematical formulations include the effects of wave diffraction. Ray paths are replaced by volumetric sensitivity kernels. Methods stem from the banana-doughnut sensitivity kernels, and consider finite frequency effects. The formulation considers frequency-dependent travel time and amplitude anomalies to achieve increased resolution (e.g., Dahlen et al. 2000; Pollitz 2007; Zhang et al. 2011). The technique provides an accurate estimate of amplitudes of velocity anomalies and their spatial resolution. This happens because the method takes into account the physics of wave propagation. This method is useful to map near-surface strutures where infinite-frequency (ray) theory has limitation because of the length scales of hetrogeneties, which at times comparable to or smaller than the wavelengths of seismic wave.

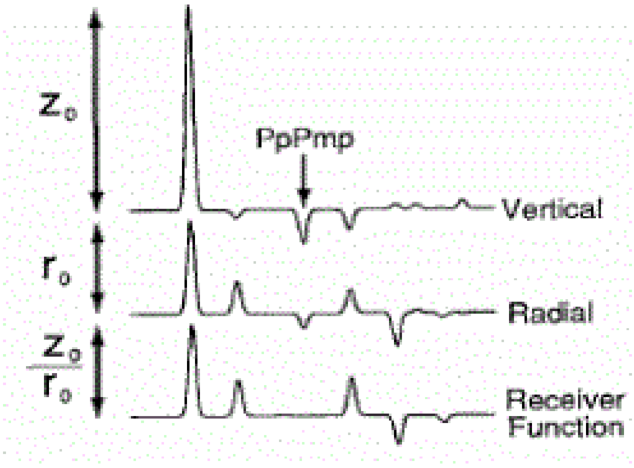

**Figure 2.2:** Vertical and radial receiver function calculated for a single layer over a half-space. The amplitude relationships are shown to the left of the traces. (Ammon, 1991)

**Receiver Function Analysis:** Burdick and Langston (1977) found that some energy traces in SV component near the P wave arrival times and inferred that it was attributed to converted seismic wave because of crustal discontinuity near the station. They carried out forward waveform modelling by taking different crustal velocity structures and obtained similarities between computed and observed waveforms. The computed time series based on three component seismograms provided information on earth structure beneath a seismic station. Thus, it was recognised that P to S converted phases contain information about the Earth structure between discountinuity and station. An algorithm to compute RF was developed by Park and Levin (2000) using Multiple-Taper spectral correlation. This method was further improved by Helffrich (2006) so that it can be applied to a longer time series. Ammon (1991) introduced an inversion method based on spectral deconvolution (Clayton and Wiggins, 1976) to estimate the velocity structure without a-priori knowledge of the local velocity model. The method involved deconvolution of the radial component from vertical component and resulted in the retrieval of response whose peaks indicates positive or negative velocity anomalies.

Because this provides structure beneath the recording station (receiver), it is called a “Receiver Function” (Figure 2.2).

A number of other techniques have also been used to obtain crustal structure, such as: studying the particle motion of Rayleigh wave (Boore and Toksoz, 1969); the use of crustal transfer function and spectral ratio between observation at different localities (e.g., Ellis and Basham, 1968; Phinney, 1969; Bakun, 1971); and determination of lateral velocity variations using least squares inversion of refraction measurements (Wesson, 1971). However, these and many other techniques have specific advantages as well as disadvantages and no single techniques are universally applicable to estimate the crustal structure.

As the scope of this thesis is limited to travel time tomography, the following sections are developed to the mathematical formulation of the problem and procedure to perform the inversion.

## 2.4 Development of Seismic Tomography

The propogation of seismic wave from source to receiver are affected by the physical properties of the medium such as: elastic, anelastic, and anisotropic parameters, and density. Seismic tomography is a promising technique to map the 3-D distribution of these properties. Tomographic models have helped analysing the subsurface–lithological structure, temperature, fracturing and faulting processs, fluid content, etc. Seismic tomography began in the mid-1970s, and has advanced to become an important mapping technique. The roots of this technique can be traced back to the research work of Keiiti Aki and co-workers. This work on regional and local-scale BWT began in 1974. Further, the work of BWT on global-scale was started by Dziewonski and co-workers in 1975 (Dziewonski et al., 1977). These early works were referred as 3-D inversion and 3-D perturbations of velocity structure instead of seismic tomography.

Radon (1917) developed theoretical background necessary to solve tomography problems. Reagan (1978) and Clayton and Hearn (1982) used the term seismic tomography first time in the study of seismic reflections and seismology, respectively.

Many different types of tomography find applications in many areas of science and technology such as medicine, biology, materials science, geology and geophysics. The basic objective of tomography is to obtain a cross-section of an object’s internal structure to infer its various properties (Nowack and Li, 2009).

The way medical tomography uses radiation and magnetic fields to image the structure of the parts of the human body, on similar principles seismic tomography can be used to produce the images of the Earth. The main aim of seismic tomography is to study the subsurface structure of the Earth on a different scale and to advance the knowledge of the Earth's internal structure. Based on the scale, seismic tomography can be divided into global and near-surface tomography. As stated earlier, the global tomography based on the data obtained from teleseismic earthquakes. And near-surface tomography deals with the mapping of the shallow subsurface structure--- a few kilometres deep, covering parts of the crust and upper mantle. The focus of the further sections is on near-surface tomography.

## 2.5 Local Earthquake Tomography

Aki & Lee (1976) were the first to study seismic tomography from the inversion of first-arrival P-wave traveltimes from local earthquakes. They estimated velocity structure and hypocenter locations in Bear Valley, California. The source-receiver geometry for this type of study is shown schematically in Figure 2.1 (a), the earthquake sources lie beneath the receiver array within the model volume. The study suggested that hypocenter coordinates, which are not accurately known, must be included in the inversion. Since this work, this branch of seismic tomography is popularly known as Local Earthquake Tomography or LET (Thurber, 1993). Aki & Lee (1976) used a constant velocity block parameterization using a homogeneous initial model and a linear inversion. Thurber (1983) used an approximate ray tracing (ART) method to facilitate an iterative non-linear inversion of P-wave traveltimes for continuously varying velocity structure and hypocenter locations. In many studies S-wave data is also included in their analysis to allow inverting for $V_P/V_S$ ratio also (e.g., Graeber & Asch, 1999). These studies suggested The VP /VS ratio is a better indicator of hydration levels than the $V_P$.

The Drawback of LET is that it can only be conducted in seismically active regions, usually located at or near the plate boundaries. LET has been carried out in many different regions including California (Aki & Lee, 1976; Thurber, 1983; Eberhart-Phillips & Michael, 1993), Taiwan (Kao & Rau, 1999), Japan (Zhao et al., 1992), South America (Bosch, 1997; Graeber & Asch, 1999), South Australia (Greenhalgh et al., 1989), Tiwan (Ustaszewski et al., 2012; Huang et al., 2014), and the Mediterranean (Luca et al., 1997; Papazachos & Nolet, 1997).

LET has been able to image the lithosphere and upper asthenosphere up to depths of 200 km in subduction zone settings (e.g., Abers, 1994; Graeber & Asch, 1999). High resolution images of the crust have also been obtained using shallow earthquakes (e.g., Thurber, 1983; Chiarabba et al., 1997). Advantages of LET include greater depth of penetration and the added structural information provided by the relocated hypocenters, e.g. the existence of double seismic zones (Hasegawa et al., 1978; Kawakatsu, 1985; Kao & Rau, 1999). However, the relocated hypocenters add to the non-uniqueness of the solution, and other phases (except first P and S arrivals) are difficult to incorporate. For this reason, LET models rarely include interfaces, although Zhao et al. (1992) included interfaces in their LET model of NE Japan by using observed SP waves converted at the Moho and PS/SP waves converted at the upper boundary of the subducted Pacific Plate.

## 2.6 Travel Time Tomography

In simple term travel time tomography is a more accurate way of referring to seismic tomography. In this technique, the important parameter to study the subsurface structure is the travel time of seismic wave. The term travel time refers to the time taken by a seismic wave from a source to the recording station after propagating through different types of subsurface structures including the reflecting boundaries. Travel time tomography seeks to estimate the propagation velocities of seismic waves from the measurements of first arrival times. Generally speaking, this data rarely fit a straight line exactly because of scatter in the data, but we attempt to "fit" a straight line—called a line of best fit. This allows the estimation of an initial velocity model which can be then be utilized for preliminary interpretation of the subsurface structure, and can serve as an initial velocity model to initiate inversion. When the 1-D model is estimated, the next step is to parameterize the 3-D velocity structure into uniform blocks of velocity perturbations. The block parameterization includes dividing a three dimensional medium represented by geometrical model into similar size blocks as illustrated in Figure (2.3). The model contains in general all paths connecting the sources and receivers. The next challenging step is to trace the exact ray path, and this is not a straightforward exercise. Several methods have been developed for solving the problem of two point rays tracing. The well-known techniques includes, the shooting method—in which the source is sampled in order to converge on the correct receiver location and the bending method— where the source and receiver are kept fixed and try to bend the ray. Other than these finite difference or graph theory, techniques have also been used. These techniques require a grid of points for ray tracing rather than block parameterization.

The travel time data required for travel time tomography become available from the analysis of suit of seismograms collected from various recording stations. The accurate picking-up different types of seismic phases requires considerable insight and experience. Picking of first P- and S-phases are considerably simple and straightforward compared to other seismic phases. From this observed travel time data, an initial velocity model is estimated adopting linear regression and an appropriate inversion technique. Obviously the data predicted from the estimated model cannot exactly match the predicted data, because of uncertainties due to the errors in picking arrival times of phases and various other factors such as: signal to noise ratio, instruments measurements and site. Due to this, we define the travel time residuals ($\delta t$) as the difference between the observed and predicted travel times and these residuals can be represented as the sum of three terms

$$\delta t = \delta t_{3D} + \delta t_{mislocation} + \delta t_{noise}$$

Considering that seismic waves are analogous to acoustic sound waves—the propagation velocity of which is known for a certain medium—we can translate the velocity information to characterize the properties of substance, structure present below the Earth's surface and thus gain a better understanding of its structure and composition. The general procedure adopted in travel time tomography can be summarized as follows:

- The first step involves identifying and reading the arrival times of seismic phases of the earthquake records collected from various seismic stations.
- The next step involves gaining an understanding of the distances travelled by seismic waves from sources to the receivers. For this we need to make assumptions on velocities. This step is accomplished by ray tracing—based on the theory of seismic wave propagation within various media. The results of ray tracing allow approximating the distances travelled from sources to receivers adopting different paths from various reflecting layers.
- In the third step, using the data from the previous two steps, the travel time equations are solved for velocity parameters. This is also known as travel time inversion because we start with observational data and infer the model parameters that could explain this data.

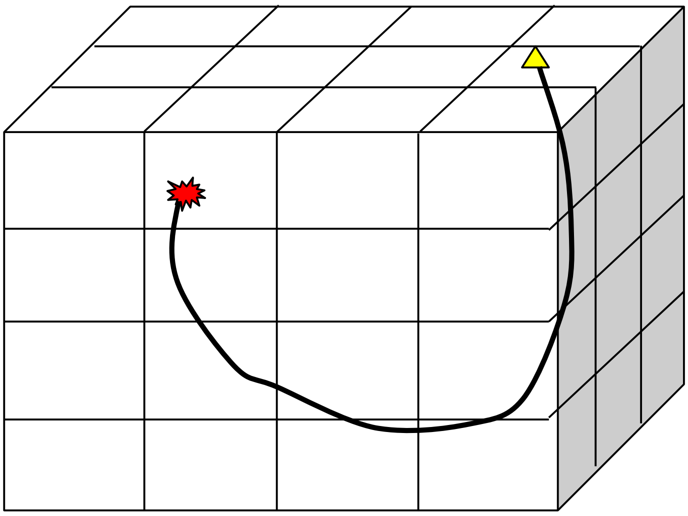

**Figure 2.3:** An example of ray path in 3-D media with different velocity blocks for tomographic inversion

### 2.6.1 Forward and Inverse Modelling

The travel time inversion used in the seismic tomography is called the inverse modelling. It is appropriate to mention the differences between forward and inversion modelling to gain a better insight of these modelling techniques.

Forward modelling involves predicting the data that an experiment would likely to produce. In the context of Earth Sciences, this means we should have a prior knowledge of the subsurface geology of the study area. After deciding the type of experiment we are likely to conduct, the model parameters for data acquisition can be inferred for such an experiment. Based on the theory and physical processes we then can predict the data from the model parameters of the geological model. However, inversion deals with how to estimate model parameters after physically running an experiment. The known data here consists of the data acquisition parameters and the data produced from the conducted experiment. We then apply a series of mathematical methods to obtain a subsurface geological model from the experiment.

While the two methods work at opposite ends they can be combined with one working as a test for the other. Any geophysical inversion can allow us to obtain a model of the subsurface structure, which fits observed data. Forward modelling is used to establish the relation between the subsurface model and the observed data. If M is a model and D is observed data, then forward modelling can be expressed as:

$$F(M) = D \tag{2.1}$$

Where; F is a forward modelling, operator, which calculates geophysical data D for a given M. Then inversion can be described as solving equation (2.1) for unknown model M. As the inverse problem is usually ill-conditioned, additional constraints are imposed and play an important role in traveltime inversion. Objective function of equation (2.1) can be minimised using L2 (the least square method) or L1 norm. L1 nomrs is more stable when there are spikes and large errors in traveltimes.

For seismic traveltime inversion, the model (2.1) is the most commonly used models. In this model D is observed traveltimes, M is a depth, velocity model and F is a forward modelling, operator, which calculates traveltimes of seismic phases.

### 2.6.2 The Non-Linearity of Tomographic Inversion

If the relation between the model parameters and the data would be linear, a result could be easily obtained. However, the tomographic problem in principle is non-linear, because the data depend on the model parameters, and the ray-path geometry. In order to be able to invert for the model parameters, the tomographic problem needs to be linearized around an approximate ray-path. Approximate ray-paths can be defined by the introduction of an initial model of the subsurface. In this initial model, the approximate ray-paths of the focusing operators can be calculated. The difference between the traveltimes of the modelled ray-paths and the observed traveltimes becomes the data to be inverted. As a consequence, the output of the inversion represents the difference between the initial model and the actual subsurface model. This relation is assumed to be linear, and forms the basis of many tomography studies [Tarantola, 1986; Nolet, 1987; Scales, 1987; Phillips and Fehler, 1991]. The relation is represented as:

$$\Delta d = A\Delta m \tag{2.2}$$

Where; Δd is the vector that contains the traveltime differences for all measurement locations, Δm is the vector that contains the model parameter updates, and A is the matrix that describes a linear relation between the differences in traveltimes and the model parameter updates. In this way, the tomographic problem is linearized, and the inversion of the traveltime differences leads to an update of the initial model parameters. It is to be noted that this linear relation is only an approximation of the true relation between Δd and Δm. In the updated model, new traveltime differences can be calculated and these differences can be inverted again, and so on. This iterative process is commonly denoted as non-linear tomography.

### 2.6.3 Method of Traveltime Inversion

In order to set up the non-linear tomographic system for the focusing operators, the following steps should be followed:

(1) Model parameterization: A set of model parameters are defined to represent the seismic structure of the area being mapped. In tomographic methods normally the preliminary estimates of model parameter have to be specified.

(2) Forward modelling: Procedure has been defined to calculate traveltimes in the initial velocity model for the source—receiver pairs. The traveltime differences between the observed and estimated traveltimes are calculated.

(3) Optimization or inverse modelling: the differences between the traveltimes of the observed and estimated traveltimes are minimized, in order to optimize the model parameters. And the adjustments of parameters are then automated to the initial parameters.

Once the velocity model is revised in the third step, we return to the second step, to further optimize the velocity model. This procedure is repeated till an accurate velocity model is obtained. In the subsequent sections further details are provided regarding the parameterization, the forward modelling, and the optimization.

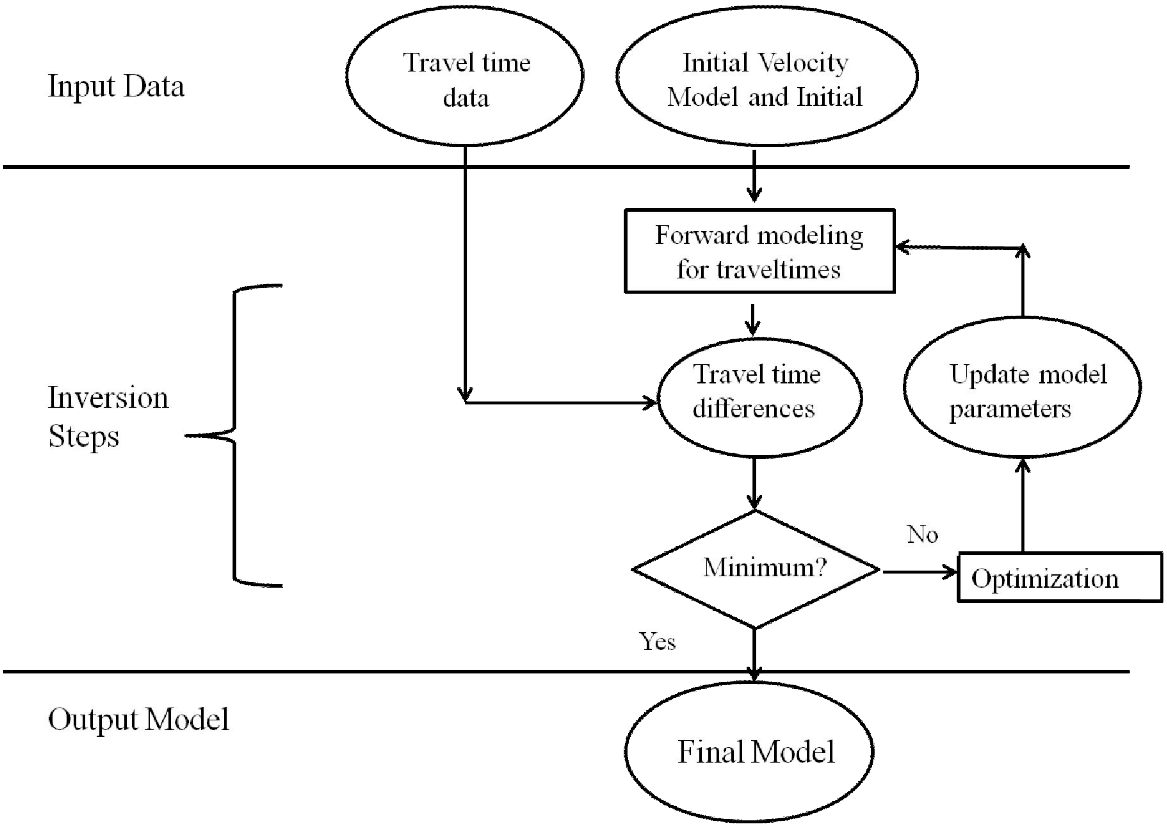

**Figure 2.4:** Flowchart of tomographic inversion

### 2.6.3.1 Parameterization of Structure

**1-D Velocity Structure:** One dimensional crustal velocity models find applications in a large number of research areas in seismology. These models are adopted to estimate hypocenter parameters and focal mechanism solutions. These models can be adopted as initial models to develop 2-D and 3-D velocity models (Kissling *et al.* 1994). The traveltimes of seismic phases have been widely used to develop a 1-D velocity model (Crosson 1976; VanDecar & Crosson 1990). The 1-D Earth model represents the Earth composed of constants velocity layers (fig. 2.5), varying with increasing depths. A number of forward modelling and inverse modelling techniques was developed to estimate the velocity structure as a function of depths from traveltimes and wavefield. These techniques include reflection method, Herglotz-Wiechert inversion, and tau-p inversion (Aki and Richert 2002; Clayton and McMechan, 1981; Fuchs and Muller 1971).

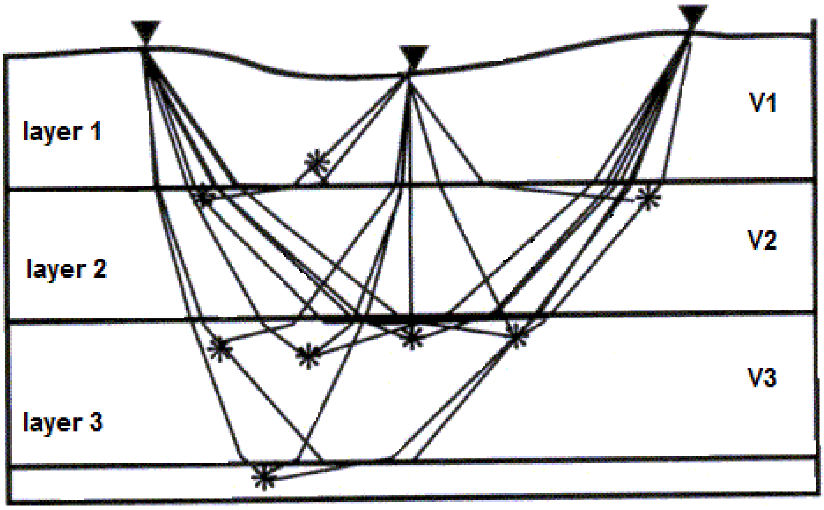

**Figure 2.5:** A systematic representation of 1-D velocity model having three layers with varying velocity along with traveled ray peths from source receiver pairs

**3-D Velocity Structure:** The velocity model of the region is defined by unknown model parameters. In the tomographic inversion, these parameters include the subsurface parameters that influence the traveltimes, the velocities, and the locations of the sources. Tomographic methods normally need preliminary estimates of the model parameter. The velocity parameterization is more complex and describes a complete area or volume, and the source parameters describe the position of each source. The key to the success in tomographic inversion is defining of an optimum number of parameters that accurately describe the subsurface velocity structure.

The traveltime of a seismic wave between source and receiver is solely depends on the velocity structure of the medium through which the wave propagates. Therefore, subsurface structure in a seismic traveltime inversion is represented by variations in P- or S-wave velocity (or slowness). Velocity variations may be defined by a set of interfaces whose geometry is varied to satisfy the data. These variations are represented by a set of constant velocity blocks or nodes with a specified interpolation function, or a combination of velocity and interface parameters (Fig. 2.6). The most appropriate choice will depend on the *a priori* information (e.g., known faults or other interfaces), whether or not the data indicates the presence of interfaces (e.g., reflections, mode conversions), whether data coverage is adequate to resolve the trade-off between interface position and velocity, and finally, the capabilities of the inversion routine. There are several methods for parameterization of the subsurface model. Some of them are discussed below:

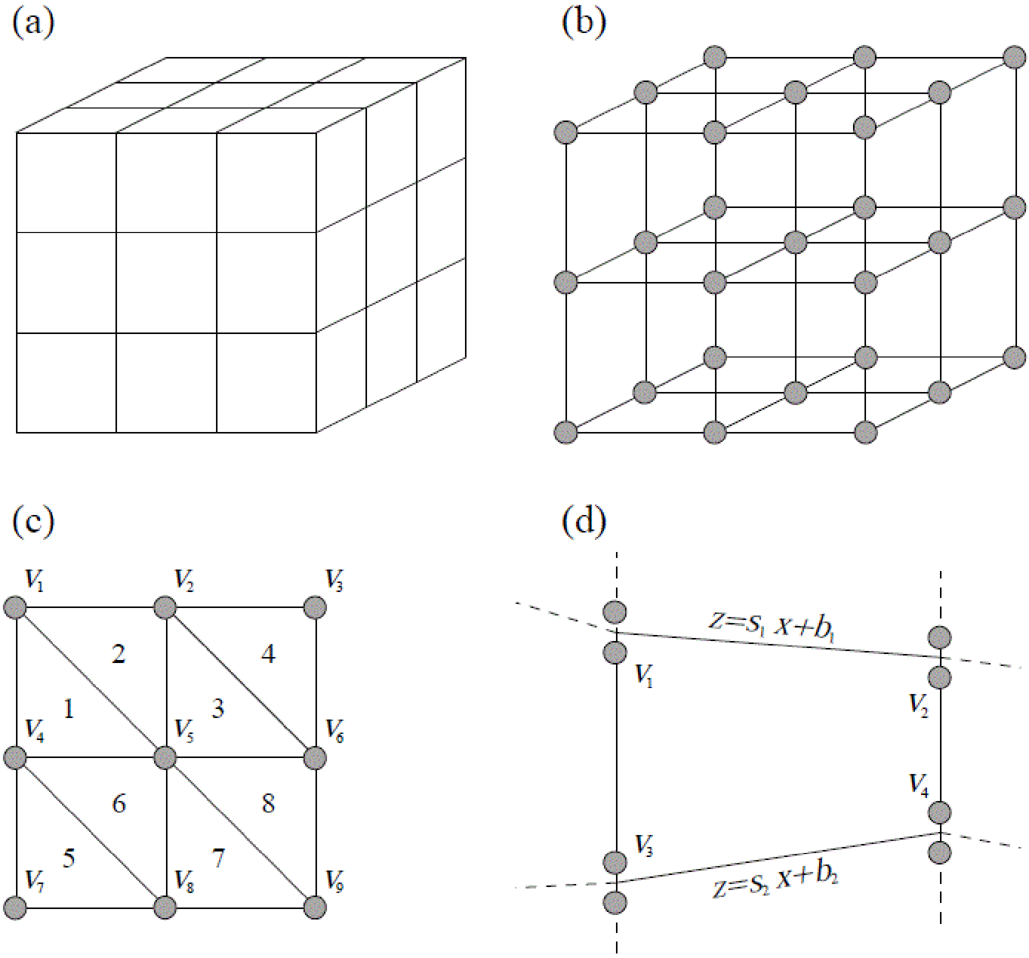

**Figure 2.6:** Different types of velocity parameterisation: (a) constant velocity blocks, (b) a grid of velocity nodes, (c) triangulated velocity grid designed for constant velocity gradient cells (after White, 1989), (d) velocity defined by a trapezoidal block (after Zelt & Smith, 1992). The four corner vertices labelled $V_1$ to $V_4$ define the velocity within the block. If adjacent nodes in vertically adjacent blocks are the same, velocity will be vertically continuous If not, then a sub-horizontal interface will be defined

**Constant Velocity Blocks:** (Fig. 2.6a) constant velocity blocks are simple to define and allow rays to be traced in a straightforward manner. Their use in inversion is to recover smooth variations in velocity. Although this parameterisation is not optimal for such a purpose, if a large number of blocks are used and smoothing is applied, then an acceptable approximation to a continuously varying velocity field is possible.

**Grid of Velocity Nodes**: An alternative approach to represent a velocity field is to define a set of discrete velocity nodes on a grid (Fig. 2.6b) together with a specified interpolation function. This approach was adopted by Thurber (1983) for local earthquake tomography. He used following function to describe the velocity at any point (x, y, z) within a rectangular grid of nodes:

$$v(x,y,z)=\sum_{i=1}^{2}\sum_{j=1}^{2}\sum_{k=1}^{2}V(x_i,y_j,z_k)\left(1-\left|\frac{x-x_i}{x_2-x_1}\right|\right)\left(1-\left|\frac{y-y_i}{y_2-y_1}\right|\right)\left(1-\left|\frac{z-z_i}{z_2-z_1}\right|\right) \tag{2.3}$$

Where; $V(x_i, y_j, z_k)$ is the velocities values of at the eight grid points around $(x, y, z)$. Equation 2.3 ensures that the velocity field will be continuous throughout the model volume, although the velocity gradient will be discontinuous from cell to cell. Needless to mention, that during the inversion process too many parameters result in an under-determined system, while too few parameters will be unable to describe the subsurface structure. Therefore, for the velocity parameterization it is important to find a method that optimally describes the subsurface.

**Constant Velocity Gradient Cell:** This method goes somewhat towards bridging the gap between a block approach and a grid approach and uses cells with a constant velocity gradient. White (1989) described a method of 2-D refraction tomography in which a rectangular grid of nodes was used to define triangular regions of constant velocity gradient (see Figure 2.6c). The velocity within each cell is defined as:

$$v(x,y)=v_0+(x-x_0)\nabla_x v+(z-z_0)\nabla_z v \tag{2.4}$$

where, $v_0$, $\nabla_x v$ and $\nabla_z v$ are computed from the velocities at the vertices of the triangle (e.g. $v_0$ = 1, $\nabla_x v$ = $(v_2 - v_1)/\nabla x$, $\nabla_z v$= $(v_5 - v_2)/\nabla z$ in cell 1 of Fig. 2.6c). In this method velocity varies continuously throughout the medium, the rays are traced analytically within each cell. However, the velocity gradient is discontinuous at each cell boundary which, in conjunction with their triangular shape, can result in difficulties in finding the source-receiver ray path. Similar methods were used by Chapman & Drummond (1982) and by Bishop et al. (1985).

**Irregular Grid Nodes**: The use of irregular blocks or grid nodes to describe the velocity distribution is not very common in traveltime tomography. However, irregular shaped elements can be adapted to suit variations in subsurface data coverage. The 2-D wide-angle inversion method of Zelt & Smith (1992) used such a method. The velocity field is discretized into a series of trapezoidal blocks, with four corner vertices used to specify the velocity within the block. Figure 2.6d shows the design of the trapezoid. The velocity within the trapezoid is given as (Zelt & Smith, 1992):

$$v(x,z)=\frac{c_1x+c_2x^2+c_3z+c_4xz+c_5}{c_6x+c_7} \tag{2.5}$$

Where; $c_i$'s are linear combinations of the corner velocities (see Zelt & Smith, 1992). Discontinuities are permitted in the velocity field through the inclusion of pairs of nodes on sub-horizontal boundaries (see Fig. 2.6d). If these nodal values are equal, the velocity field is continuous. The inherent flexibility of this technique means that a velocity structure with or without layering can be represented. If layers are present, then it is possible to vary velocity within the layers arbitrarily. Pinchouts and isolated bodies can be represented by using three-sided blocks. Finally, the size and shape of the trapezoids can be varied to suit the resolving power of the dataset.

### 2.6.3.2 The Forward Problem of Travel Time Determination

The forward problem involves calculating theoretical traveltimes of seismic waves---between the source-receiver pairs, travelling through the earth's 3-D structure for a given model M. The traveltimes are computed by the ray-tracing, form hypocenter to the recording station placed on the earth's surface. The ray in simplest form is represented by a straight line connecting the source and receiver. But, this representation is not sufficiently exact in practical applications. A better method is to assume that the seismic velocity increases with depth and the ray path forms a part of a circle connecting the source and receiver. However, the best approximation of ray tracing is to include refraction and reflection at the layer boundaries or the vertical boundaries of the blocks. Some of these parameters and their methods of computation are described in the below.

We express the traveltime of a seismic wave between source S and receiver R the following integral:

$$t=\int_S^R \frac{1}{v(x)}dl \tag{2.6}$$

Where; *dl* is differential path length, *x* is the position vector and *v* is velocity. In order to evaluate this integral the path taken by the seismic ray should be known. However, we face difficulty in performing this integration because the path taken by the wave is not known as it depends on the velocity structure. The equation that governs the geometry of ray paths can be derived from the eikonal equation by considering how a small change in time *dt* effects a point x on a wavefront (see Aki & Richards, 1980). The resultant *ray equation:*

$$\frac{d}{dl}\left(\frac{1}{v(x)}\frac{dx}{dl}\right)=\nabla\left(\frac{1}{v(x)}\right) \tag{2.7}$$

In traveltime inversion, the traditional methods of determining source-receiver traveltimes is ray tracing. These methods of traveltime determination are described below.

**Ray Tracing:** The problem of finding a ray path between a source and receiver is a boundary value problem. There are two basic methods to obtain the solution methods, viz, shooting and bending.

**Shooting Method: In this method** the ray equation (Eq. 2.7) is formulated as an initial value problem, and a complete ray path can be traced. However, the initial data in the form of source coordinates and takeoff angle of the ray are to be specified. The boundary value problem is then solved by shooting rays in the medium from the source and using information from the computed paths to update the initial ray trajectories so that they more accurately target the receivers (see Fig. 2.7). Rays may also be shot from receivers towards the sources as the principle of reciprocity applies in ray tracing.

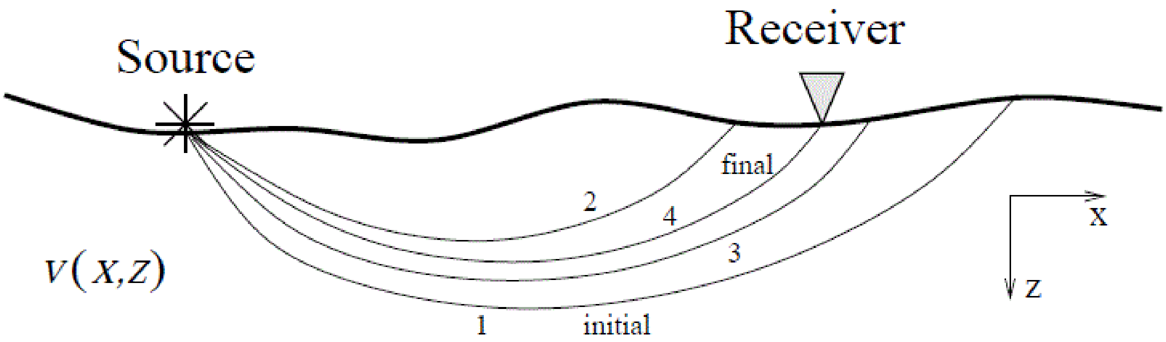

**Figure 2.7:** Principle of the shooting method. The initial projection angle of ray 1 is iteratively adjusted until the final ray (4) passes sufficiently close to the receiver. (After Rawlinson 2000)

As shown in Figure 2.7, the shooting method fixes one end of the ray path (source point), and takes initial incidence angle $i_0$ and initial azimuth $j_0$, and then uses ray path equations to find the coordinates of another end point (station).

Equation (2.6) could be rewritten as first-order equations:

$$\frac{\partial x}{\partial l} = v(x)p$$

$$\frac{\partial p}{\partial l} = \frac{\partial}{\partial l}\left(\frac{1}{v(x)}\right) \tag{2.8}$$

Where; p is the slowness. Equations (2.8) give a system of six first order ODE (ord. dif. equ.) equations (can be simplified into five independent equations), which must be integrated numerically to find the desired ray path. For *Cartesian Coordinates*, the system becomes

$$\begin{aligned}
&x' = c\sin i\cos j;\\
&y' = c\sin i\sin j;\\
&z' = c\cos i;\\
&i' = -\cos i\left[c_x\cos j + c_y\sin j\right] + c_z\sin i;\\
&j' = \frac{1}{\sin i}\left[c_x\sin j - c_y\cos j\right].
\end{aligned}$$

The solution should satisfy

$$h(i_0, j_0) = H, \tag{2.9}$$

$$g(i_0, j_0) = G \tag{2.10}$$

Here *h* and *g* are the calculated coordinates (lat. and lon.) of the end of the ray. *H* and *G* are the coordinates of the end of the desired ray.

Julian and Gubbins (1977) suggested Newton's method and False Position method to solve equation (2.9) and (2.10), and both methods have to be applied iteratively.

In the Newton's method we have:

$$\begin{bmatrix} \frac{\partial h}{\partial i_0} & \frac{\partial h}{\partial j_0} \\ \frac{\partial g}{\partial i_0} & \frac{\partial g}{\partial j_0} \end{bmatrix} \begin{bmatrix} i_0^{(n+1)} - i_0^n \\ j_0^{(n+1)} - j_0^n \end{bmatrix} = \begin{bmatrix} H - h_n \\ G - g_n \end{bmatrix}$$

However, to apply Newton's method first we need to calculate partial derivatives $\frac{\partial h}{\partial i_0}, \frac{\partial h}{\partial j_0}, \frac{\partial g}{\partial i_0}, \frac{\partial g}{\partial j_0}$.

In the false position method, we have following formulation:

$$\begin{vmatrix} k_0 - k_0^{(1)} & k_0 - k_0^{(2)} & k_0 - k_0^{(3)} \\ h^{(1)} - H & h^{(2)} - H & h^{(3)} - H \\ g^{(1)} - G & g^{(2)} - G & g^{(3)} - G \end{vmatrix} = 0, (k = i, j)$$

In these expressions the superscripts represent estimated values in three previous iterations. Further, this does not require the calculation of the partial derivatives, but convergence is slow.

In 2-D problems, a shooting approach is often used because the source-receiver array lies on a single vertical plane. This makes the shooting of a single fan of rays an effective way of obtaining nearby rays to all targets. Zelt & Smith (1992) use a bisection method to find rays that bound each required phase (e.g., a set of rays that all reflect back to the surface from a particular interface). Similar methods were used by Cassell (1982) and Langan et al. (1985). Other applications of shooting methods in 2-D reflection and/or refraction traveltime inversion include those by Farra & Madariaga (1988), White (1989), Lutter et al. (1990), Williamson (1990), Zelt & Smith (1992) and McCaughey & Singh (1997). Examples of its use in 3-D reflection and/or refraction traveltime inversions are harder to find, although several 3-D tomographic studies that combined refraction and local earthquake data (Benz & Smith, 1984; Ankeny et al., 1986; Sambridge, 1990) and some teleseismic tomography studies (Neele et al., 1993; VanDecar et al., 1995) have used shooting methods of ray tracing.

**Bending method:** As shown in figure 2.8, the bending method fixes the two ends, one at the source end and another at the receiver end, and takes some initial estimate of the ray path and adjust it until it satisfies a minimum travel-time criteria (Fermat's criteria). The bending method is derived for a continuous 3-D velocity media which traces a two point ray geometry modelled from first-order differential equations (Julian & Gubbins, 1977). Consider a ray travelling between source S and receiver R through an inhomogeneous medium with velocity *v* and slowness p. If x=x(q) represents this ray path and q can be chosen at any point on this ray path, then

$$\frac{\partial l}{\partial q} = \sqrt{\dot{x}^2 + \dot{y}^2 + \dot{z}^2} \equiv F \text{ , where } \dot{x} = \frac{\partial x}{\partial q} \tag{2.11}$$

using these expression the then equation 2.6 of travel time can be written as,

$$t = \int_{qS}^{qR} pF dq \tag{2.11}$$

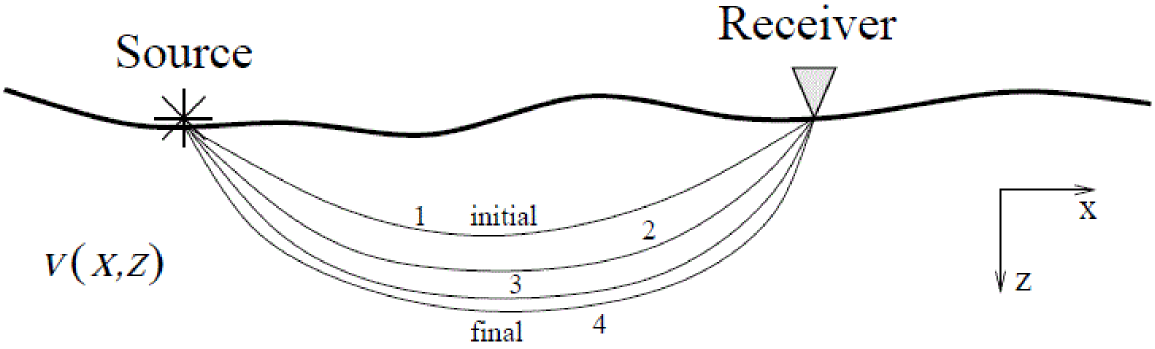

**Figure 2.8:** Principle of the bending method. The geometry of the initial path (ray 1) is adjusted until it satisfies Fermat's principle (ray 4). (after Rawlinson 2000)

According to Julian and Gubbins (1977) equation of travel time can be solved by the standard method of calculus of variation, and used an Euler's equation to represent the boundary value problem between two points A and B as:

$$\frac{d}{dq}(pF)_{\dot{x}} = (pF)_{x},$$
$$\frac{d}{dq}(pF)_{\dot{y}} = (pF)_{y},$$
$$\frac{d}{dq}(pF)_{\dot{z}} = (pF)_{z},$$
$$\frac{dF}{dq} = 0,$$

(2.12)

these equations are solved iteratively with conditions for (n+1) iterations:

$$\mathrm{x}^{(n+1)}(q) = \mathrm{x}^{(n)}(q) + \xi^{(n)} \ ,$$

(2.13)

Where; $\xi^{(n)}$ is perturbation added in nth iteration, $q=l/L$, $L$ is the total length of the ray path and $0 \le l \le L$. If $l=L$ then q represents single representation of total ray path and boundary condition will be $x(0)=x_S$, $x(1)=x_R$; $y(0)=y_S$, $y(1)=y_R$; and $z(0)=z_S$, $z(1)=z_R$. Equation 2.13 is substituted in equation 2.12 and resulting equation can be solved by linearising in the terms of $\xi^{(n)}$. Iterations are carried out until the solution converges to the specified limit of RMS (Julian and Gubbins 1977).

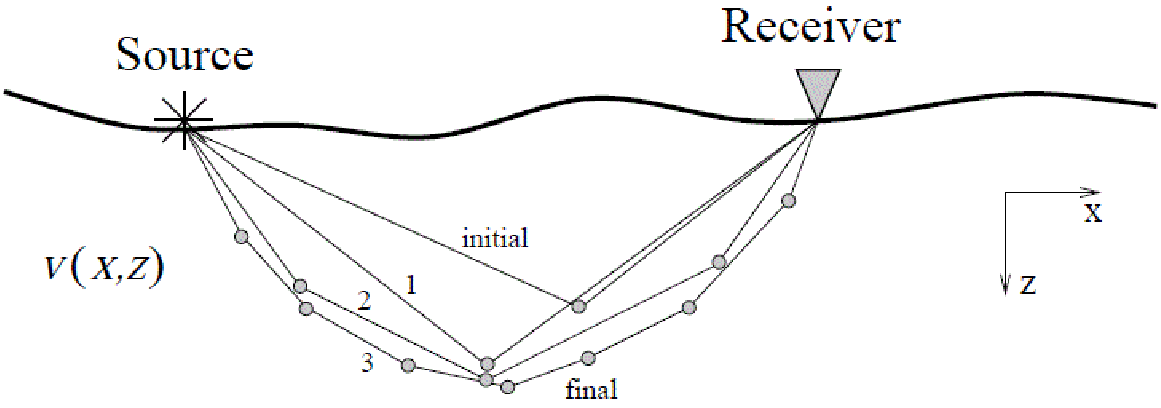

**Figure 2.9:** Principle of the pseudo-bending method of Um & Thurber (1987). An initial guess ray defined by three points is provided. The center point is perturbed to best satisfy the ray equation. Then the number of segments is doubled and the process is repeated. This figure schematically represents three such iterations. (After Rawlinson 2000)

The method of Um & Thurber (1987) called pseudo-bending technique solves the two-point ray tracing in the 3-D velocity medium. In this method after each iteration the integration step-size reduce to the half of the previous step-size. This method is comparatively much faster than the earlier bending technique. Bending methods of ray tracing have been used in a large number of studies based on the inverting that invert teleseismic data (Thomson & Gubbins, 1982; Zhao et al., 1994, 1996; Steck et al., 1998). Recently, Koulakov (2009a) used bending tracing technique for local earthquake tomography and showed bending works faster than the shooting method.

In comparing between bending and shooting methods, Julian & Gubbins (1977) found that bending is computationally faster than shooting by a factor of 10 or more in media with continuous velocity variations. When discontinuities are present, however, the formulation of the bending problem becomes much more complex.

Two alternative approaches to the ray-tracing problem include the methods based on finite-difference (Vidale, 1990) and network theory (Moser, 1991). An important aspect of these methods is the apparent ability to estimate both the global minimum time path and in Vidale's method, a crude estimation of the arrival amplitude. Vidale obtained a finite difference solution to the Eikonal equations on a 3-D grid to evaluate the entire travel time field, allowing for the subsequent assignment of ray-paths and arrival amplitudes (Vidale and Huston, 1992). Moser's method makes use of network theory to find a global minimum travel time path in an efficient manner. Accurate ray-tracing techniques such as these combined with ever more powerful computers promise to make traveltime tomography increasingly practical for large scale problem.

#### 2.6.3.3 Inversion of Travel Time and Its Solution

The inversion involves estimating adjustment vector that best satisfies the observed data, $d_{obs,}$ through the known relationship D = F(M). In case of traveltime inversion, data parameters are traveltimes and model parameters are velocities. The functional F is nonlinear because the trajectory of the ray path is a function of the velocity structure of medium through which it travels. Hence, inversion schemes should account for this nonlinearity unless it can be shown that its effects are not severe. The three techniques are adopted to solve the inversion. These techniques include backprojection, conjugate gradient methods and global optimization techniques, and are described below:

**Backprojection:** This is one of the commonly applied methods for the inversion of traveltime data. As stated below, the traveltime of a seismic ray along a raypath can be expressed as:

$$t = \int_{L(s)} p(\mathrm{x})dl \tag{2.14}$$

Where; L(s) is the path along which the integration is performed, p in the slowness vector and x is the position vector.

In forward modelling with consideration that the region to be modelled is divided into a set of blocks, the forward problem can be written as

$$t = \sum_{b} l_b p_b \tag{2.15}$$

Where; t reperesents the time delay of the ray, $p_b$ signifies slowness perturbation of the $b_{th}$ block, and $l_b$ indicates length of the $r_{th}$ ray segment in the $b_{th}$ block.

If $p(\mathrm{x}) = p_o(\mathrm{x}) + \delta p(\mathrm{x})$, then in (eq. 2.14) the modified path is $L_o + \delta L = L(p_o + \delta p,)$ and the adjusted traveltime is given as:

$$t = \int_{L0+\delta L} p_0(\mathrm{x})dl + \int_{L0+\delta L} \delta p(\mathrm{x})dl \tag{2.15}$$

Fermat's principle can be invoked to replace $Lo + \delta L$ with $Lo,$ so that the traveltime perturbation is accurate to first order:

$$\delta t = \int_{L0} \delta p(\mathrm{x})dl + O(\delta p(\mathrm{x})^2) \tag{2.16}$$

Note that $\delta t = t - t_o$ where $t_0 = \int_{L0} p_0(\mathrm{x})dl$ is the path integral for the unperturbed medium. If a medium is represented by M constant slowness blocks, then Equation 2.16 (for N rays) can be expressed as:

$$d = Gm \tag{2.17}$$

Where, d represent the componets of components of the traveltime residual vector, and m is the slowness perturbation vector. *G* is a matrix with N x M dimensions---N stands for travel time data and M signifies the number of model blocks. Ray lengths $l_{ij}$ corresponding to the distance traversed by each ray in each $m_i$. $G = \partial g / \partial m$, where *g(m)* is the model prediction. As most of the blocks are empty because rays do not pass through these blocks, most of the elements of *G* are zero. The least squares solution of this equation is given as (e.g., Aki et al., 1977):

$$G^T G m = G^T d \tag{2.18}$$

$G^T G$ has large dimension and its direct inversion is difficult. According to the simple scheme of back projection method direct inversion can be avoided and initially only the diagonals of $G^T G$ (Humphreys and Clayton, 1988) are used to obtain the inversion. Adopting this approximation the estimates of the model parameters are:

$$m = D^{-1} G^T d, \qquad \text{where } D^{-1} = dig(G^T G) \tag{2.19}$$

Although, this method is fast and needs less storage space, but the resulting model is strongly blurred. Humphreys and Clayton (1988) suggested two algorithms---iteration and filtering, to take care of blurring [e.g., Natterer, 1986]. Filtering is a deconvolutional scheme implemented either in the space or wave number domain. Iteration focuses an image through repeated backprojection of the existing residuals and is an stable procedure. However, the iteration has a limitation that focusing can be very slow along paths with few ray-crossings. Filtering provided an unstable model when ray distribution is inhomogeneous. The generalized inverse provided an ulternative means to get statbe solution (Backus and Gilbert 1968). Many studies have been carried out using backprojection method (e.g., Humphreys & Clayton, 1990; Hole, 1992; and Zelt & Barton, 1998).

Two backprojection techniques have been applied to solve equations (2.17). These techniques originally used in medical imaging include Algebraic Reconstruction Technique (ART) and Simultaneous Iterative Reconstruction Technique (SIRT). Kissling (1988) made use of parameter separation and applied ART approximation to the damped least square solution of equation 2.17. However, ART suffers from poor convergence (Blundell, 1993). SIRT takes care of some of the convergence problems associated with ART by averaging the perturbations applied to each parameter. SIRT has been used for LET, but generally applied when the hypocenter-velocity structure coupling was not treated explicitly (Walck and Clayton, 1987). Further, SIRT provides a least squares solution with different weighting than that specified by the 'user'.

**Conjugate gradient method:** Conjugate gradient method, in particular the algorithm LSQR (Least squares QR) is an effective alternative to above reconstruction techniques (Paige and Saunders 1982). It is based on Lanczos procedures used to bidiagonalize the system of equations followed by a QR decomposition to obtain the solution. This method is fast and works very well to solve on sparse linear system. The basic idea behind this method is to formulate the inversion as optimization problem and then minimize the objective function in terms of the data residuals. The details of the method are outlined in Golub and Van Loan (1983), Spakman and Nolet (1988), Scales (1987) and Van der Sluis and Van der Vorst (1987).

In this method the traveltime equation (2.15) is linearized about some initial model and the linearized equation in discrete form is represented as:

$$\Delta t = G\Delta m \tag{2.20}$$

where, $\Delta t$ represents the components of traveltime residual vector and and $\Delta m$ represents components of the differences between the model slowness and the true slowness (referred to a cell-based discretization), and G is a matrix whose element $G_{ij}$, is the distance the $i_{th}$ ray travels in the jth cell. A generalized solution (e.g., a least-squares solution of equation (2.20)) is a vector $\Delta m$ which minimizes the Euclidean norm of ($G\Delta m$- $\Delta d$). Further, since each ray travels through only a small portion of the medium, the distance matrix will be sparse, with 99 percent or more of the elements equal to zero for large problems. Singular value decomposition (SVD) (Golub and Reinsch, 1970) and the row-action methods (Censor, 1981) can directly deal with equation (1) But SVD is unsuitable for large least-squares problems because of large, dense, intermediate matrices. Scales (1987) defined application of the classic conjugate gradient algorithm of Hestenes and Stiefel (1952) to solve these large, dense, sparse matrices of travel time inversion.

Solution of equation (2.20) carried out by an iterative process where, at each step k, we have the following linear relation between the vector $t^{(k)}$ of traveltimes of all rays and the vector $m^{(k)}$ with the current estimated slowness field (Scales, 1987):

$$\Delta t^{(k)} = G^{(k)}\Delta m^{(k)} \tag{2.21}$$

Where; $\Delta \boldsymbol{t}^{(k)} = \boldsymbol{t}^{obs} - \boldsymbol{t}^{(k)}$ and $\Delta \mathrm{m}^{(k)} = \mathrm{m}^{(k+1)} - \mathrm{m}^{(k)}$

Under the assumption that error distribution in the relationship $t_{obs} \approx g(m_{true})$ is Gaussian, then L2 norms is applicable on this difference. We want to find the vector $\Delta m^{(k)}$ that minimizes $\left\| G^{(k)} \Delta m^{(k)} - \Delta t^{(k)} \right\|^2$. This can be formally stated as finding the minimum of the following objective function:

$$\Phi(\Delta m^{(k)}) = (\Delta t^{(k)} - G^{(k)} \Delta m^{(k)})^T (\Delta t^{(k)} - G^{(k)} \Delta m^{(k)}) \tag{2.22}$$

The estimated solution, also called least squares solution, is

$$[G^{(k)}]^T G^{(k)} \Delta m^{(k),est} = [G^{(k)}]^T \Delta t^{(k)} \tag{2.23}$$

Least-squares solutions very often do not provide good results and sometimes they do not even exist. Thus, eq. (2.23) now becomes

$$G^T G\, m = G^T t, \tag{2.24}$$

Where; the solution $m = m^{est}$ will be obtained through conjugate gradient schemes as presented in the next section.

The classical conjugate gradient method (Hestenes and Stiefel, 1952) to solve the least squares linear system (2.24), is often referred to as CGLS (Paige and Saundres 1982; Santos and Pierro 2006; Bazan et al., 2014) and is as follows, for a given initial guess $m_0$ and a maximum number of iterations $k^{max}$,

```
$r_0 = t - Gm_0, z_0 = G^T r_0,$ and $p_0 = z_0;$
repeat
    $w_k = Gp_k;$
    $\alpha_k = (z_k^T z_k)/(w_k^T w_k);$
    $s_{k+1} = s_k + \alpha_k p_k;$
    $r_{k+1} = r_k - \alpha_k w_k;$
    $z_{k+1} = G^T r_{k+1}$
    $\beta_k = (z_{k+1}^T z_{k+1})/(z_k^T z_k);$
    $p_{k+1} = z_{k+1} + \beta_k p_k;$
until $\Phi(k)$ reaches a local minimum or $k > k_{max}$
```

The matrix $G^T G$ is not explicitly computed, since it usually has a higher number of nonzero entries and a higher condition number than G (Scales 1987).

Other gradient optimization methods to solve the inverse problem include Gauss-Newton method (Aki et al., 1977, Zhao et al., 1994, and Steck et al. 1998), steepest-descent method (Blundell 1993), and subspace method (Kennett et al., 1988, Sambridge 1990 and Williamson 1990). These methods are explained in detail by Rawlinson (2000).

The principle advantage of the steepest descent and conjugate gradient methods over the Newton and DLS methods is that a large system of potentially ill-conditioned linear equations need not need to be solved. Consequently, these methods are much more rapid for the inversion step. However, since they only minimize in one dimension at each iteration, they tend to converge more slowly. If the procedure for solving the forward step is fast compared to solving the M × M matrix equation, then steepest descent or conjugate gradients may be preferable. However, if the forward step is slow compared to solving the matrix inverse, then a Newton or DLS approach may be quicker.

**Global Optimization:** The above inversion methods provide local minimum because they span the model space near the initial model estimates. Therefore, they are unable to provide a global minimum solution. There is a renewed interest to use global optimization techniques to solve geophysical inverse problems because of unprecedented advancements in computer power. Several types of global optimization techniques have been applied for the inversion of seismic data using random processes to search model space and find better models. These methods include Monte Carlo, genetic algorithms and simulated annealing.

The Monte Carlo approach, defined as a purely random search of model space, is the simplest of these global methods. The misfit function is evaluated at a set of points in model space that are randomly chosen. The preferred solution is the model with minimum misfit. The selection of points in model space has no dependence on previous points. A basic Monte Carlo approach is not suited to most seismic traveltime inversion problems because it requires significant computation time, even when model space is not very large. Therefore, it becomes difficult to apply this method if a large number of model parameters are involved (Sambridge & Drijkoningen, 1992; Rawlinson 2000).

Genetic algorithms, based on the concept of biological evolution, are used to develop new models from the parent generation of the randomly picked intial models. The process of producing a new set of models from a pre-existing set involves four basic steps; forward step, reproduction, mutation and crossover. Such techniques are adopted in the 1-D inversion of marine seismic data (Sambridge & Drijkoningen, 1992; Drijkoningen & White, 1995) and the 2-D inversion of refraction traveltimes (Boschetti et al., 1996). The first step involves determining traveltimes for the set of input models. The next step of reproduction involves the selection of parent population and, assigning a measure of fitness to each model in the pool based on the magnitude of the misfit function at the corresponding point in model space. The crossover step creates a pool of offspring, each of which is a “mix” of its two parents. Sambridge & Drijkoningen (1992) represented models by binary strings and perform the crossover by simply cutting and transposing two segments at a randomly chosen point along the two strings. Mutation involves randomly changing values of some parameter (or bits if a binary string representation is used) in selected models. This ensures that some “freshness” remains in the model pool, although the mutation rate should be kept low (Boschetti et al., 1996, use a mutation rate of 1%) so that “good” models are not corrupted. The basic principle behind genetic algorithms is that models with a high fitness index will pass their characteristics to subsequent generations, while those aspects of the cycle that introduce random changes of the population permit new parts of the model space to be tested.

An artificial neural network (ANN) method was used to compute least-squares fit to the measured traveltime data (Ning et al., 1966). ANN are non-linear data driven, self-adaptive approach compared to the traditional methods. This approach is quite different from the other methods, since the ANN computes the Earth-Model that provides the best explanation of the data (traveltimes). Indeed, in the other works (e.g., Roth, 1993; Roth and Tarantola 1994), the ANN learns to invert the function that allows obtaining velocities from traveltimes, from data resulting from several randomly generated Earth-Models. In these works, different Earth-Model structures and ray-tracing algorithms were used. Neural networks can be viewed as applications that map one space, the input space, into some output space (Roth and Tarantola, 1994). Baraez et al. (2002) have used Modular Neural Networks for Seismic Tomography and showed that the modular approach is best suited for the inversion problem. This method was advocated and used by various researchers (e.g., Baraez et al., 2002; Roth and Tarantola, 1994; Langer et al., 1996; Calderon-Macias et al., 1998).

Technique of simulated annealing is analogous to physical annealing in thermodynamic systems. This technique can be applied to optimize the model parameters. Weber (2001) demonstrated a method for finding an optimal, irregular triangular cell parameterization for 2D traveltime tomography that best suits the raypath geometry (fig. 2.9). He defined a cost function, whose minimization is equivalent to the minimization of the null space of the tomographic matrix and used a nonlinear optimization algorithm of simulated annealing to find the optimal parameterization. They proved that the optimal triangulated model provides more accurate and reliable inversion results than the regular grid model in 2-D traveltime tomography.

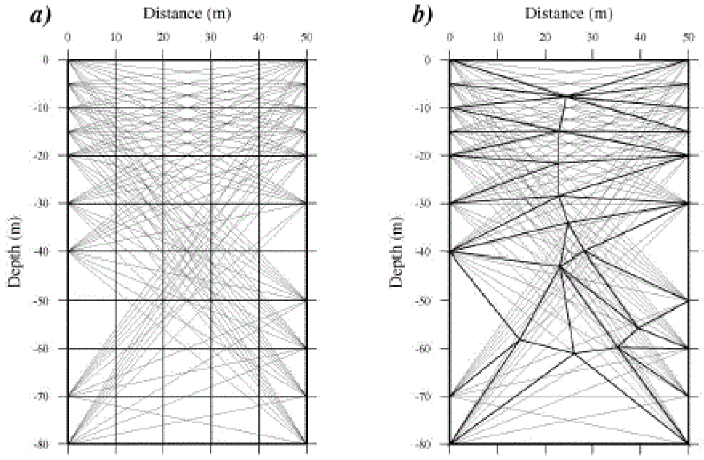

**Figure 2.10:** An example of optimized model parameterization (a) Raypath geometry with rectangular grid parameterization. (b) Raypath geometry with optimized triangular cell parameterization (after Weber 2001)

Global optimization techniques based on stochastic methods are fast developing field of optimization. However, current applications of these techniques in the traveltime inversion are restricted because of excessive computation cost. Global optimization techniques can find global minimum solutions to highly nonlinear inverse problems, but the computational expense when a large number of parameters are involved currently limits their use in seismic data inversion.

### 2.6.4 Analysis of Solution Quality

A solution obtained from inversion using the above methods has to be checked for its robustness or quality. A solution without knowledge of resolution or non-uniqueness may lead to erroneous interpretation. Two methods are commonly used to assess the solution robustness in traveltime tomography. The first method under the assumption of local linearity estimates model covariance and resolution matrices; and the second method envolves testing resolution by reconstructing a synthetic model from the same source-receiver geometry as in the real experiment.

**Data Resolution Matrix:** After computing a generalized inverse $G^{-g}$, we solve for the model parameters $m^{est} = G^{-g} d$. We can calculate data resolution matrix by using $m^{est}$ into the equation

$Gm = d$ . The relation between the observed and predicted data ($d^{obs}$ and $d^{pre}$) may be written as:

$$d^{pre} = Gm^{est} = G\left[G^{-g}d^{obs}\right] = \left[GG^{-g}\right]d^{obs} = Hd^{obs} \tag{2.25}$$

Where $H$ is the data resolution matrix that describes how well the prediction matches the data. If $H=I$ (identity matrix), then $d^{pre} = d^{obs}$ and the prediction error is zero. In case H is not equal to I the prediction error is non-zero.

The diagonal elements of the matrix $H$ provide important information regarding the data resolution and their values always lie between 0 and 1. The row of the matrix $H$ describes how well the neighbouring data can be independently predicted or resolved.

**Model Resolution Matrix:** The model resolution matrix determines whether the model parameters can be independently predicted or resolved. Let us assume a true but unknown set of model parameters $m^{true}$ and $Gm^{true} = d^{obs}$. We seek the transformation that links the estimated model parameters $m^{est}$ with the true model $m^{true}$.

$$m^{est} = G^{-g}d^{obs} = G^{-g}(Gm^{true}) = (G^{-g}G)m^{true} = Rm^{true} \tag{2.26}$$

Where; $R$ is known as the model resolution matrix. In case, $R = I$, then this implies that each model parameter is uniquely resolved. A small number in the $i^{th}$ diagonal element of $R$ indicates the poor resolution of the $i^{th}$ model parameter. A non-zero off-diagonal element indicates a trade-off between two model parameters.

**Model and Data Covariance matrices:** The covariance of model parameters depends on the covariance of the data and the manner in which error is mapped from data space to model space. The unit model covariance matrix describes the degree of error amplification that occurs in the mapping. If the data are uncorrelated and having equal variance $\sigma^2$, the unit model covariance matrix $\mathrm{cov}_u\, m$ is defined as

$$\left[\mathrm{cov}_u\, m\right] = \sigma^2 G^{-g} G^{-gT} \tag{2.27}$$

σ denotes the standard error in the data.

In case of unequal variance, $\mathrm{cov}_u\, m$ can be written as

$$\left[\mathrm{cov}_u\, m\right] = \sigma^2 G^{-g}\left[\mathrm{cov}_u\, d\right] G^{-gT} \tag{2.28}$$

$\text{cov}_u m$ is unit data covariance matrix. Square roots of the diagonal elements of the model covariance matrix are a measure of the standard errors in the model parameters.

**Synthetic parameterization:** The parameterizations that describe continuous velocity field often opt for resolution tests that attempt to reconstruct a synthetic model using the same source-receiver geometry as the real experiment. The rationale behind this approach is that if a known structure with similar length scales to the solution model can be recovered using the same (for linearized solutions) or similar (for non-linear solutions) ray paths, then the solution model should be reliable. The quality criterion is the similarity between the recovered model and the synthetic model. The is the common test model "checkerboard test", in which the synthetic model is divided into alternating regions of high and low velocity with a length scale equal to the smallest wavelength structure recovered in the solution model. Regions in which the checkerboard pattern is recovered clearly are those regions in which structure in the solution model can be considered to be well resolved. Lévéque et al. (1993) demonstrated that such an approach is not necessarily as reliable as it might seem. It is possible that in the checkerboard test the small scale structure well retrieved while the large-scale structure is poorly retrieved. Furthermore, if the non-linearity of the problem is accounted for, the ray paths through the synthetic model may have significantly different geometries to those through the solution model. Under these situations, testing a number of different synthetic models is advisable, especially if the solution model is complex.

Teleseismic traveltime tomography studies that used checkerboard resolution tests include those by Glahn & Granet (1993), Achauer (1994) and Seber et al. (1991). Ritsema et al. (1998) used several different synthetic models rather than checkerboards and analyzed the accuracy of their recovered model. In local earthquake tomography, checkerboard tests have been implemented by Walck & Clayton (1987); Walck (1988); Chiarabba et al. (1997); Graeber & Asch (1999); Dinc et al. (2010); Koulakov (2009a); Kanaujia et al. (2016). Koulakov et al. (2009) defined various synthetic representations, including checkerboard to test the Local earthquake tomographic algorithm.

## 2.7 Coupled Hypocenter Velocity Model Problem

A general methodology adopted by many investigators involves first determining the 3-D structure by fixing the earthquake locations and then obtaining the earthquake locations by fixing the velocity structure. However, theoretical and numerical studies have demonstrated that this type of methodology introduces bias in the estimates of both locations and structure (e.g., Thurber, 1992; Roecker *et al.*, 2006). To substantiate the nature of this problem we provide the following analysis given by Roecker *et al.* (2006). This problem can be stated as:

$$Hdh + Sds = \mathrm{r} \tag{2.29}$$

where $H$ and $S$ represent the derivative matrices and $dh$ and $\boldsymbol{ds}$ signify perturbation vectors for hypocenters and slowness, respectively. The SVD of $H$ is

$$H = U\Lambda V^T = \left[U_P \middle| U_0\right]\Lambda V^T \tag{2.30}$$

Where, $\mathrm{U}_p$ is the range space of H and $\mathrm{U}_0$ is the null space of H (Aster *et al.*, 2005). Multiplying the original equation by $\mathrm{U}^{\mathrm{T}}$ and separation of the $p$ and 0 components provides:

$$\begin{bmatrix} U_P^T & H \\ U_0^T & H \end{bmatrix} dh + \begin{bmatrix} U_P^T & S \\ U_0^T & S \end{bmatrix} ds = \begin{bmatrix} r_p \\ r_0 \end{bmatrix} \tag{2.31}$$

Note that $U_0^T H = 0$ by definition and, if we initially relocate the earthquakes, then $\boldsymbol{r}_p$=0 also, we have

$$\begin{bmatrix} U_P^T & H \\ & 0 \end{bmatrix} dh + \begin{bmatrix} U_P^T & S \\ U_0^T & S \end{bmatrix} ds = \begin{bmatrix} 0 \\ r_0 \end{bmatrix} \tag{2.32}$$

Thus, we have two sets of equations

$$U_p{}^{\mathrm{T}} Hdh + U_p{}^{\mathrm{T}} Sds = 0 \tag{2.33}$$

and

$$U_0{}^{\mathrm{T}} Sds = r_0 \tag{2.34}$$

Second set of equations allows calculating ds. This is the decoupled problem (the method of separation of parameters of Pavlis and Booker (1980)). In case we seek solution for the entire system involving *ds* by ignoring *dh* in equation (2.32), we actually solve the reduced system represented by equation:

$$\begin{bmatrix} U_P^T & S \\ U_0^T & S \end{bmatrix} ds = \begin{bmatrix} 0 \\ r_0 \end{bmatrix} \tag{2.35}$$

This amounts to solving equation (2.34) but with the constraint that the weighted sum of ***ds*** will be zero. This bias occurs because full simultaneous inversion is not conducted.

The above description provides insight into some features of a joint hypocenter–velocity structure inversion (JHVI) versus a velocity-only inversion (VOI). In a VOI, the added constraints (2.35) force *ds* to be small. This means that subsequent estimates of *dh* will be small as well. The *ds* term is kept small at a cost of misfits to the data. Because when *ds* is small, the fit to $r_0$ will be degraded. This property, documented in Thurber (1992), can be observed in VOI tests with real data – both *dh* and *ds* are too small in a VOI, even when alternated with hypocenter relocation, and the data fit is poor.

Thurber (1992) showed by the practical example of a 1-D velocity model that, the VOI substantially underestimates the velocity contrast, while the simultaneous inversion recovers the velocity structure to within 1% and the events are located within 100 m. He concluded that for LET, solving the full system of equations is important to allow obtaining unbiased estimates of velocity structure.

Many algorithms utilize the fast sparse-matrix solvers such as LSQR, but the historical use of subspace methods (e.g., Kennett *et al.*, 1988) for efficient inversion is worth mentioning. In particular, these methods deal with large matrix size when many earthquakes are included in an inversion. For LET, three research groups published comparable methods for separating hypocenter parameters from velocity model parameters. These methods, allow the efficient solution of smaller matrix in place of one giant matrix (Pavlis and Booker, 1980; Spencer and Gubbins, 1980; Rodi *et al.*, 1981). For example consider an LET problem with 10000 earthquakes recorded on an average at 50 stations, and with 20000 model parameters. The size of matrix to represent full system would be (50×10000) by (4×10 000+20000), or 500000 by 60000. If we adopt the annulling method of Pavlis and Booker (1980), we can decompose the JHVI system of equations for each earthquake *i* as:

$$H_i dh_i + S_i ds_i = r_i \tag{2.36}$$

where, $H_i$ and $S_i$ are the derivatives matrices of arrival times with respect to hypocenter and model parameters, respectively. $dh_i$ and $\mathbf{ds}_i$ are the corresponding parameter perturbations. Using the orthogonal matrix $U_{0i}$ that satisfies $U_{0i}H_i=0$ allows us to recast the decoupled equations in the following form:

$$U_{0i} H_i dh_i + U_{0i} S_i ds_i = U_{0i} r_i \quad \text{, or} \quad S_i' \, ds_i = r_i' \tag{2.37}$$

The matrix-size of the original partial system in eq. (2.36) would be 40 by 20004, whereas the matrix-size of the decoupled system in eq. (2.37) would be 36 by 20000. If we consider all the earthquakes in this manner, the size of the resulting system of equations is 460000 by 20000, which shows a substantial reduction in size. We can further reduce the problem size by incrementally constructing the normal equations, $S'^T S' = S'^T r'$ (Spencer and Gubbins, 1980). The resulting system of equations now has a size of 20000 by 20000 only.

Unfortunately, the last step results in squaring of the condition number of the system matrix, which leads to a loss of matrix sparseness. As stated earlier the single-step 'tomographic' inversion underestimates velocity contrast, while the 'simultaneous inversion' recovers the true structure and event location nearly exactly. And by ignoring explicit hypocenter-velocity structure coupling leads to bias in the derived 'tomographic' models (Walck and Clayton, 1987; Lees and Crosson, 1989).

## 2.8 Review of Various Models of Northwestern Himalaya

### 2.8.1 1-D Velocity Models

Several crustal velocity models have been proposed for various segments of the Himalaya based on the study of surface wave dispersion and crustal phases (Chauhan and Singh, 1965; Kaila *et al.*, 1968; Tandon and Dubey, 1973; Verma, 1974; Chander *et al.*, 1986; Kumar *et al.*, 1987; Kumar *et al.*, 1994; Sarkar *et al.*, 2001; Kumar and Sato, 2003; Mukhopadhyay and Kayal, 2003, Malik, 2009).

Chauhan and Singh (1965) estimated the depth of Mohorovicic discontinuity between 50 km and 60 km in the Himalaya with the average P-wave velocity of 5.5 km/sec in the granitic layer and 6.6 km/sec in the basaltic layer. The P-wave velocity of 7.8 km/sec was estimated at the Moho boundary.

Kaila *et al.* (1968) estimated the crustal structure in the foothills area of the northwestern Himalaya from the travel times of crustal P-wave phases. In the study the effect of the sedimentary layers was also considered. The study showed that the crustal structure in the Himalayan foothills area of northern India consists of three layers—a 6 ± 1 km thick sedimentary layer with P-wave velocity of 2.7 km/sec, 8 ± 5 km thick Granitic layer with P-velocity 6.2 ± 0.1 km/sec and 14 ± 7 km thick basaltic layer with velocity 6.9 ± 0.1 km/sec giving a total crustal thickness of 28 ± 8 km (Fig 2.11). The upper mantle P-wave velocity in this area was 8.2 ± 0.1 km/sec.

Tandon and Dubey (1973) used the body wave phases from the earthquakes with epicentres in the Himalaya and recorded by the observatories situated close to the foothills of the Himalaya. They proposed a three-layer crustal model---Granite I (thickness 22.7 km), Granite II (thickness

11.3 km), and the Basaltic layer, with P-wave velocities of 5.48 km/sec, 6.00 km/sec, and 6.45 km/sec, and S-wave velocities of 3.33 km/sec, 3.56 km/sec, and 3.90 km/sec, respectively (Fig. 2.11). The estimates of the upper mantle P- and S-wave velocities are 8.07 km/sec, and 4.57 km/sec, respectively. The study showed that beneath the Himalaya the crust is relatively thick (~ 58 km) and crustal and sub crustal velocities have a lower trend under the mountain.

Verma (1974) from the time-distance plots of P- and S- phases of the earthquakes occurring in the foothills of Himalaya, found a bi-layered crust in this region (Fig. 2.11). The study showed the crustal thickness of 30.1 km with 13.4 km thick Granitic layer and 16.7-km-thick basaltic layer. The P- and S-wave velocities were found to be 5.92 ± 0.03 km/sec and 3.54 ± 0.01 km/sec in the Granitic layer, and 6.80 ± 0.03 km/sec and 3.92 ± 0.01 km/sec in the basaltic layer, respectively. The P- and S-wave velocities, at the Moho-depth were found to be 8.00 ± 0.03 km/sec and 4.54 ± 0.02 km/sec, respectively.

Chander *et al.*, (1986) used the P-wave arrival times of local earthquakes recorded at the stations deployed in the Garhwal Himalaya. A P- wave velocity of 5.2 km/sec was estimatedthe upper crust in the vicinity of the Main Central thrust. A study conducted by Kumar *et al.*, (1987) provided P-wave velocity as 6.0 km/sec in the second crustal layer in the Garhwal Himalaya.

Kumar *et al.*, (1994) proposed a local velocity model for the Garhwal Himlaya considering the 15 km thick first layer based on the study of Chander *et al.*, (1986) and the depth of second layer upto 46 km based on study of Kumar *et al.*, (1987). The velocity below 46 km depth was taken from the study based on Tandon (1954). Because of lack of knowledge of velocity structure for the Garhwal Himalaya, Kumar *et al.*, (1994) used this hybrid crustal velocity model to locate the local earthquakes recorded by a digital telemetered array deployed in Garhwal Himalaya.

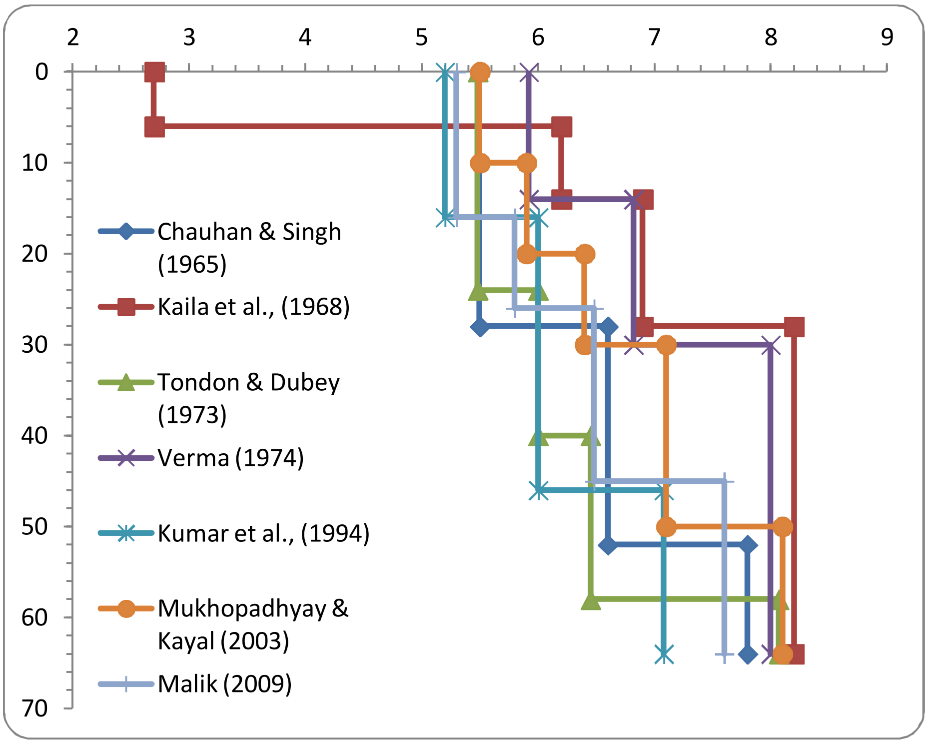

**Figure 2.11:** 1-D P-wave velocity structure for Himalaya region

Sarkar *et al.*, (2001) from the inversion of the body wave arrival time data estimated velocity model for the Garhwal Himalaya. The main findings of the study include significantly low velocities within the Middle-Lesser Garhwal Himalaya, and higher velocities in the interface zone between the Middle-Lesser and Higher Garhwal Himalaya. Further, seismic activity was found to be mostly confined to a relatively narrow northeast dipping zone in the upper 4 km of the crust, which is characterized by a relatively higher P-wave velocity. This seismic activity represented thrusting along steep north-easterly dipping parallel slip surfaces forming a ramp in the crystalline formations of the Higher Himalaya.

Kumar and Sato (2003) estimated P-wave velocities of 4.72 km/sec and 5.89 km/sec and S-wave velocities as 2.90 km/sec and 3.39 km/sec for the upper crustal and the lower crustal layers, respectively beneath the Garhwal Himalaya. These estimations were obtained in the vicinity of the Main Central thrust. The 1-D crustal velocity models proposed by various workers are summarized in Fig. 2.11.

Kumar et al (2009) estimated the 1-D velocity model of northwest Himalaya. They proposed a new seismotectonic model of the region from the distribution of local events and their fault plane solutions. The 1-D velocity model is deduced using program VELEST. This study is conducted using a P- and S-phase data of 172 local earthquakes collected from a seismic network deployed in the region. The minimum 1D velocity model proposed in this work showed that the average 44-km-thick crust consists of four layers beneath the study area. The top ~10 km-thick-layer represented the metamorphosed sediments of the Chamba nappe that dominates the surface geology of the study area. The study suggested a thin low-velocity layer at 15 km depth. This layer marked the detachment zone that separates the down going Indian plate from the overriding sedimentary wedge.

Malik (2009) proposed an average 1-D crustal velocity structure for the Garhwal Himalaya from the inversion of travel time data of local earthquake. In this study the 1-D crustal velocity model of Tandon and Dubey (1973), Kumar *et al.*, (1994) and Mukhopadhyay and Kayal (2003), were taken as trial models for the 1-D inversion. The new model is computed using program VELEST. This average 1-D velocity model was used as input to the 3-D velocity inversion. The P and S phases of the local events used in this study were collected from the operation of a digital local network deployed in the Garhwal Lesser Himalaya from April 1995 to December 2007. This study proposes a three layers crustal model over a half space with average P-wave velocities of 5.32 km/sec, 5.80 km/sec, and 6.48 km/sec with depths of the layer at 16 km, 26 km and 46 km, respectively. The half space has a P-velocity of 7.60 km/sec. The model is shown in Fig. 2.11.

Mahesh et al (2013) reported a 1-D velocity model of the Kumaon‑Garhwal Himalaya. This model is based on the analysis traveltimes of 385 local earthquakes. This model was obtained using the VELEST program (Kissling et al., 1994; Kissling, 1995) and provided three velocity layers upto a depth of 20 km from the surface. The model was used to locate 1150 local earthquakes ($1 < M < 5$) occurred in the region. The main findings of the study include occurrence of a majority of these earthquakes (~75%) in the upper 20 km of the crust, largely above the Main Himalayan thrust, a ~10-km-wide seismicity zone that follows the surface trace of the Munsiari thrust, a parallel band of earthquakes, located about 70 km to its southwest of the Tehri dam in the Lesser Himalaya, and ~15% of activity confined to the Tethys Himalaya and beneath the Ganga basin.

Other than above mentioned models there are at the most recent work on high resolution imaging of the Northwestern Himalaya by Kumar et al, 2014, Velocity structure of northeast Himalaya using receiver functions (Dipok et al., 2014), Mapping of Moho profile using lateral phases travel time at northeast Himalaya by Dipok and Baruah, crustal velocity structure of the Gujrat region (Chopra et al, 2014).

### 2.8.2 3-D Velocity Model

Mukhopadhyay and Kayal (2003) carried out 3-D inversion using P- and S-arrivaltimes of aftershocks of the Chamoli earthquake. They found that majority of well-located aftershocks occurred to the southwest of the mainshock epicenter and lie above the plane of detachment. The study brought out a prominent, nearly-vertical, east–west–trending Low Velocity Zone (LVZ) from the surface to a depth of 15 km, The LVZ conforms to the surface trace of the Alakananda fault. The LVZ is quite broad and heterogeneous at shallower depth (0–10); narrowed at a deeper level (12–15 km) and well defined in the 15-km-depth slice. The results of this study agree with those of Rajendran *et al.* (2000), who reported an anticlinal structure close to the Chamoli area. This structure is delimited on two sides by almost vertical faults—the east–west trending Alakananda fault to the south and a north-northwest to south-southeast trending fault in the east.

Mukhopadhyay and Sharma (2010) studied the variation of seismic velocities (VP and VS, respectively) and VP/VS ratio from the local earthquake tomography (LET) beneath the Garwhal-Kumaun Himalaya. The results are interpreted to study the structure of the Himalaya and the underlying Indian crust in this part of the Himalaya. The LET was carried out using Thurber (1993) method and involved simultaneous inversion of the dataset of P- and S-phase readings from 505 earthquakes recorded at 70 seismic stations in the Garwhal-Kumaun Himalaya. The study could not resolve the Moho configuration. The important findings of this study include a southwest dipping zone of low $V_P/V_S$ beginning at the high Himalaya, a crustal level folding and faulting in the region indicating deformation of Indian crustal material and variation in the mode of deformation along the trend of the Himalaya. The authors attributed the variation in the mode of deformation to the more oblique convergence between India and Eurasia compared to the Nepal Himalaya.

Kumar et al. (2013) mapped the 3-D velocity structure beneath the Kangra–Chamba region of western Himalaya using LET (Thurber, 1993; Eberhart-Phillips, 1990). Phase data of 159 local events was inverted to obtain velocity structure. Inverted velocity tomograms could resolve velocity structure up to a depth of 18 km and showed 14% variation in $V_P$ and $V_S$ and 6% variation in the $V_P/V_S$ across the major tectonic zones in the region (tomographic section is shown in Figure 2.12). From the study of various attributes of seismicity, velocity structure, focal mechanisms, and stress distribution, the study concluded that three different source regions control the regional seismotectonics. These three seismic regimes at different depths produce intense seismicity in a block of 30 × 30 km dimension centered northeast to the epicenter of the Kangra earthquake.

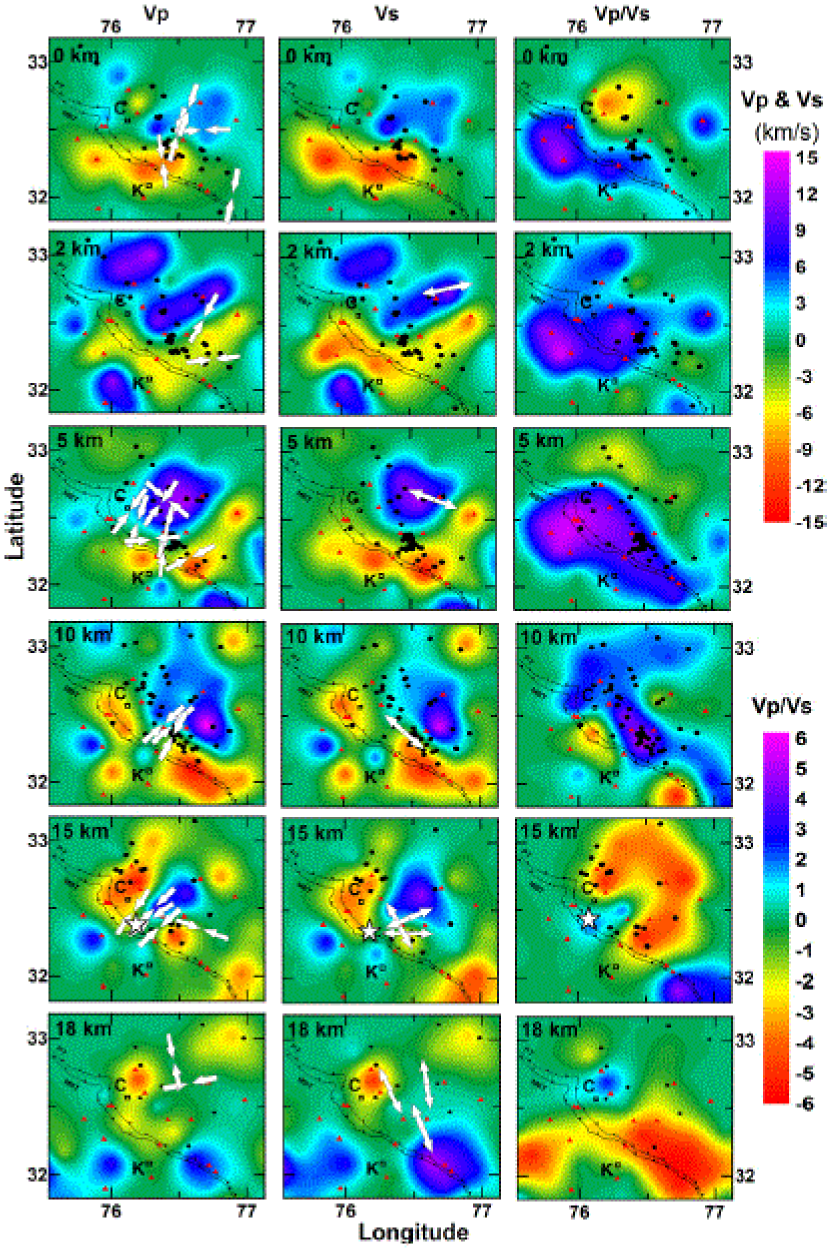

**Figure 2.12:** Tomographic results of the Kagra-Chamba region estimated by Kumar et al. (2013)

Koulakov et al. (2014) studied variation of the crustal thickness in the Nepal Himalaya from the tomographic inversion of regional earthquake data. They combined total information from 78 seismic stations installed in India and Nepal, and a total of 821 events were selected for the study. The inversion was performed using the algorithm LOTOS (Koulakov, 2009a). The study brought out a low-velocity anomaly in the upper part of the model down to depths from 40 to 80 km and the lower limit of this anomaly represented variation of the Moho depth. It was found that thinner crust patterns correspond to lower gravity values and vice versa. Some correlation of velocity anomalies with magnetic field was also inferred. Higher magnetic anomalies correspond to the major areas of thicker crust. The study suggested that higher magnetic anomalies can be associated with more rigid part of the Indian crust, resulting in compression of thrust zone, which leads to more thick crustal.

## 2.9 Other Related Studies in the Northwestern Himalaya

**Receiver Function Studies:** Caldwell et al. (2013) mapped the structure of the Main Himalayan Thrust (MHT) below the Garhwal Himalaya adopting common conversion point (CCP) technique.

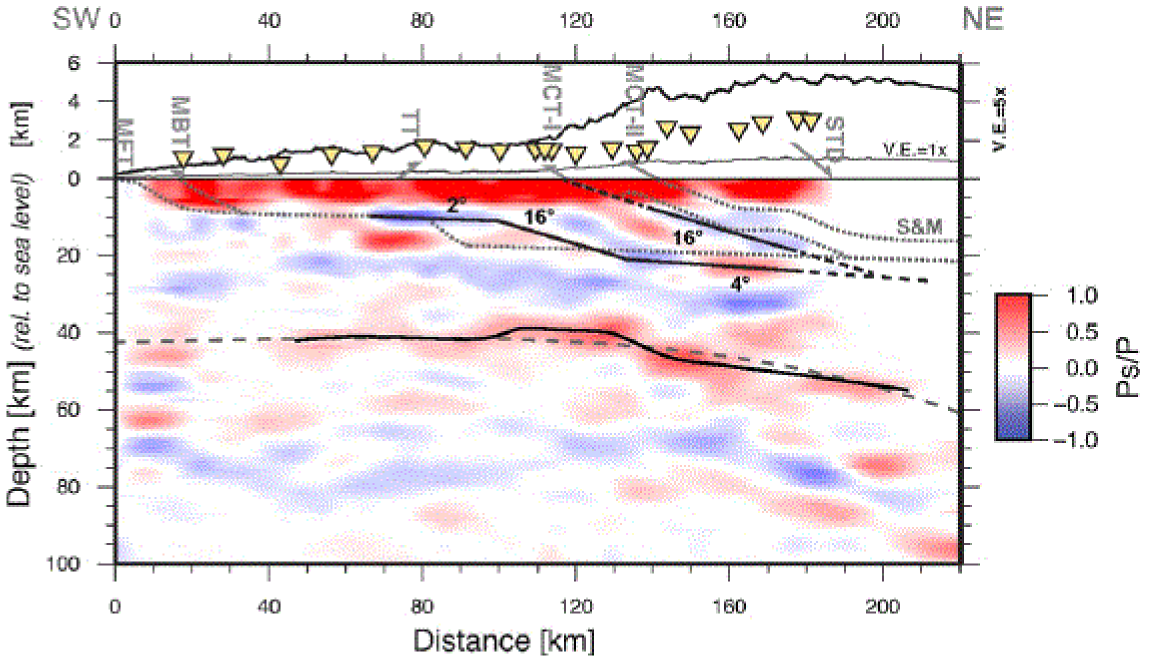

**Figure 2.13:** Section showing common conversion point (CCP) stack of receiver functions of Caldwell et al. (2013)

For this purpose the data of teleseismic earthquakes collected from a seismic array of 21 broadband seismographs deployed in the region during 2005-2006 was used. The array station locations cover the region form 79°–81° E, between the MFT and the South Tibet Detachment and spanned the Himalayan thrust wedge. They interpreted from the CCP images (Figure 2.13) that the MHT has a flat-ramp-flat geometry. Further, the study brought out a negative impedance contrast for the upper flat, and a positive impedance contrast for the ramp, located beneath the surface trace of the Munsiari Thrust. The seismic image indicated that the upper flat is ~10 km below sea level and dips to the north at ~21°, connecting to a ~10 km high mid-crustal ramp which dips at ~16°. The lower flat is 20–25 km below sea level and dips at ~4°.

The Moho is nearly horizontal at a depth of 35–45 km beneath the Sub Himalaya, and deepens to about 50 km beneath the Higher Himalaya.

**Gravity and Magnetic studies:** Gravity studies carried out in the Himalaya and Ganga basin show a negative isostatic anomaly (-120 m gal) over the Ganga basin and positive anomaly (+100 m gal) in the Himalaya (Qureshy and Kumar, 1992). The negative anomaly over the Ganga-foredeep suggests about 5-km-thick Quaternary-Tertiary sediments in the IGP, while the positive anomaly is attributed to both densification and thickening of the crust beneath the Himalaya (Qureshy and Midha, 1986). A detailed quantitative modelling of gravity data suggested flexure as well as thickening of the curst in the Higher Himalaya and Tibet (Lyon-Caen and Molnar 1983). The excess mass of the Himalaya is compensated at depth by the thickened crust. According to Lyon-Caen and Molnar (1983) the dip of the Moho varies from about 3° beneath the Ganga-basin and the Lesser Himalaya to about 15° beneath the Greater Himalaya. They also inferred a decrease in the flexural rigidity of the plate as it moves northward, and suggested ramping of the Himalayan crust over the steep northern edge of the Indian plate. This correlates with the sudden change in the elevation of the Greater Himalaya and steep dip of the MCT (Lyon-Caen and Molnar, 1983; and Pandey *et al*., 1995). Further, gravity measurements across Himalaya show high gradient of Bouguer Gravity anomaly (of the order of 1.3 milli-gal/km) beneath the Higher Himalaya in central Nepal (Cattin *et al*., 2000), in the Sikkim Himalaya (Tiwari *et al*., 2006), and in the northwest Himalaya (Chamoli *et al*., 2011).

Based on these gravity observations the proposed models show that the Moho dips at less than 3° beneath the Lesser Himalaya and 10-22° beneath the Higher Himalaya. Some of these models suggest that this transition occurs abruptly, within a distance of ten or tens of km horizontally (Lyon-Caen and Molnar, 1985; Tiwari *et al*., 2006). Combined interpretation of gravity and magnetic data collected across the eastern Himalaya revealed variation in the Moho depth from 36 km to 74 km (Tiwari *et al*., 2008). Flexure of the Indian lithosphere with an effective elastic thickness of 50±10 km could be the cause of these variations in the Moho depth. In the Western Himalaya, Mishra and Rajsekhar (2006) suggested a 40-km-thick crust south of Lahore-Sargodha ridge to about 70-km-thick crust under Karakoram Range. Geomagnetic investigations in the western Himalaya revealed the existence of a localized conductive zone at depth, embedded in a narrow high seismicity zone (Arora and Singh, 1992).

**Magnetotelluric (MT) Studies:** Several magnetotelluric (MT) studies were conducted along the various segments of the Himalayan belt for delineation of geoelectric crustal structure.

Lemonnier *et al.* (1999) based on modelling of MT data along a profile in Nepal inferred a high conductivity zone at a depth of 20-30 km beneath the Higher Himalaya (Fig. 2.14). The high conductivity is attributed to the presence of metamorphic fluids released due to the under thrusting of the Indian plate and/or distributed brittle deformation around the ramp by an interseismic stress build-up. In the region studied the seismicity concentrates on the ramp structure and correlates with the conductive zone.

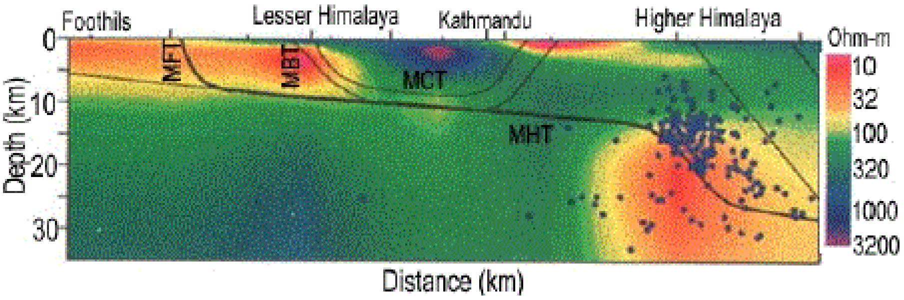

**Figure 2.14:** Section of resistivity model obtained from the MT profile along the central Himalaya, Nepal (Lemonnier *et al.,* 1999)

In the Garhwal Himalaya, two MT experiments were conducted and their results are summarized here. Israil *et al.* (2008), carried out Magnetotelluric investigations in the Garhwal Himalaya along a profile that runs from IGP to the Higher Himalaya. Their conductivity- depth model (Fig. 2.15) indicates a near surface, shallow conductive zone in the IGP and Lesser Himalaya region. They found a correlation between the seismicity and a high conductivity zone beneath the MCT similar to the observations of Lemmonier *et al.* (1999) in the Nepal-Himalaya. The high conductivity zone is interpreted to show a partial molten layer and increased heat flow in the vicinity of the MCT. The conductive zone also appears to be related to the zone of strain accumulation in the Himalaya. This study suggests smooth dip of the Indian plate as it underthrusts beneath the Himalaya supporting the ramp type structure of MHT in the region.

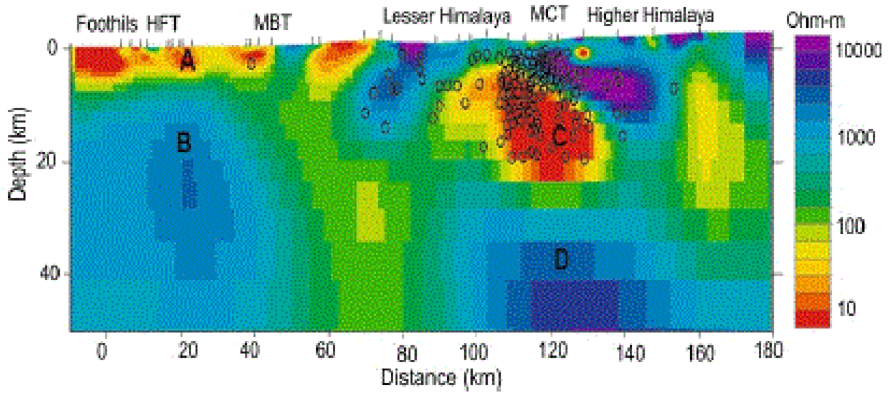

**Figure 2.15:** 2-D geoelectric structure of the Kumauon-Garhwal Himalaya (Israil *et al*., 2008)

In the recent MT experiment in Garhwal Himalaya (Fig. 2.16), Rawat et al. (2014) inferred a conductive zone at a shallow depth of 10-15 km beneath the IGP. This zone dips at a low angle and extends as a continuous layer right up to the MCT. The high conductivity zone mapped beneath the MCT, correlates well with the results of Isarail *et al.* (2008) and Lemonnier *et al.* (1999).

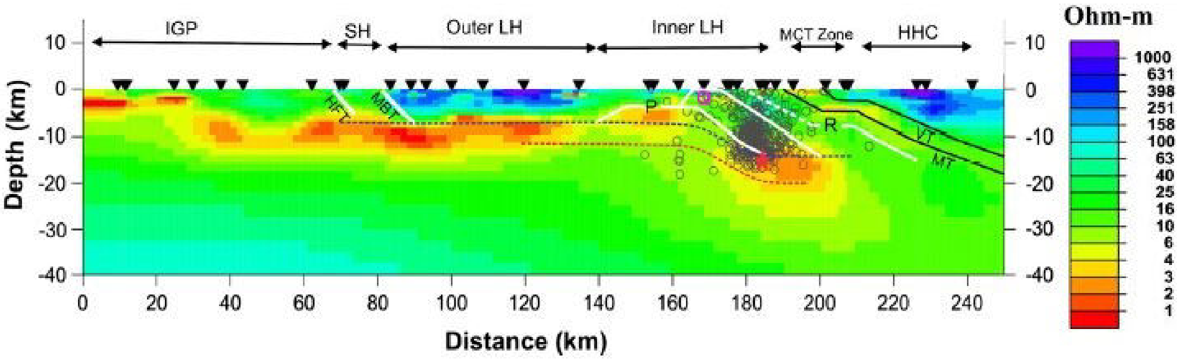

**Figure 2.16:** 2D Geoelectric section of the Kumauon Himalaya (after Rawat et al., 2014)

In the Eastern Himalaya, MT investigations in the Sikkim region show the presence of high conductivity zones at the mid-crustal depths (Patro and Harinarayana, 2009; Manglik *et al.*, 2013), which are interpreted as zones of metamorphic fluids.

## 2.10 Concluding Remarks

In this chapter a brief description of the various methods employed to model 1-D and 3-D velocity structure (seismic tomography) and mathematical background to solve the travel time tomography problem is provided. In nut-shell many new ways have been evolved to exploit seismic traveltime information and to solve tomographic problems. The main application of seismic traveltimes includes determining the structure and composition of the crust and lithosphere from tomographic inversion. The chapter also contains discussion on the coupled hyopenter and velocity model problem, a brief review of the 1-D velocity models for the study region in the Northwest Himalaya region, recent 1-D velocity models proposed for the study region, and a few tomographic studies (3-D velocity structure) carried out particularly for northwestern Himalaya. This chapter concluded with the brief account of studies over Himalaya based on gravity, magnetic and MT methods.

# Chapter 3

# Development of One-Dimensional Local Velocity Model around Tehri Region

---

## 3.1 Introduction

This chapter deals with the estimation of a one-dimensional (1-D) velocity model around the Tehri region in the Garhwal Himalaya from the simultaneous inversion of travel times data of local earthquakes. The estimated parameters include hypocenters and velocity parameters. 1-D velocity models are still the most preferred and widely employed velocity models to estimate hypocenter parameters, although the 3-D velocity models are becoming increasingly popular. These models are a basic requirement to estimate hypocenter locations at many seismological centers engaged in the real time monitoring of seismicity (e.g., Hutton et al., 2006; Midzi et al., 2010). The use of 1-D velocity models provides very rapid earthquake locations, because ray tracing is computationally fast in 1-D velocity models compared to 3-D velocity models (e.g. Hutten et al 2006; Imposa et al, 2009). Needless to mention that 3-D models provide improved locations. However, in the absence of high quality data it is not possible to estimate 3-D models and accurate mapping of hypocenters is still a major requirement. In such cases the computation of a 1D velocity model is the only way to consistently obtain reliable hypocenter locations. 1D velocity models are also the only choice for data quality assessment prior to a 3D tomography study (Husen et al. 2003) and to detect systematic errors in arrival time data (Maurer et al. 2010). In view of these considerations, there was a need for reliable 1D velocity model for the Tehri region for the locating the local earthquakes.

## 3.2 Seismotectonics of the Study Area

The study area, namely, the Tehri region lies between the Main Central Thrust (MCT) and Main Boundary Thrust (MBT) in the Garhwal Lesser Himalaya. The region falls in a seismic gap between the rupture zones of the 1905 great Kangra earthquake, and the 1934 Bihar-Nepal earthquake which was identified by the space time pattern of seismicity (Khattri, 1987). For the past about 50 million years, the process of continuous convergence between Indian and Eurasian tectonic plates at a rate of about 4 cm/year resulted in the formation of the Himalayan orogen and lifting of the Tibetan plateau [*Bilham et al.*, 1997; *Bilham and Gaur*, 2000]. Because of this crustal shortening, several thrust zones have been developed along the 2400-km-long Himalayan arc, bordering the northern edge of the Indian subcontinent. The major boundary thrusts attributed to Himalayan orogeny include: the Main Central thrust (MCT), the Main Boundary thrust (MBT), and the Main Frontal thrust (MFT) (e.g., Seeber and Armbruster, 1981a). It has been postulated that these thrusts are formed due to rupturing of the detachment surface, and along these thrust planes the penetration of the Indian plate below the Eurasian plate still continues (e.g., *Seeber and Armbruster*, 1981a; *Ni and Barazangi*, 1984; *Molnar*, 1990; *Cattin and Avouac*, 2000; Mishra, 2014). It is suggested that the great Himalayan earthquakes, viz., the 1905 Kangra earthquake ($M_W$ 7.8) the 1934 Bihar-Nepal earthquake ($M_W$ 8.0) and the 1950 Assam earthquake ($M_W$ 8.6 ), occurred because of rupturing of the detachment, that lies below the Sub Himalaya and the Lesser Himalaya (e.g, *Seeber and Armbruster*, 1981a,b; *Molnar*, 1990; *Bilham et al.*, 1997; *Cattin and Avouac*, 2000) whereas the moderate earthquakes in the Himalaya occur along the Himalayan seismicity belt (HSB). The HSB is located to the south of the MCT between the Lesser Himalaya and the Higher Himalaya. The hypocenters of moderate earthquakes of the region seem to lie either along or above the detachment (e.g., *Seeber and Armbruster*, 1981a; *Ni and Barazangi*, 1984; *Molnar*, 1990). It is opined that further to the north beyond the MCT, the convergence between the two plates is accommodated aseismically (*Bilham et al.*, 1997; *Gahalaut and Chander*, 1997).

To explain the occurrence of earthquakes and to understand the seismotectonics of the Himalayan collision zone, various models have been proposed for the evolution of the Himalaya. Of these, the steady state model and the evolutionary model have gained significant recognition. These models advocate that the style of contemporary deformation in the Himalaya is attributed to the under thrusting of the Indian plate below the Eurasian plate along the detachment surface, also called the MHT. The steady state model postulates that the MCT and the MBT are active low angle contemporary thrusts. These thrusts are rooted in the plane of detachment that defines the interface between the subducting Indian plate and overlying sedimentary wedge (*Seeber and Armbruster,1981b)*. Figure 3.1 shows the steady state tectonic model postulated by Seeber et al. 1981 with some modifications incorporated by Kayal 2010. Part of the shallow dipping detachment zone to the south of the MCT is called the basement thrust, where the steeply dipping MCT merges with the detachment surface. The Lesser Himalaya is characterized by northwardly dipping thrust zone and the rocks are highly folded and faulted. The evolutionary model postulates that the zone of plate convergence has progressively shifted towards south and is defined by the position of intracontinental thrusts (e.g., *Ni and Barazangi* (1984). According to this model the MBT is the most active thrust sheet and the moderate earthquakes occur in a 50 km wide zone between the MBT and MCT. It is further suggested that the ruptures of great Himalayan earthquakes nucleate in the interplate thrust zone and propagate southward along the detachment surface. Because of this the MBT and the subsidiary blind thrusts located to the south of the MBT are the most active thrusts rooted in the detachment. The recent study in this region suggests that the major thrusts in the region show southward younging and shallowing depths, migration of the main deformation front (*Pant and Paul 2007*). The recent seismic activities also show high seismicity in the region between SNT and the MCT. The MCT and the MBT run almost parallel to the Himalayan arc. There are tectonics and structural features, trending transverse to the Sub-Himalaya, buried beneath the alluvium cover of the Indo-Gangetic plain. The Delhi-Haridwar ridge (DHR) is one such feature whose probable extension beneath the Garhwal Lesser Himalaya is postulated (Khattri et al 1989; Mahesh et al., 2013). Figure 2.2(b) shows the surface expressions of the MBT, the MCT and other regional and local thrusts/faults mapped in the study area that lies in the Garhwal Himalaya between latitudes 29°50ˈN–31°50ˈN and longitudes 77°E–80°E.

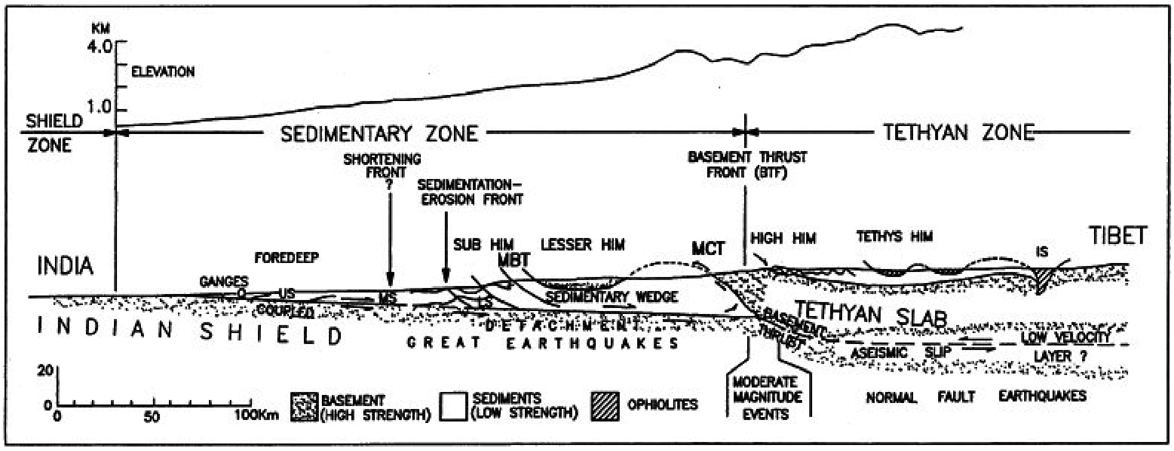

**Figure 3. 1:** Generalised Seismotectonic model across the Himalaya (modified by Kayal, 2010; Kayal, 2001; from Seeber et al., 1981). Q – Quaternary, US, MS, LS: Upper, Middle and Lower Siwaliks, IS- Indus Suture, MBT – Main Boundary Thrust, MCT – Main Central Thrust, MFT - Main Frontal Thrust, MHT -Main Himalayan Thrust

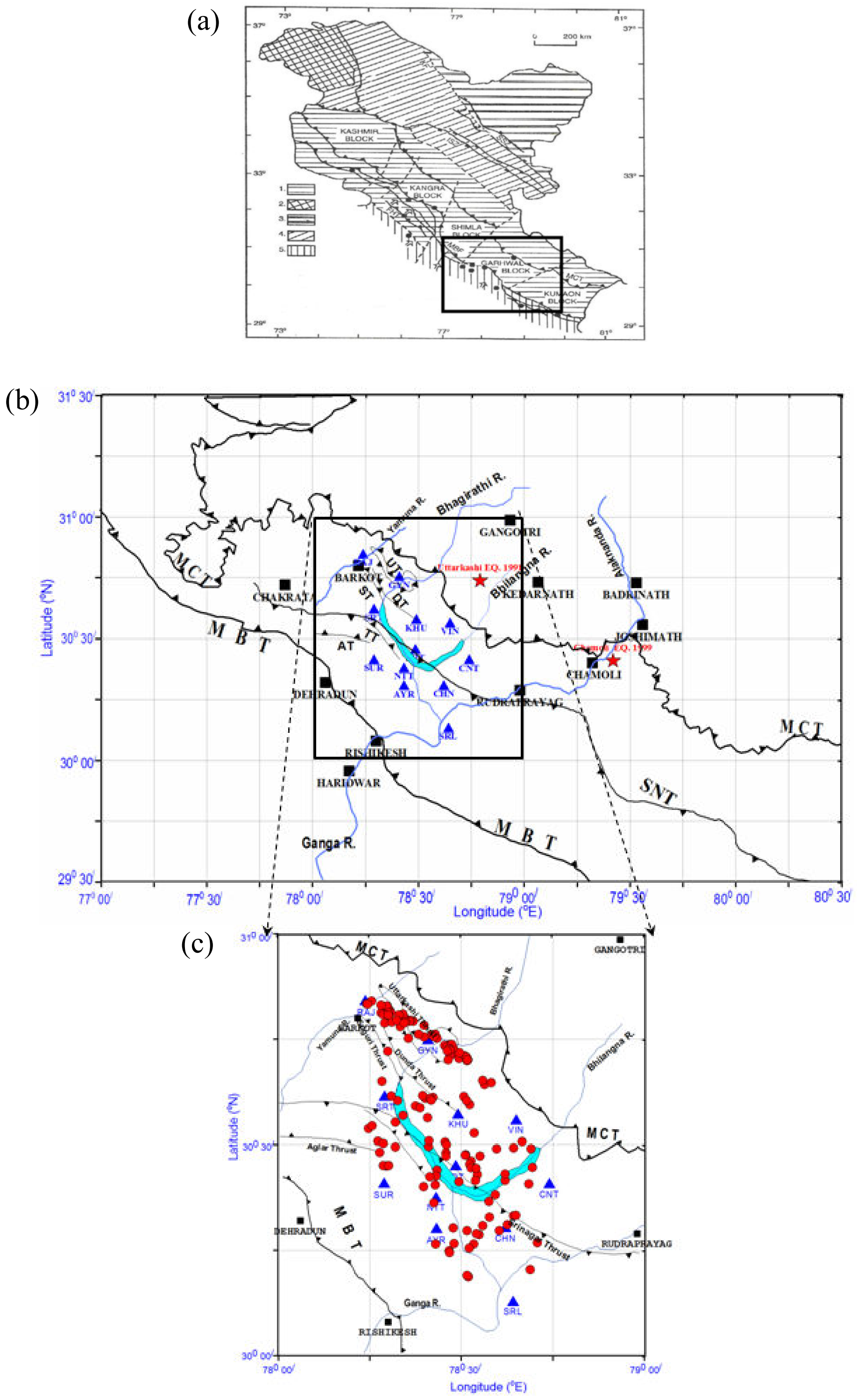

**Figure 3.2:** The simplified tectonic map of the study area. The asterisks show various districts in the area, two star show the Uttarkashi and Chamoli earthquake location, filled circles shows the initial locations data of the events consider for the velocity inversion and the trangles showing seiamic stations. On the map Major and minor trust and faults are plotted. Blue lines on the map show rivers. The inset shows the Seismotectonic domains of the NW Himalayan seismic belt. 1. Main Himalayan Seismic Zone (MHSZ); 2. Kashmir Syntaxial Seismic Zone (KSSZ); 3.High Plateau Seismic Zone (HPSZ); 4 High Himalayan Seismic Zone (HHSZ); 5. Foot Hill Seismic zone (FHSZ), within that small rectangular box shows Garhwal lesser Himalaya block (Narula, 2000)

## 3.3 Data Set used

The area considered in the present study is bounded between latitude 29°45'N and 31°00' and longitude 77°30' and 80°00' (Figure 3.2). Most of the study area falls in the Garhwal Lesser Himalaya and lies between the MCT and the MBT. Some part of the area that falls in the Sub Himalaya and the Higher Himalaya has also been covered. To study the local seismicity of the region around Tehri a 12-station telemetered network has been continuously operating by Department of Earthquake Engineering, Indian Institute of Technology Roorkee since January 2008. The local network encompasses an area of 100 km x 80 km. Triaxial short-period seismometer (Model: CMG 40T-1) (1 Sec natural period), has been installed at each remote station to sense and record the three component ground motion. Data acquisition system (DAS) (Model: 130-01/03) is used to record digital data. Digital data is recorded at a sampling rate of 100 samples/Sec. The parameter of remote stations in the terms of station's code, geographical coordinates, and elevation values is listed in Table 3.1 and shown in Figure 3.2(b). Local events were identified at each stations and arrival times of P-and S-phases were picked using the SEISAN software package (Ottemoller et al., 2011). HYPOCENTER program has been adopted to compute the hypocenter parameters, viz, origin time, latitude, longitude and focal depth of each event. This program was implemented through SEISAN software. The phase data of 1456 local events collected from Jan 2008 to June 2011 through the operation of seismological network has been used in this study. These events fall in the magnitude range from 0 to 4 ($0<M < 4$) and depth range from less than one km 0.1 to 45 km. The preliminary locations of the events are obtained employing three-layer 1-D velocity model (Kumar *et al,.* 1994). Epicenters of a large number of events located using the available data set follow the trend of the MCT and the MBT. However, the majority of events that occurred in the study area are located outside the network. This happened because the network is located primarily to map the local seismicity of the region around the Tehri dam and covers a relatively small area of the Lesser Himalaya compared to the dimensions of the study area. Further, most of the events occur in the vicinity of the MCT and the area encompass by the network is relatively less active. In view of these considerations less number of events are located within the area covered by the network. Although a large data set of local events is available, but for the purpose of travel time inversion only events located within the network have been considered. Out of 1456 events, only 145 events (Appendix II) with azimuth gap ≤180° between individual event and recording stations, and having minimum six P-and S-phase readings were selected for travel time inversion.

**Table 3.1:** Network stations and their Geographical coordinates

| S. No. | Station Names | Locations | | Elevation (meters) |
|---|---|---|---|---|
| | | Latitude (N) | Longitude (E) | |
| 1 | AYR | 30°-18.18' | 78°-25.86' | 2106 |
| 2 | CHN | 30°-18.31' | 78°-37.14' | 2244 |
| 3 | NTT | 30°-22.58' | 78°-25.78' | 1914 |
| 4 | GYA | 30°-45.34' | 78°-25.26' | 2113 |
| 5 | KHU | 30°-34.81' | 78°-29.68' | 1730 |
| 6 | PRT | 30°-27.48' | 78°-28.54' | 2128 |
| 7 | RAJ | 30°-50.64' | 78°-14.29' | 1908 |
| 8 | SIR | 30°-07.92' | 78°-38.03' | 1424 |
| 9 | VIN | 30°-33.99' | 78°-39.32' | 1640 |
| 10 | CHT | 30°-24.59' | 78°-44.69' | 1953 |
| 11 | SRT | 30°-36.76' | 78°-17.93' | 1617 |
| 12 | SUR | 30°-24.66' | 78°-17.39' | 2754 |

## 3.4 Methodology Adopted for the Estimation of Minimum 1-D Model

1-D velocity models are used as initial reference models for estimating 3D velocity models. Kissling et al. (1994) stated that an inappropriate initial reference model may affect both the quality of the 3-D image by introducing artifacts and influence the confidence in calculations by underestimating the uncertainties of the results. Therefore, Kissling et al. (1994) has advocated two step procedure to obtain the 3D velocity model; the first step involves inversion formation to determine hypocenter and one dimensional velocity model parameters; including station corrections; and second step involves 3D inversion. They called the resulting velocity model of first step as ‘the minimum 1-D model’.

Many earthquake location techniques search for the spatial location and origin time that based on a local minimization of arrival time residuals (the observed minus predicted travel times) for a set of earthquake arrivals. These techniques require computation of predicted travel times from the assumed velocity model, and therefore the choice of velocity model and computational scheme/algorithm affects the accuracy of the location. To take care of the inaccuracies in locations introduced on account of assumed velocity model, simultaneous inversion is preferred and is described below.

**Simultaneous Inversion and Coupled Hypocenter Velocity Model Problem:** The travel time of a seismic wave from source to a recording stations is a nonlinear function of the station coordinates(s), the hypocenter parameters (h), and velocity field (m)

$$t_{obs} = f(s,h,m) \tag{3.1}$$

In general, neither the true hypocenter parameters nor the velocity field is known. The only measurable quantities are the arrival times and station locations being, and with these data eq. (3.1) cannot be solved directly. More details need to be added. However, from the assumption of starting velocity model, velocity parameters ($m_i$) and trial hypocenters, travel times from source to receiver pairs can be computed ($t_{calc}$). A linear relationship between the travel time residual and adjustments to the hypocenter ($h_k$) and velocity ($m_i$) parameters is expressed as (Kissling et al., 1994):

$$t_{res} = t_{obs} - t_{calc} = \sum_{k=1}^{4} \frac{\partial f}{\partial h_k} \Delta h_k + \sum_{i=1}^{n} \frac{\partial f}{\partial m_i} \Delta m_i + e \tag{3.2}$$

In matrix notation the above expression which represents the coupled hypocenter velocity model parameter relation can be written as:

$$t = Hh + Mm + e = Ad + e \tag{3.3}$$

Where,

t = Vector of travel time residuals;

H = Matrix of partial derivatives of travel time with respect to hypocenter parameters;

h = Vector of hypocenter parameter adjustments;

M = Matrix of partial derivatives of travel time with respect to model parameters;

m = Vector of model parameter adjustments;

e = Vector of travel time errors, including contributions from errors in measuring the observed travel times, error in $t_{calc}$ due to errors in station coordinates, use of the wrong velocity model and hypocenter coordinates, and errors caused by the linear approximation;

A = Mmatrix of all partial derivatives;

d = Vector of hypocenter and model parameter adjustments.

Generally, the solution to (3.3) is taken as the least squares solution that minimizes a weighted combination of the squared error ($e^Te$) and a measure of the velocity model change, typically its Euclidean norm ($m^Tm$) [Spakman and Nolet, 1988]. Under the assumption of normally distributed errors and model perturbations, the least squares formulation result is the most likely solution that belongs to the same family of solutions as the initial reference-model. By seeking a solution in the neighbourhood of the initial reference model, defects in the reference model may lead to artifacts in the 3-D tomographic images, particularly when the solution is not refined through model updating and iteration. Because the parameter space commonly contains several thousand unknowns, simple iteration schemes may be incapable of avoiding local minima and thus may not converge to the global minimum. To overcome this artifact, Kissiling et al. (1994) emphasized Minimum 1-D model as described below:

**The concept of the minimum 1D model:** The concept to compute an initial reference model for a subsequent 3D local earthquake tomography was introduced by Kissling (1994). A minimum 1D model is computed by simultaneous inversion of travel time data from local earthquake for hypocenter location, seismic velocities, and station delays. Hence, it represents a full solution to the coupled hypocenter-velocity problem (Kissling 1988; Kissling et al. 1994). The computation of a minimum 1D model explicitly solves the coupled hypocenter-velocity problem, and thus it also provides suitable velocity models for routine earthquake locations, where a similar accuracy in earthquake location is required for each single earthquake (Kissling 1988). The solution is computed by using a damped least square approach (Kissling, 1988) and each inversion consists of several iterations. The inversion terminates when model adjustments become insignificant and a significant reduction in data variance has been achieved. As stated earlier, a minimum 1-D model can be used for data quality assessment prior to local earthquake tomography (Husen et al. 2003). Further, the 1-D model can detect systematic errors in arrival time data (Maurer et al. 2010), because the minimum 1-D model yields an average minimum data fit and may not absorb systematic errors in arrival time data as it is highly over determined. An additional advantage of the 1-D model is that, the non-linearity in solving 1-D problems as compared to 3-D problems is less severe due to the small size of solution space Husen et al. (2011).

The routine procedure to compute minimum 1-D model is given in the VELEST users Guide (Kissling, 1995; Kissling et al. 1994). This is a trial and error procedure adopting different initial velocity models, initial hypocenter locations, and damping and control parameters to seek a solution for the coupled inverse problem. Many authors have used VELEST for calculation of minimum 1-D model worldwide. Huslinger et al. (1999), using VELEST computed minimum 1-D model from local earthquake data, to use it as an initial model for the 3-D tomography of the Gulf of Arta located around the Ionian region, NW Greece. Imposa et al. (2009) calculated minimum 1D model using VELEST for the Middle-Durance Fault Zone, southeastern France. Husen et al. (2011) has completed one regional minimum 1D model and three local minimum 1D models for the selected sub-regions of the Swiss Alpine region. They demonstrated that the local minimum 1D model provides more realistic hypocenter locations and better data fits than a single model for the Alpine region.

## 3.5 Estimated 1-D Model and Its Validation

### 3.5.1 1-D Velocity Model from Travel Time Curve

Travel time curves have been traditionally adopted to estimate the 1-D velocity structure of a homogeneous layered earth model. In view of this to begin with, the preliminary velocity model of the region was estimated using the travel time curves. For this purpose the arrival times of the P- and S-phases were plotted against the epicentral distances considering the local events with focal depths not more than 10 km, and the epicentral distances up to 300 km. The travel time curves as depicted in figure 2.3 have brought out three linear trends corresponding to the arrival times of Pg, $P^*$ and Pn. From the slope of these three linear trends, the P-wave velocities and thicknesses of two layers have been estimated using the standard method. A similar exercise was done for the travel time curves of Sg, $S^*$and Sn phases. From the regression analysis of the data, the velocities of Pg, $P^*$, and Pn phases were estimated at $5.41\pm0.07$, $6.23\pm0.09$ and $8.34\pm0.10$ km/sec and the two layer thicknesses as 16.51 and 29.96 km, respectively, with the Moho depth of 46.47 km. Similar linear regression analysis was carried out for S-wave travel-time curves, and the velocities of $S_g$, $S^*$, and Sn phases were estimated as $3.17\pm0.05$, $3.39\pm0.01$ and $4.86\pm0.04$ km/sec, respectively. The estimated depths of the layers by and large remained same. The thicknesses of the two layers estimated using S-arrival-time data were 16.81 and 30.8 km, and remained almost same as obtained from the P-wave travel-time curves. The average value of the $V_P/V_S$ ratio estimated from this analysis is 1.74 for the whole region. The layer parameters are listed in Table 3.2, and the velocity model is depicted in Figure 2.3.

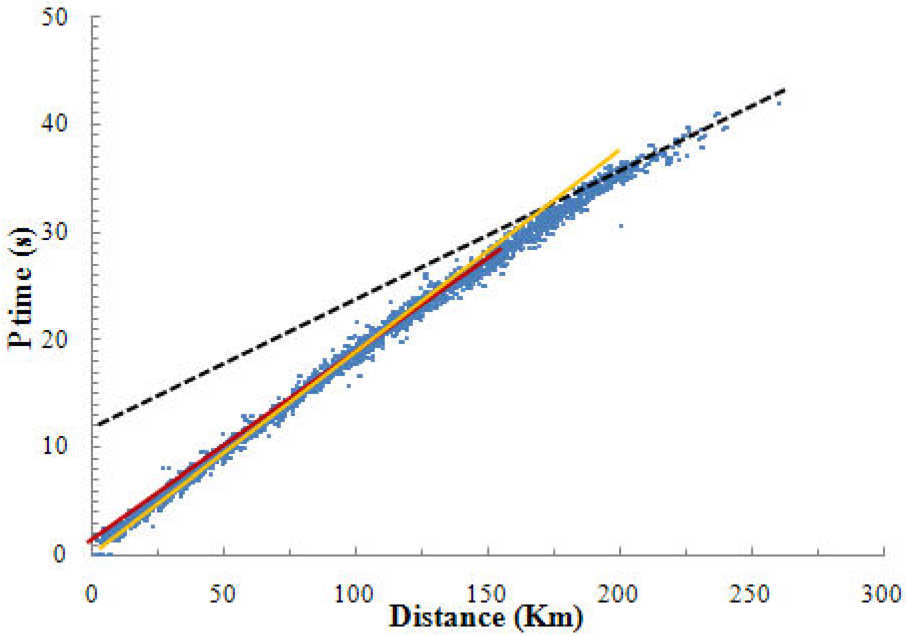

**Figure 3.3:** Travel time curve of P-wave arrivals

**Table 3.2:** Velocity model from Travel time curve

| **Thickness (km)** | **$V_P$ (km/s)** | **$V_S$ (km/s)** | **$V_P/V_S$** |
|---|---|---|---|
| 16.51 | 5.41±0.07 | 3.17±0.05 | 1.70 |
| 29.96 | 6.23±0.09 | 3.39±0.01 | 1.83 |
| Half-space | 8.34±0.10 | 4.86±0.04 | 1.70 |
| **Average ($V_P/V_S$)** | | | 1.74 |

### 3.5.2 Determination of Minimum 1-D Velocity Model from Travel Time Inversion

For the determination of the minimum 1D velocity model, the widely known algorithm VELEST has been adopted (Kissling *et al.,* 1984; Kissling, 1988). This algorithm involves, joint inversion of travel time data and allows estimating a 1-D velocity model along with revised hypocenter coordinates and station corrections. The estimation of the model is based on a trial and error process that ideally starts with the collection and selection of *a priori* information about the subsurface structure. Since this process can lead to ambiguous results, particularly when more than one *a priori* 1-D model have been established, several parameters which control the inversion procedure need to be varied and the corresponding results need to be evaluated (Kissling *et al.*, 1994). The algorithm used is based on solving the forward problem of ray tracing from source to receiver, and then inverse problem is solved employing damped least square method. The problem is non-linear due to the heterogeneity of earth and is linearized to solve the problem. The solution is obtained iteratively, where single iteration consists of solving the complete forward problem and the complete inverse problem. The final inverted model depends upon the spatial distribution of recording stations, seismic sources and a priori initial velocity model.

The root mean square residuals (RMS), defined by the sum of all travel-time residuals, provide the measure of goodness of the fit. A set of 145 well-located events with RMS lower than 0.9 sec, the azimuthal gap between recording stations and individual events is ≤180°, and with at least six or more P- and S-phase readings are selected for inversion. Maximum epicentral distances of these events are up to 50 km between an event and stations. A total of 1177 P-phases and 1090 S-phases were inverted. The distribution of events shows that the central block bounded between 30.15° N and 30.80° N, and 78.25° E and 78.75° E are well-covered, thus, defining the representative region for the estimation of velocity model.

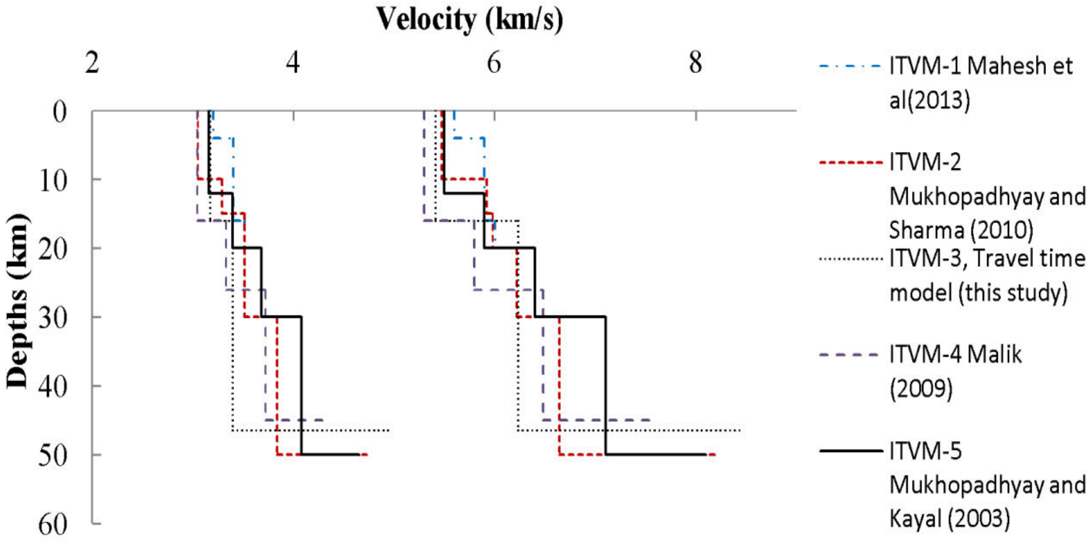

**Figure 3.4:** Representing various 1-D Velocity models used in the travel time inversion as the initial trial velocity models (ITM'S), left for S-wave and right for P-wave

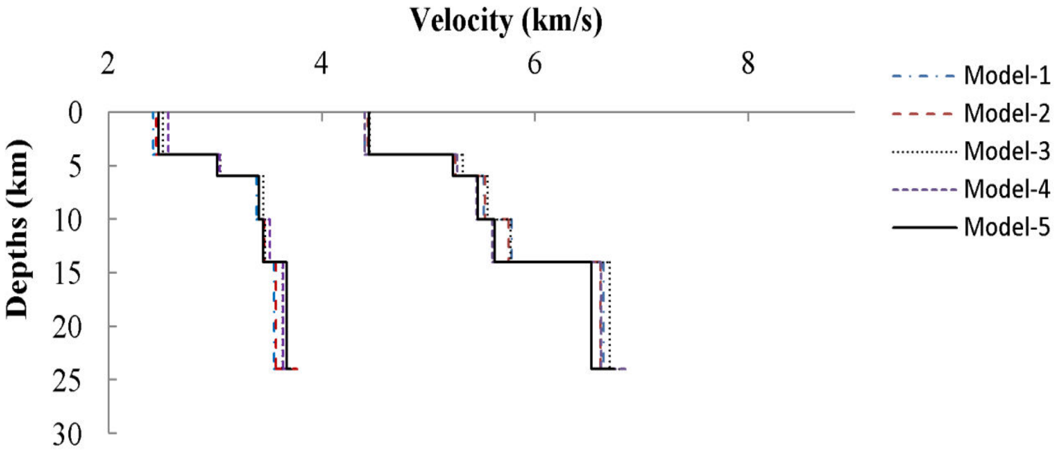

**Figure 3.5:** Representing resulting 1D velocity model after travel time inversion without consideration of low velocity, left for S-wave and right for P-wave

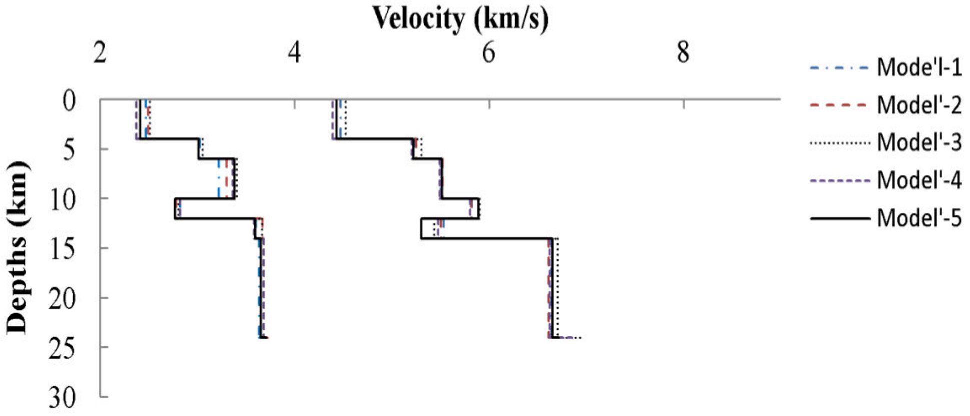

**Figure 3.6:** Representation of resulting 1D velocity model with low velocity layer after travel time inversion, left for S-wave and right for P-wave

### 3.5.3 Minimum 1-D Model Estimation

The initial Hypocenter locations are primarily confined to depths up to 20 km with some events having depths up to 25 km. A very few events are scattered in the depth range between 25 and 30 km. Because of this shallow nature of seismicity, the inversion of travel-time paths could resolve the velocity structure of the upper part of the crust up to about 24 km or so. The current data set is unable to resolve the depth of the Moho. The Moho depth of ~46 km as estimated from travel-time-distance plots (Table 3.2) is used as a priori information. We tested several initial a priori velocity models given for the Himalayan regions for joint inversion of the earthquake hypocenters and 1-D velocity model. The range of a-priori models tested includes: the velocity model for Kangra-Chamba region

(Kumar *et al.*, 2009); models for north-west Himalaya (Mukhopadhyay and Sharma, 2010; and Mukhopadhyay and kayal, 2003); a model for the Garhwal Himalaya (Malik, 2009) and above mentioned three layer model obtained from the present analysis of travel-time-distance plot (Table 3.2). In further discussion all Initial trial velocity Models are called as ITVMs and output models resulting from travel-time inversion are referred as Models, and are shown in figure 3.4. Each ITVM was initially parameterized as stack of 2 km thick layers up to a depth of 24 km and a stack of 4 km thick layers from 24 km to 50 km. The inverted velocity model was then iteratively simplified by fusing similar velocity layers to generate the next input velocity model. For each ITVM, the process of inversion was terminated when average RMS did not change significantly in successive iterations.

This procedure has been carried out for two types of independent results: 1) without considering low velocity layer in the output model, and 2) considering apparent low velocity layers in the middle of gradient model. For both results average RMS and hypocenter parameter resolution coefficients have been compared.

In all cases that involved inversion without considering low velocity layer, the resulting models are able to resolve layers up to a depth of about 24 km. An observed common characteristic of all inverted models is the decrease of first layer velocity to a significant value as compared to the velocity in initial velocity models. This feature of resulting models is checked with the inputs from several velocity profiles, but each time results converge to the decreased value only. For all resulting models, The first layer velocity value ranges from 4.40 to 4.52 km/sec for P-wave and 2.45 to 2.65 km/sec for S-wave respectively with a depth of 4 km calculated from the surface (Figure 3.5). As seen in figure 6 inverted velocity models in all cases support five layer velocity structure up to a depth of 24 km. Layers beyond 24 km depth are not possible to resolve due to the poor ray coverage. The 4km-depth first layer is also supported by the ITVM-1 given by Mahesh et al. (2013). However, ITVM-1 signifies no further layers up to a depth of 16 km. This is also observed in model resulting from travel time plot in the present study. Inverted resulting models in this study indicate distinctive velocity interfaces, at depths of 6 km, 10 km and around 14 km. To check the reliability of these depth partitions we tested hundreds of initial velocity models by varying the depths interfaces up to ± 1 km. The inverted velocity models did not portray the interfaces in between these partitions, but in case, the partition is introduced in between then velocity transition was nominal at about ±0.5 km/sec. Velocity transitions were stronger for layers depths of 4 km, 6 km, 10 km and 14 km. Beyond 14 km depth, inverted models show a strong velocity transition at a depth of 24 km only. Below this depth, no change over in velocity values could be interpreted when tested by varying the thickness of layers by ± 2 in the input velocity models.

**Table 3.3:** Quality check parameters for resulting velocity models

| **Hypocenter parameter resolution from increasing gradient model :( Diagonal elements of resolution matrix)** | | | | |
|---|---|---|---|---|
| **Model-1** | **Model-2** | **Model-3** | **Model-3** | **Model-4** |
| 0.9987 | 0.9981 | 0.9981 | 0.9976 | 0.9977 |
| 0.96 | 0.9608 | 0.9604 | 0.9564 | 0.9597 |
| 0.9697 | 0.9691 | 0.9688 | 0.9679 | 0.9691 |
| 0.9136 | 0.8867 | 0.8873 | 0.8722 | 0.8358 |
| **Avg. RMS travel time residuals (sec)** | | | | |
| 0.2409 | 0.2407 | 0.2415 | 0.2421 | 0.241 |
| **Hypocenter parameter resolution from velocity model with low velocity layer : (Diagonal elements of resolution matrix)** | | | | |
| **Model'-1** | **Model'-2** | **Model'-3** | **Model'-4** | **Model'-5** |
| 0.9984 | 0.9983 | 0.9984 | 0.9983 | 0.9983 |
| 0.9596 | 0.9596 | 0.9586 | 0.9593 | 0.9591 |
| 0.9699 | 0.9696 | 0.9692 | 0.9695 | 0.9694 |
| 0.9281 | 0.9345 | 0.951 | 0.9447 | 0.9681 |
| **Avg. RMS travel time residuals (sec)** | | | | |
| 0.2426 | 0.2416 | 0.2394 | 0.2395 | 0.2391 |

In the resulting velocity models, the average RMS values have reduced significantly compared to the initial average RMS values of trial hypocenters. The average RMS values with respect to each Model decreased from 0.7 sec (average RMS of initial trial events) to 0.24 sec (Table 3.3). Further, the parameters of individual layers were well resolved as the principle diagonal elements of the resolution matrix were above the critical threshold value of 0.5. Hypocenter parameters of relocated events are also well resolved. However, the focal depth was found to be less resolved compared with other hypocenter parameters (Table 3.3).

The low-velocity-layer option was not incorporated until this step in the inversion because the low-velocity layers introduce instability in the early stages of inversion. After estimating the acceptable gradient velocity model, an attempt is made to refine the model by introducing the option of low velocity layers with appropriate choice of damping factors in the inversion. In the initial iteration, the damping values of 5 and 10 were applied to the first and last layer, respectively. Using these damping values, a low velocity layer was extracted between 12 and 14 km depth for P-wave. However, for the S-wave model, a low-velocity layer was obtained between a depth of 10 and 12 km depth. P-wave velocity and S-wave velocity were treated as two independent variables. This preliminary finding of low velocity layers was tested with a large number of varying velocity profiles and damping values through a large number of iterations. It is found that low velocity layer is consistently shown by each pair of initial input and inverted velocity model (Fig. 2.6)

Kissling (1988) has shown that the low-velocity layer introduces some computation instabilities in locations on the regional scale. When the low-velocity-layer model was used to represent the velocity structure around Tehri, the resolution of hypocenter parameters, particularly hypocenter-depths, was improved. Further, the comparison of the average RMS values those obtained from the earlier gradient velocity model, showed a decrease in the average RMS values. The improved hypocenter depths conform to the tectonic setting of the region. When compared with the layer parameters of the increasing gradient velocity model, the low-velocity-layer parameter was less resolved because of its decreased resolution coefficient. However, the resolution coefficient of hypocenter parameters showed a reasonable increase (Table 3.3).

One of the criteria to validate the stability of the inverse problem is based on total number of observed phases with respect to the number of unknown parameters. There are total 598 unknown parameters that include: $145 \times 4$ hypocenter parameters, six layers with P-and S-velocity models (five in case of gradient model) and 12 station corrections. The total P- and S- phase observations are 2267. Therefore, the value of overall determination factor is approx 3.7. Both the velocity models (increasing gradient model and low-velocity-layer model) are shown in figures 3.5 and 3.6. The diagonal elements of the velocity resolution matrix range between 0.92 and 0.98 and standard deviations of the velocity values are confined within $\pm 0.15$ km/sec.

In the light of above computations and discussion, Model'-5 (Fig. 3.6) has been chosen as the preferred velocity model. This model shows less average RMS value and best resolved hypocenter parameters (Table 3.3) among all five resulting models and is adopted as a minimum 1D model for the region under study.

### 3.5.4 Optimum 1-D Crustal Velocity Model

From travel time inversion, a Minimum 1-D velocity model of the region is obtained with six layers over a half space at a depth 24 km with a low velocity layer in between. On the basis of the travel time plot we inferred the overall thickness of the crust at about ~46 km which defines boundary of Moho having P-wave velocity 8.34 km/sec and S-wave velocity 4.86. Travel time plot also allowed estimation of two layered velocity model, with first layer having thickness of ~16 km and second layer as ~30 km. By combining the information gleaned from travel time plot and minimum 1-D model, we propose an optimum 1-D velocity model that represents a crustal velocity structure up to the Moho.

The Moho depth in the northern Himalaya has been previously estimated by various researchers (e.g., Monsleve *et al*., 2006; Caldwell *et al.,* 2013; Rai *et al.,* 2006; Kumar *et al.,* 2009). According to these studies the Moho depth the is below or around 45 km or more in this section of the Himalaya with area-wise slight variations attributed to the complex tectonic structure. Caldwell *et al.* (2013) mapped the characteristics of Main Himalayan Thrust (MHT) in the Garhwal Lesser Himalaya with receiver function CCP stacking method. According to this study the Moho boundary is nearly horizontal at 35–45 km depth beneath the Sub-Himalaya and Lower Himalaya and deepens up to 50 km depth or more beneath the Higher Himalaya. The estimated thickness of subducted Indian crust in the Garhwal Himalaya is 20-28 km. Their study area encompasses the study area of present study which primarily lies in the Lesser Himalaya. Rai *et al.* (2006) estimated the Moho depth of 40 km around Delhi in the Indo-Gangetic plains (IGP) and depth of 75 km beneath the Higher and Trans-Himalaya (Karakoram) from the regional Moho profile across the entire northern Himalaya.. They mapped this depth of the Moho from receiver function analysis of P- and S- waveforms of teleseismic events and inferred that the Moho dips towards north.

In view of the above considerations optimum 1-D velocity model, given in Table 3.4, is the best representation of the velocity structure of the study region. This model is derived from a minimum 1-D model that divides the upper 24-km-thick of a crust into six velocity layers including a 2-km-thick velocity layer at 12 km depth. The lower crust velocities are obtained from the travel time plot, thus defining the velocity model covering a full description of crust. Needless to mention, that velocities and layer-thicknesses in the upper crust are well-resolved compared to the lower crust. Because most of the seismicity of the region occurs in the upper part of the crust, therefore, the well resolved upper crust layer parameters are appropriate for the local and regional studies. The estimate of first-layer P-wave velocity of 4.42 km/sec is much lower compared to those reported in the previous studies conducted for the regional crust. This low P-wave velocity can be ascribed to the sedimentary wedge beneath the study region.

**Table 3.4:** Optimal 1-D Velocity Model

| Depth (km) | $V_P$ (km) | $V_S$ (km) |
|---|---|---|
| 0 | 4.43 | 2.41 |
| 4 | 5.22 | 3.01 |
| 6 | 5.51 | 3.38 |
| 10 | 5.89 | 2.77 |
| 12 | 5.30 | 3.59 |
| 14 | 6.65 | 3.65 |
| 24 | 6.81 | 3.71 |
| 46 | 8.34 | 4.86 |

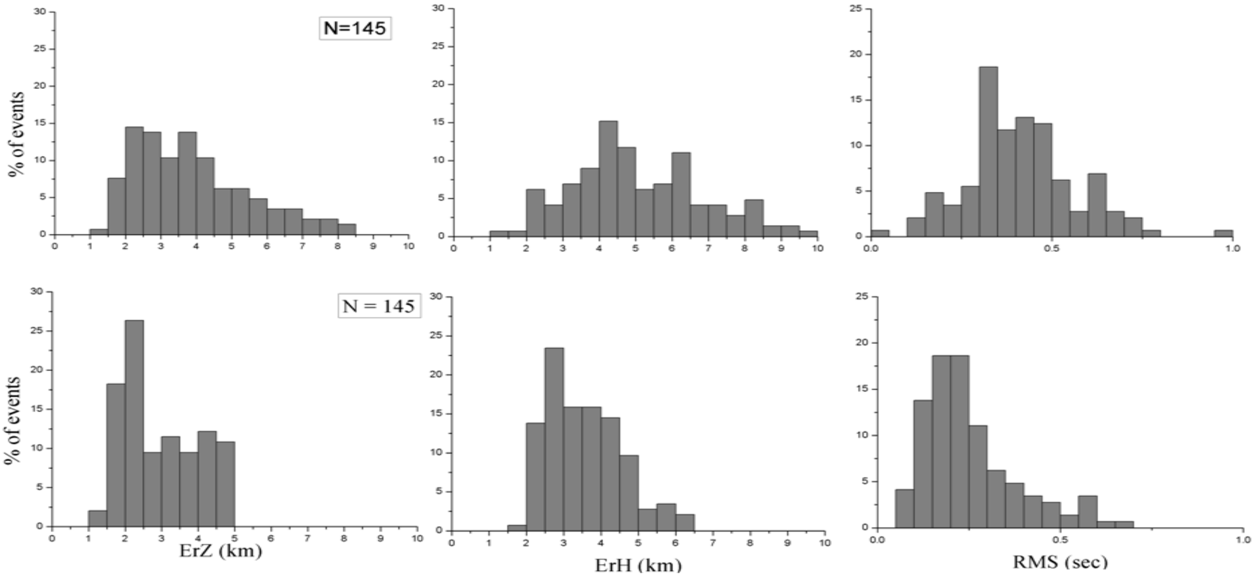

**Figure 3.7:** Histogram showing error statistics for hypocenter location (km), depth (km) and travel time residuals(s) (a) Initial (b) Optimum 1D model

### 3.5.5 Validation

The performance of the proposed optimum 1-D velocity model was tested by comparing error statistics of the well-located local events having constrained GAP $<180^0$. For this purpose, the initial locations of these events were compared with those obtained using the optimum 1D model. Figure 3.7 shows the comparison between RMS residuals, standard errors in epicenters and focal depths for events located using initial 1D velocity models and the optimum 1D model. A significant decrease in the values of error parameters is clearly demonstrated. RMS residuals of relocated events are mostly confined to 0.0 to 0.5 sec compare to 0.0 to 1 sec in the initial locations. Similarly the errors in locations and depths are also shifted to the smaller values compared to the earlier error range.

### 3.5.6 Station Corrections

It is well known that Earth's heterogeneity exhibits lateral and vertical velocity variations. To minimize the effect on account of such heterogeneities, measurements of station correction are incorporated to take care of velocity deviations in 1D velocity model on account of topography and near surface structural variations (Kissling, 1995). Topography of the study area varies from 1100 m to 2700 m. By incorporating the station elevations in VELEST program, the biases on the station corrections due to topographical effects are excluded. The calculated values of station corrections for P- and S-waves are listed in Table 3.5. PRT was taken as reference station. The choice of PRT as reference station is guided by two factors: a) this station is located almost at the center of the network, and b) maximum number of phase readings are available from the station. As prescribed in the program, the station correction of the reference station was fixed as zero. Negative and positive station corrections correspond to higher and lower actual velocities beneath the recording stations, with respect to velocities beneath the reference station.

**Table 3.5:** Geographical coordinates of the stations and station corrections values obtained using the optimum velocity model

| S. No. | Station Names | Locations | | Elevation (meters) | P-wave Station Corrections | S-wave Station Corrections |
|---|---|---|---|---|---|---|
| | | Latitude (N) | Longitude (E) | | | |
| 1 | AYR | 30°-18.18' | 78°-25.86' | 2106 | -0.15 | -0.14 |
| 2 | CHN | 30°-18.31' | 78°-37.14' | 2244 | 0.08 | 0.07 |
| 3 | NTT | 30°-22.58' | 78°-25.78' | 1914 | -0.01 | -0.07 |
| 4 | GYA | 30°-45.34' | 78°-25.26' | 2113 | -0.36 | -0.58 |
| 5 | KHU | 30°-34.81' | 78°-29.68' | 1730 | -0.02 | -0.03 |
| 6 | PRT | 30°-27.48' | 78°-28.54' | 2128 | 0.0 | 0.0 |
| 7 | RAJ | 30°-50.64' | 78°-14.29' | 1908 | -0.15 | -0.27 |
| 8 | SIR | 30°-07.92' | 78°-38.03' | 1424 | 0.02 | 0.16 |
| 9 | VIN | 30°-33.99' | 78°-39.32' | 1640 | 0.08 | 0.09 |
| 10 | CHT | 30°-24.59' | 78°-44.69' | 1953 | 0.02 | -0.14 |
| 11 | SRT | 30°-36.76' | 78°-17.93' | 1617 | -0.29 | -0.28 |
| 12 | SUR | 30°-24.66' | 78°-17.39' | 2754 | 0.13 | 0.3 |

### 3.5.7 Significance of Low Velocity Layer

A low velocity layer is observed at depths below 10 km, and the effect of the low velocity layer is visible on the depth distribution of local seismicity along various sections to be described later. Either a very few events occur in the region of low velocity zone or the region is marked by a nearly horizontal distribution of hypocenters. Such low velocity layer has also been observed in other studies, e.g., in the Kangra Chamba region of the Himanchal Himalaya by Kumar et al., 2009 and in the Chamoli region of Garhwal Himalaya by Mukhopadhyay and Kayal 2003. Various scientific explanations are given to the existence of a low velocity zone, notably among these are the fluid filled fractured zone, presence of molten materials, mechanically weaker crusts, the separation between the brittle and weaker part of the crust. In the study area the formation of a low velocity layer at a depth around 10-12 km can be attributed to the weakening of the crustal material at the interface between the overriding Himalayan block and the upper part of the under thrusting the India plate on account of its frequent rupturing due to earthquakes.

### 3.5.8 Concluding Remarks

An Optimum 1 D velocity model is proposed for the region around Tehri in the Garhwal Himalaya based on the travel time inversion of 145 local earthquakes with azimuthal Gap < $180^0$ and travel time curves of crustal phases. The model consist of six layers with P-wave and S-wave velocities ranging from 4.42 to 6.78 km/sec and 2.41 to 3.71 km/sec respectively up to a depth of 24 km. Mohorovicic discontinuity seems to be at a depth of about 46 km with P-wave and S-wave velocities of 8.34 km/sec and 4.86 km/sec respectively. A 2-km-thick low velocity layer has been deciphered between 12 and 14 km depths. The existence of a low-velocity-layer is possibly attributed to fractured basement thrust because of weakening of the crustal material at the interface between the overriding Himalayan block and the upper part of the under thrusting India plate. This is also supported by the large number of local events occurring in the vicinity of the MCT in the Garhwal Inner Lesser Himalaya.

# Chapter 4

# Characteristics of Contemporary Local Seismicity Based on the 1-D Velocity Model

## 4.1 Introduction

This chapter deals with the study of the characteristics of local seismicity based on the spatial and depth distribution of events located using the 1-D velocity model derived in the chapter 3. Determination of accurate hypocenters are necessary to identify the earthquake clusters that delineate on a seismically active fault or seismogenic sources. The area of study is bounded between the latitude $29^o45'$N and $31^o00'$N and the longitude $77^o30'$E and $80^o00'$E (Fig. 3.2 (b)) and primarily falls in the Garhwal Lesser Himalaya between the MCT and the MBT. Small parts of the area fall in the Sub Himalaya and the Higher Himalaya. To allow studding the characteristics of the study area, 1468 events recorded between January 2008 and December 2011 have been relocated with the 1-D velocity model and station corrections. To study the seismicity patterns along and across the trend of major tectonic features, several depths sections have been drawn by projecting hypocenters on vertical cross sections. Following sections describe the details on various aspects of seismicity and proposed seismotectonic model.

## 4.2 General Seismicity of the Region

Several medium to large size earthquakes ($1<M<8$) have occurred in this region, according to the historical and instrumental records, reported by India Meteorological Department (IMD). In Uttarakhand state one of the earliest disastrous earthquakes (magnitude 6.5) as reported by IMD was of magnitude 6.5, which occurred on July 15, 1720 at Latitude 28.37°N and Longitude 77.1°E. Other prominent earthquakes experienced in this region include: (i) the Feb 28, 1906 earthquake (M 7.0), (ii) the June 04, 1945 earthquake (M 6.5), (iii) the Feb 23, 1953 earthquake (M 6.0), (iv) the July 14, 1962 earthquake (M 5.5), (v) the July 29, 1980 Dharchula earthquake (M 6.1) (vi) the Uttarkashi earthquake of Oct 20, 1991 (M 6.4) and (vii) the March 29, 1999 Chamoli earthquake (M 6.8). The earthquake of July 14, 1962, (M 5.5), was felt strongly at Mukteshwar and triggered landslides near Joshimath

(GSI, 2000). The 1991 Uttarkashi earthquake affected various parts of Uttarkashi and nearby areas. It took a toll of more than 727 human lives, injured several thousand people and caused severe to partial damage to about 100,000 houses. The 1999 Chamoli earthquake also caused extensive damage to life and property in the meizoseismal area that encompassed the Chamoli and Rudraprayag districts of Garhwal region. According to official estimates the earthquake took a toll of 103 human lives. The effects of this earthquake were spread in varying degrees in Tehri, Bageshwar, Uttarkashi and Pauri districts of Uttarakhand. Maximum epicentral intensity was close to VIII on MMI scale.

## 4.3 Relocating Events Employing JHD

The 1486 local events collected from January, 2008 to June, 2011 from the operation of the 12-station local network was used in this study. These events fell in the magnitude range from 0 to 4 ($0<M_L< 4$) and their depths ranged from 1 km to 45 km. The preliminary locations of the events, obtained by employing a three-layer 1-D velocity model (Kumar et al., 1994), brought out that the epicenters of a large number of events follow the trend of the MCT, and that majority of the events occurring in the study area were located outside the network.

The hypocenters of all recorded events numbering 1486 were relocated using joint hypocenter determination (JHD) method. VELEST in the single event mode was adopted for this purpose (Kissiling, 1995). Using the optimum 1D velocity model and station corrections (explained in the previous chapter), events was relocated to study the distribution of seismicity of the region on the local and regional scale. Dimensions of the network cover only a small part of the study region, therefore, to study the distribution of seismicity occurring outside the network, events, falling outside the network, are also required to be relocated.

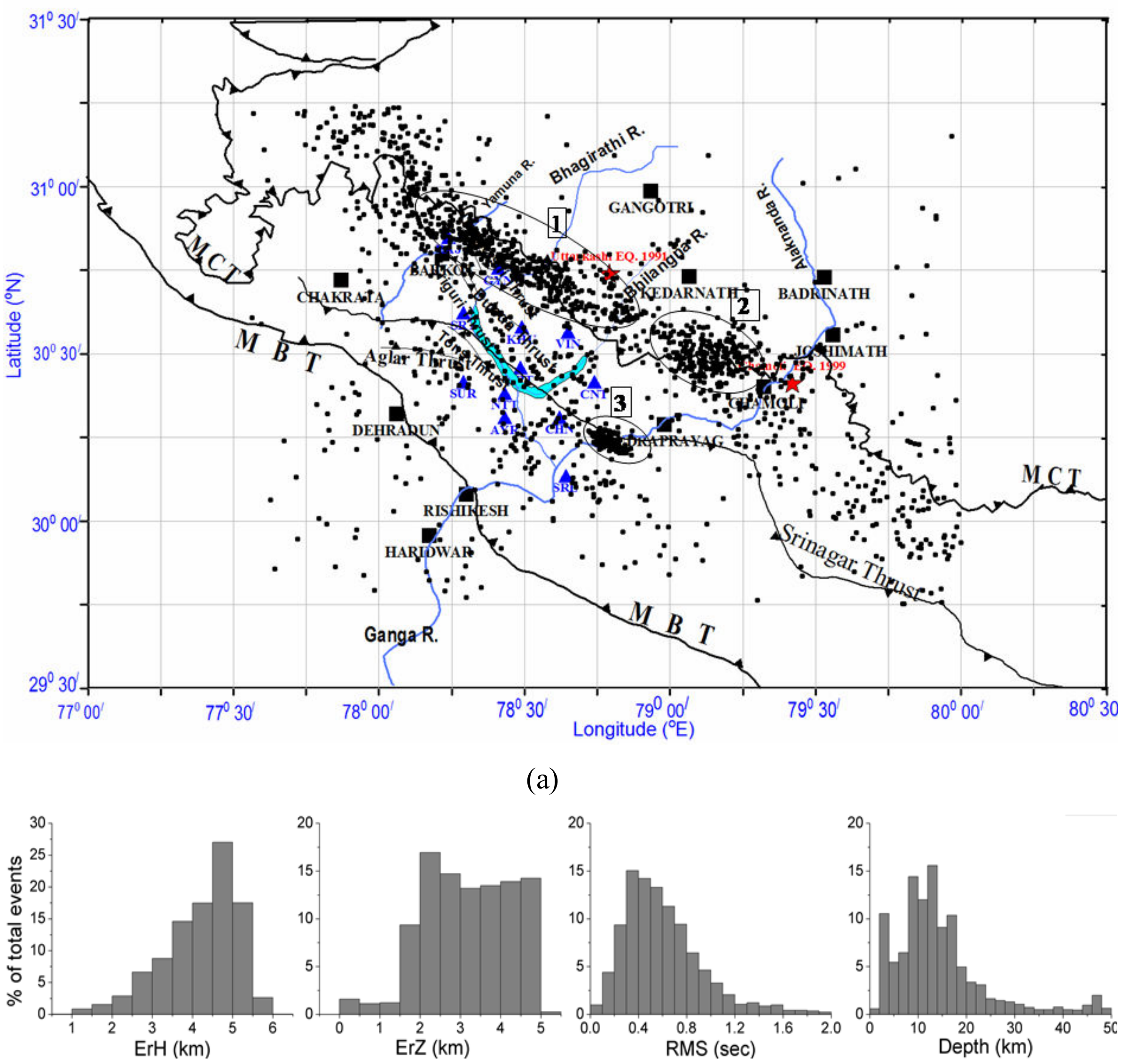

(a)

(b)

**Figure 4.1:** (a) Study area showing distribution of epicenters of relocated events. Prominent clusters of seismicity are marked as ellipses. (b) Histogram showing error statistics for hypocenter location (km), depth (km) and travel time residuals(s)

In view of this, hypocenters of events excluded from travel time inversion were also relocated and used in the interpretation of the seismotectonic model of the region. Data of events considered now include events occurring in all azimuth directions from 0° – 360°. Due to lack of azimuth coverage for events falling outside the network, errors are introduced in the estimation of hypocenter parameters. To investigate this effect of azimuth coverage, the total number located events were divided into three categories according to their azimuth directions, namely, 0° -180°, 180° -270°, and 270° -360°. Histograms showing the distributions of standard errors and focal depth distribution of the entire located activity are depicted in Figure 4.1 (b), whereas Figure 4.2 portrays the effect in standard errors due to azimuth for three different groups of events. A shift in the standard errors in the epicenters (ErH) and RMS has been observed towards the higher values with increasing azimuth gap. However, the standard errors in focal depths have brought out almost a consistent trend with increasing azimuth gap. It is also observed that the number of events with focal depths less than 5 km increased with the increase in the azimuth gap values.

The seismicity picture emerged on the basis of locatable events along with the prominent tectonic features mapped in the study region is presented in Figure 4.1(a).

## 4.4 Characteristics of Local Seismicity

### 4.4.1 Distribution Patter of Epicenters

Based on the distribution of relocated events, it can be seen that seismic activity occurs in the Ganga fore-deep (south of the MFT), in the Sub Himalaya (between the MFT and the MBT), in the Lesser Himalaya (between the MBT and the MCT), and in the Higher Himalaya (north of the MCT). However, the majority of the locatable events defined northwest-southeast trending seismicity zone, which almost follows the surface trace of the MCT. This seismicity zone seems to corroborate with the basement thrust zone postulated by Seeber et al. (1981) and is primarily confined to the Inner Lesser Himalaya between the Srinagar Thrust and the MCT. It is conspicuous to observe that the strike direction of the MCT (about 30 km north of Chakrata) changes almost $90^0$ from north-west to south-west; and a sizable number of events located in this area occur to the north of the MCT. Towards the southeast, over a distance of about 40 to 50 km, seismic activity occurred south of the MCT. Southeast of Uttarkashi, the strike of the MCT changes again, and seismic activity occurred north of the MCT. West of Chamoli, the MCT is striking east-west and the seismic activity observed straddles the trace of the MCT. The strike direction of MCT near Chamoli takes a northwest-southeast trend, and seismic activity is primarily scattered over a wide area between Srinagar Thrust and the MCT. East of Badrinath in the Higher Himalaya, an approximately 50 km long north-south trending narrow zone of seismicity is delineated.

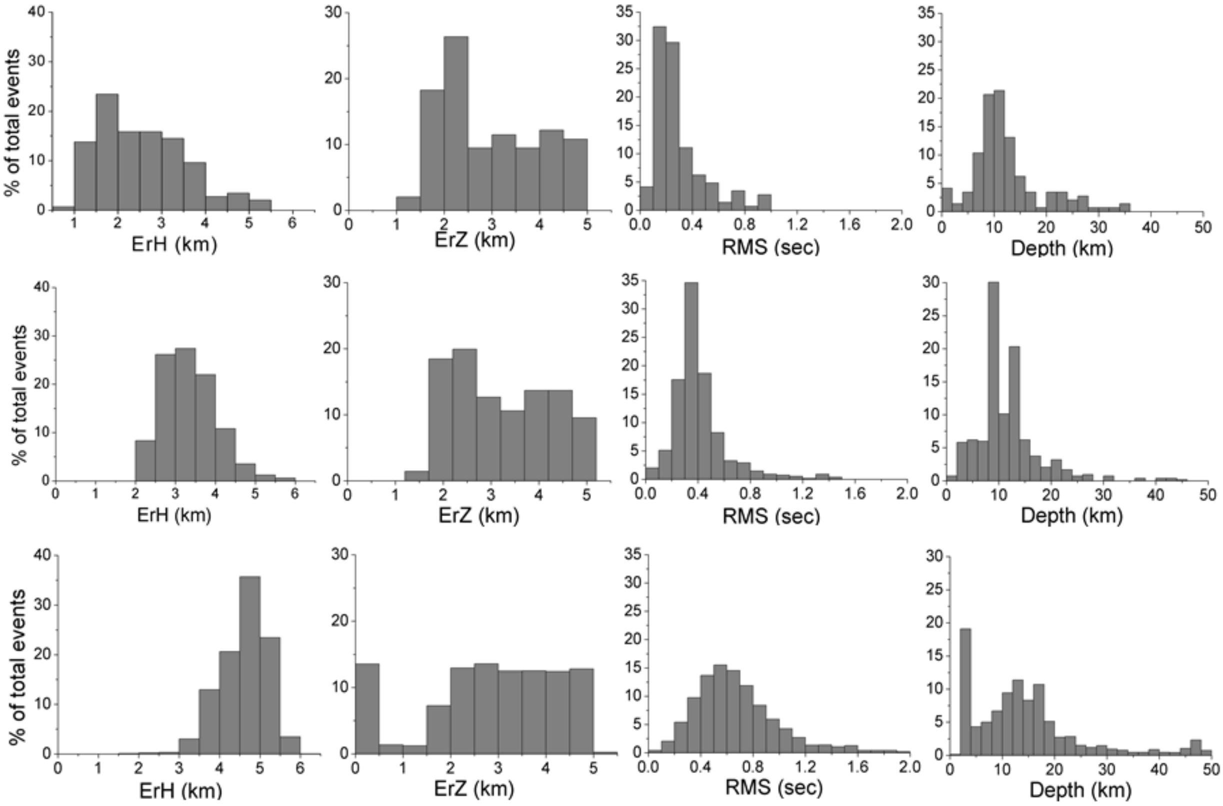

**Figure 4.2:** Error statistics for hypocenter location (km), depth (km) and travel time residuals(s) and their depth distributions according to Azimuthal Gap distribution of events (a) Gap < $180^0$ (b) $180^0$< Gap < $270^0$ (c) $270^0$< Gap < $360^0$

Part of the activity primarily running parallel to the Ganga River near to the south of Rishikesh seems to be associated with Ganga-tear-fault. Some of the events, particularly those located to the south-west to the Haridwar occur in the Ganga fore-deep. Some of the activity occurring in the vicinity of Dehradun seems to be either related to the transverse features running across the MBT or due to the Main Foothill thrust (MFT). As we proceed towards the north of the MBT, the level of local seismicity increases in the Lesser Himalaya and scatters over a wider area as compare to the activity observed in the Sub Himalaya. However, the activity observed in the Lesser Himalaya (the part of the Himalaya between the MBT and the MCT) can further be categorized into two parts: the activity occurring between the Srinagar thrust and the MBT, which is called Outer Lesser Himalaya, and between the Srinagar Thrust and the MCT, which is called the Inner Lesser Himalaya. It is observed that activity in the Outer Lesser Himalaya is less than the Inner Lesser Himalaya. It is evident from this description that most of the activity almost 70% occurs in the vicinity and south of the MCT. The distribution of local seismicity appears to spread as we proceed from southwest to northeast and acquires a ‘T’ type structure. It is quite likely that the observed pattern of local seismicity is due to the stresses generated by the Delhi Haridwar

Ridge buried below the alluvium and its continuation is postulated in the Sub Himalaya and Lesser Himalaya (Khattri et al., 1989). The axis of the postulated ridge almost lies in the center of this delineated zone of seismicity.

Based on the concentration of events, three prominent clusters of seismic activity can be identified. These clusters are marked as elliptical areas (1), (2), and (3) in Figure 4.1. Cluster (1) is in the vicinity and northwest of Uttarkashi, while cluster (2) is located west of Chamoli, cluster (3) on the other hand comparatively small in size and is located south of Chamoli. Cluster (1) is elongated and larger than other two clusters, and most of the events belonging to this cluster have occurred in the south, in close proximity of the MCT. Events associated with this cluster occurred at shallow depths (< 20 km), and a number of them have focal depths less than 5 km, or between 10 and 20 km. Events associated with the second cluster, falling west of Chamoli, have almost similar depths up to 20 km. However, few events have occurred at depths between 20 and 30 km, and below 30 km. Cluster (3) is located almost between the MCT and the MBT. Events belonging to this cluster have occurred at shallow depths and seem to represent the tectonic activity of the Srinagar Thrust. In the same area a seismicity cluster has been delineated in a recent study reported by Mahesh et al. (2013). We conducted detailed and critical analysis of local events (total 146 events) recorded during the period 2008 – 2011. This time period has 6 months of overlap with the recording period taken by Mahesh et al. (2013). We found that several local events recorded from this area are blasts-data and therefore do not represent the local seismicity associated with the cluster delineated by Mahesh et al. (2013). It is also observed that these events occurred daily in the same time slot for the entire duration of recording. These blasts were carried out for the excavation work at the Srinagar dam project site. Remaining 11 events, (after excluding 134 blasts) are plotted in Figure 4.3 and it is seen that cluster (3) now has almost disappeared.

### 4.4.2 Depth Distribution of Local Seismicity

To study the depth distribution of seismicity vertical cross-sections are drawn along six traverses in the study area. These traverses are drawn along and across the regional strike direction of the geological structure. Hypocenters of events confined to a narrow zone approximately ±10 km wide on either side of these traverses are projected on a vertical plane passing through these traverses. Out of six, three traverses AA’, BB’ and CC’ are drawn to study the distribution of seismic activity primarily occurring in the Ganga fore-deep, sub Himalaya, Lesser Himalaya and the Higher Himalaya and passes through Seismicity cluster (1).

One traverse, DD’ is drawn to study the distribution of activity occurring in the Lesser Himalaya and the activity located to the west of Chamoli region which passes through the seismicity cluster (2) and (3). Two traverses GG’ and FF’ are drawn along the geological structure to study the depth distribution of seismic activity in the Lesser Himalaya and the zone of seismicity that is delineated almost parallel to the trace of the MCT. In addition a north-south trending traverse DD’ is drawn to study the distribution of seismicity located to the east of Badrinath.

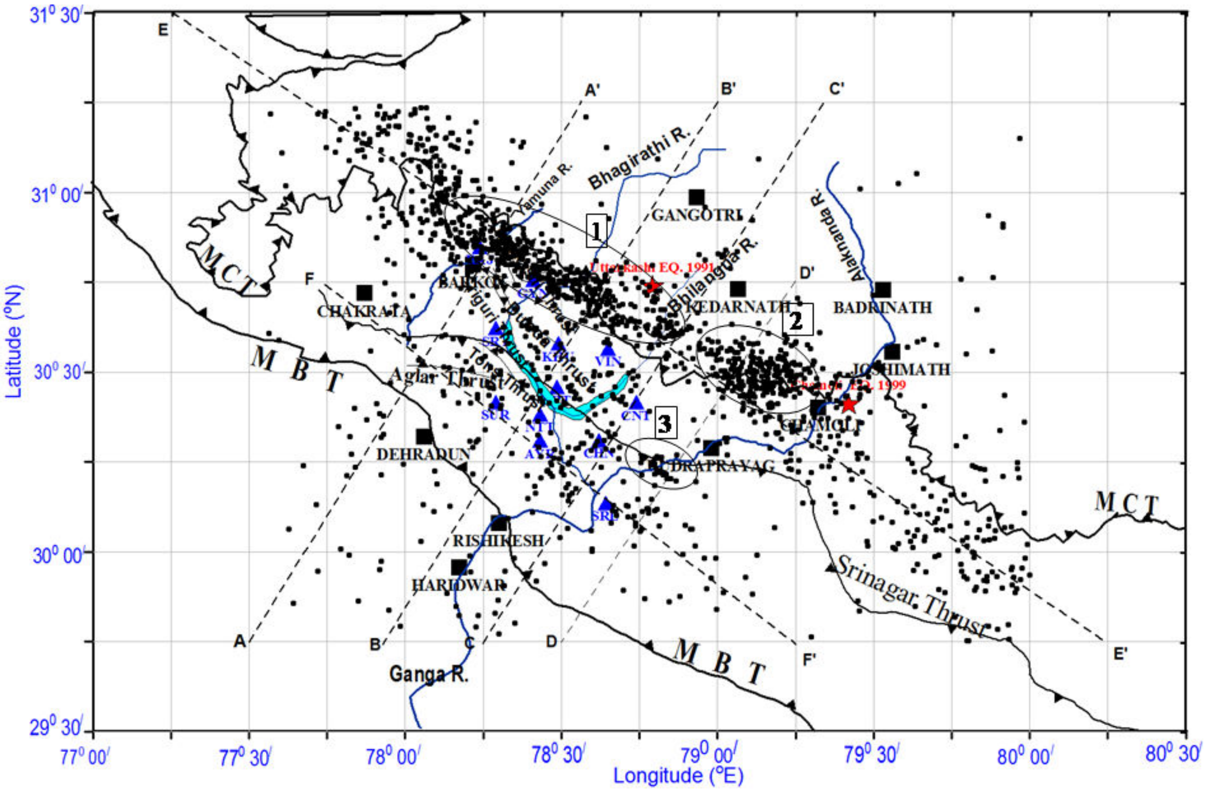

**Figure 4.3:** Distribution of epicenters of relocated events in the study area (excluding the blast events in cluster 3). Lines AA’, BB’, CC’, DD’, EE’ and FF’ show six cross-section along which depth sections are drawn to study in depth distribution of seismicity.

Section AA’, drawn from Ganga fore-deep to the Higher Himalaya, cuts across the MBT, the Srinagar Thrust (SNT), the MCT and local thrusts such as Algar Thrust (ALT), Sriguri Thrust (ST) and Uttarkashi Thrust (UT). This section primarily depicts the seismic activity that occurs in the south of the MBT (in the Vicinity of Dehradun) and seismicity that occurs in the Inner Lesser Himalaya in the vicinity of MCT (near the station RAJ) (Figure 4.4 (a)). The events located to the south of the MBT occur at a deeper level with focal depths between 20 and 40 km. It is interpreted that this seismic activity is associated with the brittle upper part of the Lithosphere of Indian plate. The majority of events in the vicinity of MCT occurs at shallow depths up to 20 km. Part of the seismic activity in the vicinity of MCT occurs at very shallow depths (less than 5 km) and seems to be attributed to the tectonic activity of the local tectonic features such as UT and ST. A dense cluster of seismicity is observed at a depth around 10 km. Because this cluster of seismic activity occurs to the south of the north dipping MCT, it does not relate to the seismic activity of MCT and we attribute this activity to the contemporary seismic activity of basement thrust (BT) zone which was postulated by Seeber et al. (1981) in the vicinity of MCT. This BT zone is formed where the steeply dipping MCT merges with the upper part of the gently dipping India plate. Further, at a depth of about 12 km, a distinct change in the pattern of seismicity is observed as the hypocenters scatters over a wider area. This could be the discontinuity representing the upper part of the under-thrusting India Plate. This depth by and large agrees with that postulated by Seeber et al. (1981) from the study of micro earthquake activity in the region around Tarbela Dam in the Lesser Himalaya of the Northern Pakistan. One of the characteristic features of the seismicity distribution is on an average the focal depths of events decrease from Sub Himalaya to Lesser Himalaya.

The section BB', drawn almost parallel to the section AA', shows almost similar distribution of local seismicity as observed along section AA'. This section passes in the close proximity of Tehri Dam. Along this section, seismicity located very close and to the south of the MBT occurs at a deeper level as compared to the events located away from MBT in the Ganga fore-deep (at a distance about 30 km). In the Lesser Himalaya the activity scatters over a wider area and some of the events are concentrated at depths between 10 and 12 km. From the trend of the located events at shallow depths in the Lesser Himalaya, it seems that this seismic activity is associated with the tectonic activity of the MBT. In the vicinity and to the south of MCT, seismic activity clusters at depths from about 12 to 15 km. However, at depths between 10 and 12 km no seismic activity is observed. This is in contrast to the nature of seismicity observed along section AA'. The possible reasons for this observation could be variation in states of stress on a local scale because the trace of MCT takes a bend and changes its strike direction. To the north of MCT seismic activity primarily confined to the focal depths between 10 and 20 km.

Along section CC' the seismic activity located very close to MBT occurs at shallow depths between 10 and 12 km and represents the seismicity of Ganga tear fault which runs almost parallel to Ganga River. This activity has also been observed by Mahesh et al., (2013).

Further, in the immediate vicinity and to the north of MBT the events occur at a deeper level. In the Lesser Himalaya, the seismic activity is primarily occurring between 5 and 16 km. A few events occur at a depth less than 5 km. A small cluster of seismicity is delineated at a depth of about 25 km namely 1 in figure 4.4 (c). This cluster is located in the vicinity of CNT station and no tectonic feature is mapped in this area. In the vicinity and to the south of MCT, the seismicity observed in the earlier two sections has almost disappeared in the present section. To the north of the MCT the seismic activity primarily concentrated between 7 km and 22 km few events occur at shallow depth from 2 to 5 km and can be attributed to the seismic activity of the north dipping MCT. If that is so, then the MCT dip seems to be about $60^0$ in this section. It appears from the distribution of seismic activity along these three sections viz., AA', BB' and CC', that events, to the north of MCT, occur at greater depths as compared to the south of the MCT. In the Higher Himalaya a few events occur at shallow depths around 10-12 km, and a seismicity zone is delineated at depths between 50 and 60 km (marked as 2 in Figure 4.4 (c)) which needs further detailed study.

The depth distribution of seismic activity along section DD' is portrayed in Figure 4.4 (d). The section passes through the cluster (2) and (3) (Fig. 4.3). The depth distribution pattern of seismic activity observed to the south of MBT, and in the Lesser Himalaya (between MBT and SNT), by and large remained same as observed along the section CC'. However, some of the events located at very shallow depths (less than 8 km) in the vicinity of SNT seem to indicate that the segment of the SNT in this area is seismically active, because SNT dips towards south-west based on geological evidence (Kumar & Agarwal, 1975; Valdiya, 1980). It seems that the SNT is only active locally, because at shallow depths in the vicinity of SNT the seismic activity is nearly absent on sections AA', BB' and CC'. The region to the north of SNT (about 20 km wide) is devoid of seismic activity. The activity mapped on both sides of the MCT occurs either at very shallow depths less than 5 km or at depths between 10 and 18 km. Very few events are located at a depth between 5 and 10 km. A notable feature of activity is that the hypocenters of events are almost aligned horizontally at a depth of about 10 km. This depth seems to define possible boundary that represents the detachment surface (e.g., Seeber et al., 1981) now called the MHT. Baring a few events, the activity almost ceases below 30 km depth. Based on these observations, it is interpreted that the thickness of the brittle upper part of the under-thrusting Indian crust is about 20 km between 10 and 30 km depths.

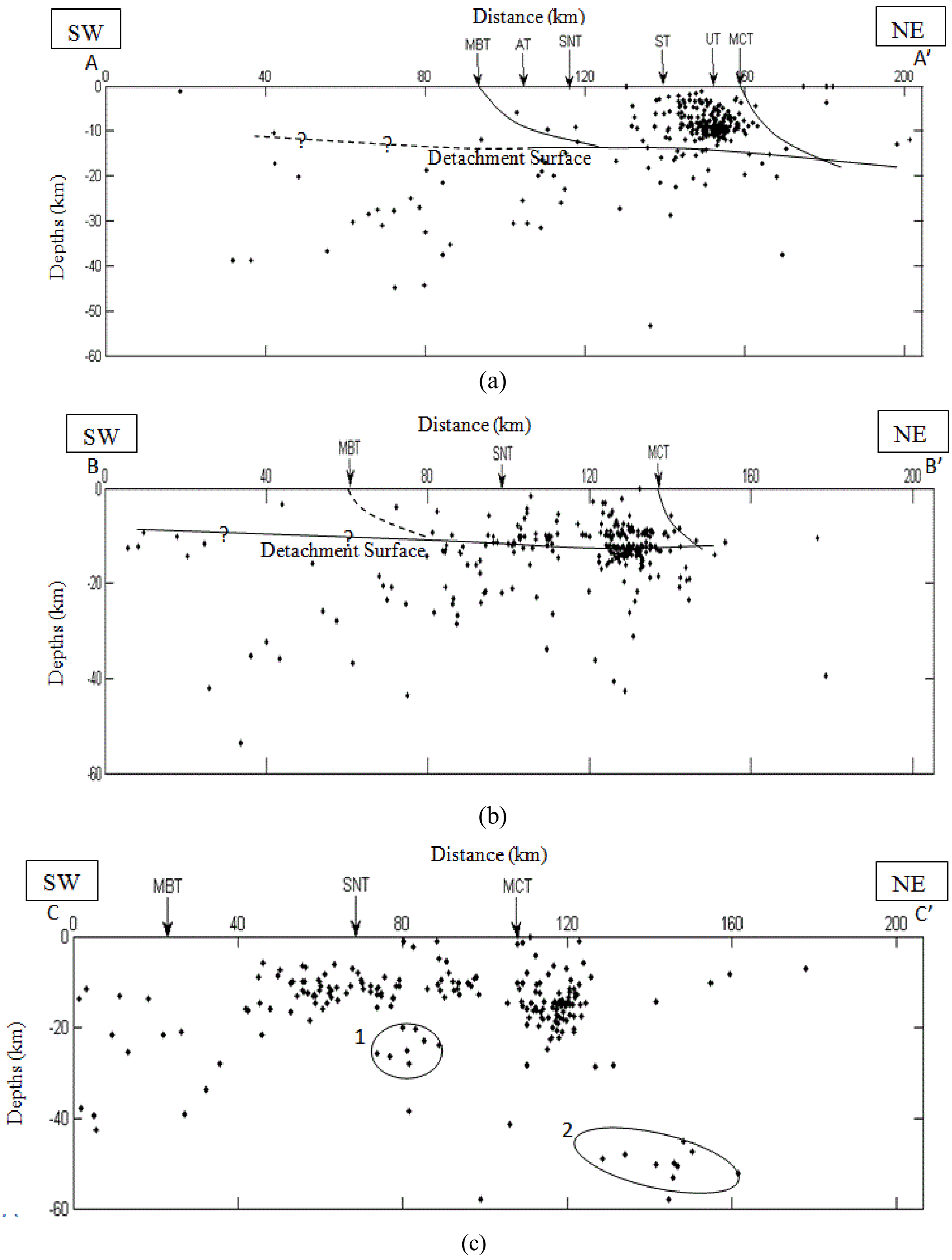
SW
NE
Distance (km)
A
A′
MBT
AT
SNT
ST
UT
MCT
0
40
80
120
160
200
Depths (km)
-10
-20
-30
-40
-50
-60
?
?
Detachment Surface
(a)
SW
NE
Distance (km)
B
B′
MBT
SNT
MCT
?
?
Detachment Surface
(b)
SW
NE
Distance (km)
C
C′
MBT
SNT
MCT
1
2
(c)

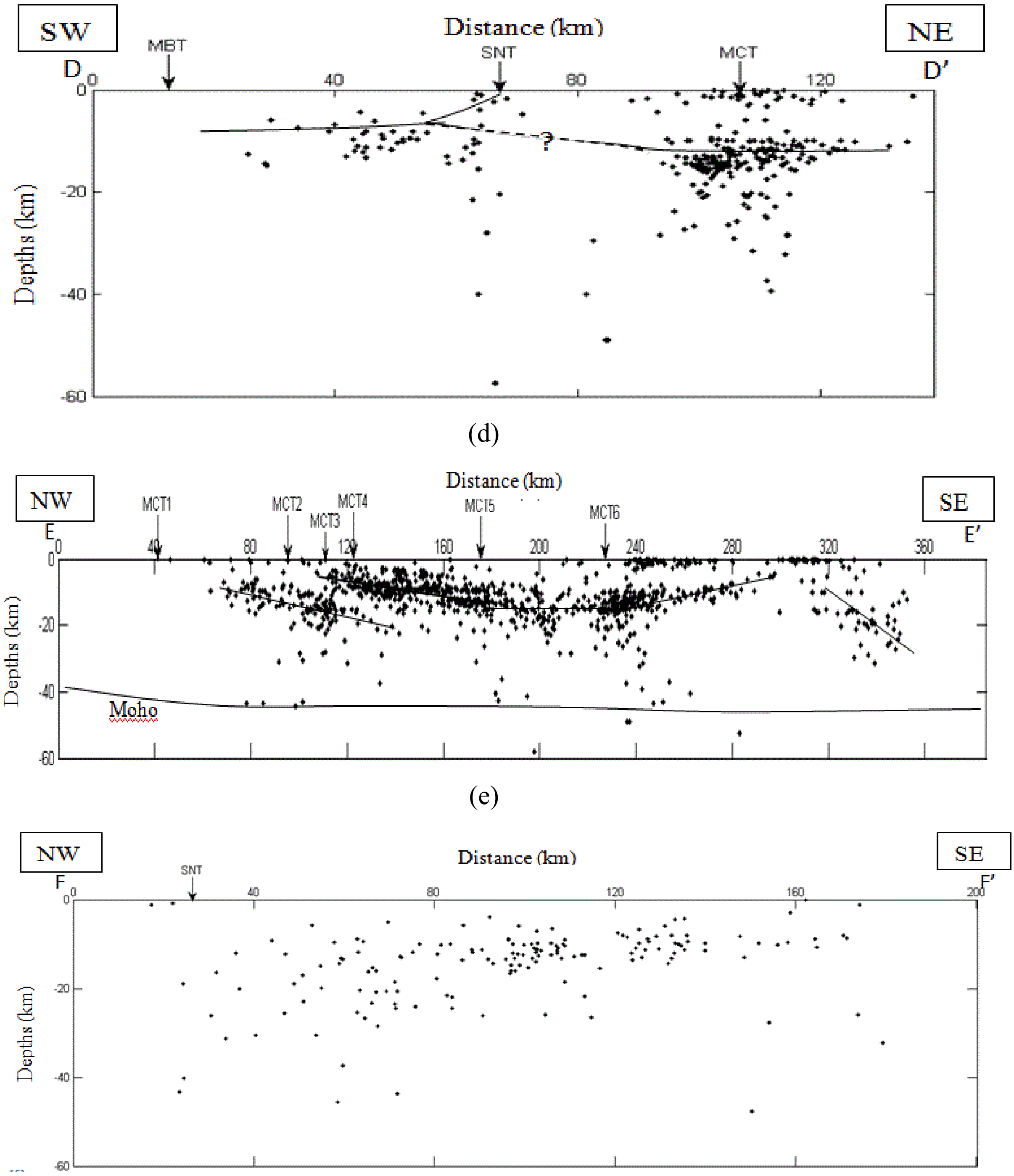

(d)

(e)

(f)

**Figure 4.4:** Depth Sections (a) Along line AA'(b) Along line BB' (c)Along line CC' (d)Along line DD' (e)Along line EE' (f)Along line FF'

Two depth sections EE' and FF' are drawn to study the depth distribution of seismic activity along the strike direction of the geological structure. Traverse FF' is drawn along a corridor running almost parallel to the MCT and second traverse runs in the Lesser Himalaya almost between the MBT and the SNT.

Section EE' describes the depth distribution of seismicity along a 370 km long northwest-southeast trending segment of MCT that extends about 100 km northwest of Uttarkashi to about 100 km southeast of Chamoli. Along this section the surface trace of the MCT is not straight but has an undulating structure. In view of this the traverse cuts the trace of the MCT at several locations which are marked as MCT1 to MCT6 on the section (Figure 4.4 (e)). Broadly speaking on the regional scale the MCT is a major tectonic boundary thrust which is dipping towards north east. However, it is clear from the section that on the local scale the dip of MCT is changing along its strike direction. Particularly, to the northwest of the section, the strike of the MCT changes from northwest to southeast, and to the west of Chakrata the strike of the MCT takes $180^0$ turn and almost strikes northeast southwest. Because of this distorted character the traverse cuts the MCT at four locations (MCT1 to MCT4). The trace of MCT is almost straight from the north of RAJ station to the northwest of the VIN station. Further to the southeast, the MCT takes a swing and changes its strike direction. About 30 km northeast of CNT station to Chamoli the MCT strikes east-west. To the east of Chamoli the MCT strikes almost northwest southeast. The seismic activity located towards northwest of MCT4 by and large occurred to the north of MCT. The depth distribution of this activity as reflected in the depth section indicates that seismicity zone dips towards southeast with depths of events between 10 and 20 km. The activity to the north of the MCT occurs at the deeper level as compared to the southeast. Further to the south of MCT3, between MCT4 and MCT5, the depth distribution reflects the activity that primarily occurred in the Inner Lesser Himalaya. This seismic activity exhibits a distinct change in the pattern and most of the events occurred at shallower depths defining a gently dipping seismicity zone with a dip of about $10^0$. The strike of the MCT changes between MCT5 and MCT6, and from the depth distribution it is evidenced that the zone defining the seismic activity dips towards northwest. Thus, there is a reversal in the direction of dip between MCT5 and MCT6. As the depth distribution of local seismic activity is interpreted to represent the structure of the upper part of the Lithosphere/detachment surface in the vicinity of MCT, the depth distribution has clearly brought out that the shape of the brittle part of the Lithosphere is gently undulating and does not have a gentle dip as given in the depth sections reported in the earlier studies (e.g., Figure 4 in Khattri et al, 1989). We can postulate two fracture zones: one between MCT5 and MCT6 where the dip direction along the strike of the MCT changes, and second between MCT3 and MCT4. Towards the east of Chamoli the traverse mainly passes through the Inner Lesser Himalaya and depth distribution reflect the activity occurring to the south of the MCT. The activity occurs up to depths of 30 km and scatters over a wider area.

Along section FF' the depth distribution of seismic activity is depicted in the Lesser Himalaya. It is observed that from northwest to southeast the scatter of activity as well as focal depths of events reduced. For example, between 20 to 60 km distances, the events occur at depths between 10 and 30 km and for distances from 60 to 120 km most of the seismic activity occurs between 10 and 20 km. The activity observed towards the southeast of the section occurs at depths around 10 km. Two aspects of the observed distribution of activity are worth mentioning: 1) the scatter in the activity reduces from northwest to southeast, 2) the activity almost terminated at shallow depths in the southeast. The pattern of depth distribution seems to reflect the structure of the brittle part of the under-thrusting lithosphere below the Lesser Himalaya. It seems that either the lithosphere is becoming thinner or is more ductile in nature towards the southeast.

## 4.5 Proposed Seismotectonic Model Based on Local Seismicity

A seismotectonic model is proposed for the region based on the distribution of hypocenters of relocated local events (Figure 4.5). For this purpose hypocenters of all events located within 40 km on either side of traverse BB' are projected onto a vertical plane passes through this traverse. It is seen that most of the local seismicity clusters in the vicinity of the MCT and define two prominent zones of hypocenters located to the southwest (upper flat zone) and to the northeast (lower flat zone) of the MCT. A striking feature of these zones is that the southwest zone terminates below the MCT whereas the zone located to the northeast of the MCT continues towards southwest. These zones have a vertical separation of about 5 km. Other studies have postulated a ramp like structure of the Main Himalayan Thrust (master detachment surface) in the vicinity of MCT (e.g., Pandey et al. 1995, Caldwell et al. 2013). A ramp like structure at mid crustal depths, inferred from geological and geophysical evidence, was further corroborated from the distribution of intense microearthquake activity and frequent small earthquake activity (Pandey et al. 1995). This ramp connects almost flat decollement below the Sub Himalaya and the Lesser Himalaya with the deeper decollement below the Higher Himalaya. In a recently reported study, based on the CCP image technique, a ramp like structure is postulated in the Garhwal Himalaya. The upper flat is located at a depth of about 10 km below the sea level and dip about $2^0$, this upper flat connects the mid crustal ramp which is about 10 km high and dips about $16^0$. The lower flat is at a depth of about 20-25 km below the sea level and dips at $4^0$(Caldwell et al. 2013). In the model proposed in the present study the flat-ramp-flat type structure of the decollement in the vicinity of MCT is delineated. The gently dipping upper seismicity zone at a depth of 10-12 km, representing upper flat, appears to terminate in the vicinity of MCT, whereas the southwest end of the lower seismicity zone at a depth of about 15 km, representing lower flat, continues in the Inner Lesser Himalaya. The transition zone between the upper flat and lower flat is marked by the observable seismic activity. This activity occurs in the region where these two flats overlap (with a vertical separation of about 5 km) and this region can be interpreted as a ramp. Further, toward northeast end, the lower flat seems to have a fork like structure as brought out from the distribution of hypocenters. It is postulated that the under thrusting front of the Indian crust (upper part of the India plate) fractured and resulted in the formation of two almost parallel decollements (two flats) separated by a vertical distance about 5 km connected by a ramp. Further to the north, MCT seems to be steeply dipping and flattens at depth and merges with the Main Himalayan Thrust at a depth of about 15 km. It is further observed that the distribution of seismicity in the Lesser Himalaya conforms to the broad geological structural trend and is marked by regions of salients (outburst) and recesses (depression) to the southwest of the MCT and below the SNT respectively. Salients are supposed to be associated with the crystalline rocks in the vicinity of MCT, and recess seems to be associated with the sedimentary wedge of the India plate. The MBT seems to be less active and dips towards northeast and merges with the Main Himalayan Thrust viz., detachment surface at a depth of about 10 to 12 km.

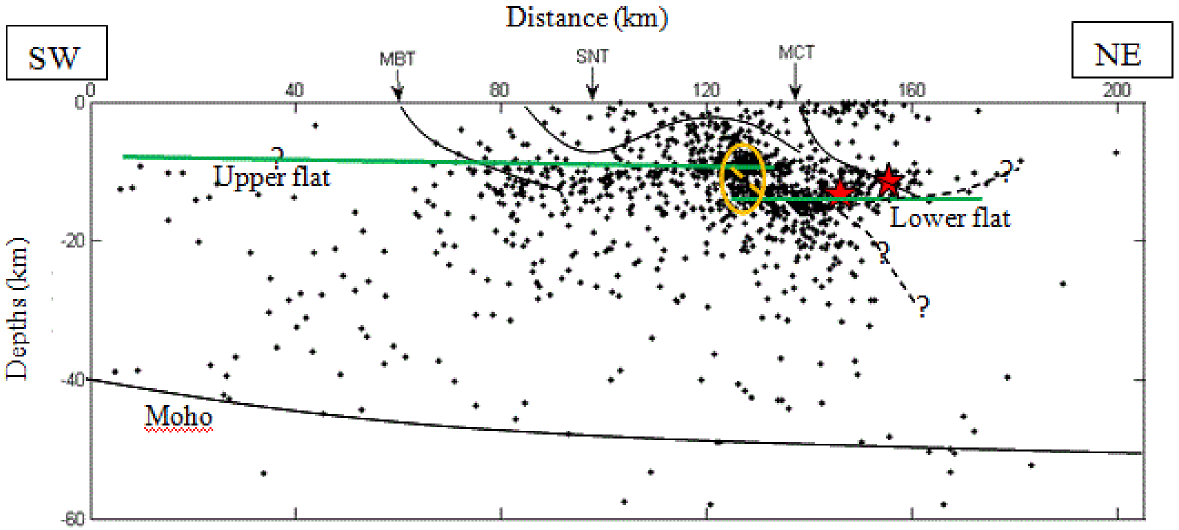

**Figure 4.5** Proposed seismotectonic model of the region based on the distribution of hypocenters of relocated events

Based on the locations and depth distribution of 252 local earthquakes Khattri et al. (1987) explained the possible geometry of the basement thrust representing the upper surface of the India Plate in the vicinity of MCT and below the Sub Himalaya and Lesser Himalaya. In our model the proposed depth of the upper surface of the India Plate in Ganga fore-deep (south of the MBT) is about 10-12 km which is in agreement with the model proposed by Khattri et al. (1987). However, our model provides a detailed geometry of the basement thrust, i.e., Main Himalayan Thrust, below more than 300 km long segment of the MCT. According to Khattri et al. (1987), the postulated basement thrust, representing the upper surface of the India plate in the vicinity of the MCT, dips gently towards northwest, but the reverse is true in our model. The major difference in the two models is regarding the observed focal depths of local earthquakes. Focal depths of most of the local earthquakes observed by Khattri et al. (1987) are above 10 km and very less activity is observed at depths between 10 and 20 and, seismic activity ceases below 20 km. In our model major seismic activity occurs up to a depth of 20 km and a number of events have depths between 20 and 40 km and seismic activity almost terminated in the close vicinity of the MCT. Based on the locations of events at a deeper level, the likely depth of Mohovichic discontinuity is about 40-50 km from Sub Himalaya to Higher Himalaya. This depth conforms to that estimated from the optimum 1D velocity model and from other reported studies in the region. Based on the distribution of seismicity it seems that the MBT and the MCT are listric in nature, fattens at depths, and merges with basement thrust representing the upper surface of the Indian plate. The variation pattern of local seismicity between the MBT and MCT conforms to the local geological structure. The driving front of the India plate seems to bifurcate somewhere in the closed proximity of the MCT because to the north and in the vicinity of MCT, the activity occurs at a depth of about 15 km and then the region is devoid of activity. In the proposed model, the propagating front of the under-thrusting India plate (the brittle part of the Indian crust) is clearly demarcated at a depth of about 18-20 km where the seismicity zone representing the upper part of lower flat bifurcates into two zones indicating further slicing of the upper part of the lower flat (Figure 4.5 marked by dashed lines). The zone at shallow depth pinches out towards the northwest, whereas, hypocenters associated with deeper zone defines an inclined zone of seismicity. Based on the depth distribution of events associated with this zone, the postulated thickness of the brittle part of the under thrusting Indian crust is about 20 km in the vicinity of MCT. The Hypocenters of recently occurred Uttarkashi earthquake and Chamoli earthquake are plotted and it appears that they nucleated at the lower flat.

## 4.6 Concluding Remarks

Distribution of more than 1400 events, relocated using Optimum 1-D velocity model, brought out that about 70% of the seismic activity occurred in the Inner Lesser Himalaya between the MCT and the Srinagar thrust. The majority of locatable events defined more than 300 km long northwest-southeast trending seismicity zone that follows the trace of the MCT. The level of seismic activity increased from the Sub Himalaya to the Higher Himalaya. About 5% of the seismic activity occurred to the south of the MBT in the Sub Himalaya and Ganga fore-deep. Part of this activity seems to be associated with the tectonic activity of Ganga-tear-fault. In the Lesser Himalaya activity scatters over a wide area. Two prominent clusters of seismicity are identified: to the northwest of the MCT, and to the west of Chamoli. It is found that in the Lesser Himalaya the activity occurred at shallow depths compared to the Sub Himalaya. The depth distribution of seismicity along the strike direction of MCT brought out two shallow dipping fractured zones which seem to represent seismically active thrust zones dipping in opposite directions. The postulated depth of the basement thrust in the vicinity of MCT is about 10-12 km.

Two prominent zones of seismicity are delineated at depths of about 10 km and 15 km to the southwest and northeast of the MCT with a vertical separation of about 5 km. The southwest zone terminates below the MCT whereas northeast zone continues about 10 km in the Inner Lesser Himalaya. This delineated structure almost conforms to the flat-ramp-flat type structure of the Main Himalayan thrust (MHT) in the vicinity of the MCT. The seismicity zone representing the lower flat bifurcates into two zones indicating the further slicing of the upper part of the lower flat. In the vicinity of MCT, the postulated thickness of the brittle part of the underthrusting Indian crust is about 20 km.

## Chapter - 5

# Three-Dimensional Velocity Structure around the Tehri Region of the Garhwal Himalaya

## 5.1 Introduction

The motivation for the tomographic studies around the Tehri region of the Garhwal Himalaya has been mainly to understand the lateral variation of crustal structure and in tectonic processes operating in the region. Because the Earth structure is inherently three-dimensional, there are many applications of 3-D velocity models obtained using seismic tomography. To allow understanding of the seismotectonics and mechanism of large earthquakes, we require crustal and upper mantle velocity structure of seismically active regions at local and regional scale. In this context, the knowledge of the 3-D velocity structure can play an important role. The knowledge of 3-D P and S-wave velocity structure of the Garhwal Himalaya is required to carry studies related to understanding of seismotectonics of the study region. These studies include estimation of hypocenter parameters, focal mechanisms solutions, source moment tensors studies, inversion for velocity, attenuation or anisotropy, analysis of controlled-source data, and any other study that depends on the geometry of ray paths of seismic wave within or near the fault zones. The accuracy of all such studies critically depends on a realistic 3-D velocity model for this region. Further, 3-D velocity structure will allow studying the variations in physical properties within and along the fault zones to a scale of a few kilometers and shall provide valuable information on the segmentation of the fault zones, the nature and distribution of fault zone materials, and the locations and extent of possible asperities or nucleation zones. In view of these considerations P- and S-wave tomographic images of the upper crust in the study area has been mapped. The results obtained cast new light on the complex seismic structure of the region.

## 5.2 Data set

The dataset used in the study became available from a 12-station telemetered network deployed in the Tehri region of the Garhwal Lesser Himalaya. The network with inter-station spacing between 10 and 20 km covers an area of about 100 km x 80 km around Tehri dam (Fig. 5.1).

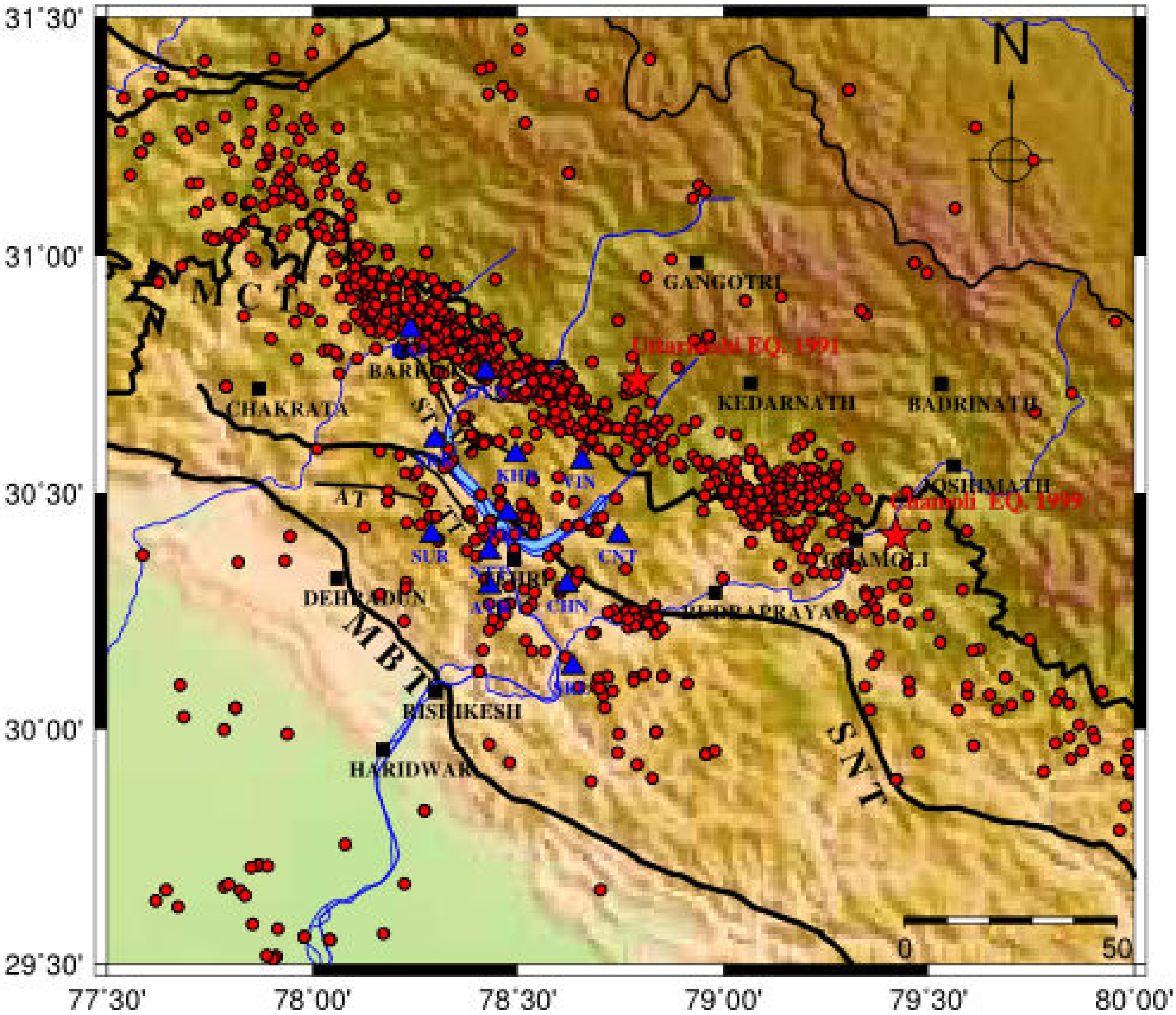

**Figure 5.1:** Spatial distribution of Initial seismic events (red circles) in the study area that are used in Tomographic study. Blue triangles show the locations of network stations, blue filled part within the network shows the reservior of Tehri Dam; small rectangles shows locations of major city /towns; and tiny blue lines show various rivers. The tectonic features in the study area include MCT: Main Central thrust, MBT: Main Boundary thrust, SNT: Srinagar thrust, UT: Uttarakhand thrust, DT: Dunda thrust, ST: Siriguri thrust, TT: Tons thrust, and AT: Aglar thrust

Each remote station houses a triaxial short-period seismometer (Model CMG 40T-1 (natural period 1 s), manufactured by M/s Guralp System, UK) to sense the three components of ground motion. The digital data is collected at a rate of 100 sample/s, and the phase picking errors are estimated to be less than 0.05 s and 0.1 s for *P* and *S* waves, respectively. The SEISAN software (*Ottemoller et al.*, 2011) is used for earthquake analysis and preliminary event location.

From January 2008 to December 2012, a total of 2079 events ($M_L \leq 4$) was located in the study region. The selection criteria for the events considered in the 3-D inversion include: (i) the number of picks for each event to be more than 12 (P+S phase), and (ii) the maximum distance of an event to the nearest station to be less than 100 km. Thus, the events located outside the network are also included in the inversion. The reasoning to include such events in the inversion process is precisely advocated by the *Koulakov* (2009a). According to *Koulakov* (2009a) inclusion of events located outside the network for 3 D tomography helps obtaining better resolution in velocity estimation. The ray paths of such events provide important information on the velocity structure of deeper regions. In view of the uncertainties in the locations of events, *Koulakov* (2009a) conducted several synthetic velocity model tests to investigate the reliability and working efficacy of the inversion algorithm. The test results showed that the algorithm works perfectly well with initial uncertainties in locations and for well recorded events falling outside the network. *Mukhopadhyay and Sharma (2010)* showed the similar observations for the 1-D and 2-D velocity model parameters. Because of these scientific considerations, the events located outside the network are included in the study to enlarge the database of events. After applying the selection criteria, 1368 events are included in the iterative source locations and tomographic inversion (Fig. 5.1). A total of 25,030 phase readings (12,794 *P* phases and 12,236 *S* phases) are used in the inversion.

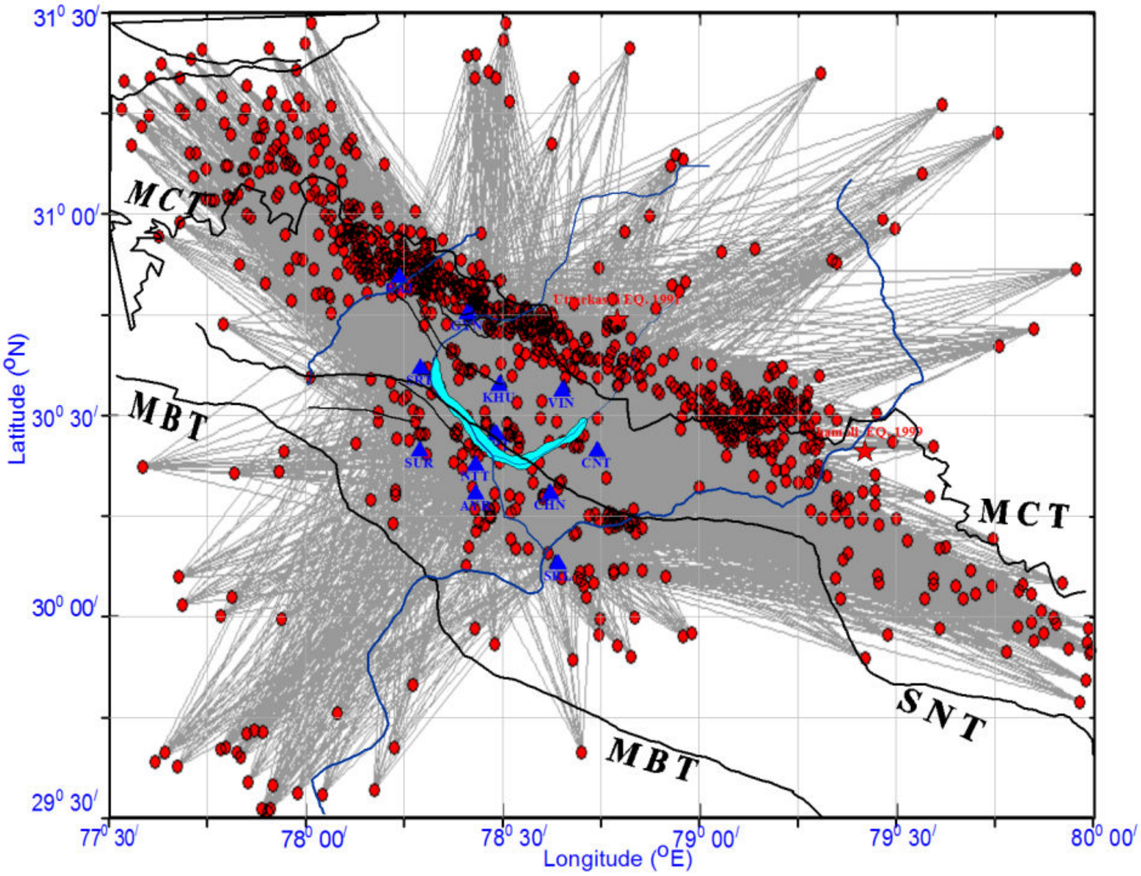

**Figure 5.2**: Spatial distribution of initial seismic events (red circles) in the study area that are used in tomographic study. Blue triangles show the locations of network stations. Gray lines are showing the ray-path coverage from epicenters to the network stations in the investigated region

Plots of ray coverage help identifying well resolved parts of the model. Ray coverage is determined by the geometry of the receivers and sources. Ray path coverage in lateral as well as vertical directions gives the idea of the area covered by the input sequences, and the results will be conformed for these regions only. Fig. 5.2 shows the ray path coverage in the lateral direction. In the vertical direction the ray path coverage is up to 20 km depth because the maximum seismic activity occurs at shallow depths. Parameterization nodes for the inversion depend on the ray density, therefore in the vertical direction the model could well resolve up to 20 km depth only.

## 5.3 Methodology

For the 3D tomography, local earthquake tomography software (LOTOS-12) an iterative tomographic algorithm has been adopted in this study (*Koulakov*, 2009a). One of the key features of the *LOTOS-12* code is a ray tracing algorithm based on the Fermat principle of travel time minimization called bending tracing (see *Koulakov*, 2009a). The processing starts with preliminary source locations with the use of reference table containing travel times in the 1-D model. For the parameterization of velocity distribution a grid of nodes is defined. These grids are automatically defined in the area, according to the density of ray paths from source to receiver pairs. The inversion is performed simultaneously for the 3-D P- and S-velocity distributions, source parameters and station corrections. The matrix is inverted using the LSQR method (e.g., *Paige and Saunders*, 1982; *Nolet*, 1987).

Input data for the code requires the coordinates of the stations and the arrival time data of earthquakes located at regional and local distances. The hypocenter coordinates and their origin times are not strictly required because the absolute locations are determined during the process of computations. However, the preliminary hypocenter locations are used to increase the speed of the calculations. In addition, a file containing the starting 1-D velocity model and a set of free parameters for performing different steps (e.g., source locations, parameterization grid construction, inversion) is necessary.

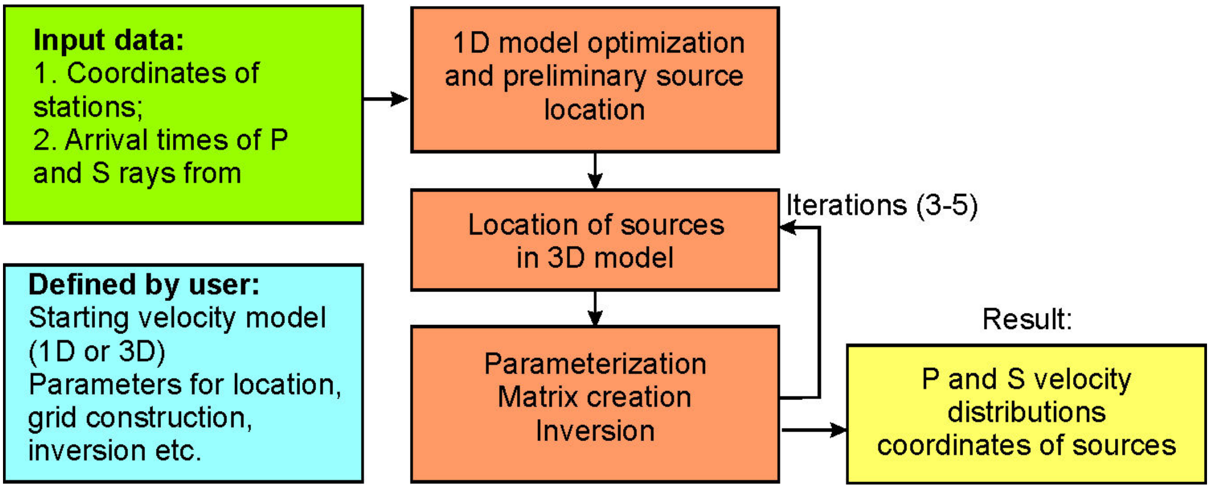

**Figure 5.3:** Working steps of the LOTOS code (Kaulakov 2009)

The tomographic inversion involves two stages: The first stage involves obtaining the procedure relates to iteratively procedure for preliminary source locations and the optimization of the 1-D velocity model iteratively. Each complete iteration consists of: calculation of the reference travel time table from the initial 1-D velocity model; relocations of sources using tabulated travel times with a grid search algorithm; computation of the first derivative matrix; and simultaneous inversion for 1-D P- and S-velocity parameters and source parameters.

The second stage involves nonlinear tomographic inversion, by using source locations and the 1-D velocity model obtained from the first stage, as starting parameters. This nonlinear inversion is an iterative process and have following four steps:

Step 1— Ray tracing and source location in the 3-D velocity model: Ray tracing is performed using bending method [*Koulakov, 2009a*] based on the Fermat principle. Earthquake sources are then updated using gradient method.

Step 2— Grid construction: Nodes of the grids are installed according to the concentration of ray paths in the 1-D model at various depths. *Koulakov* (2009a) suggested that, the spacing of the grid should be choosen to be considerably smaller than the expected size of the anomalies in order to reduce the bias of the resulting models due to the grid configuration. Process of inversions on various grid parameterizations is then repeated using several grid configurations with different basic orientations (e.g., 0°, 22°, 45°, and 66°) to decrease the influence of the parameterization on the results. The individual results obtained from these grids are then combined into one model by simply averaging. Independence of tomographic results of grid configurations was shown in few previous studies based on the LOTOS code [*Koulakov et al.*, 2007, 2009b; *Koulakov*, 2009a].

Step3— Inversion: The simultaneous inversion is performed for P- and S-velocity anomalies and source parameters with respect to the 1D model (as reference model) derived in the previous iteration. To control the amplitude of velocity anomalies and smoothing of the solution, inverted velocity anomalies are damped by using two additional matrix blocks. The sparse matrix is inverted using the least-squares QR method [*Paige and Saunders*, 1982; *Sluis and Vorst*, 1987].

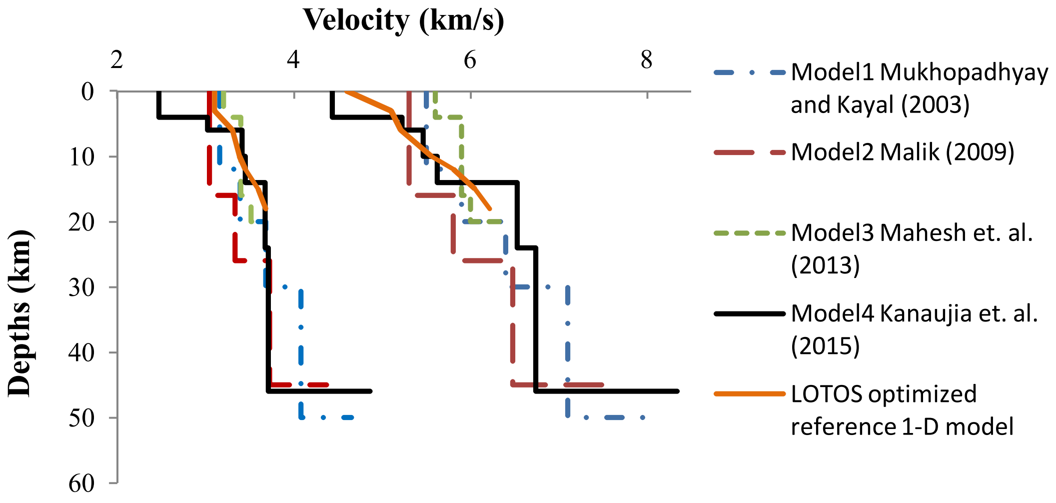

**Figure 5.4:** 1-D velocity models used as the trial velocity models for tomographic inversion and LOTOS optimized reference 1-D model: (left) S-wave models and (right) P-wave models

Step4— Averaging: The models derived using different grids are then averaged and combined to provide a 3D model of absolute P and S velocities. This model is then used for the next iteration, which consists of three steps —ray tracing, inversion and averaging.

The damping parameters are evaluated after the inversion of the synthetic datasets. The values of the damping parameters are optimized by maximizing the similarity between the initial model, both in terms of amplitude and the positions of the synthetic patterns.

## 5.4 Parameters and Estimation

The procedure of the first stage is performed iteratively and related to preliminary source locations and the optimization of the 1D velocity model, which. Every iteration consists of the following steps (see also Koulakov, 2009a):

1.) Calculation of the table of reference travel times for the 1D velocity model for all possible epicentral distances and source depths.
2.) Location of sources in the 1D velocity model using tabulated times to speed up the calculations. This step is based on a grid search method that makes the location very stable and allows the location of an earthquake independent of the search start point.
3.) Computing the first derivative matrix that represents time variations of each ray due to unit velocity changes at different depths.
4.) Simultaneous inversion for P- and S-velocity variations in the 1D model and source parameters.

The source locations and the 1D velocity model obtained after the preliminary stage are used as starting parameters for the second step of the nonlinear tomographic inversion. This part consists of the following steps which are performed in several iterations:

1.) Locating the sources using the 3D velocity model. The algorithm updates the coordinates of a source using a gradient method. The rays in a 3D velocity model are computed using the bending method.
2.) Parameterization. The LOTOS code allows for the parameterization of the velocity model either with nodes or with cells. In both cases, the nodes/cells are installed according to the distribution of rays in the 1D model.

The grid spacing of the nodes is kept considerably smaller than the expected size of the anomalies in order to reduce the bias of the resulting models due to the grid configuration. Moreover, in order to further decrease the influence of the parameterization on the results, the inversion is repeated using several grids configurations with different basic orientations (e.g., 0°, 22°, 45°, and 66°). The results obtained for these grids are combined into one model by simple averaging. Independence of tomographic results of grid configurations was shown in few previous studies based on the LOTOS code (e.g., Koulakov et al., 2007; Koulakov, 2009a; Koulakov et al., 2009b).

The inversion was performed simultaneously for P- and S-velocity anomalies with respect to the model derived in the previous iteration and for the source parameters. Alternatively, in this study the inversion was also carried out for $V_P$ and the $V_P/V_S$ ratio using the algorithm described by Koulakov et al. (2007). The inverted velocity anomalies are damped by using two additional matrix blocks that control amplitude and smoothing of the solution.

The sparse matrix is inverted using the least-squares QR method (Paige and Saunders, 1982; van der Sluis and van der Vorst, 1987). The models derived using different grids are then averaged and combined to provide a 3D model of absolute P- and S-velocities. This average model is used for the next iteration that consists of the steps 1, 3, and 4.

Following Koulakov et al. (2007), the damping parameters are evaluated after the inversion of the synthetic data sets. The values of free parameters are optimized by maximizing the similarity between the initial model, both in terms of amplitude and the positions of the synthetic patterns.

## 5.5 Observed Data Inversion

The data processing starts with preliminary source locations and optimization of the 1-D velocity model. To initiate inversion, a starting 1-D velocity model, estimated in chapter 3 using VELEST software, has been used. This model has been used as the reference 1-D model in 3-D tomographic inversion. Two velocity models have been proposed in the chapter 3: an increasing gradient velocity model and a model with the low velocity layer. An increasing gradient velocity model has been used here because introduction of the low velocity layer at the initial stage of tomographic inversion leads to ambiguous results (*Kissling,* 1988). As the results of a tomographic inversion critically depend upon careful selection of initial 1-D model, different starting velocity models are used in order to select one which gives optimum locations. Thus, we tested four initial velocity models including the one estimated by the VELEST algorithm (Fig. 5.4). Based on the analysis of the resulting velocity distributions and the RMS residuals, It is found that the 1-D velocity model (model 4) provides the least RMS residuals. This model, given in Table 5.1, was estimated using VELEST algorithm, and is adopted as a starting model for the 3-D tomographic inversion. Preliminary source locations used in this study are relocated precisely using VELEST with the minimum 1-D velocity model. The data of preliminary source-locations and starting velocity model are then selected for final optimization step of the LOTOS algorithm. The resultant model of the 1-D optimization step is the reference 1-D model, which is shown in figure 5.4 as LOTOS optimized reference 1-D model.

An inversion for $V_P$ and $V_S$ is carried out and the free parameters for inversion (smoothing and amplitude damping) were selected according to the synthetic test results. As stated earlier the grid spacing should be less than the minimum resolution limit. 3-D grids were formed with a vertical separation of 2 km (in Z direction) and nodes were separated horizontally by 2 km in the latitude and longitude directions. The uppermost level of the nodes is fixed at -3 km to include the elevation effect of the network stations. The first layer of the reference 1-D velocity model is also defined at -3 km. Each run of LOTOS involved five iterations as these were sufficient to converge to the minimum RMS value. Before concluding the final inversion process, hundreds of trial and error runs of LOTOS were performed with different initial velocity depth-layer-variations and varing the values of model parameters to study the effect of different parameters.

**Table 5.1:** Reference 1-D model for tomographic inversion obtained after the 1-D optimization step

| **Depth (km)** | **$V_P$ (km/s)** | **$V_S$ (km/s)** |
|---|---|---|
| 1 | 4.60 | 3.10 |
| 3 | 5.10 | 3.10 |
| 5 | 5.21 | 3.30 |
| 10 | 5.56 | 3.38 |
| 12 | 5.80 | 3.45 |
| 15 | 6.05 | 3.59 |
| 18 | 6.22 | 3.68 |

Table 5.2 shows the P- and S- RMS residuals and their reductions after five iterations of final LOTOS run according to the $V_P$ - $V_S$ scheme. In the $V_P$ - $V_S$ scheme, the P- and S- residuals are minimized separately. The residuals obtained after first iteration are similar to the location-residuals in the 1-D model. The RMS values corresponding to the following iterations show that the 3-D velocity inversion leads to an improved data fit. The residuals of the data set initially were 0.29 sec and 0.43 sec for P and S data, respectively. Fig. 5.5 shows resulting P and S-velocity anomalies with respect to the 1-D starting model in

horizontal slices at 1, 5, 10, 12, 15, and 18 km depths. Reference model velocities at their respective depths are also mentioned on the tomograms.

**Table 5.2:** Average P and S residuals and variance reductions of tomographic inversions of real data with various initial velocity models

| **Initial 1-D velocity model** | **Average residual (s)** | | | | **Toal variance reduction in final Iteration** | |
|---|---|---|---|---|---|---|
| | **Initial** | | **After 5th iteration** | | **Initial** | |
| | **P-wave** | **S-wave** | **P-wave** | **S-wave** | **P-wave** | **S-wave** |
| Mukhopadhyay and Kayal (2003) | 0.2954 | 0.5242 | 0.2451 | 0.3125 | 22.12 | 37.25 |
| Malik (2009) | 0.3124 | 0.5012 | 0.2325 | 0.3021 | 25.12 | 38.25 |
| Mahesh *et al.* (2013) | 0.2580 | 0.4506 | 0.1901 | 0.2865 | 26.31 | 36.41 |
| Kanaujia *et al.* (2015) | 0.2451 | 0.4539 | 0.1747 | 0.2419 | 29.14 | 46.65 |

## 5.6 Synthetic Modelling and Inversion

The results of 3-D inversion are checked for their resolution capacity. Resolution capacity depends on the precision in the locations of the events used in tomographic inversion. This is also an important condition for accurate velocity model estimation. The LOTOS algorithm allows defining various synthetic models, either in the form of periodic anomalies in the checkerboard test or by drawing polygons manually in the horizontal or vertical sections. To check the resolution capability of earthquake-receiver configuration checkerboard synthetic test is performed. The travel times for the synthetic tests are computed by 3-D ray tracing between sources and receivers corresponding to the source-receiver-configuration (Fig. 5.2). Gaussian noise is added to the synthetic data to simulate realistic picking error up to 0.05 sec for *P* waves, and 0.1 sec for *S* waves. This allowed to incorporate almost same picking error distribution in the synthetic data as in the original travel time-data. In addition, events are randomly shifted from their initial positions in the horizontal (from 0 to 5 km) and vertical (from 0 to 10 km) directions in order to simulate the effect of (relatively large) errors in source locations due to the unknown 3-D velocity structure.

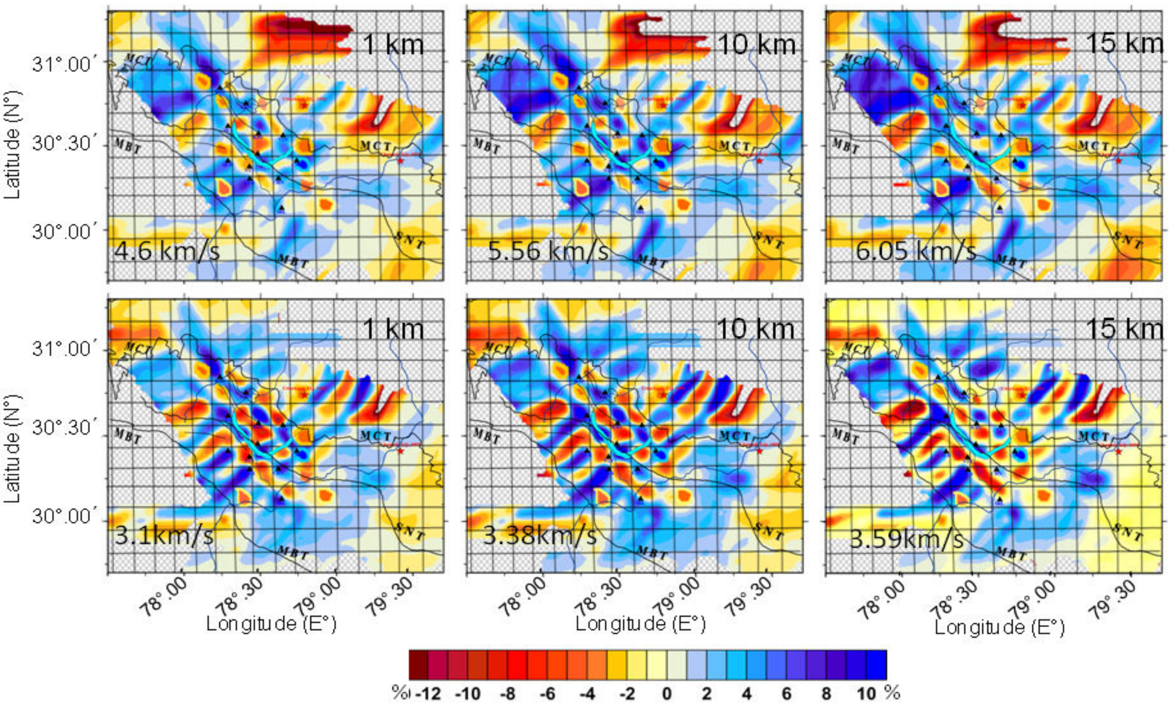

**Figure 5.5.** Checkerboard synthetic test results. Images in first and second row show test results of P- and S-wave at depths of 1 km, 10 km and 15 km, respectively. The lines plotted over the resulting anomalies are the contour lines of the synthetic checkerboard formed by considering the alternative box with varying velocity anomalies of amplitudes ±4%. Reference velocity at each depth is mentioned on the tomograms, Velocity anomalies are calculated with respect to this reference velocity. The color scale indicates the velocity anomaly as a percentage

### 5.6.1 Checkerboard Test results

As stated above the checkerboard test is performed to evaluate the horizontal resolution of features in different parts of the study area. Fig. 5.5 presents the results of a synthetic model defined by periodic anomalies in 20 x 20 km in lateral direction. The anomalies remained unchanged at all depths, and their amplitudes vary by ±4% with respect to the starting model (model 4 given in Table 5.1). The same source-receiver pairs are used as for the real data analysis. The computed synthetic travel times were perturbed with random noise having average deviation of 0.05 s and 0.1 s for P- and S- waves, respectively. This enabled the same variance reduction as for the real data inversion described earlier. After computing synthetic travel times using the 3-D ray tracer, program forgot all information on the velocity distributions and source locations. Then the full data processing was performed, including the steps of source locations. Fig. 5.5 shows the results of *P* and *S* model construction after five iterations. From the test results it is found that only large-scale features in the velocity model could be resolved. The best resolution is achieved in the middle part of the study area where the network stations are located. In other parts, there is a significant horizontal spreading along the predominant ray-paths. Furthermore, the model is well resolved in depth range between 5 and 18 km. The amplitudes of the anomalies are slightly overestimated in the well-resolved area and underestimated otherwise. For the S model, this effect is more pronounced. Relocated earthquake positions are found to agree well with the initial positions, with average location error of 1.45 km. The lateral resolution of the model anomalies seems to be robust up to a depth of 18 km.

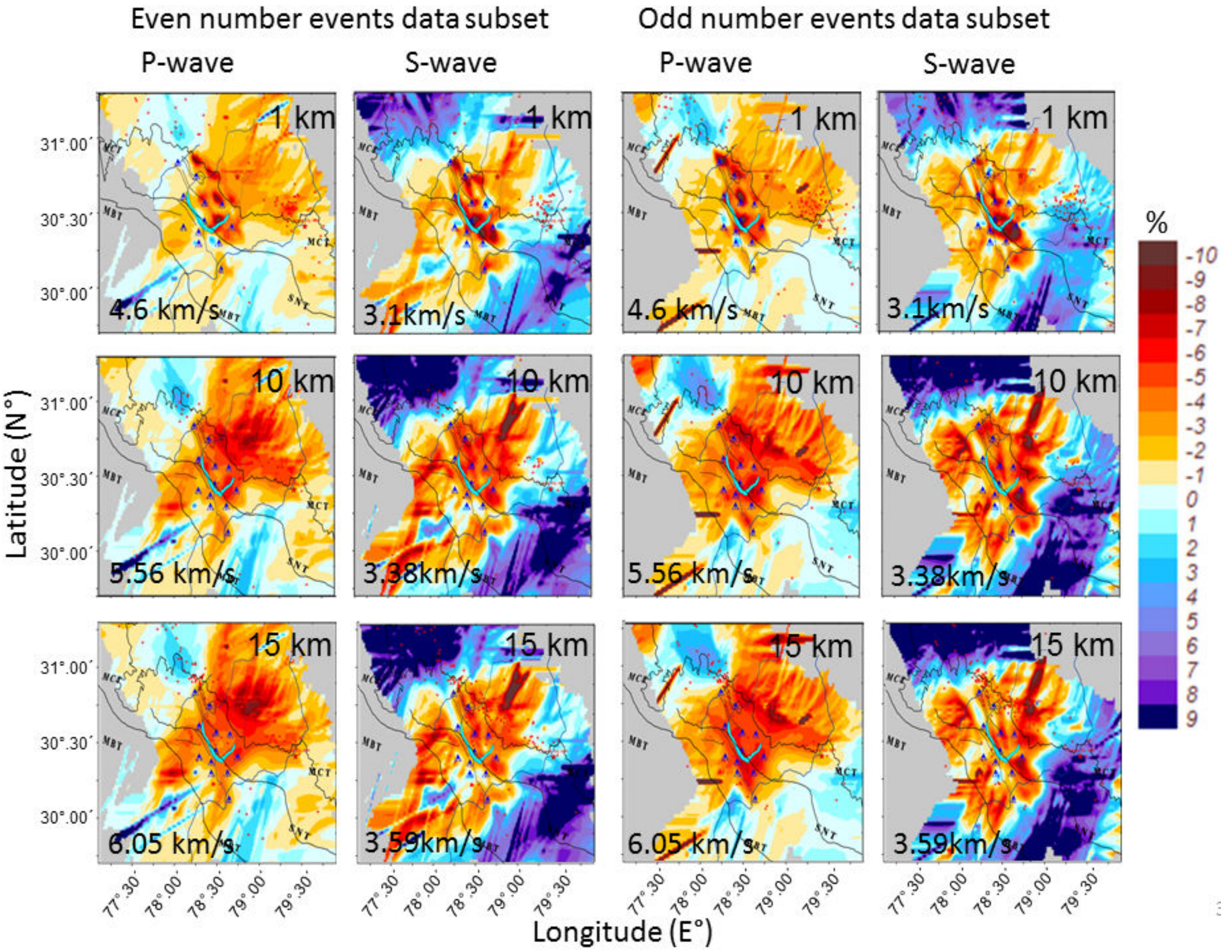

**Figure 5.6:** Tomographic inversion based on two independent subsets of the data. Results for the subsets with odd and even event-numbers are shown on the left and right, respectively. Reference velocity at each depth is mentioned on the tomogram, velocity anomalies are calculated with respect to this reference velocity. The similarity of the results indicates the robustness of the inversion with respect to random factors. The color scale indicates the velocity anomaly as a percentage

**Table 5.3:** Average P and S residuals and variance reductions of tomographic inversions using checkerboard test and various subsets of real data

| **Tests** | **Average residual (s)** | | | | **Toal variance reduction in final Iteration** | |
|---|---|---|---|---|---|---|
| | **Initial** | | **After 5th iterarion** | | | |
| | **P-wave** | **S-wave** | **P-wave** | **S-wave** | **P-wave** | **S-wave** |
| Checkerboard test | 0.1559 | 0.2877 | 0.1408 | 0.1989 | 9.2287 | 30.8535 |
| Odd events dataset | 0.2429 | 0.3619 | 0.2162 | 0.3125 | 10.9586 | 13.6500 |
| Even eventdataset | 0.2515 | 0.3387 | 0.2125 | 0.3068 | 15.5222 | 9.4203 |
| Random dataset1 | 0.2268 | 0.3298 | 0.1772 | 0.2594 | 21.8680 | 21.3393 |
| Random dataset2 | 0.2282 | 0.3441 | 0.1847 | 0.2672 | 19.0371 | 22.3462 |
| Random dataset3 | 0.2338 | 0.3581 | 0.2032 | 0.3078 | 13.0699 | 14.0465 |

### 5.6.2 Inversion with Random Datasets

The Inversion has also been performed using five independent subsets of data to allow assessing the bias in the tomographic images due to random noise in the data. These data subsets include two subsets of events taken from a catalogue with odd and even numbers, and three subsets of 900 events each selected randomly from the data. In case noise plays an important role in the data, it will lead to different inversion results. Fig.5.6 shows an example of results obtained from the even and odd data subset tests. The same scheme and same free parameters are used in these calculations as are used for inverting the entire real data set. Results showed practically similar patterns in anomaly distributions independent of the subset of data used, hence suggest a fair quality of data and a low noise level. This is also confirmed by low values of the final residuals as shown in Table 5.3.

## 5.7 Results and Discussion

### 5.7.1 P-wave Tomograms

To study the pattern of anomalies on the tomograms, in the form of distributed anomalies, a nomenclature to identify different high and low velocity anomalies is given. This nomenclature will lead to a better and easy understanding of these complex tomograms.

From south to north, the study area is divided into four sections according to geological settings. These areas are as labeled '1',' 2', '3' and '4' where, '1' stands for Sub Himalaya, '2' for Outer Lesser Himalaya, '3' for Inner Lesser Himalaya, and '4' for Higher Himalaya. We denote high velocity anomalies by 'H' and low velocity anomaly by 'L'. Thereafter, anomalies in each section are counted and numbered sequentially. In each section, the anomalies are labeled according to: section number- high/low anomaly (H or L)-number of anomaly. For example, in case of two high anomalies in Sub Himalaya, and to identify first high anomaly, a number 1H1 is assigned to this anomaly, similarly first low velocity anomaly is labeld as 1L1. Following this nomenclature the anomalies are labeled and marked on the P-and S- wave tomogram of 1 km depth (Figure 5.8).

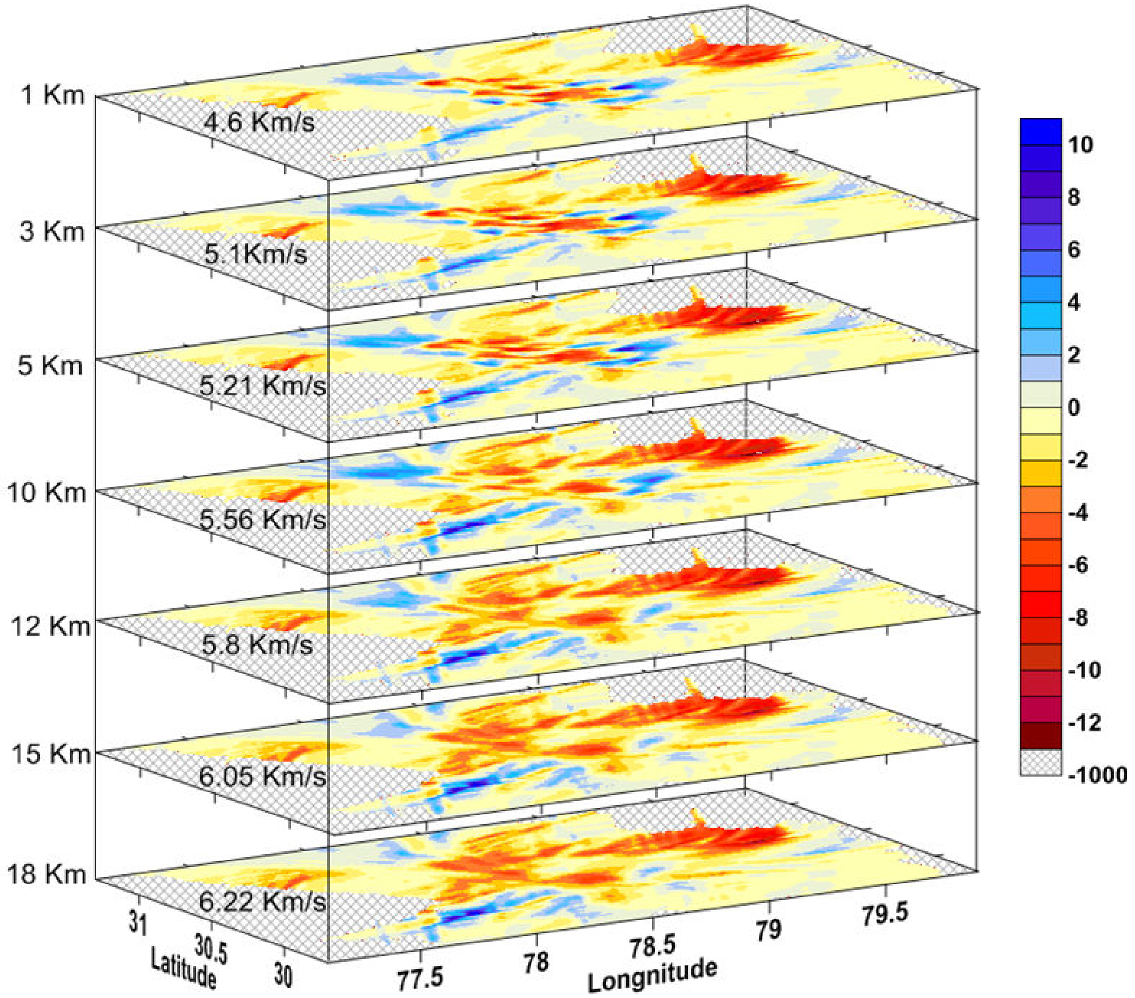

**Figure 5.7:** P-wave tomograms in the stacked view from the subsurface depth 1 Km to the Upper crust depth of 18 Km. reference velocity for each depth is given on its respective tomogram, Velocity anomalies are calculated with respect to this reference velocity. The color scale indicates the velocity anomaly as a percentage

From the inverted tomograms, several anomalous areas of high and low velocity have been delineated. These anomalies are interpreted in relation to the broad geological framework and regional tectonic features of the area. In the Sub Himalaya to the southwest of the MBT, a major elongated anomaly trending east-northeast to west-southwest has been delineated on all the horizontal slices at various depths. In the tomograms at 5 km depth this anomaly is very consistent both in pattern and dimension. This anomaly broadens with increasing depth and becomes stronger on the tomograms at deeper level. Further, it is observed that, on all tomograms up to a depth of 18 km, this anomaly continues up to the AYR station in the Outer Lesser Himalaya. The position/location of this anomaly corroborates with the location of postulated Delhi Haridwar Ridge (DHR) in the IGP and below the Sub Himalaya. Due to its consistency and nature of, this anomaly it is interpreted to represent the geometry of the buried DHR in the IGP and below the Sub Himalaya. On the P-wave tomograms, no other conspicuous anomaly is found in the Sub Himalaya. Therefore, this area seems to be more homogeneous in character compared to the areas of the Lesser Himalaya and the Higher Himalaya.

In the Outer Lesser Himalaya between the MBT and the SNT there are two patches of high velocity anomalies denoted as (2H1 and 2H2) delineated in the vicinity of the SUR and the CHN stations. The anomaly 2H2 further appears to continue in the Inner Lesser Himalaya and anomaly 2H1 lies at the eastern end of the Algar thrust. Between these two high-anomalies, there lies a broad, low velocity anomaly (about 50-km-long), and follow the trace of the SNT. Major part of this broad anomaly falls in the Inner Lesser Himalaya. A small LVZ is located in the vicinity of SRL station. It appears that the anomaly 2H2, which is almost trending east west, is the continuation of the anomaly 1H1, mapped in the Sub Himalaya. The anomaly 2H2 is consistent in nature up to 5 km. On the tomogram at a depth of 10 km, anomaly 2H1 disappears and anomaly 2H2 seems to be oriented in the northeast to southwest direction almost conforming to the trend of 1H1 anomaly observed in the Sub Himalaya. On the tomograms below 10 km depth, no footprints of 2H1 and 2H2 are observed. From the distribution of anomalies, it appears that Outer Lesser Himalaya is more inhomogeneous in character compared to the Sub Himalaya.

In the Inner Lesser Himalaya between the SNT and the MCT several areas of low and high anomalies are outlined. This signifies that the Inner Lesser Himalaya is more inhomogeneous compared to the Outer Lesser Himalaya and Sub Himalaya. The region encompassed by the network in the Inner Lesser Himalaya, exhibits high velocity and five low velocity anomalies on the surface tomograms sclice at 1 km depth. The pattern of these anomalies is almost is found to be almost consistent up to 5 km depth. However, a significant change in the pattern of these anomalies has been observed at 5,10,12,15 and 18 km depths. Two high velocity anomalies are observed in the vicinity of the CNT and the VIN stations. The anomaly in the vicinity of CNT station is stronger and seems to be a continuation of anomaly 2H2 observed in the Outer Lesser Himalaya. To the northwest of the RAJ station, a broad high velocity anomaly straddling the trace of the MCT is observed. A week high velocity anomaly is observed northwest of the SRT station. It appears that the characteristics of the Low velocity anomalies are influenced by the complex sub-surface geological structures. All the low velocity anomalies are almost parallel to the mapped tectonic features at very shallow depths. The low velocity anomaly (3L1) mapped in the vicinity of RAJ station almost mimics the mapped trend of the Uttarkashi thrust, and is slightly shifted in the northeast direction because these local thrust are dipping in the northeast direction. It seems that, the pattern of this anomaly is related to the low velocity material (fault gouge) at the fault zones. Further, the area encompassed by RAJ, GYN, KHU and SRT stations exhibits a high level of tectonic activity as evidenced by the presence of several local tectonic features. It is pertinent to note that the low velocity anomaly around RAJ and KHU stations lie at the tip of the local thrusts. The low velocity zones, which appear at the tips of the faults, seem to represent the cohesive zones which are formed at the end of the fault zones. However, their dimensions are on the higher sides. A broad, low velocity anomaly (3L5), encompassing the region between NTT, PRT, CNT and CHN stations follows the trend of the SNT. This anomaly, becomes more prominent on the tomogram at 5 km depth, and appears at the contact of the Outer Lesser Himalaya and the Inner Lesser Himalaya, almost parallel to SNT defined by the low and high velocity materials. From the distribution of anomalies in various tomograms it can be interpreted that the local tectonic features and geological structure have significantly influenced the characteristics of anomalies from surface to a depth of about 5 km. Beyond the depth of 5 km, it seems that the distributions of anomalies are not affected by the local tectonic features. At a depth of 10 km the area becomes more homogeneous and anomaly 3H1 becomes stronger. The low velocity anomaly 3L5 persists up to a depth of 18 km with changes in shape/pattern on each deeper level tomogram. A very broad, low velocity anomaly can be seen on the tomogram at a depth of 15 km depth. It appears that this anomaly represents the combination of anomalies 3L1, 3L2, 3L3 and 3L4 observed on tomograms at depths of 10 and 12 km. In addition, a low velocity of the MCT trending southwest is delineated about 100 km northwest of the network in the vicinity of the MCT. This anomaly has been observed up to 18 km depth and becomes stronger with depth. Its amplitude is maximum at 10 km depth and then decreases. This could be the artifact due to the less coverage of ray paths.

In the Higher Himalaya, apart from very broad low velocity zone which is delineated about 10 km to the north of the Chamoli earthquake, no other conspicuous velocity anomaly is observed. This anomalous zone, trending east to west in the vicinity of the MCT, becomes more intense with depth and spreads over a broad area. The maximum concentration of the anomalies is in the southern part (in the close proximity of the MCT) with a linear dimension of about 15 km. This small part could be the focal zone from where the Chamoli earthquake nucleated. This low velocity anomaly appears to spread in the west-northwest direction below 10 km depth. This spreading might be attributed to the 1991 Uttarkashi earthquake that occurred in this area at the depth of about 12 km, and was accompanied by a large number of aftershocks. These low velocity anomalies seems to have some relation with the rupture zone of the Uttarkashi earthquake and to the tectonic motions associated with the aftershock activity.

### 5.7.2 S-wave Tomograms

From the inverted S-wave tomograms two high velocity anomalies have been delineated in the Ganga fore-deep. First high velocity anomaly, running orthogonal to the MBT, is located in the Ganga fore-deep and corroborates with the anomaly on the P-wave tomogram. Second, high velocity anomaly, straddling the trace of MBT, is delineated in the vicinity of the MBT. This anomaly continues in the Outer Lesser Himalaya upto the SRL station. The anomaly is comparatively broader in size than the anomaly 1H1, and trends northeast to southwest. To the southeast, a low-velocity runs almost parallel of the 1H1 anomaly, is observed. In all S-wave tomograms, these high and low velocity anomalies are consistently observed, and become stronger with increasing depths. A comparatively small high velocity anomaly (1H3) is observed in the Ganga fore-deep at a distance of about 30 km to the southwest of the MBT.

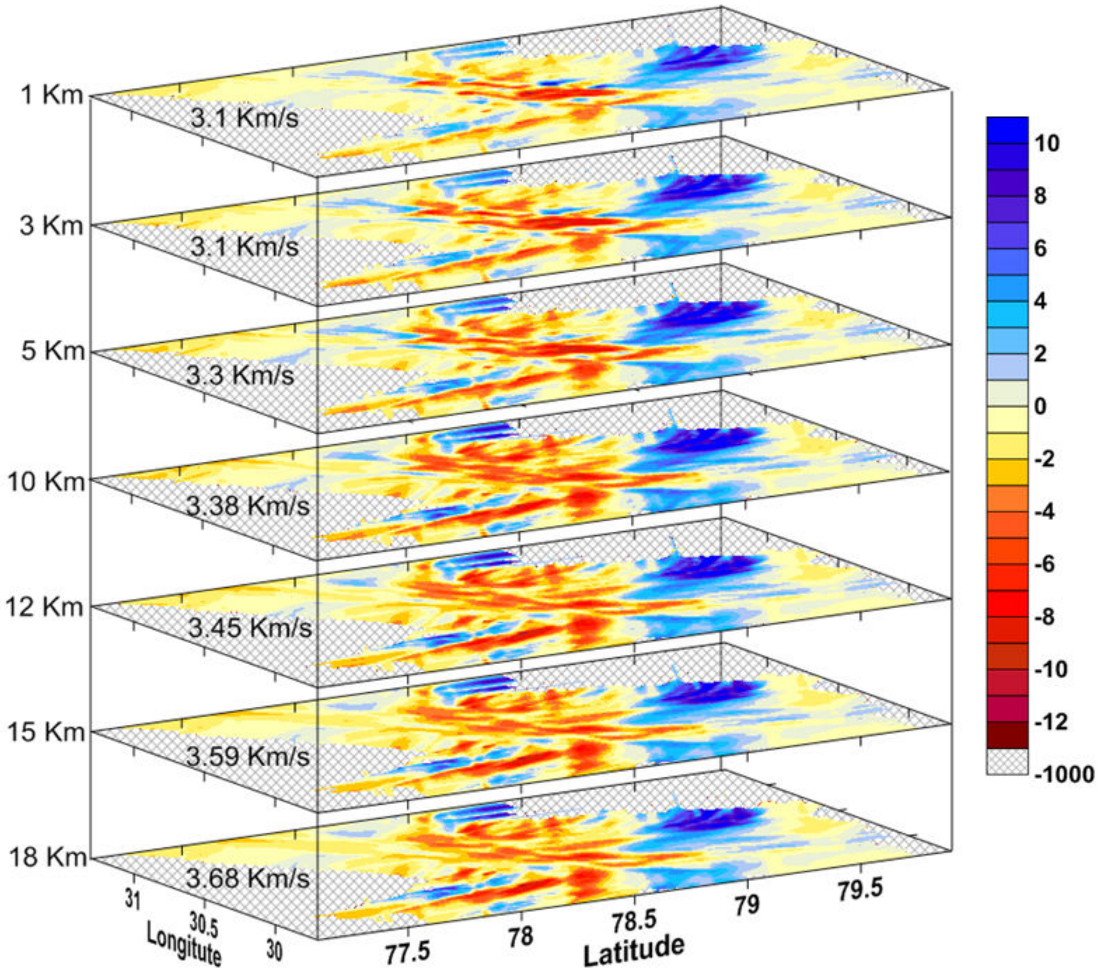

**Figure 5.8:** S-wave tomograms in the stacked view from the subsurface depth 1 Km to the Upper crust depth of 18 Km. reference velocity for each depth is given on its respective tomogram, Velocity anomalies are calculated with respect to this reference velocity. The color scale indicates the velocity anomaly as a percentage

In the Outer Lesser Himalaya the prominent high velocity anomaly which is denoted as 1H2, continues. In addition, there are small, feeble high velocity anomalies in the vicinity of SUR, AYR and CHN stations. The high velocity anomalies observed in the vicinity of CHN station appears to be related to 1H1. Although, these anomalies are very feeble, but exist in all the tomograms at 1 km, 3 km and 5 km depths. A low velocity anomaly 2L1 is observed in the region around the SRL station. This anomaly is observed on all the other tomograms and becomes more prominent with depth. There is a distinct change in the pattern of anomalies beyond 5 km and a significant consistency of low velocity anomaly is observed at 10, 12 to 15 km depths.

From the pattern of distribution of anomalies in the IGP and Sub Himalaya it appears that upper part of the crust is highly inhomogeneous in nature and has undulating shape. The undulating type structure is composed of ridges and valleys, high velocity anomalies seem to be related to many ridge type structures mapped by other geophysical methods and in-between low velocity material define the valley type structure. It also appears that the structure defined by 1H2 anomaly penetrates the Outer Lesser Himalaya.

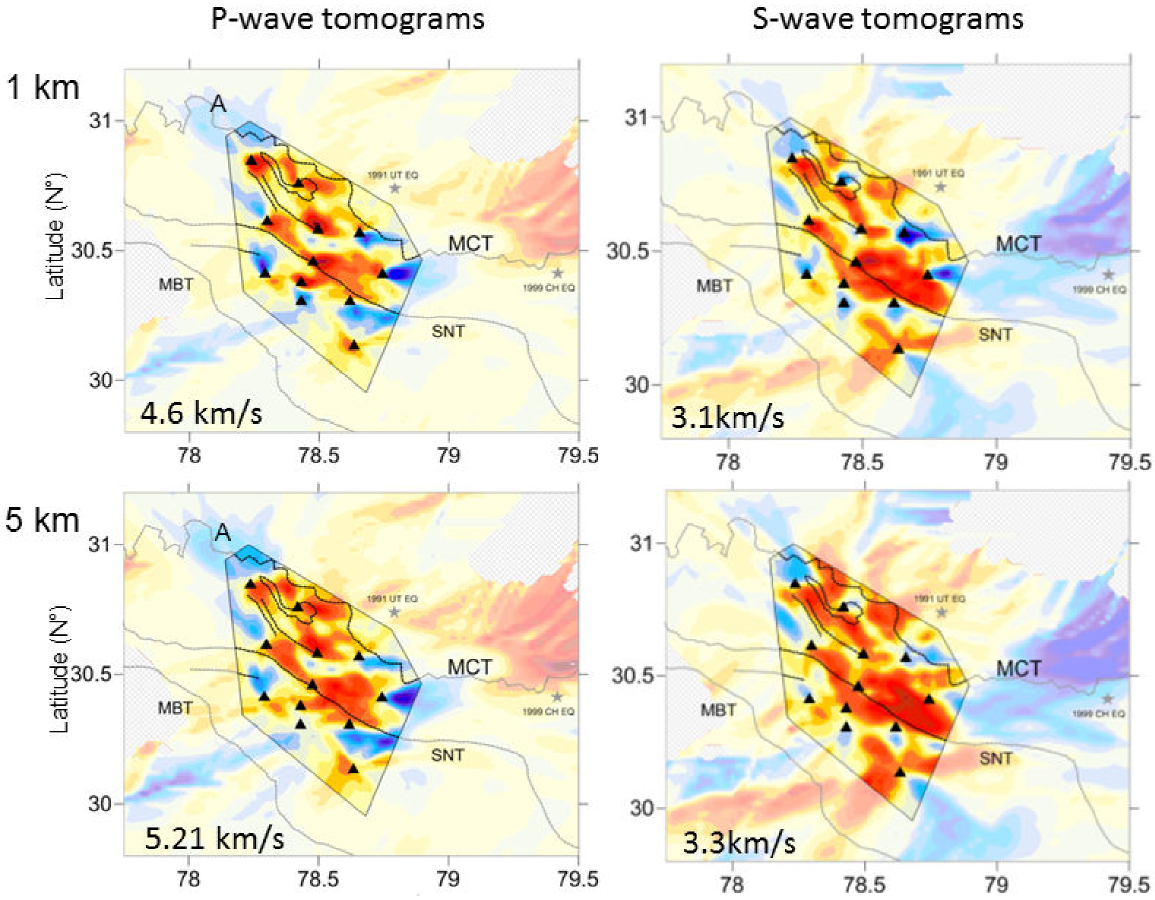

**Figure 5.9:** Results of real data inversion for P-wave and S-wave. Tomograms show the horizontal slices at: 1) 1 km, 2) 3 km, 3) 5 km, 4) 10 km, 5) 12 km, 6) 15 km, and 7) 18 km, depths. Area within the polygon shows the well resolved anomalies, and anomalies outside the polygon are masked by 60% Regional and local thrusts and faults are shown as black lines on the tomograms; triangles show the network stations; two stars show the projected epicentres of the Uttarkashi and the Chamoli Earthquakes on each tomograms. Reference velocity at each depth is mentioned on the tomograms, Velocity anomalies are calculated with respect to this reference velocity. The color scale indicates the velocity anomaly as a percentage. 'A' are the reference points used in the description (for details see text).

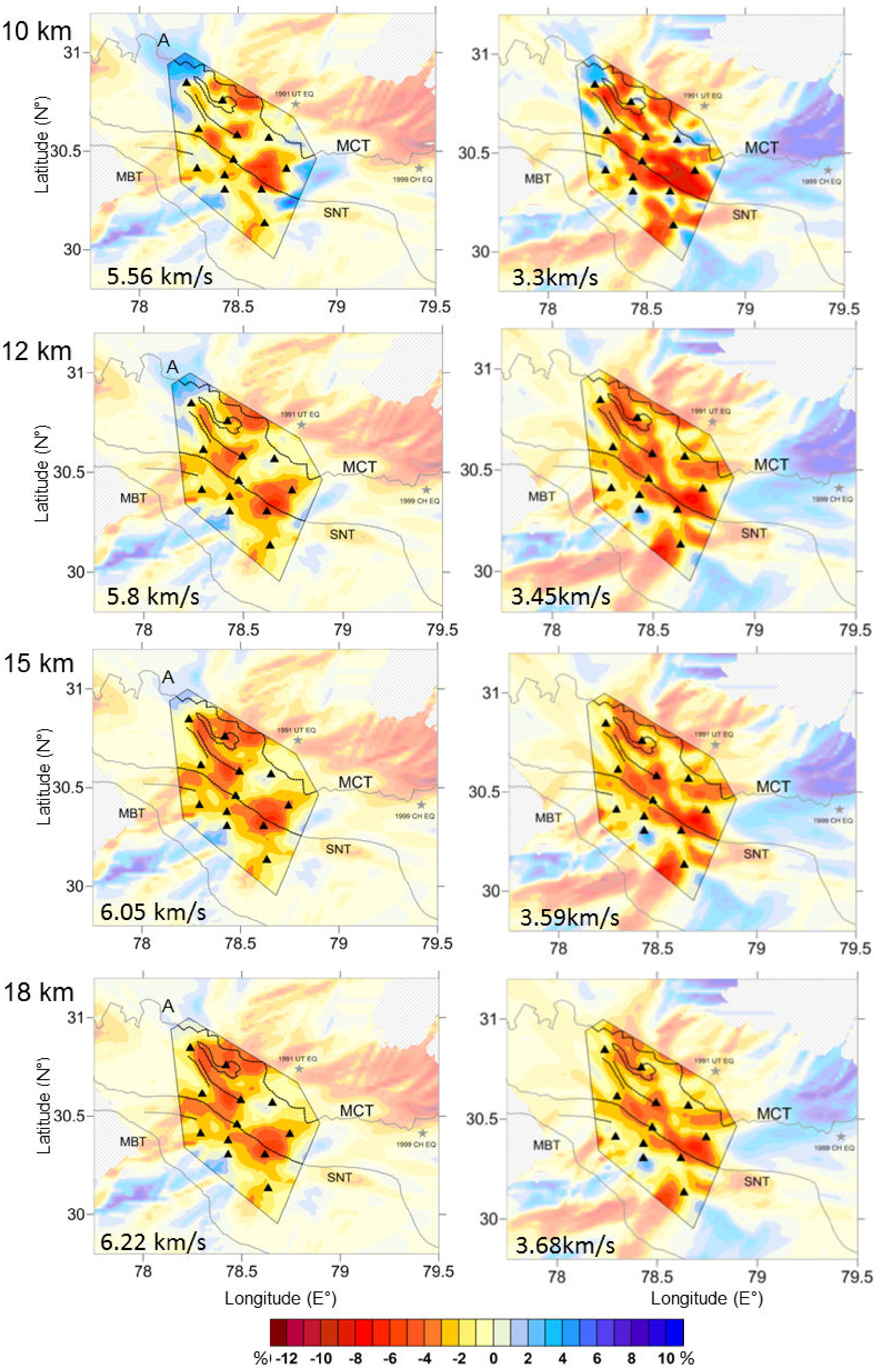

**Figure 5.9: Continued.**

The Inner Lesser Himalaya is characterized by prominent high- and low-velocity anomalies. A very good prominent high-velocity anomaly is observed to the east of the CNT station. With depth this anomaly becomes more prominent, and shifts to the east, and becomes feeble beyond 12 km. Positive S-wave anomalies are observed in the vicinity of VIN and GYN stations. Several low-velocity anomalies are outlined in the region encompassed by the network, which indicate that the Inner Lesser Himalaya is more inhomogeneous in character. One of the prominent Low velocity anomaly (3L1), running almost parallel to the SNT, extends from SRT station to about 50-km-east of CHN station. This anomaly is consistently appears in the tomograms of 3 and 5 km depth. The small, low velocity anomalies observed in the region around Uttarkashi thrust and other local tectonic features are on account of extensive tectonic activity. On the tomograms beyond 5 km depth, there is a significant change in the pattern of anomalies at depths of 10, 12 and 15 km. The amplitudes of anomalies are maximum on the tomograms at 12 and 15 km depth and, beyond 15 km anomalies are with reduced amplitudes.

In the Higher Himalaya, a prominent high S-wave anomaly 4H1 is observed. From the pattern of distribution of this anomaly, it appears that it is a continuation of 3H1 anomaly observed in the Inner Lesser Himalaya but anomaly is stronger to the north of the MCT. In this area a prominent low P-wave anomaly has been observed. In the region of high S-wave anomaly, no high P-wave anomaly is discernible, but the shape/trend of P-wave low velocity anomaly is almost similar to high S-wave high-velocity anomaly.

## 5.8 3-D Velocity Structure

The 3-D variations in $V_P$ and $V_S$ anomalies for the well resolved central part of the study area are shown in Fig. 5.9 as horizontal slices at 1, 5, 10, 12, 15, and 18 km depths. Because the anomalies mapped outside the network are less resolved, a polygon enclosing the area slightly more than the network dimensions have been drawn. The anomalies outside the polygon are masked by 60%. The velocity anomalies in each horizontal section are estimated as percentage perturbation of the reference model velocity at the respective depths. This indicates the true nature of even weak lateral velocity variation at any given depth. Further, the results of resolution test (checkerboard test) and the inversion with random datasets assure almost similar reliability of P- and S-models. Although in the dataset, number of S-phase picks is slightly less than the P-phase picks. To overcome the instability in the inversion results, we used 1.5 times larger damping parameter for inversion of S model than the P model.

The horizontal sections of the P- and S-velocity anomalies (Fig. 5.9) include several interesting features. Numerous elongated high and low velocity anomalies, oriented sub-parallel and transverse to the regional and local strike direction of the geological structure, are delineated in different parts of the study area. Within the resolution limits, these images clearly represent the strong lateral heterogeneities within the investigated area from 1 to 18 km depth. The strong heterogeneities in the velocity structure have been reported around the Chamoli region of the Garhwal Himalaya [*Mukhopadhyay and Kayal*, 2003] and beneath the Hazara arc in the Pakistan Himalaya [*Ni et al.*, 1991]. Based on the pattern of anomalies with depth, the tomograms are grouped in to two categories: the tomograms at 1, 3, and 5 km depths are grouped in the first category and those at 10, 15, and 18 km depths are grouped in the second category. The tomograms in each category exhibit almost similar distribution pattern of anomalies with increasing and decreasing amplitudes. However, while making transition from group 1 to group 2 (from 5 km to 10 km sections), it is observed that some features of anomaly pattern are more or less carried forward, whereas some features totally vanish. The Vp and Vs tomograms show discontinuous low velocity zones (LVZ) in the Inner Lesser Himalaya between the SNT (also known as the NAT) and the MCT. These broad LVZs almost follow the trend of the SNT. On the Vp tomograms, a broad, low-velocity anomaly (shown as masked anomaly) is delineated in the Garhwal Higher Himalaya (GHH) to the north of the Chamoli earthquake. However, in the vicinity of MCT the amplitude of the anomaly is high and the anomaly is trending east-west. The amplitudes of the low velocity anomalies broaden with depth upto 10-12 km and these anomalies become slightly less prominent at 15 and 18 km depths. In the same area Vs tomograms exhibit high velocity anomalies with almost similar positive amplitudes. These anomalies may not represent the true characteristics of the medium because they fall outside the region of high resolution. These anomalies are explained in the next section.

To the southwest of the study area, in the Indo Gangatic plains (IGP) and the Sub Himalaya, the $V_P$ and $V_S$ tomograms indicate a prominent high velocity anomaly. The trend of this anomaly is almost transverse to the strike direction of the MBT. The anomaly extends below the Sub Himalaya and the Lesser Himalaya and terminates in the vicinity of the MCT. The anomaly straddles the SNT and maintains almost similar trend, in the Inner Lesser Himalaya. However, in the Outer Lesser Himalaya, the anomaly shows a lateral offset in the east-southeast direction. The anomaly runs across the SNT and continues in the Inner Lesser Himalaya. These images of high velocity anomalies are almost consistent from surface to 15 km depth. Because spatial location and trend of these anomalies corroborate with the postulated location of the Delhi-Haridwar ridge below the IGP, these patterns of anomalies are interpreted to represent the images of the DHR below the IGP, the Sub Himalaya and the Lesser Himalaya. To the southeast all Vs tomograms show low velocity anomalies trending parallel to the high velocity anomalies.

The Vp and Vs tomograms of group 1 show prominent sequences of low and high velocity anomalies at shallow depths up to 5 km. Some of the features of these low velocity anomalies are observed in the tomograms of group 2 but their pattern of distribution have changed (e.g., low velocity anomaly delineated in the vicinity of the SNT). These anomaly sequences are found in the Inner Lesser Himalaya between the SNT and the MCT where the network stations are located. In the vertical direction the velocity variation is gradual. However, the lateral variations in the velocity seem to be affected by the geological regime of the region. The LVZs are better developed and aligned in the Vs tomograms, and some of these LVZs may be partly attributed to the varying degree of pore fluid filled saturations.

## 5.9 Physical Interpretation of Tomograms

The structural configuration and continuation of the DHR beneath the IGP, the Sub Himalaya and the Lesser Himalaya has been a subject of active debate among the earth scientists. Attempts have been made by various researchers to map the location and configuration of the DHR below the IGP and its possible extension below the Lesser Himalaya. From the pattern of Vp and Vs anomalies it is found that the DHR trends east-northeast beneath the IGP and the Sub Himalaya, and runs transverse to the strike direction of the MBT. From the tomographic images it appears that the DHR continues upto the MCT with a lateral off-set near the SNT. This off-set indicates that the frontal portion of the DHR has been displaced in the east-southeast direction because of the high compressional tectonic stress operative in the region. The DHR travelled in a direction transverse to the strike direction of the MBT and the MCT. As a result of compressional tectonic regime, the part of the DHR seems to have squeezed, and its frontal portion has fractured and drifted. The DHR, representing the extension of Aravali Mountain ranges, constitutes high velocity anomaly rock materials. The signatures of these anomalies are present in all tomographic sections from the near-surface to a depth of 10 km. These images gradually fade away on the tomograms at deeper levels (12, 15 and 18 km) particularly in the Lesser Himalaya. In Vs tomograms the low velocity anomalies running almost parallel to high velocity anomalies possibly represent the low-velocity sediments deposited in the IGP and the Sub Himalaya. These sediments seem to indicate highly fractured material primarily composed of sedimentary rocks deposited at the southestern boundary of the DHR.

From the pattern of distribution of anomalies it appears that Outer Lesser Himalaya is more inhomogeneous in character compared to the Sub Himalaya. However, the image resolution is less in the Sub Himalaya as the area falls outside the periphery of the network. In view of this more observational data is required to substantiate this inference. Further, the shape of anomalies in the IGP and the Sub Himalaya, also indicate that upper part of the crust is highly inhomogeneous and undulating but in the absence of appropriate resolution it is difficult to interpret these anomalies. It seems that these anomalies represent ridge and valley type structures. Such block like structures have been mapped in the western part of the Ganga basin from the spectral analysis of Bouguer gravity anomaly by *Mishra and Laxman* (1997). The structure, outlined in the IGP by the broad high S-wave anomaly (3%), straddles the MBT and continues in the Outer Lesser Himalaya.

The broad low velocity anomalies outlined on the tomograms at 10, 12, and 15 km depths are more prominent on the S-wave tomograms. In the IGP, the Sub Himalaya, and the Outer Lesser Himalaya these anomalies trend almost east-northeast to southwest, perpendicular to the strike direction of the geological structure. However, in the Inner Lesser Himalaya the trend of the anomalies is essentially parallel to the regional strike direction of the tectonic features.

To the north of the Chamoli Earthquake epicenter, high S-wave anomalies have been observed. In this area low P-wave anomalies are discernible. However, the amplitudes and the trend of low P-wave anomalies and high S-wave anomalies are almost similar. These anomalies are masked on the tomograms because they have less resolution. The area falls to the north of the rupture zone of the Chamoli earthquake ($M_w$ 6.4). This rupture zone, mapped from the locations of aftershocks, seems to be highly fractured. The high S-wave anomalies in the Higher Himalaya are attributed to high grade metamorphic rocks. The prominent low P-wave velocity anomalies depict redistribution of fluid due to the Chamoli earthquake. Several studies attributed P-wave low velocity anomalies to the redistribution of fluids in fractured zones (e.g., Mukhopadhyay and Kayal, 2003). The velocities of S-waves are not affected by the change in the bulk modulus, and therefore low

S-wave anomalies have not been observed. S-wave velocity depends upon shear modulus, and is not affected by the presence of fluids in the rock-matrix. The opposite nature of P- and S-wave anomalies has resulted in the low Vp/Vs ratios in the aforesaid area. Such areas with low Vp and low Vp/Vs anomalies may reflect the presence of Quartz rich upper crust [*Kern*, 1982]. The areas with the low Vp/Vs ratios also suggest the presence of water-filled-cracks with high percentage of porosity in the earthquake source zones [*Mukhopadhyay and Kayal*, 2003; *Mahesh et al.*, 2012]. This is likely to affect the faulting process and associated earthquake activity of the region.

## 5.10 Concluding Remarks

The 3-D P and S velocity structure of the Garhwal Himalaya has been mapped from the travel time data of 1367 local earthquakes. Images of horizontal velocity anomalies indicate the strong lateral heterogeneities within the investigated area from 1 to 18 km depths. The tomograms show low velocity zones (LVZ) in the Inner Lesser Himalaya between the SNT and the MCT. The high velocity images allowed mapping the trend and configuration of the DHR beneath the Sub Himalaya and the Lesser Himalaya. The DHR seems to continue up to the MCT with a lateral off-set in the vicinity of the SNT. Although some of the images falling outside the network have less resolution.

From the distribution of anomalies it appears that Outer Lesser Himalaya is more inhomogeneous in character compared to the Sub Himalaya. From broader prospective it appears that low velocity anomalies in Sub Himalaya, IGP and Outer Lesser Himalaya are trending almost east-northeast to southwest---almost perpendicular to broad geological trends, whereas, in the Inner Lesser Himalaya the trend of the anomalies essentially is parallel to the trend of the tectonic features.

In the region of high S-wave anomaly, no high P-wave anomaly is discernible. However, the shape/trend of low P-wave anomaly is almost similar to high S-wave anomaly. This anomalous area encompasses aftershock zone of the Chamoli earthquake. Due to the aftershocks of this earthquake the area is highly fractured. The higher Himalaya comprises high grade metamorphic rocks and this could be a reason for the observed high S-wave anomaly in this area. On the contrary, observed low P-wave anomaly primarily depicts redistribution of fluid in and around rupture zone of Chamoli earthquake. The saturation of redistributed fluids in fractured zones resulted in the low P-wave anomaly zone. The velocity of S-waves is not affected by the change in the bulk modulus because S-wave velocity is primarily the function of shear modulus.

The opposite nature of P- and S-wave anomalies resulted in the low $V_P/V_S$ ratio in the aforesaid region. The low $V_P/V_S$ ratio for this type of seismically active region suggests the presence of water-filled cracks with varying percentages of porosity in the earthquake source regions. This is likely to affect the faulting process and associated earthquake activity of the region.

## Chapter 6

# The 3-D Velocity Structure and its Relationship with the Regional Seismicity

## 6.1 Introduction

The descriptions of the 3-D P- and S-anomalies beneath the Garhwal Himalaya are given in chapter 5. The relationship of these anomalies with the local seismicity and tectonics is the subject matter of this chapter 6. For this purpose hypocenters of 890 events relocated simultaneously with the 3-D velocity structure are utilized. Hypocenters of events are plotted on the tomograms at different depth levels. Tomograms are then interpreted in the backdrop of the tectonic and geological regime of the region. From the 3-D velocity parameters and space depth distribution of hypocentre of events, an attempt is made to constrain the geometry of the underthrusting Indian plate beneath the Garhwal Himalaya.

## 6.2 Relationship of 3-D Velocity Structure with Seismicity Distribution

To study the relationship between seismicity distribution and 3-D velocity structure, the revised hypocenters of events, obtained simultaneously with 3-D inversion, are plotted on the tomograms. In order to explain the distribution of events, we first provide a brief description of the geological and tectonic framework of the region. The Himalaya in general and the Garhwal Himalaya in particular, has been divided into three broad tectonic domains: the Sub Himalaya, the Lesser Himalaya, and the Higher Himalaya. This division is based on the broad geological structure and mapping of major intercontinental thrusts. The MBT and the MCT are the major Intra-continental thrusts that define the boundaries between the Sub Himalaya and the Lesser Himalaya, and between the Lesser Himalaya and Higher Himalaya. The Garhwal Lesser Himalaya has been further divided into the Garhwal Outer Lesser Himalaya (GOLH) and the Garhwal Inner Lesser Himalaya (GILH) by the Srinagar thrust. In the study area, the northwest-southeast trending MBT passes in the close proximity of Dehradun and Rishikesh towns. According to the Seismotectonic Atlas of

India (GSI, 2000), the Main Foothill thrust (MFT) is located about 12 km southeast of the Haridwar. There are two neotectonic tear faults mapped in the vicinity of the Haridwar. The first fault with a linear extent of about 15 km trends northeast-southwest. This fault strikes parallel to the Ganga River. The second fault trends north-south and is located about 12 km to the east of Haridwar. The MBT has experienced lateral (north-south) displacement because of the second tear fault. We shall describe the distribution of local seismic activity, keeping in view this geological and tectonic framework.

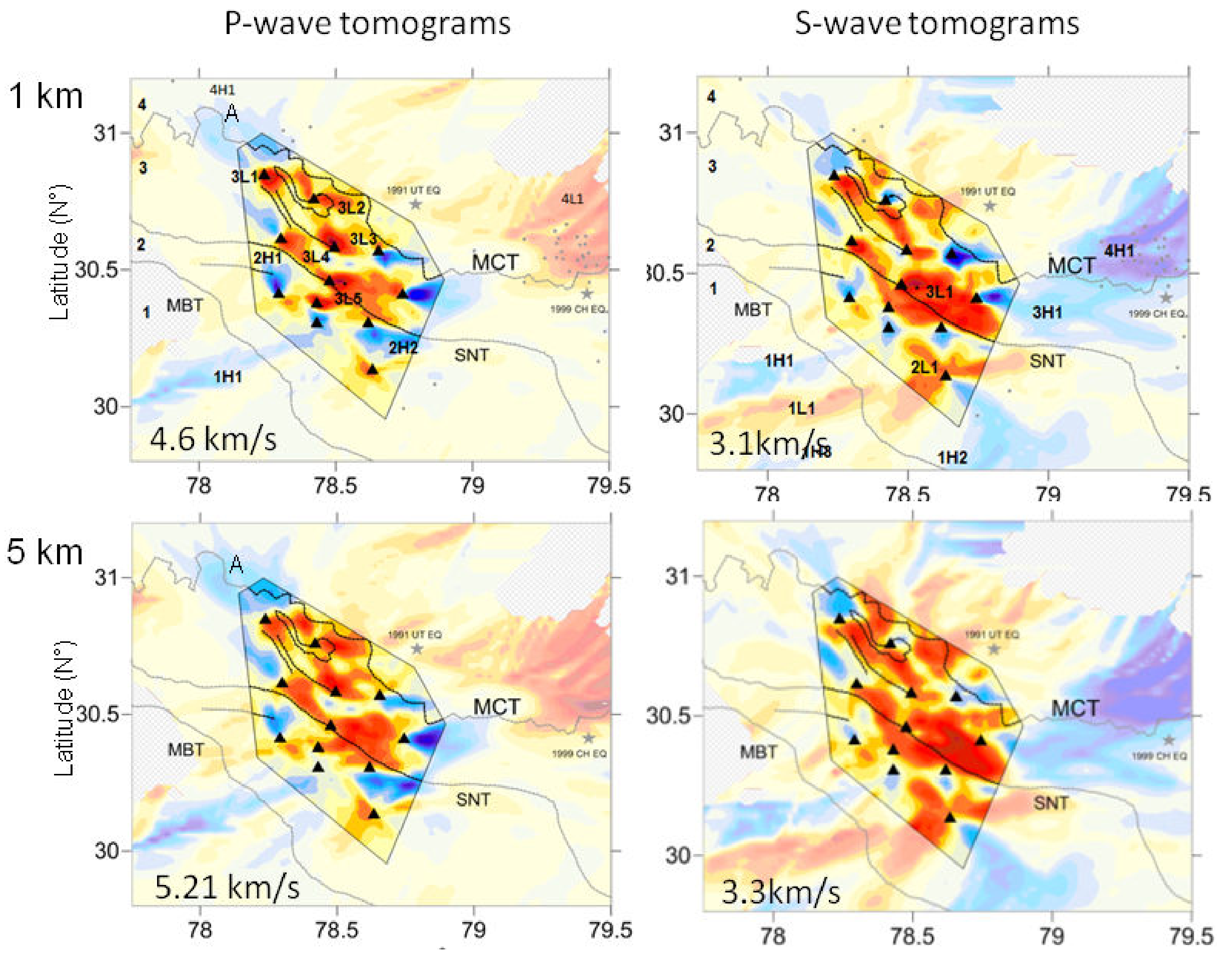

**Figure 6.1 :** Depth-wise distribution of seismic events at their respective P-wave and S-wave tomograms. N shows the number of events in a prescribed depth range, and 'A',' B', 'C' are the reference points used in the description (for details see text). The color scale indicates the velocity anomaly as a percentage. For enlarge view of these tomograms please refer appendix 1.

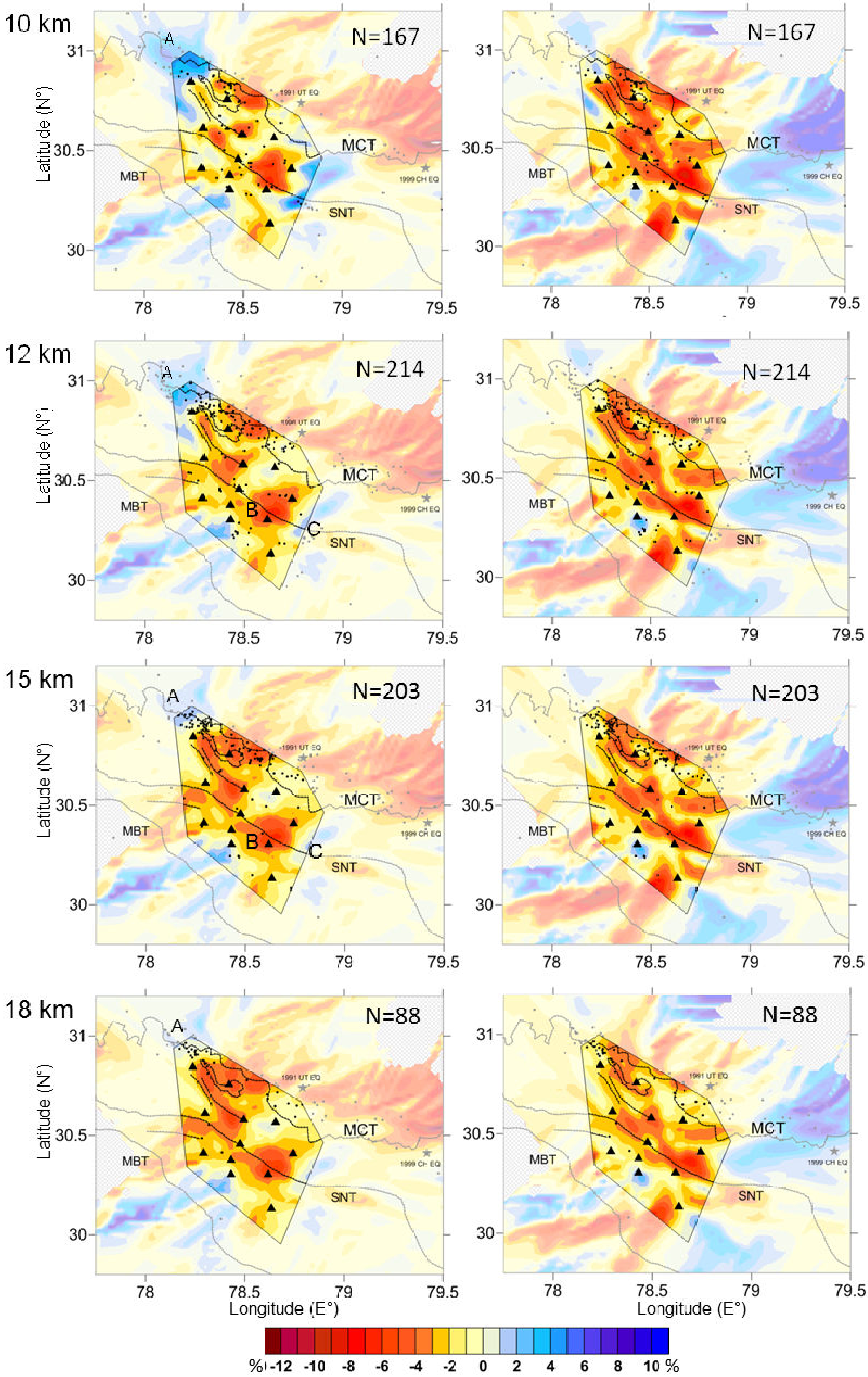

**Figure 6.1:** Continued

On the P-tomogram at a depth of 5 km, seismic activity at very shallow depth upto 5 km, primarily confined to the areas in the GHH and GILH. In the GHH the seismic activity occurs at about 100 km to the east from the centre of the network (Fig. 6.1). The area of seismic activity is located to the north the Chamoli earthquake epicentre, and is marked by significant low P-velocity anomalies. In GILH very few events occur to the south-southeast of the Chamoli earthquake epicentre. To the northwest, few events occur in an anomalous high velocity area (about 2-3%) straddling the trace of the MCT. This area is located about 55 to 90 km west-northwest from the Uttarkashi earthquake epicentre. The area within the network show low P-velocity anomalies of the order of ~5 %. This area is almost devoid of seismic activity barring few events located near the SNT. From the distribution of activity it appears that most of the events occur at the transition boundaries between high and low velocity anomalies.

The locations of 167 events with focal depths from 5 to10 km are plotted on the tomogram at a depth of 10 km. The spatial distribution shows that the events occur over wide areas in the GHH, GILH and GOLH. In the GHH, events located to the northwest of the Uttarkashi earthquake define a weak northwest-southeast trending linear zone over a distance of ~80 km. The events located to the northwest of the Chamoli earthquake also have a similar northwest-southeast trend over a distance about 20 km. In the GILH, seismic activity primarily occurs to the northwest of the Uttarkashi thrust (around the point 'A' in Fig. 1), and in the area enclosed by the network. Within the network area, activity either occurs between the Uttarkashi Thrust (UT) and the MCT or scatters between the SNT and the Dunda thrust. Between the UT and the MCT seismic activity occurs at the transition boundary of low velocity anomaly, whereas near point 'A' (Fig. 6.1) seismic activity occurs at the transition boundary of the high velocity anomaly. In the GOLH, seismic activity primarily occurs in the vicinity of the SNT. By-and-large these events are located at the low velocity transition boundary (around point 'B') and at the high velocity transition boundary (around point 'C') (Fig. 6.1).

The tomogram at 12 km depth depicts the spatial distribution of 214 events with focal depths between 10 and 12 km. The spatial distribution delineates about 80-km-long northwest-southeast trending local seismicity zone between points 'A' and the hypocenter of Uttarkashi earthquake. This seismicity zone, spanning the region of the GHH and GILH in the vicinity of the MCT, seems to reflect the contemporary seismic activity of the basement thrust zone (Seeber et al., 1981). In this zone, events to the northwest of the UT occur in the region of high and low velocity anomalies. To the southwest of the Uttarkashi earthquake, the seismic activity occurs at the transition boundaries of the low velocity anomalies. In the GHH, a seismicity zone is located to the northwest of Chamoli. This zone trends almost east-west and runs parallel to the MCT. In the GOLH, the seismic activity occurs far away from the SNT. Part of this activity occurs at the termination zone of postulated DHR.

The spatial distribution of seismic activity between 12 and 15 km depth is mapped in the tomogram at 15 km depth. Distribution shows that, a large number of events occur in a small area of the GILH. This area is located to the north and northwest of the UT. These events fall at the transition boundary of high and low velocity anomalies. The activity appears to shift to the north and is confined to a small area compared to the previous section. In the GOLH, the seismic activity at the termination zone of postulated DHR persists at this depth also. Only 88 events occur in the depth range between 15 and 18 km. This shows significant reduction of activity with depth. The events are distributed in the GHH and GILH and majority of the events are concentrated in the high velocity region (near point 'A') that straddles the trace of the MCT. The distribution of events defines a narrow seismicity zone with a linear dimension of about 20 km in the proximity of the MCT.

Above pattern of seismicity provides evidence that a prominent zone of seismicity is located to the north and northwest of the UT in the vicinity of the MCT between 10 and 18 km depth. This zone falls in the high velocity anomalous area, constricts with depth, and has a "cone" like pattern. We interpret this zone as a geometrical asperity on the basement thrust in the vicinity of the MCT as the region indicates higher strength than the surroundings. At 10 km depth the events are found to occur at the periphery of this asperity zone because of increased friction relative to the surrounding area. This increased friction is attributed to the underthrusting of high velocity material that constitutes upper part of the Indian crust. It appears that the strain energy, accumulating in this high strength area, may be released in future, causing a moderate earthquake. To the east-southeast of this area at a distance of about 40 km Uttarkashi earthquake occurred in 1991, and further to the southeast moderate earthquake occurred in Chamoli region in 1999. However, no moderate earthquake has occurred in the region outlined by the asperity. Figure 6.2 shows the overall distribution of seismicity over the investigated area.

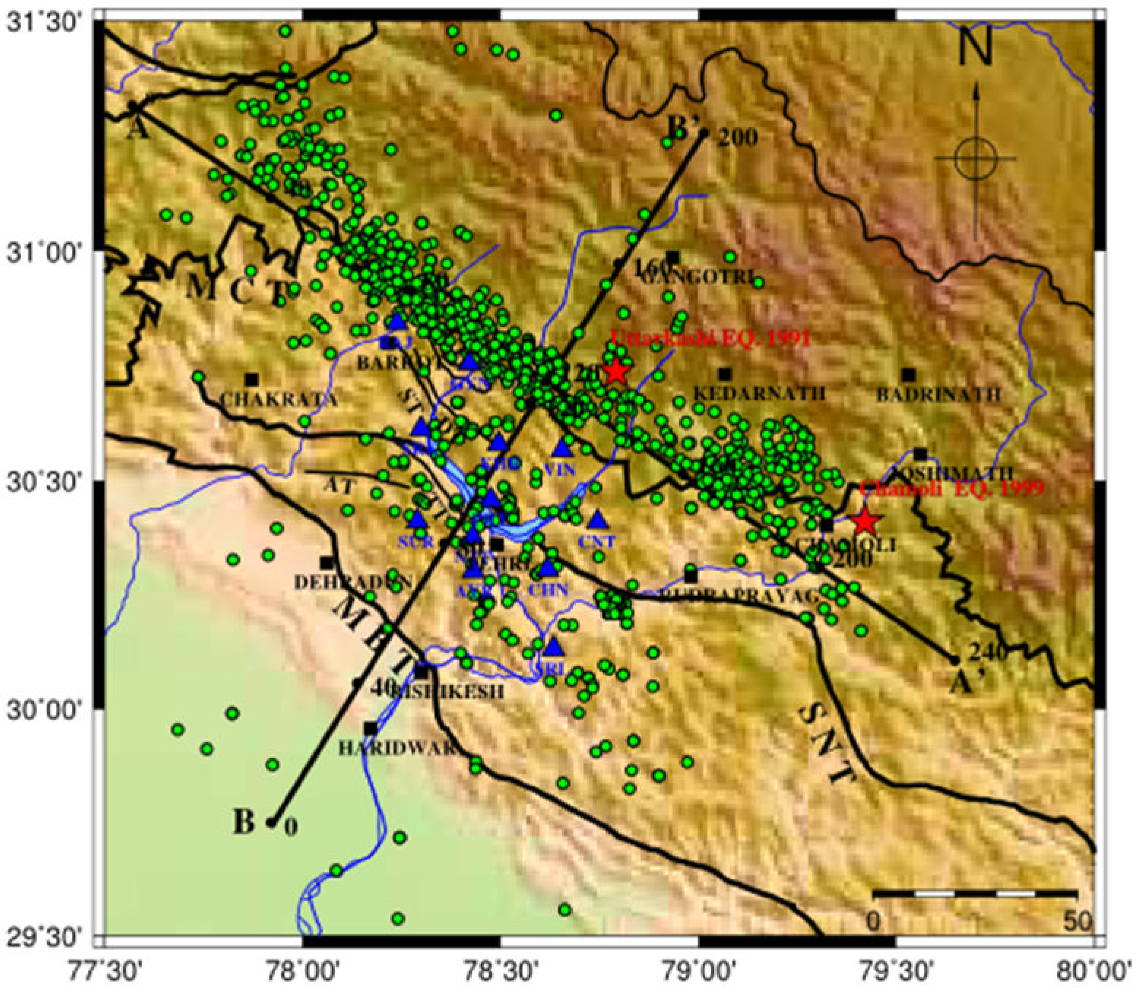

**Figure 6.2:** Relocated epicenters of events (green circles) after the final iteration of LOTOS. AA' and BB' shows the traverses along which velocity distributions and depth-distributions of seismicity are studied

## 6.3 Constraints on Geometry of the Indian Plate

An attempt is made to constrain the geometry of the underthrusting Indian plate beneath the Garhwal Himalaya, the 3-D velocity parameters and space-depth distribution of hypocenters of the events (Figure 6.2). Variations of $V_P$, $V_S$, and $V_P/V_S$ ratio with depth are shown along AA' and BB' traverses to decipher the geometry of various velocity layers. Lateral variation in rock types at the same depth level leads to lateral variation in velocity and $V_P/V_S$ ratio. Only the broad features observed in velocity and $V_P/V_S$ models could be interpreted. It is well known that, $V_P/V_S$ ratio is directly related to the Poisson's ratio ($\sigma$) which is an important indicator of various crustal rock properties and their brittle and ductile nature. The $V_P/V_S$ ratio, being a direct measure of the $\sigma$, provides a tighter constraint for tracking the lithological boundaries or physical state of the medium (e.g., saturation state). Crustal level folding and thrusting across the trend of the Garhwal Himalaya is evident from fig 6.3. Many workers have suggested the presence of a gently northward dipping detachment surface, which decouples upper crustal folded and faulted rock formations from underlying relatively deformation free basement comprised of Indian crust [e.g., *Seeber & Armbruster* 1981; *Ni & Barazangi* 1984; *Molnar* 1990]. Further research has demonstrated that the detachment surface has a ramp like structure at a depth between 15-20 km [*Pandey et al.*, 1995; *Caldwell et al.*, 2013; *Kanaujia et al.*, 2015]. This interpretation is based on the concentration of local seismicity at a specific region in the vicinity of the MCT. This region defines the ramp like structure of the detachment surface. Further, moderate and major Himalayan earthquakes occur in the vicinity of the MCT with focal depths between 15 and 20 km.

From the vertical tomograms along two sections (AA' and BB') an attempt is made to glean the flat-ramp-flat structure of the MHT below the Garhwal Himalaya. Broadly speaking, the distribution of $V_P$ and $V_S$ remains almost similar except for some anomalous features which show broad folding and faulting effects in $V_P$ and $V_S$ tomograms, but these features are more prominent in $V_P/V_S$ tomograms. As shown in fig. 6.3 along both the sections AA' and BB', areas of low Vp are characterized by low Vs and high $V_P/V_S$ ratio. This by-and-large agrees with the findings from the minimum 1-D velocity model (Kanaujia et al., 2015) that showed a low velocity layer between 12 and 14 km depth. The low velocity layer is ascribed to the presence of fluids and is a conspicuous feature of the Garhwal and Kumaun Himalaya (Arora, 2003; Kumar et al., 2013). To the southwest, near the MFT on BB' section, the high $V_P/V_S$ ratio defines a gently dipping surface which continues as far as the MCT in the northeast. Below the MCT, a patch of high $V_P/V_S$ ratio of about 1.78-1.80 is found inbetween the relatively low $V_P/V_S$ regions. This patch probably defines the part of the crust which has more strength and should exhibit sizable seismic activity. This is confirmed by the observed concentration of local seismicity in this region (Fig. 6.4(b)). Such regions between high and low velocity zones represent areas with high accumulation of strain energy and result in the seismic activity [e.g., *Kumar et al.*, 2013]. This arrangement seems to define the existence of a ramp on the MHT which further merges with the second shallow dipping flat surface (Fig. 6.3 and Fig. 6.4(b)). The location of the ramp on the MHT defines the most seismically active region of the Garhwal Himalaya. Most of the moderate earthquakes seem to nucleate in the areas close to this ramp in the vicinity of the MCT (e.g., hypocenters of the Uttarkshi and Chamoli Earthquakes shown in Fig. 6.4).

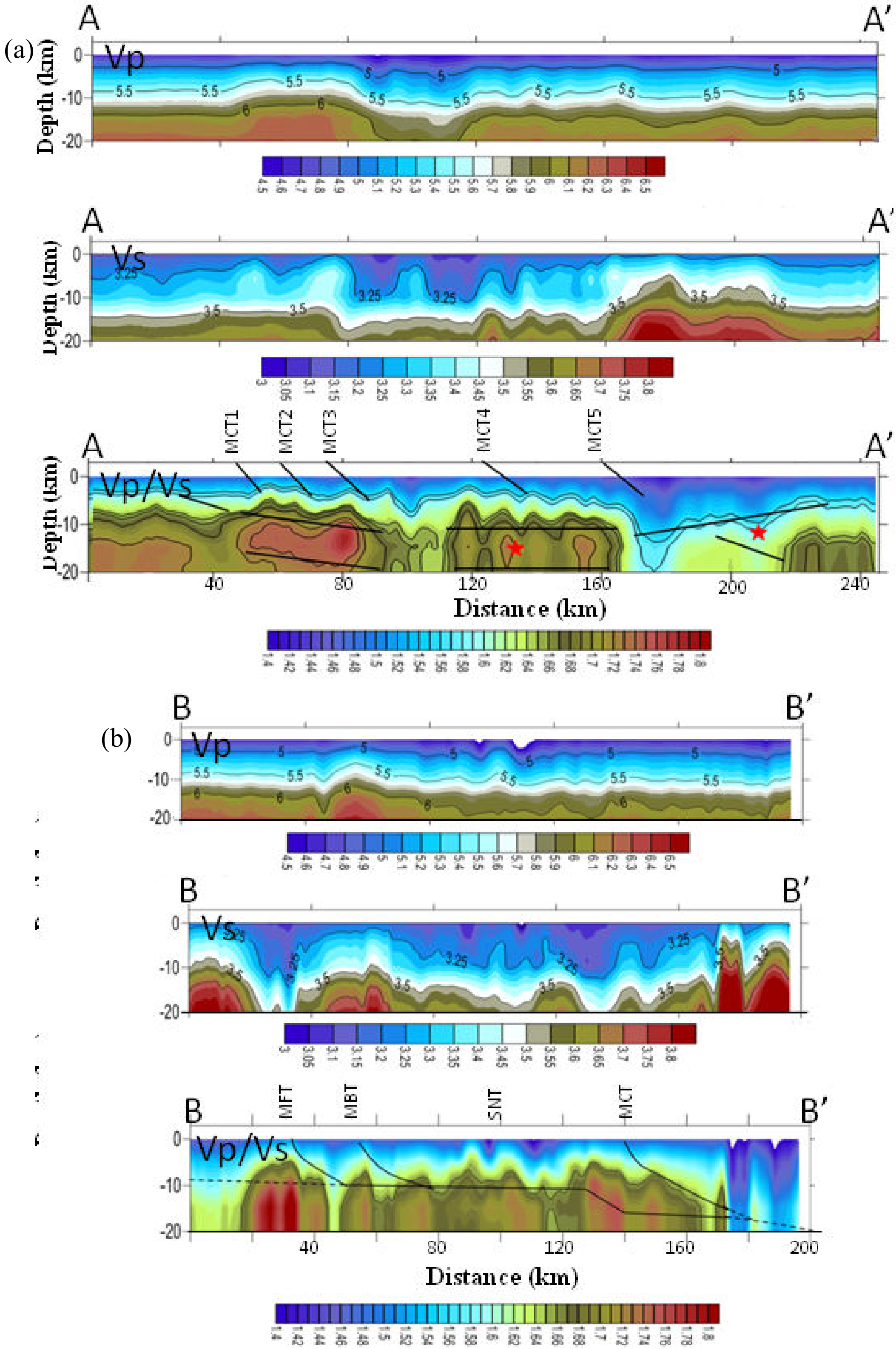

**Figure 6.3:** Distribution of a) absolute Vp, absolute Vs, and Vp/Vs ratio in vertical depth sections along the traverses AA’, and b) Distribution of a) absolute Vp, absolute Vs, and Vp/Vs ratio in vertical depth sections along the traverses BB’. The section AA' cuts the surface trace of the MCT at several locations which are marked as MCT1 to MCT5 and the possible positions of the regional faults/thrusts on BB' are marked in the section

The low $V_P/V_S$ ratio between 1.54 and 1.6 in the upper 4-5 km resulted in $\sigma$ between 0.15 and 0.18. This is attributed to the sediments deposited in the upper part of the crust. Below this depth, $V_P/V_S$ ratio increases upto 1.7-1.73 and in some parts its value are up to 1.8. These areas of high $V_P/V_S$ ratio are the areas defined by low Vs values. From a broad perspective, the areas with $V_P/V_S$ ratio $\leq 1.73$ ($\sigma \leq 0.25$) define the rigid/brittle crust. Such areas accumulate strain energy that can be released in the form of earthquakes. The areas with $V_P/V_S > 1.73$ ($\sigma > 0.25$) are more ductile in nature and likely to deform but will not fracture easily.

The depth distribution of local seismicity can be used to demarcate the brittle part of the seismogenic crust and the transition boundary between the brittle and ductile part of the crust [*Sibson*, 2002]. Two depth sections are drawn along traverse AA'---that runs along the regional strike direction of the MCT; and traverse BB'---that runs across the regional strike direction of the major tectonic features; to study the space-depth distribution of local seismicity and its tectonic implications. Depth section AA' shows the depth distribution of 574 local events located within a distance of 10 km on either side of the traverse AA'. This depth distribution defines the configuration and boundary of the brittle upper crust of the Indian plate along the MCT. It appears that the thickness of brittle part of the crust is not uniform along the MCT. Based on the distribution of seismicity two boundaries have been marked to define the brittle part of the Indian crust. Upper boundary seems to define a basin like structure, whereas the lower boundary defines the brittle-ductile interface.

Seismic activity is more scattered at both ends of the section compared to the middle part of the section (Fig. 6.4 (a)) where the thickness of the seismogenic part of the upper crust is about 10-12 km. To the southeast the seismic activity seems to scatter with depth. This activity occurs to the south of the MCT in the GILH. The events located at deeper level have been used to constrain the Moho depth along the MCT.

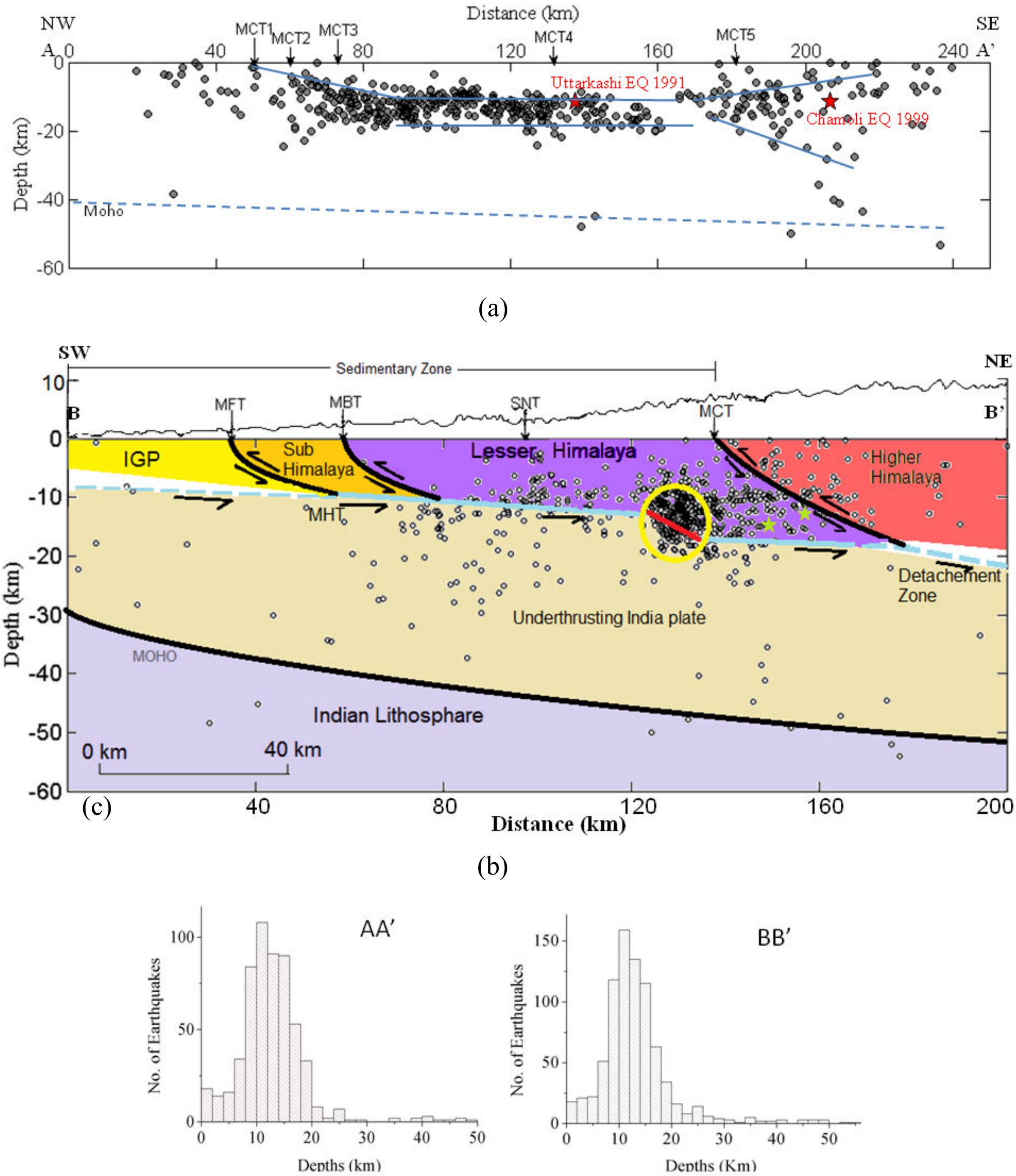

(a)

(b)

(c)

**Figure 6.4:** Depth sections of seismicity: a) Section AA', drawn along the strike direction of the MCT, shows the thickness of the brittle part of the Indian crust below the MCT with basin like structure (blue lines). The section cuts the surface trace of the MCT at several locations which are marked as MCT1 to MCT5; and b) section BB' shows the structure of the underthrusting Indian plate below the study region. The possible positions of the regional faults/thrusts are marked in the section. The ellipse outlines the ramp (shown as inclined red line) that lies on the MHT in the vicinity of MCT; c) histograms showing the number of events at different depth levels plotted in sections AA' and BB'

Depth section BB’ shows the depth distribution of local seismicity along the dip direction of the underthrusting Indian plate (figure 6.4 (b)). The hypocenters of 811 local events confined to a corridor about 50-km-wide on either side of the BB' traverse are projected on this section. Most of the events are found to cluster in the vicinity of the MCT between 8 and 16 km depth. About 10 km to the northeast of the MCT, seismicity almost ceases below the detachment zone. This seems to indicate that the crust below the higher Himalaya is deforming aseismically. To the southwest, no seismic activity occurs in the vicinity of the MFT and the MBT, whereas significant seismic activity occurs in the Lesser Himalaya between 6 and 20 km depth (particularly near the SNT). Fig. 6.4(b) shows the postulated structure of the underthrusting Indian plate based on the distribution of local seismicity. From the clustered seismicity below the MCT, a geometrical asperity in the vicinity of the MCT is postulated. Based on almost similar seismicity distribution, a geometrical asperity and ramp like structure of the MHT was interpreted in the Nepal Himalaya [*Pandey et al.,* 1995]. We observe that below the MCT, the seismic activity almost terminates at a depth of about 20 km. On this basis the inferred depth of the detachment zone is about 18-20 km in the GILH. The delineated zone of clustered seismicity shows that the MHT has undergone fracturing, and the fractured zone can be mapped as a ramp like structure combining the northeast (upper flat) and southwest (lower flat) segments of the MHT. The delineated structure of the MHT from local seismicity closely agrees with that mapped from the tomographic images. The ramp can be defined by a 10-km-long surface inclined at an angle of approximately 25° from horizontal, with vertical separation of 5-8 km. About 80% of the local seismicity is found to cluster in the area around the ramp. The upper flat continues from the MFT to the middle part of the Inner Lesser Himalaya. Below the SNT, the upper flat exhibits sizable seismic activity. Part of this activity seems to represent the tectonic activity of the SNT—a regional thrust found to be seismically active in this part of the Garhwal Himalaya [*Kanaujia et al.*, 2015]. The steeply dipping MCT flattens at depth and merges with the lower flat at a depth of about 18-20 km. Beyond the MCT, the lower flat is underthrusting aseismically because the region is almost devoid of seismic activity. This flat-ramp-flat structure seems to define the detachment zone of the Indian plate. Events at deeper level with focal depths upto 40-50 km are interpreted to define the depth of the Indian Moho. Various researchers postulated the Moho depth in the Himalaya between 40 and 50 km and ~46 km in the Garhwal Himalaya [e.g., *Rai et al.*, 2006; *Caldwell et al.*, 2013; *Kanaujia et al.*, 2015].

## 6.4 Concluding Remarks

Most of the seismicity in the investigated area occurs at the transition boundaries of high and low velocity anomalies. The seismicity along such transition zones occurs because of stress amplification. These zones of high rigidity contrast are the areas of high energy accumulation and are prone to fracturing because of stress failure resulting in seismic events. These transition boundaries can create a tension zone, in addition to an oblique compression movement between two different velocity materials.

The flat-ramp-flat subsurface geometry of the underthrusting Indian plate below the Garhwal Himalaya has been outlined from the velocity distribution and depth distribution of more than 800 relocated hypocenters. This subsurface structure of the Indian plate is in conformity with the current understanding of the Indian crust. The subsurface low velocity anomalies indicate the thickness of sedimentary rocks is about 4 km. This sedimentary rocks have relatively low $V_P$ and $V_S$ velocity, low $V_P/V_S$ value and the $\sigma$ range from 0.14-0.18.

An area of the geometrical asperity is found to the northwest of the UT. This area is located on the basement thrust in the vicinity of MCT. The asperity region is defined by the high strength material which has the capacity to accumulate high strain energy that can be released in the future in the form of moderate earthquake. The narrow zone of seismicity delineated between the UT and the MCT seems to be the nucleation zone of the future earthquake. This earthquake might nucleate at a depth of about 15 km. In view of these findings this area needs detailed investigation adopting other geophysical techniques to ascertain the level of tectonic stress.

# Chapter 7

# Conclusions and Future Scope

## 7.1 Introduction

This study aimed at developing 1-D and 3-D velocity models around the Tehri region of the Garhwal Himalaya, and to study the local seismicity and seismotectonics of the region. For this purpose the high quality local earthquake data collected from January 2008- December 2012 has been utilised. The data has been acquired from a 12-station telemetered seismic network deployed in the region since January 2008. Earthquake locations obtained using 1-D and 3-D models are interpreted to elucidate the local seismicity and seismotectonics of the Garhwal Himalaya. The significant results from the study are summarized below.

## 7.2 Summary of Results on 1-D Velocity Model

A one-dimensional (1-D) crustal velocity model around the Tehri region of the Garhwal Himalaya has been estimated from the travel time inversion of 145 well located earthquakes each with at least six or more *P* and *S* phase readings and azimuthal gap <180°. The travel time data used in the study include 1177 *P*- and 1090 *S*- wave phases. The 1-D velocity model is fairly well-constrained, as testified by the small residuals in the earthquake locations. A significant reduction of the misfits compared to previous models demonstrated the sensitivity of the hypocenter locations to small variations in the velocity model used for locations. The salient features of the proposed model are given below.

7.2.1. The model consists of six layers up to 24 km depth, with P- and S- wave velocities ranging from 4.42 to 6.78 km/sec and 2.41 to 3.71 km/sec, respectively.

7.2.2. The depth of Moho, estimated from the travel-time curves of crustal phases, is about 46 km.

7.2.3. A low-velocity layer deciphered between 12 km and 14 km depth is ascribed to fractured basement thrust representing the upper surface of the Indian plate. The formation of this layer can be attributed to the weakening of the crustal material at the interface between the underthrusting Indian plate and overriding Himalayan block because of frequent occurrence of microearthquakes and small earthquakes.

7.2.4. The estimates of station corrections correlate well with the local geology. Negative and positive station corrections correspond to higher and lower actual velocities beneath the recording stations, with respect to velocity beneath the reference station.

## 7.3 Summary of Results on Characteristics of Local Seismicity

Using the proposed 1-D velocity model, 1457 events have been relocated adopting joint hypocenter determination method (JHD). Spatial distribution of relocated events shows that the seismic activity occurs in the Ganga-foredeep (south of the MFT), in the Sub-Himalaya (between the MFT and the MBT), in the Lesser Himalaya (between MBT and MCT), and in the Higher Himalaya (north of the MCT). The pattern of the seismicity and characteristics of the proposed seismotectonic models are described below.

7.3.1. About 70% of the locatable events occur in the Inner Lesser Himalaya between the Main Central thrust (MCT) and Srinagar thrust (SNT). The spatial distribution of majority of these events define a northwest-southeast-trending seismicity zone, that follows the surface trace of the MCT. This seismicity zone, primarily confined to the Inner Lesser Himalaya between the SNT and MCT, seems to corroborate with the postulated basement thrust (BT) zone.

7.3.2. About about 5% of the seismic activity occurred in the Ganga-foredeep. Part of this activity seems to be associated with tectonic activity of the Ganga-tear-fault.

7.3.3. From southwest to northeast, the local seismicity appears to spread and acquires a ‘T’ type structure which seems to be due to the stresses generated by the Delhi Haridwar ridge, because the axis of the postulated ridge almost lies in the centre of this delineated zone of seismicity.

7.3.4. The space-depth distribution of seismicity delineates the geometry of the seismically active Main Himalayan thrust (MHT) below a 300-km-long segment of the MCT. It is found that the MHT is composed of two shallow-dipping fracture zones that seem to represent seismically active thrust zones dipping in opposite directions. The postulated depth of basement thrust in the vicinity of the MCT is about 10─12 km.

7.3.5. The space-depth distribution of seismicity across the strike direction of the MBT and the MCT delineates two seismicity zones, at 10 and 15 km depth with a 5 km vertical separation. These zones define a flat-ramp-flat type structure of the MHT in the Vicinity of the MCT. Most of the local seismicity clusters in the vicinity of the MCT, and defines two prominent zones of hypocenters located to the southwest of the MCT (upper flat zone) and to the northeast of the MCT (lower flat zone).

7.3.6. A Flat-ramp-flat seismotectonic model is proposed for the region. The lower-flat seismicity zone bifurcates into two, indicating further slicing of the lower-flat zone.

7.3.7. The postulated thickness of the brittle part of the underthrusting Indian crust is about 20 km in the vicinity of the MCT.

## 7.4 Summary of Results on 3-D Velocity Model

The 3-D velocity structure of the upper crust beneath the Tehri region of the Garhwal Himalaya has been investigated from the Local tomographic inversion based on a dataset of 1365 events collected from January 2008 to 2012. The important characteristics of 3-D velocity structure are described below.

7.4.1. The near-surface and sub-surface images of high velocity regions identified in the Sub Himalaya and the Lesser Himalaya seems to define the trend and configuration of the postulated Delhi-Haridwar-ridge (DHR) beneath the IGP, the Sub Himalaya and the Lesser Himalaya. From the tomographic images it has been infered that the DHR continues up to the MCT with a lateral offset in the vicinity of the SNT.

7.4.2. Within the resolution limits, the images clearly represent the strong lateral heterogeneities within the investigated area from 1 km to 18 km depth. The Vp and Vs tomograms showed low velocity zones (LVZ) in the Inner Lesser Himalaya between the SNT and the MCT.

7.4.3. The subsurface geological structure defined by distributing velocity anomalies indicates the thickness of sedimentary rocks is about 4 km from the surface. This sedimentary layer has relatively low $V_P$ and $V_S$ velocity, low $V_P$/Vs value and the Poisson's ratio range from 0.14 to 0.18.

7.4.4. Strong heterogeneities in the velocity structure were observed in the Chamoli region of the Garhwal Himalaya. In this region, a high S-wave anomaly with a low P-wave anomaly was found. This area is located near the aftershock zone of the 1999 Chamoli earthquake, and it is seems that the region is highly fractured because of the aftershocks of the Chamoli earthquake.

## 7.5 Constraints on the Geometry of Underthrusting Indian Plate

The 3-D P- and S- velocity structure combined with the spatial and depth distribution of relocated hypocenters of events provided constraints on the geometry of the underthrusting Indian lithosphere in the Garhwal Himalaya. The salient characteristics of the seismicity and seismotectonic model are given below.

7.5.1. It is found that most of the seismicity in the investigated area occurs at the transition boundaries of high and low velocity anomalies. These boundaries define the contact zones of the high velocity material and the low velocity material. Seismicity along such zones occurs because of stress amplification. These zones of high rigidity contrast, are the areas of high energy accumulation and prone to fractures because of stress failure and cause seismic events.

7.5.2. The flat-ramp-flat type subsurface geometry of the underthrusting Indian plate below the Garhwal Himalaya has been outlined from the velocity and depth distributions of more than 800 relocated hypocenters. The ramp has been defined by 10 km long surface inclined at an angle of about 25° from horizontal with vertical separation of 5-8 km. The MCT flattens at depth and merges with the lower flat at a depth of about 18-20 km.

7.5.3. Below the 300 km surface trace of the MCT of the Garhwal Himalaya the depth of seismogenic crust is about 20 km.

7.5.4. An area of the geometrical asperity has been found on the basement thrust in the vicinity of MCT. The asperity region is defined by the high strength material with capacity to accumulate high strain energy that can be released in future in the form of a moderate earthquake. The narrow zone of concentrated seismic activity between the Uttarkashi thrust and the MCT seems to be the nucleation zone of this future earthquake.

## 7.6 Limitations and Future scope

The study conducted has provided some interesting results and enhanced the knowledge and understanding of the contemporary local seismicity and seismotectonics of the Garhwal Himalaya, thickness of the seismogenic crust and 3-D velocity structure of the upper crust in the study region. Nevertheless, the present data set enabled mapping of the 3-D velocity structure of the upper crust (<18 km) only. A more sophisticated analysis would require waveform modelling of some form, since the ray theoretical approach has limitations as the first arrival times of observed waves are considered the 'direct' ray theoretical arrivals. The resolution of the results depends on the amount of data used and the coverage of the study area by seismic stations. For more detailed estimates of the crustal velocity structure with improved resolution a larger data set with more number of recording stations should be used. Therefore, the results obtained in the present study could be improved and resolved if an enhanced dataset with more station coverage is used. The estimated crustal velocity structure of this study should be compared with the crustal structure obtained using different methods (such as receiver function analysis, surface wave dispersion analysis) and different dataset. An anisotropy study of the crust with local earthquakes should be carried out to provide additional structural control for better understanding of the seismogenesis. The present work is based on the use of first arrival phase data, and due to this, the crustal structure could be resolved only up to shallow depths where maximum concentration of events. Therefore, the resulting velocity structure lacks the resolution up to the Moho or other deeper reflection boundaries. To overcome this limitation attempts should be made to include lateral phase-arrivals in the tomographic inversion.

# BIBLIOGRAPHY

3. Abers, G. A. (1994), Three-dimensional inversion of regional P and S arrival times in the East Aleutians and sources of subduction zone gravity highs. J. Geophys. Res., 99, 4395–4412.

4. Abt, D. L. and K. M. Fischer, (2008), Resolving three-dimensional anisotropic structure with shear wave splitting tomography. *Geophys. J. Int.*, 173:859–886.

5. Achauer, U. (1994), New ideas on the Kenya rift based on the inversion of the combined dataset of the 1985 and 1989/90 seismic tomography experiments. *Tectonophysics*, 236, 305–329.

6. Akcelik, V., J. Bielak, G. Biros, I. Epanomeritakis, A. Fernandez, O. Ghattas, E. J. Kim, J. Lopez, D. O., Hallaron, T. Tu, and J. Urbanic (2003), High-resolution forward and inverse earthquake modeling on terascale computers. *Proceedings of the 2003 ACM/IEEE conference on supercomputing,* Page 52, New York.

7. Aki, K. and P. G. Richards (1980), Quantitative Seismology: Theory and methods, San Francisco : Francisco, Volume I: 557, 413-429.

8. Aki, K. and P. G. Richards (2002), *Quantitative Seismology, 2nd Ed.* Quantitative Seismology, 2nd Ed., by Keiiti Aki and Paul G. Richards. Published by University Science Books, ISBN 0-935702-96-2, 704pp.

9. Aki, K. and W. H. K. Lee (1976), Determination of the three-dimensional velocity anomalies under a seismic array using first P arrival times from local earthquakes: 1. A homogeneous intial model, *J. Geophys. Res.,* 81, 4381–4399.

10. Aki, K., A. Christoffersson and E. S. Husebye (1977), Determination of the three-dimensional seismic structure of the lithosphere, *J. Geophys. Res.,* 82(2), pp. 277–296.

11. Ammon C. J. (1991), the isolation of receiver effects from teleseimic P-waveform, Bull. Seismol. Soc. Am., 81(6), 2504-2510.

12. Anderson D. L. and A. M. Dziewonski (1984), Seismic tomography. *Scientific American* 251, 60–68.

13. Ankeny, L. A., L. W. Braile and K. H. Olsen (1986), Upper crustal structure beneath the Jemez Mountains volcanic field, New Mexico, determined by three-dimensional simultaneous inversion of seismic refraction and earthquake data. *J. Geophys. Res.,* 91, 6188–6198.

14. Arora B. R. and B. P. Singh (1992), Geomagnetic and geoelectric investigations for seismicity and seismotectonics of the Himalayan region. In: Gupta G. D. (Ed.), *Himalayan Seismicity. Geol. Soc. India, Mem*. 23, 1-21.

15. Backus G. and F. Gilbert (1968), The resolving power of gross earth data. *Geophysical J. of the Royal Astronomical Soc.* 16, 169–205.

16. Bakun, W. H. (1971), Crustal model parameters from P-wave spectra. *Bull. Seism. Soc. Am.* 61, 913-935.

17. Barraez, D. S. Garcia-Salicetti, B. Dorizzi, M. Padron and E. Ramos (2002), Modular neural networks for seismic tomography. *Proceedings of the 16th Int. Conference on Pattern Recognition (ICPR'02), IEEE Computer Society Washington, DC,* Volume 3, pp. 30407.

18. Baźan, F. S. V., M. C. C. Cunha and L. S. Borges (2014), Extension of GKB-FP algorithm to large-scale general form Tikhonov regularization. *Numerical Linear Algebra with Applications*, 21(3), 316–339.

19. Benz, H. M. and R. B. Smith (1984), Simultaneous inversion for lateral velocity variations and hypocenters in the yellowstone region using earthquake and refraction data. *J. Geophys. Res.,* 89, 1208–1220.

20. Bilham, R., and V. K. Gaur (2000), Geodetic contributions to the study of seismotectonics in India. *Curr. Sci.,* 79(9), 1259–1269.

21. Bilham, R., K. Larson, J. Freymueller, and M. Project Idylhim (1997), GPS measurements of present-day convergence across the Nepal Himalaya. *Nature*, 386, 61–64.

22. Bishop, T. P., K. P. Bube, R. T. Cutler, R. T. Langan, P. L. Love, J. R. Resnick, R. T. Shuey, D. A. Spindler, and H. W. Wyld (1985), Tomographic determination of velocity and depth in laterally varying media. *Geophysics*, 50, 903–923.

23. Blundell, C. A. (1993), Resolution analysis of seismic P-wave velocity estimates using reflection tomographic inversion, Ph.D. thesis, Monash University, Australia.

24. Bois, P., M. La Porte, M. Lavergne and G. Thomas (1971), Essai de determination automatique des vitesses sismiques par mesures entre puits, *Geophys. Prospect.,* 19: 42-83.

25. Boore, D. M. and M. N. Toksoz (1969), Rayleigh wave particle motion and crustal structure. *Bull. Seism. Soc. Am.* 59, 331-346.

26. Bosch, M. (1997), P wave velocity tomography of the Venezuelan region from local arrival times. *J. Geophys. Res.,* 102, 5455–5472.

27. Boschetti, F., M. K. Dentith and R. D. List (1996), Inversion of seismic refraction data using genetic algorithms. *Geophysics*, 61, 1715–1727.

28. Bucher, R. L. and R. B. Smith (1971), Crustal structure of the eastern Basin and Range Province and the northern Colorado Plateau from phase velocities of Rayleigh waves, in The Structure and Physical Properties of the Earth's Crust. *Geophys. Monogr. Ser.*, Vol. 14, edited by J. G. Heacock, pp. 59-70, AGU, Washington, D.C.

29. Burdick, L. J. and C. A. Langston (1977), Modeling crustal structure through the use of converted phases in teleseismic body waveforms. *Bull. Seism. Soc. Am.* 67, 677-692.

30. Calderon–Macias, C., M. K., Sen and P. L. Stoffa (1997), Hopfield neural networks, and mean field annealing for seismic deconvolution and multiple attenuation. *Geophysics*, 62, 992–1002.

31. Caldwell, W. B., S. L. Klemperer, J. F. Lawrence, S. S. Rai, and Ashish (2013), Characterizing the Main Himalayan Thrust in the Garhwal Himalaya, India with receiver function CCP stacking. *Earth Planet. Sci. Lett.*, 367, 15–27.

32. Carlson, W. D. (2006), Three-dimensional imaging of earth and planetary materials. *Earth and Planetary Science Letters,* 249(3-4), 133–147.

33. Carpenter, E. W. (1965), Explosion Seismology: Capabilities and limitations of long-range methods for detecting and recognizing explosions are discussed. *Science (New York, N.Y.)*, 147 (3656), 363–373.

34. Cassell, B. R. (1982), A method for calculating synthetic seismograms in laterally varying media. *Geophys. J. Royal Astr. Soc*., 69, 339–354.

35. Cattin, R., and J. P. Avouac (2000), Modeling mountain building and the seismic cycle in the Himalaya of Nepal. *J. Geophys. Res.,* 105(B6), 13389-13407.

36. Censor, Y. (1981), Row action methods for huge and sparse systems and their applications: Soc. Industr. *Appl. Math. Rev*., 23, 444-466.

37. Chamoli, A., A. K. Pandey, V. P. Dimri, P. Banerjee, (2011), Crustal configuration of the northwest Himalaya based on modeling of gravity data. *Pure Appl. Geophys.,* 168, 827-844.

38. Chander, R., I. Sarkar, K. N. Khattri, and V. K. Gaur (1986), Upper crustal compressional wave velocity in the Garhwal Himalaya. *Tectonophysics* 124, 133–140.

39. Chapman, C. H. and R. Drummond (1982), Body-wave seismograms in inhomogeneous media using Maslov asymptotic theory. *Bull. Seism. Soc. Am*., 72, S277–S317.

40. Chauhan, R. K. S. and R. N. Singh (1965), Crustal studies in Himalayan region. *J. Ind. Geophys*. Un. II, V1, pp. 51-57.

41. Chiarabba, C., A. Amoto and M. Meghraoui (1997), Tomographic images of the El Asnam fault zone. *J. Geophys. Res.,* 102(B11), 24485–24498.

42. Chopra, S., T. M. Chang, S. Saikia, R. B. S. Yadav, P. Choudhury, and K. S. Roy (2014), Crustal structure of the Gujarat region, India: New constraints from the analysis of teleseismic receiver functions, *Journal of Asian Earth Sciences, 96*, 237-254.

43. Chopra, S., V Kumar, A Suthar, P Kumar (2012), Modeling of strong ground motions for 1991 Uttarkashi, 1999 Chamoli earthquakes, and a hypothetical great earthquake in Garhwal–Kumaun Himalaya, *Natural hazards 64 (2)*, 1141-1159

44. Clayton R. W. and G. A. McMechan (1971), Inversion of refraction data by wavefield continuation. *Geophysics*, 46, 860-868.

45. Clayton R. W. and R. A. Wiggins (1976), Source shape estimation and deconvolution of teleseismic body waves. *Geophys. J. Int.*, 103, 301-320.

46. Clayton R. W. and T. M. Hearn (1982), A tomographic analysis of lateral velocity variations in Southern California. *EOS Transactions of the American Geophysical Union* 63: 1036.

47. Crosson, R.S. (1976), Crustal structure modeling of earthquake data 2. Velocity structure of the Puget Sound region, Washington. *J. geophys. Res.,* 81, 3047–3054.

48. Dahlen, F. A., S. -H. Hung and N. Guust (2000), Frechet kernels for finite-frequency traveltimes- I.Theory. *Geophys. J. Int.,* 141, 157–174.

49. Dinc, A. N., I. Koulakov, M. Thorwart, W., Rabbel, E. R. Flueh, I. Arroyo, W. Taylor, and G. Alvarado (2010), Local earthquake tomography of central Costa Rica: transition from seamount to ridge subduction. *Geophys. J. Int.* 183 (1), 286-302.

50. Dipok K Bora, and S. Baruah (2012), Mapping the crustal thickness in Shillong–Mikir Hills Plateau and its adjoining region of northeastern India using Moho reflected waves, *Journal of Asian Earth Sciences, 48*, 83-92.

51. Dipok K. Bora, D. Hazarika, K. Borah, S. S. Rai, and S. Baruah (2014), Crustal shear-wave velocity structure beneath northeast India from teleseismic receiver function analysis, *Journal of Asian Earth Sciences, 90*, 1-14

52. Drijkoningen, G. G. and R. S. White (1995), Seismic velocity structure of oceanic crust by inversion using genetic algorithms. *Geophys. J. Int.,* 123, 653–664.

53. Dziewonski, A.M., B.H. Hager and R.J. O'Connell (1977), Large-scale heterogeneities in the lower mantle. *J. Geophys. Res.* 82, 239–255.

54. Eaton, J. P. (1969), HYPOLAYER: A computer program for determining hypocenter of local earthquake in an earth consisting of uniform flat layer over a half space. *U.S. Geol. Surv., Open-File Rept.*, 155 pp.

55. Eberhart-Phillips D. and A. J. Michael, (1993), Three-dimensional velocity structure, seismicity and fault structure in the Parkfield Region, central California, *J. Geophys. Res.* 98(B9), 15737–15758.

56. Ellis, R. M. and P. W. Basham (1968), Crustal characteristics from short-period P waves. *Bull. Seism. Soc. Am.* 58, 1681-1700.

57. Ellsworth, W. (1977), Three dimensional structure of the crust and mantle beneath the island of Hawaii, PhD Thesis, Mass. Inst. Tech, Cambridge, Massachusetts, US.

58. Ewing, M., and F. Press, (1959), Determination of crustal structure from phase velocity of Rayleigh waves, III, The United States, *Geol. Soc. Amer. Bull.*, 52, 1031-1035,

59. Farra, V. and R. Madariaga (1988), Non-linear reflection tomography. *Geophys. J.*, 95, 135–147.

60. Fuchs K. and G. Muller (1971), Computation of synthetic seismograms with reflectivity method and comparision with observations. *Geophs. J. of Royal Astro. Soc.,* 23, 417-433

61. Gahalaut, V. K., and R. Chander (1997), On interseismic elevation changes and strain accumulation for great thrust earthquakes in the Nepal Himalaya. *Geophys. Res. Lett.*, 24 (9), 1011–1014.

62. Gaherty, J. B., T. H. Jordan and L. S. Gee (1996), Seismic structure of the upper mantle in a central pacific corridors. *J. Geoph. Res.,* 101, 22291-22309.

63. Gee L. S. and T. J. Jordan (1992), Generalized seismological data functionals. *Geophys. J. Int.* 111, 363–390.

64. Geological Survey of India (GSI) (2000), Seismotectonic Atlas of India and its Environs. Geol. Surv. India, Sp.Pub., P.L. Narula, S.K. Acharya and J. Banerjee (ed.), pp. 86.

65. Glahn, A. and M. Granet (1993), Southern Rhine Graben: Small-wavelength tomographic study and implications for the dynamic evolution of the graben. *Geophys. J. Int.*, 113, 399–418.

66. Golub, G. H., and C. F. Van Loan (1983), Matrix computations, North oxford Academic, Oxford.

67. Golub, G., and C. Reinsch (1970), Singular value decomposition and least squares solution. *Numer. Math*., 14, 403-420.

68. Graeber, F. M. and G. Asch (1999), Three-dimensional models of P wave velocity and P-to-S velocity ratio in the southern central Andes by simultaneous inversion of local earthquake data. *J. Geophys. Res.,* 104, 20237–20256.

69. Greenhalgh, S. A., D. Tapley and R. Singh (1989), Crustal heterogeneity in South Australia, earthquake evidence. *Geophys. J.,* 96, 85–99.

70. Gubbins, D. (1992), Seismology and plate tectonics, *Cambridge University Press*, Cambridge.

71. Hasegawa, A., N. Umino and A. Takagi (1978), Double-planed deep seismic zone and upper-mantle structure in the northeastern Japan arc. *Geophys. J. Royal Astr. Soc.,* 54, 281–296.

72. Haslinger, F., E. Kissling, , J. Ansorge, D. Hatzfeld, E. Papadimitriou, V. Karakostas, K. Makropoulos, H. G. Kahle, and Y. Peter (1999), 3D crustal structure from local earthquake tomography around the Gulf of Arta (Ionian region, NW Greece), *Tectonophysics*, **304**, 201–218.

73. Healy J. H. (1971), A comment on the evidence for a worldwide zone of low seismic velocity at shallow depths in the earth's crust, in the structure and physical properties of the Earth's crust, Geophys. Monogr. Ser., edited by J. G. Heacock, *AGU, Washington D.C.,* 14, 35-40.

74. Helffrich, G. (2006), Extended-time multitaper frequency domain cross-correlation receiver function estimation. *Bull. Seism. Soc. Am*., 96 (1), 344-347.

75. Hestenes, M., and E. Stiefel (1952), Methods of conjugate gradients for solving linear systems. *Nat. Bur. Standards J. Res*., 49, 409-436.

76. Hole, J. A. (1992), Nonlinear high-resolution three-dimensional travel-time tomography. *J. Geophys. Res.*, 97, 6553–6562.

77. Huang, H. H., Y. M. Wu, X. Song, C. H. Chang, S. J. Lee, T. M. Chang, and H. H. Hsieh (2014), Joint Vp and Vs tomography of Taiwan: Implications for subduction-collision orogeny, *Earth Planet. Sci. Lett.*, 392, 177-191

78. Humphreys, E. and R. W. Clayton (1988), Adaption of back projection tomography to seismic travel time problems. *J. Geophys. Res.,* 93, 1073–1085.

79. Humphreys, E. D. and R. W. Clayton (1990), Tomographic image of the Southern California Mantle. *J. Geophys. Res.,* 95, 19,725–19,746.

80. Husen, S., E. Kissling, and J. F. Clinton (2011), Local and regional minimum 1D models for earthquake location and data quality assessment in complex tectonic regions: Application to Switzerland, Swiss. *J. Geosci.* 104, no. 3, 455–469.

81. Husen, S., R. Quintero, E. Kissling and B. Hacker (2003), Subduction-zone structure and magmatic processes beneath Costa Rica constrained by local earthquake tomography and petrological modeling, *Geophys. J. Int.* 155, 11–32.

82. Hutton, K., E. Hauksson, J. Clinton, J. Franck, A. Guarino and N. Scheckel (2006), Southern California Seismic Network update. *Seismol. Res. Lett.* 77, 389–395.

83. Imposa, S., J.-P. Fourno, R. Raffaele, A. Scaltrito, and L. Scarfi (2009), Accurate hypocentre locations in the Middle-Durance Fault Zone, South-Eastern France. Central European, J. Geosci., 1, 416–423.

84. Inoue, H., Y. Fukao, K. Tanabe and Y. Ogata (1990), Whole mantle P-wave travel time tomography. *Phys. Earth Planet. Inter*., 59, 294–328.

85. Israil, M., D. K. Tyagi, P. K. Gupta and S. Niwas (2008), Magnetotelluric investigations for imaging electrical structure of Garhwal Himalayan corridor, Uttarakhand, India. *J. Earth Syst. Sci.,* 117 (3), 189-200.

86. Julian, B. R. and D. Gubbins (1977), Three-dimensional seismic ray tracing. *J. Geophys.,* 43, 95–113.

87. Kaila, K. L., R. P. Reddy and H. Narain (1968), Crustal structure in the Himalayan foot hills area of north India from P wave data of shallow earthquakes. *Bull. Seismol. Soc. Am.*, 58, 597-612.

88. Kanaujia, J., A. Kumar, and S. C. Gupta (2015), 1D Velocity Structure and Characteristics of Contemporary Local Seismicity around the Tehri Region, Garhwal Himalaya, *Bull. Seismol. Soc. Am.,* 105(4), 1852–1869.

89. Kanaujia, J., A. Kumar, and S.C. Gupta (2016), 3-D velocity structure around tehri region of the garhwal lesser himalaya: constraints on geometry of the underthrusting indian plate. *Geophys. J. Int.*, 205(2), 900-914.

90. Kao, H. and R. J. Rau (1999), Detailed structures of the subducted Philippine Sea plate beneath northeast Taiwan: A new type of double seismic zone. *J. Geophys. Res.*, 104, 1015–1033.

91. Katzman R., L. Zhao, T.H. Jordan (1998), High-resolution, two-dimensional vertical tomography of the central Pacific mantle using *ScS* reverberations and frequency-dependent travel times. *J. Geophys. Res.*, 103 (B8), 17933–17971.

92. Kawakatsu, H. (1985), Double seismic zone in Tonga. *Nature*, 316, 53–55.

93. Kayal, J. R. (2010), Himalayan tectonic model and the great earthquakes: An appraisal, Geomat. *Nat. Haz. Risk 1*, *no. 1*, 51–67.

94. Kennett, B. L. N., M. S. Sambridge and P. R. Williamson (1988), Subspace methods for large scale inverse problems involving multiple parameter classes. *Geophys. J. Int.,* 94, 237–247.

95. Kern, H. (1982), Elastic-wave velocity in crustal and mantle rocks at high pressure and temperature: the role of the high-low quartz transition and of dehydration reactions. *Phys. Earth Planet. Inter.,* 29(1), 12–23.

96. Khattri, K. N. (1987), Great earthquakes, seismicity gaps and potential for earthquake disaster along the Himalaya plate boundary. *Tectonophysics,* 138(1), 79–92.

97. Khattri, K. N., R. Chandra, V. K. Gaur, I. Sarkar, and S. Kumar (1989), New seismological result on tectonics of Garhawal Himalaya. *Proc. Indian Acad. Sci. (Earth Planet. Sci.)* 98(1), 91–109.

98. Kissling, E. (1988), Geotomography with local earthquake data. *Rev. Geophys*. 26, 659–698.

99. Kissling, E. (1995), Program VELEST User's Guide – Short Introduction (Second Draft Version), Institute of Geophysics, ETH Zurich, Switzerland, pp. 26.

100. Kissling, E., W. L. Ellsworth, D. Eberhart, and U. Kradolfer (1994), Initial reference models in local earthquake tomography. *J. Geophys. Res.* 99(B10), 19635–19646.

101. Koch, M. (1983a), Die Bestimmung lateraler Geschwindigkeitsinhomogenit¨aten aus der linearen und nichtlinearen Inversion tele- und lokalseismischer Laufzeiten - Anwendung auf die seismische Zone Vrancea, Rum¨anien. PhD thesis, Geophysikalisches Institut, Uni Karlsruhe.

102. Koch, M. (1983b), Die Bestimmung lateraler Geschwindigkeitsinhomogenit @ : aten aus der linearen und nichtlinearen Inversion tele- und lokalseismischer Laufzeiten - Anwendung auf die seismische Zone Vrancea, Rumanien. *Geophysikalisches Institut, Uni Karlsruhe*, University of Karlsruhe.

103. Koch, M. (1985a), A theoretical and numerical study on the determination of the 3D structure of the lithosphere by linear and nonlinear inversion of teleseismic travel times. *J. Geophys. Res.*, 56, 160–173.

104. Koch, M. and J. Kalata (1992), Simultaneous Determination of Hypocenter Location and Crustal Structure in the Virginia Seismic Region. *J. Geophys. Res.*, 97(B12), 17481–17502.

105. Kosminskaya, I. P. (1969), The Earth's Crust and Upper Mantle (P. J. Hart, ed.), *American Geophysical Union.,* Washington, D. C.,

106. Koulakov, I. (2009a), Out-of-network events can be of great importance of improving results of local earthquake tomography. *Bull. seism. Soc. Am.,* 99(4), 2556–2563.

107. Koulakov, I. et al. (2007), velocity structure of the crust and the upper mantle beneath central Java from local tomography inversion. *J. Geophys. Res.,* 112(B8), 1–19.

108. Koulakov, I., (2009b), LOTOS code for local earthquake tomographic inversion: benchmarks for testing tomographic algorithms, *Bull. seismol. Soc. Am.,* 99(1), 194–214.

109. Koulakov, I., G. Maksotova, S. Mukhopadhyay, J. Raoof, J. R. Kayal, a. Jakovlev, and a. Vasilevsky (2014), Variations of the crustal thickness in Nepal Himalayas based on tomographic inversion of regional earthquake data. *Solid Earth Discuss*., 6, 207-216.

110. Koulakov, I., T. Yudistira, B. G. Luehr and Wandono (2009), P, S velocity and $V_P/V_S$ ratio beneath the Toba caldera complex (Northern Sumatra) from local earthquake tomography. *Geophys. J. Int.,* 177(3), 1121–1139.

111. Kumar, A., A. D. Pandey, M. L. Sharma, S. C. Gupta, A. K. Verma, and B. K. Gupta (1994), Processing and preliminary interpretation of digital data obtained from digital seismic array in Garhwal Himalaya. *Proc. 10th Symposium on Earthquake Engineering,* University of Roorkee, Roorkee, India, 16–18 November 1994, Vol. 1, 141–152.

112. Kumar, G., and N. C. Agarwal (1975), Geology of the Srinagar-Nandprayag area (Alaknanda Valley), Chamoli, Garhwal and Tehri Garhwal districts, Kumaun Himalaya, Uttar Pradesh. *Himalayan Geol.* 5, 29–59.

113. Kumar, N., A. Aoudia, D. Hazarika, D. K. Yadav (2014), High resolution maping of the crustal architecture by ambient noise tomography in the North Western Himalaya, AGU Fall Meeting Abstracts, abstract #S22B-07.

114. Kumar, N., B. R. Arora, S. Mukhopadhyay and D. K. Yadav (2013), Seismogenesis of clustered seismicity beneath the Kangra-Chamba sector of northwest Himalaya: constraints from 3-D local earthquake tomography. *J. Asian Earth Sci.,* 62, 638–646.

115. Kumar, N., J. Sharma, B. R. Arora, and S. Mukhopadhyay (2009), Seismotectonic model of the Kangra–Chamba sector of NWHimalaya: Constraints from joint hypocenter determination and focal mechanism. *Bull. Seismol. Soc. Am.* 99, 95–109.

116. Kumar, S. and T. Sato (2003), Compressional and Shear wave velocities in the crust beneath the Garhwal Himalaya North India. *J. Him. Geol.* 24, 77–85.

117. Kumar, S., R. Chander and K. N. Khattri (1987). Compressional wave speed in the second crustal layer in Garhwal Himalaya. *J. Assoc. Explor. Geophys*. 8, 219–225.

118. Lahr, J. C. (1980), HYPOELLIPSE/MULTICS: A computer program for determining local earthquake hypocentral parameters, magnitude, and first motion pattern, U.S. *Geol. Surv. Open-file rep.*, 80-59.

119. Landisman M., S. Muller, and B. J. Mitchell (1971) Reviw of evidence for velocity invesrsions in the continental crust, in the structure and physical properties of the Earth's crust, Geophy. Monogr. Ser., vol. 14, edited by J. G. Heacock, pp 11-34, AGU, Washington, D.C.

120. Langan, R. T., I. Lerche, and R. T. Cutler (1985), Tracing of rays through heterogeneous media: An accurate and efficient procedure. *Geophysics*, 50, 1456–1465.

121. Langer, H., G. Nunnari and L. Occhipinti (1996), Estimation of seismic waveform governing parameters with neural networks. *J. Geophys. Res.,* 101, 20109–20118.

122. Lee, W. H. K. and V. Pereyra (1993), Mathematical introduction to seismic tomography, in Seismic tomography: theory and practice, edited by H. M. Iyer & K. Hirahara, *Chapman & Hall, London,* 9–22.

123. Lee, W. H. K., R. E. Bennett and L. Meagher (1972), A method for estimating magnitude of local earthquakes from signal duration. Open file report, USGS.

124. Lees, J. M . and R. S. Crosson (1989), Tomographic imaging for three dimensional velocity structure of Mount St. Helens using earthquake data. *J. Geophys. Res., 94(B5),* 5716-5728.

125. Lei, J. and D. Zhao (2006), Global seismic tomography: on the effect of various mantle and core phases. *Phys. Earth Planet. Inter.,* 154(1), 44-69.

126. Lemonnier , C., G. Marquis, F. Perrier, J. P. Avouac, G. Chitrakar, B. Kafle , S. Sapkota, U. Gautam, D. Tiwari and M. Bano (1999), Electrical structure of the

Himalaya of central Nepal: high conductivity around the mid crustal ramp along the MHT. *Geophys. Res. Lett.*, 26, 3261-3264.

127. Lèvèque, J. J., L. Rivern and G. Wittlinger (1993), On the use of the checker-board test to assess the resolution of tomographic inversions. *Geophys. J. Int.*, 115, 313–318.
128. Lienert, B. R. E., E. Berg, and L. N. Frazer (1986), HYPOCENTER: An earthquake location method using centered, scaled, and adaptively least squares. *Bull. Seismol. Soc. Am.* 76, 771–783.
129. Luca, G. D., L. Filippi, D. Caccamo, G. Neri and R. Scarpa (1997), Crustal structure and seismicity of southern Tyrrhenian basin. *Phys. Earth Planet. Inter.,* 103, 117–133.
130. Lutter, W. J. and R. L. Nowack (1990), Inversion for crustal structure using reflections from the PASSCAL Ouachita experiment. *J. Geophys. Res.,* 95, 4633–4646.
131. Lyon-Caen, H. and P. Molnar (1983), Constraints on the structure of the Himalaya from an analysis of gravity anomalies and a flexure model of the lithosphere. *J. Geophys. Res.,* 88(B10), 8171-8191.
132. Mahesh, P., S. Gupta, S. S. Rai, and P. R. Sharma (2012), Fluid driven earthquakes in the Chamoli Region, Garhwal Himalaya: Evidence from local earthquake tomography. *Geophys. J. Int.,* 191(3), 1295–1304.
133. Mahesh, P., S. S. Rai, K. Sivaram, A. Paul, S. Gupta, R. Sarma, and V. K. Gaur (2013), One-dimensional reference velocity model and precise locations of earthquake hypocenters in the Kumaon-Garhwal Himalaya. *Bull. Seismol. Soc. Am.,* 103(1), 328–339.
134. Malik, S. (2009), 3D Crustal structure modeling of Garhwal Himalayas, Ph.D. Thesis, Indian Institute of Technology, Roorkee, India, 136 pp.
135. Manglik, A., G. Pavan Kumar and S. Thiagarajan (2013), Transverse Tectonics in the Sikkim Himalaya: A magnetotelluric study. *Tectonophysics*, 589, 142-150.
136. Maurer, V., E. Kissling, S. Husen, and R. Quintero (2010), Detection of systematic errors in travel-time data using a minimum 1 D model: Application to Costa Rica seismic tomography. *Bull. Seismol. Soc. Am.* 100, 629–639.

137. McCaughey, M. and S. C. Singh, (1997), Simultaneous velocity and interface tomography of normal incidence and wide-aperture seismic traveltime data. *Geophys. J. Int.,* 131, 87–99.

138. Michelini, A. and T. V. Mcevilly (1991), Seismological studies at Parkfield. I. Simultaneous inversion for velocity structure and hypocenters using cubic B-splines parameterization. *Bull. Seismol. Soc. Am.,* 81(2), 524–552.

139. Midzi, V., I. Saunders, M.B.C, Brant, and T., Molea (2010), 1-D velocity model for use by SANSN in earthquake locations. *Seismol. Res. Lett.,* 81,460-466.

140. Mishra, D. C., and G. Laxman (1997), Some major tectonics elements of western Ganga basin based on Bouguer anomaly map. *Curr. Sci.,* 73(5), 436-440.

141. Mishra, D. C., and R. P. Rajasekhar (2006), Crustal structure at the epicentral zone of the 2005 Kashmir (Muzaffarabad) earthquake and seismotectonic significance of lithospheric flexure. *Curr. Sci.,* 90, 1406-1412.

142. Mishra, O. P. (2014), Intricacies of Himalayan seismotectonics and seismogenesis: Need for integrated Research, *Curr. sci., 106 (2)*, 176 - 187.

143. Molnar, P. (1990), A review of the seismicity and the rates of active underthrusting and deformation at the Himalaya. *J. Himal. Geol.,* 1(2), 131–154.

144. Monsalve, G., A. Sheehan, V. Schulte-Pelkum, S. Rajaure, M. R. Pandey, and F. Wu (2006), Seismicity and one-dimensional velocity structure of the Himalayan collision zone: Earthquakes in the crust and upper mantle. *J. Geophys. Res.* 111, no. B10301.

145. Moser, T. J., (1991), Shortest path calculation of seismic rays, *Geophys.*, 56, 59- 67.

146. Mukhopadhyay, S., and J. R. Kayal (2003), Seismic tomography structure of the 1999 Chamoli earthquake source area in the Garhwal Himalaya. *Bull. Seismol. Soc. Am.,* 93(4), 1854–1861.

147. Mukhopadhyay, S., and J. Sharma (2010), Crustal scale detachment in the Himalayas: A reappraisal. *Geophys. J. Int.* 183, 850–860.

148. Muller. St., and M. Landisman, (1966), Seismic studies of the earth's crust in continents, 1, Evidence for a low-velocity zone in the upper part of the lithosphere. *Geophys. J. Int.*, 10, 525-538.

149. Narula, P. L., R. Shanker, and S. Chopra (2000), Rupture mechanism of Chamoli earthquake on 29 March 1999 and its implication for seismotectonics of Garhwal Himayala. *J. Geol. Soc. India* 55, 493–503.

150. Natterer, F., (1986), The Mathematics of Computerized Tomography. Stuttgart, B. G. Teubner and Chichester etc., John Wiley & Sons. X, 222 S., DM 72,–. ISBN 3-519-02103-X and 0-471-90959-9

151. Neele, F., J. Van Decar and R. Snieder (1993), The use of P wave amplitude data in a joint inversion with travel times for upper mantle velocity structure. *J. Geophys. Res.,* 98, 12,033–12,054.

152. Ni, J. F., A. Ibenbrahim, and S. W. Roecker (1991), Three-dimensional velocity structure and hypocenters of earthquakes beneath the Hazara Arc, Pakistan: Geometry of the underthrusting Indian Plate. *J. Geophys. Res.,* 96(B12), 19865.

153. Ni, J., and M. Barazangi (1984), Seismotectonics of the Himalayan Collision Zone: Geometry of the underthrusting Indian Plate beneath the Himalaya. *J. Geophys. Res.: Solid Earth,* 89 (B2), 1147–1163.

154. Ning, M., W.Yanping, H. Zhengyi and B. Zongdi (1996), An Iterative Algonthrn Using a Neural Network for Nonlinear Traveltime Tomography. *Proceedings of ICSP'96*, pp. 130-136.

155. Nolet, G. (1987), Waveform tomography, in Seismic tomography: With applications in global seismology and exploration geophysics, (ed. G. Nolet), 301–322, D. Reidel, Dordrecht.

156. Nolet, G. (1990), Partitioned waveform inversion and two-dimensional structure under the network of autonomously recording seismographs. *J. Geophys. Res.,* 95, 8499–8512.

157. Nowack, R. L. and C. Li (2009), Methods and Applications of Seismic Tomography, in Handbook of Signal Processing in Acoustics (eds. D. Havelock, S. Kuwano and M. Vorlander), Springer-Verlag, 1633-1653.

158. Ottemöller, L., P. Voss, and J. Havskov (2011), SEISAN Earthquake Analysis Software for Windows, Solaris, Linux and MacOSx (Version 9.1).

159. Paige, C., and M. Saunders (1982), LSQR: An algorithm for sparse linear equations and sparse least squares. *ACM Transactions on Mathematical Software*, 8(1) 43–71.

160. Pandey, M. R., R. P. Tandukar, J. . Avouac, J. Lave, and J. P. Massot (1995), Interseismic Strain Accumulation on the Himalayan Crustal Ramp (Nepal). *Geophys. Res. Lett.,* 22(7), 751–754.

161. Pant, C. C., and A. Paul (2007), Recent trends in seismicity of Uttaranchal. *J. Geol. Soc. India,* 70, 619 626.

162. Papazachos, C. and G. Nolet (1997), P and S deep velocity structure of the Hellenic area obtained by robust nonlinear inversion of travel times. *J. Geophys. Res.,* 102, 8349–8367.

163. Park, J. and V. Levin (2000), Functions from Multiple-Taper Spectral Correlation Estimates. *Bull. Seismol. Soc. Am*., 90, 6, 1507–1520.

164. Patro, P. K. and T. Harinarayana (2009), Deep geoelectric structure of the Sikkim Himalayas (NE India) using magnetotelluric studies. *Phys. Earth Planet. Int.,* 173, 171-176.

165. Pavlis, G. L., J. R. Booker (1980), The mixed discrete continuous inverse problem:application to the simultaneous determination of earthquake hypocenters and velocity structure. *J. Geophys. Res.,* 85 (B9), 4801-4810.

166. Perkins, W. E., and R. A. Phinney (1971), A reflection, study in the wind river uplift Wyoming. *Am. Geophys. Uni., Geophys. Mono.* 14, 14-50.

167. Phillips, W. S., and M. C. Fehler (1991), Traveltime tomography: A comparison of popular methods. *Geophys.*, 56(10), 1639–1649.

168. Phinney, R. A., (1969), Structure of the earth's crust from spectral behavior of Long-period body wave. *J. Geophy. Res.* 69, 2997-3017.

169. Pollitz, F. F. (2007), Finite-frequency traveltime tomography of San Francisco Bay region crustal velocity structure. *Geophys. J. Int.*, 171(2), 630–656.

170. Press, F., and S. Biehler, (1964), Inference on crustal velocities and densities from P-wave delays and gravity anomalies. *J. Geophys. Res.,* 69, 2979-2995.

171. Qureshy, M. N., and R. K. Midha (1986), Deep crustal signature in India and contignous regions from satellite and ground geophysical data, In: Reflection seismology, The continental crust, Eds. M. Barazangi and L. Brown, *Geodynamic series,* 14, AGH pp. 77-94.

172. Qureshy, M. N., and S. Kumar (1992), Isostasy and neotectonic of north west Himalaya and foredeep, *Mem., Geol. Soc. India*, 23, 201-222.

173. Radon, J, 1917: On the determination of functions from their integrals along certain manifolds (Translation), Ber, Verbhandl. Sachs. Akad. Wiss, Leipzig, Math-Phys, 69: 262-277.

174. Rai, S. S., K. Priestley, V. K. Gaur, S. Mitra, M. P. Singh, and M. Searle (2006), Configuration of the Indian Moho beneath the NW Himalaya and Ladakh. *Geophys. Res. Lett.,* 33(15), L15308.

175. Rajendran, K., C. P. Rajendran, S. K. Jain, C. V. R. Murty, and J. N. Arlekar (2000), The Chamoli earthquake, Garhwal Himalaya: Field observations and implications for seismic hazard. *Curr. Sci.,* 78(1), 45–51.

176. Rawat, G., B. R. Arora and P. K. Gupta (2014), Electrical resistivity cross-section across the Garhwal Himalaya: Proxy to fluid-seismicity linkage, *Tectonophysics*, 637, 68-79.

177. Rawlinson, N. (2000), Inversion of Seismic Data for Layered Crustal Structure, Ph.D. thesis, Monash University, Australia.

178. Rawlinson, N. and M. Sambridge (2003), Seismic Traveltime Tomography of the Crust and Lithosphere. *Adv. in Geophys.*, 46(C), 81–198.

179. Reagan R.L. (1978), A Finite-Difference Study of Subterranean Cavity Detection and Seismic Tomography. PhD Thesis, University of Missouri-Rolla. pp. 229.

180. Ritsema, J., A. A, Nyblade, T. J. Owens, C. A. Langston and J. C. VanDecar (1998), Upper mantle seismic velocity structure beneath Tanzania, east Africa: Implications for the stability of cratonic lithosphere. *J. Geophys. Res.,* 103, 21, 201–21, 213.

181. Rodi W. L., Jordan T. H., Masso J. F. and J. M. Savino (1981), Determination of the three-dimensional structure of eastern Washington from the joint inversion of gravity and Earthquake data. *Report: Systems Sciences and Software SSS-R-80-4516*, La Jolla, CA.

182. Roecker S, C. Thurber, K Roberts and L. Powell (2006), Refining the image of the San Andreas Fault near Parkfield, California using a finite difference travel time computation technique. *Tectonophysics,* 424.

183. Roecker S.W. (1977), Seismicity and tectonics of the Pamir-Hindu Kush region of central Asia, PhD Thesis, Mass. Inst. Tech. Cambridge, Massachusetts, US.

184. Roth G., (1993), Application des reseaux de neurones aux problemes inverres sismiqee.s. PhD thesis lnstitut de Physique du Globe de Paris, Univrrsite de Paris 7, Paris.

185. Roth, G. and A. Tarantola (1994), Neural networks and inversion of seismic data. *Journal of Geophgsicnl Research, American Geophysical Union, Washington. USA*, 99(B4), 6753-6768.

186. Sambridge, M. S. (1990), Non-linear arrival time inversion: Constraining velocity anomalies by seeking smooth models in 3-D. *Geophys. J. Int.*, 102, 653–677.

187. Sambridge, M. S. and G. Drijkoningen (1992), Genetic algorithms in seismic waveform inversion. *Geophys. J. Int.,* 109, 323–342.

188. Santos, R. J. and A. de Pierro (2006), The effect of the nonlinearity on GCV applied to conjugate gradients in computerized tomography. *Computational and Applied Mathematics,* 25, 111–128.

189. Sarkar, I., R. Jain, and K. N. Khattri (2001), Mapping of shallow three dimensional variations of P-wave velocity in Garhwal Himalaya. *J. Asian Earth Sci.*, 19(1-2), 155–163,

190. Scales, J. (1987), Tomographic inversion via the conjugate gradient method. *Geophysics,* 52(2), 179–185.

191. Seber, D., M. Barazangi, B. A. Tadili, M. Ramdani, A. Ibenberahim and D. B. Sari (1991), Three-dimensional upper mantle structure beneath the interplate Atlas and interplate Rifmountains of Morocco. *J. Geophys. Res.,* 101, 3125-3138.

192. Seeber, L., and J. G. Armbruster (1981), Great detachment earthquakes along the Himalayan arc and long term forecasting. Earthquake Prediction—An International Review, Maurice Ewing Series, in AGU, Wiley Online Library, Washington, DC, Vol. 4, pp. 259–277,

193. Seeber, L., and J. R. Armbruster (1981), Some elements of continental subduction along the Himalayan front. *Tectonophysics* 105, 263–278.

194. Seeber, L., J. Armbruster, and R. Quittmeyer (1981), Seismicity and Continental Subduction in the Himalayan Arc, in Zagros, Hindu Kush, Himalaya: Geodynamic Evolution, H. K. Gupta and F. M. Delany (eds.), Geodynamics Series. *American Geophysical Union, Washington*, D.C., Vol. 3, 215–242.

195. Sibson R. H. (2002), Geology of crustal earthquak sources, In: W. H. K. Lee, H. Kanamori, P.C. Jennings and C. Kisslinger (eds.) *Int. Handbook of Earthquake and Eng. Seismology- Part A*, Academic press, New York, 455-473.

196. Singh, S. K., R. S. Dattatrayam, N. M. Shapiro, P. Mandal, J. F. Pacheco and R. K. Midha (1999). Crustal and upper mantle structure of Peninsular India and source parameters of the 21 May 1997, Jabalpur earthquake (Mw= 5.8): Results from a new regional broadband network, *Bull. Seism. Soc. Am.* **89(6)**, 1631-1641.

197. Sluis, A. Van der, and H. Van der Vorst (1987), Numerical solution of large, sparse linear algebraic systems arising from tomographic problems, in Seismic tomography, pp. 49–83.

198. Spakman W. and G. Nolet (1988), Imaging algorithms: Accuracy and resolution in delay time tomography. In: Vlaar NJ, Nolet G, Wortel M, and Cloetingh S (eds.) Mathematical Geophysics: A Survey of Recent Developments in Seismology and Geodynamics, pp. 155–188.

199. Spencer C., and D. Gubbins (1980), Travel-time inversion for simultaneous earthquake location and velocity structure determination in laterally varying media. *Geophysical Journal of the Royal Astronomical Society* 63: 95–116.

200. Steck, L. K., C. H. Thurber, M. Fehler, W. J. Lutter, P. M. Roberts, W. S. Baldridge, D. G. Stafford and R. Sessions (1998), Crust and upper mantle P wave velocity structure beneath Valles caldera, New Mexico: Results from the Jemez teleseismic tomography experiment. *J. Geophys. Res.*, 103, 24,301–24,320.

201. Tandon, A. N., and R. K. Dube (1973), A study of the Crustal structure beneath the Himalayas from body waves, Pure Appl. Geophys. PAGEOPH, 111, 2207–2215.

202. Tarantola, A. (1987), Inverse problem theory, methods for data fitting and model parameter estimation. *Amsterdam Elsevier,* New York.

203. Tarantola, A. and B. Valette (1982a), Generalized nonlinear inverse problems solved using the least squares criterion. *Rev. Geophys. Space Phys.*, 20:219–232.

204. Tarantola, A. and B. Valette, (1982b), Inverse problems = Quest for information. *J. Geophys. Res.,* 50:159 – 170.

205. Tarantola, A., (1986), A strategy for nonlinear elastic inversion of seismic reflection data. *Geophysics* 51, 1893–1903.

206. Thomson, C. J. and D. Gubbins (1982), Three-dimensional lithospheric modelling at NORSAR: linearity of the method and amplitude variations from the anomalies. *Geophys. J. Royal Astr. Soc.*, 71, 1–36.

207. Thurber C. H. (1992), Hypocenter–velocity structure coupling in local earthquake tomography. Special Issue: Lateral Heterogeneity and Earthquake Location. *Phys.Earth and Planetary Interiors* 75, 55–62.

208. Thurber, C. H. (1983), Earthquake Locations and Three-Dimensional Crustal Structure in the Coyote Lake Area, Central California, *J. Geophys. Res.,* 88(B10), 8226–8236.

209. Thurber, C. H. (1993), Local earthquake tomography: Velocities and $V_P/V_S$ - theory, in Seismic tomography: theory and practice, (eds. H. M. Iyer & K. Hirahara), *Chapman & Hall*, London, 563–583,.

210. Thurber, C. H. and K. Aki (1987), Three-Dimensional Seismic Imaging. *Ann. Rev. Earth Planet. Sci*, 15:115–139.

211. Thurber, C. H., (1981), Earth structure and earthquake locations in the Coyote Lake area, central California. PhD thesis, Dept. of Earth and Planetary Sciences, *Massachusetts Institute of Technology, Cambridge, Massachusetts, US.*

212. Tiwari, V., M. V. Rao, D. Mishra and B. Singh (2006), Crustal structure across Sikkim, NE Himalaya from new gravity and magnetic data. *Earth and Planet. Sci. Lett.,* 247 (1-2), 61- 69.

213. Tromp, J., C.H. Tape, Q. Liu (2005), Seismic tomography, adjoint methods, time reversal and banana-doughnut kernels. *Geophysical Journal International* 160, 195–216.

214. Um, J. and C. Thurber (1987), A fast algorithm for two-point seismic ray tracing. *Bull. Seism. Soc. Am.,* 77, 972–986.

215. Ustaszewski, K., Y. M. Wu, J. Suppe, H. H. Huang, C. H. Chang, and S. Carena (2012), Crust–mantle boundaries in the Taiwan–Luzon arc-continent collision system determined from local earthquake tomography and 1D models: Implications for the mode of subduction polarity reversal, *Tectonophysics 578*, 31-49.

216. Valdiya, K. S. (1980), Geology of Kumaun Lesser Himalaya, Interim Record: Dehradun. *Wadia Institute of Himalayan Geology, Dehradun*, India, pp. 291.

217. Van der Sluis A. and H. van der Vorst (1990), SIRT- and CG-type methods for the iterative solution of sparse linear least-squares problems. *Linear Algebra and its Applications*, **130** (1990), 257–303.

218. VanDecar, J. C., D. E. James and M. Assumpcão (1995), Seismic evidence for a fossil mantle plume beneath South America and implications for plate driving forces. *Nature,* 378, 25–31.

219. VanDecar, J.C. and R.S. Crosson (1990), Determination of teleseismic relative phase arrival times using multi-channel cross-correlation and least-squares. *Bull. seism. Soc. Am.,* 80, 150–169.

220. Vasco D.W., L. R. Johnson and J. Pulliam (1995), Lateral variations in mantle velocity structure and discontinuities determined from P, PP, S, SS and SS-SdS travel time residuals. *J. of Geophysical Research* 100, 24037–24059.

221. Verma, G.S. (1974) Structure of the foothills of the Himalaya. *Pure & Appl. Geophys*., 112, 18-26.

222. Vidale, J. E. (1990), Finite-difference calculations of traveltimes in three dimensions. *Geophysics*, 55, 521–526.

223. Walck, M. C., (1988), Three-dimensional Vp/Vs variations for the Coso region, California, *J. Geophys. Res.*, 93, 2047–2052.

224. Walck, M. C., and R. W., Clayton, (1987), P wave velocity variations in the Coso region,California, derived from local earthquake travel times, *J. Geophys. Res.*, 92, 393–405.

225. Wang, B., L.W. Braile (1996), Simultaneous inversion of reflection and refraction seismic data and application to field data from the northern Rio Grande rift. *Geophys. J. Int.,* 125 (2) 443–458.

226. Wang, Y., and R. G. Pratt, (1997), Sensitivities of seismic traveltimes and amplitudes in reflection tomography, *Geophys. J. Int.*, 131, 618–642.

227. Wang, Z., J. Tromp, and G. Ekstrom, (1998). Global and regional surface-wave inversions: A spherical-spline parameterization, *Geophys. Res. Lett.*, 25, 207–210.

228. Wason, H. R. and M. L. Sharma (2000), Source parameters study of local earthquakes in the Garhwal Himalaya Region based on the digital broadband data. *Proc. 12th World conference on earthquake Engineering.* Wesson, R. L., (1971), Travel time

inversion for laterally inhomogeneous crustal velocity models, BUll. Seismol. Soc. Am., 61, 729-746.

229. Weiland, C. M., L. K. Steck, P. B. Dawson, and V. A. Korneev (1995), Nonlinear teleseismic tomography at Long Valley caldera, using three-dimensional minimum travel time ray tracing, *J. Geophys. Res.*, 100, 20379–20390.

230. White, D. J., (1989), Two-dimensional seismic refraction tomography, *Geophys. J.*, 97, 223–245.

231. Wiechert, E. (1910), Bestimmung des Weges von Erdbebenwellen. I., *Theoretische. Phys. Z.*, 11, 294–304.

232. Wiggins, S. M., L. M.Dorman, , B. D. Cornuelle, and J. A. Hildebrand (1996), Hess deep rift valley structure from seismic tomography, *J. Geophys. Res.*, 101, 22,335–22,353.

233. Williamson, P. R. (1990), Tomographic inversion in reflection seismology. *Geophys. J. Int.,* 100, 255–274.

234. Zelt, C. A. and P. J. Barton (1998), Three-dimensional seismic refraction tomography: A comparison of two methods applied to data from the Faeroe Basin. *J. Geophys. Res.,* 103, 7187–7210.

235. Zelt, C. A. and R. B. Smith (1992), Seismic traveltime inversion for 2-D crustal velocity structure. *Geophys. J. Int.,* 108, 16–34.

236. Zhang, F. -X., Q.-J. Wu, J.-T. Pan, G.-C. Zhang, and Q.-Q. Feng, (2011), The computation of a finite-frequency travel time sensitive kernel for P-waves in the AK135 earth model. *Applied Geophysics*, 8(2), 158–163.

237. Zhang, H. and C. H. Thurber (2003), Double-Difference Tomography: The Method and Its Application to the Hayward Fault. *California Bulletin of the Seismological Society of America,* 93 (5), 1875–1889.

238. Zhao, D. P., (2001), New advances of seismic tomography and its applications to subduction zones and earthquake fault zones: a review. *Island Arc* 10(1), 68–84.

239. Zhao, D. P., (2015), Multiscale seismic tomography, Earth Sciences and Geography Geophysics and Geodesy, *Springer Geophysics*, pp 304.

240. Zhao, D., (2009), Multiscale seismic tomography and mantle dynamics. *Gondwana Research*, 15 (3-4), 297–323.

241. Zhao, D., A. Hasegawa and H. Kanamori (1994), Deep structure of Japan subduction zone as derived from local, regional, and teleseismic events. *J. Geophys. Res.,* 99(B11), 22313-22329.

242. Zhao, D., A. Hasegawa, and S. Horiuchi (1992), Tomographic imaging of P and S wave velocity structure beneath Northeastern Japan. *J. Geophys. Res.,* 97(B13), 19909–19928.

243. Zhao, D., H. Kanamori and E. Humphreys (1996), Simultaneous inversion of local and teleseismic data for the crust and mantle structure of southern California. *Phys. Earth Planet. Inter.,* 93, 191–214.

244. Zhao, D., Hasegawa, A. and Horiuchi, S. (1992), Tomographic imaging of *P* and *S* wave velocity structure beneath northeastern Japan. *J. Geophys. Res.,* 97(B13), 19909-19928.

# APPENDIX I

Enlarge view of Vp tomograms with distributed seismicity upto each depth level

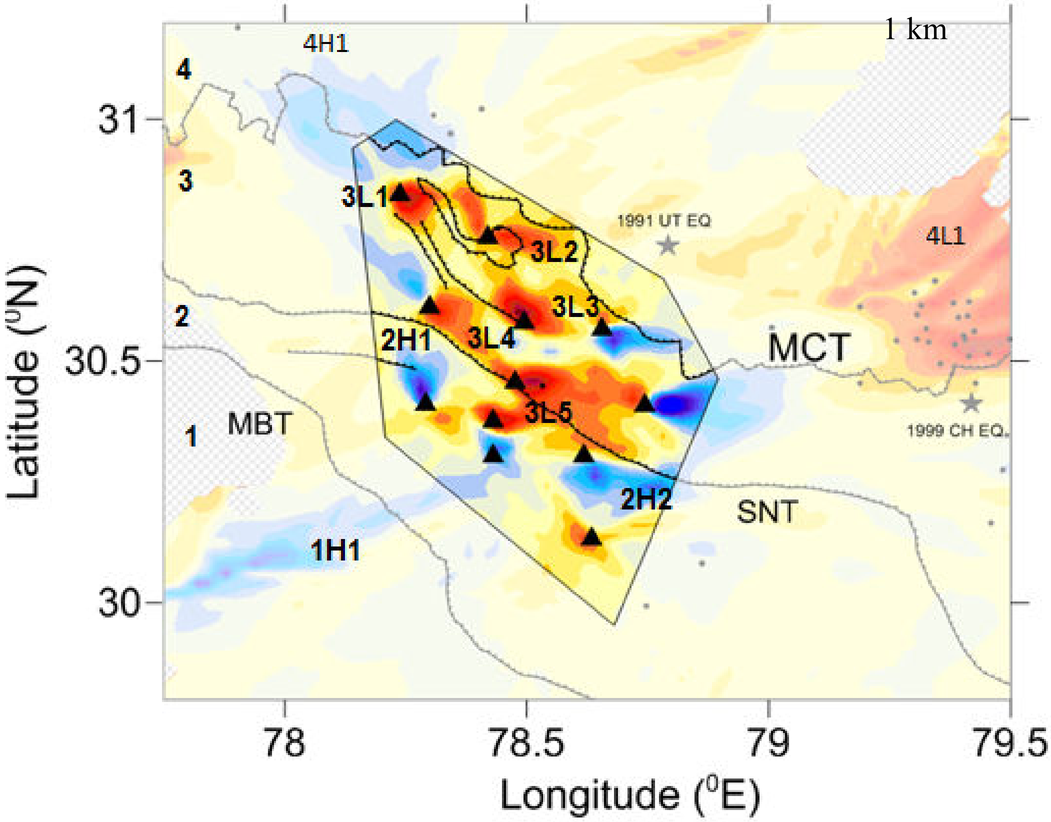

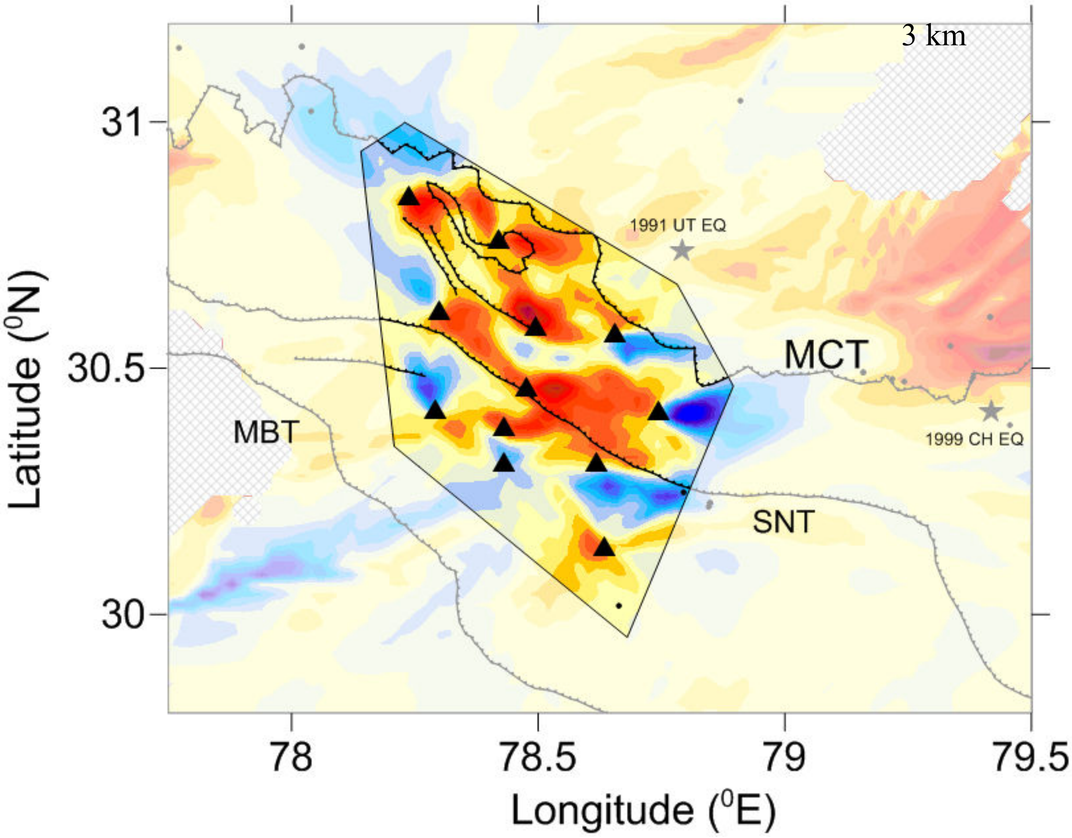

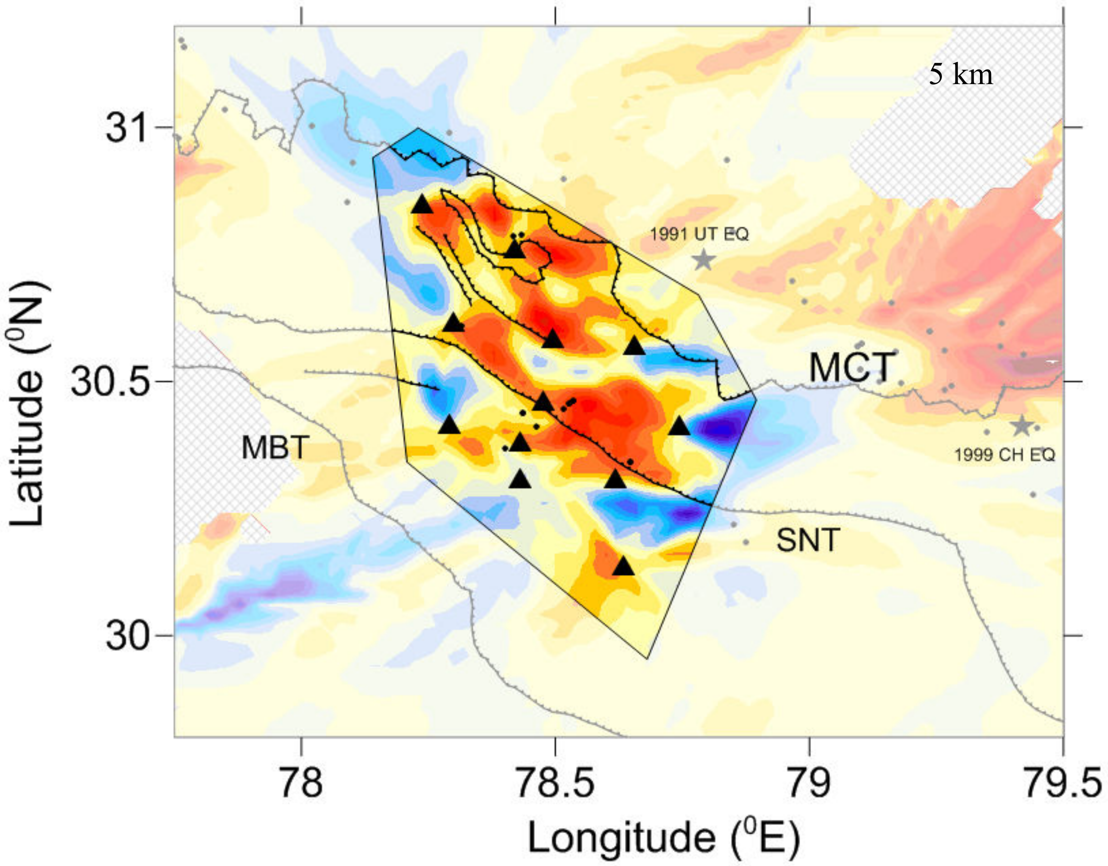
5 km
1991 UT EQ
MCT
1999 CH EQ
MBT
SNT
31
30.5
30
78
78.5
79
79.5
Latitude ($^0$N)
Longitude ($^0$E)

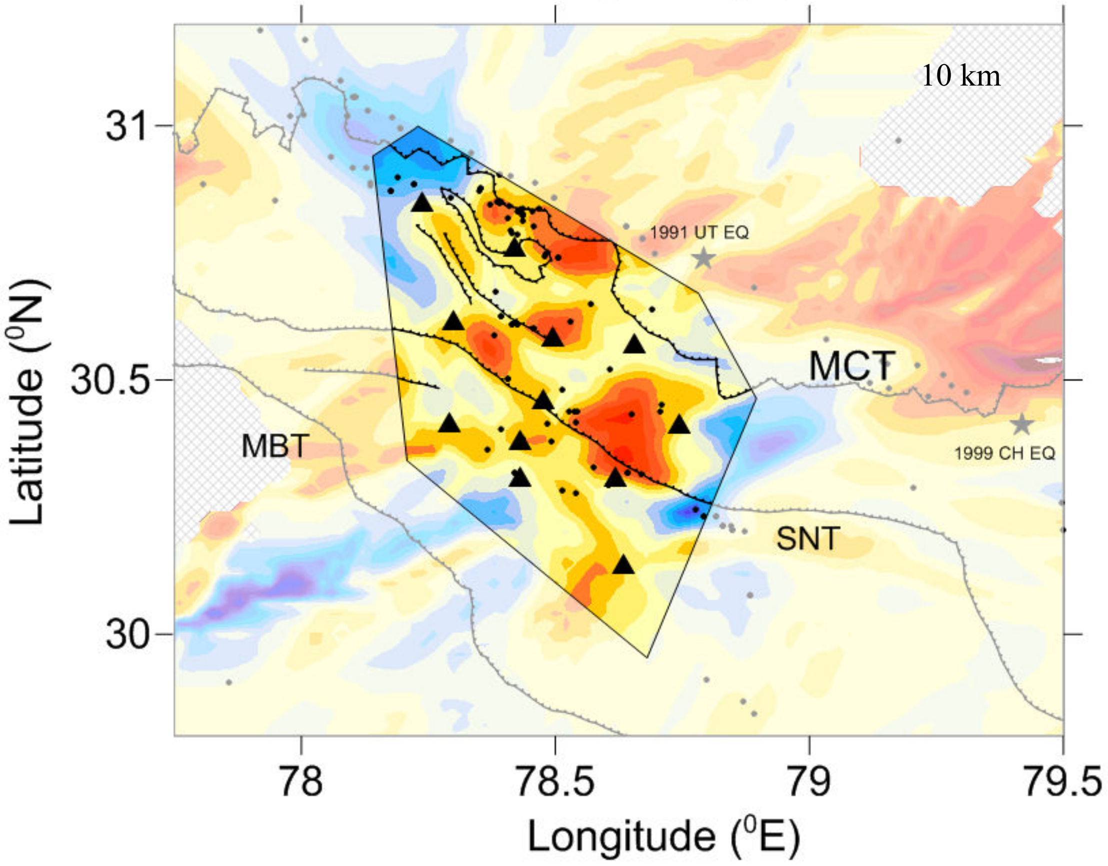
10 km
1991 UT EQ
MCT
1999 CH EQ
MBT
SNT
31
30.5
30
78
78.5
79
79.5
Latitude ($^0$N)
Longitude ($^0$E)

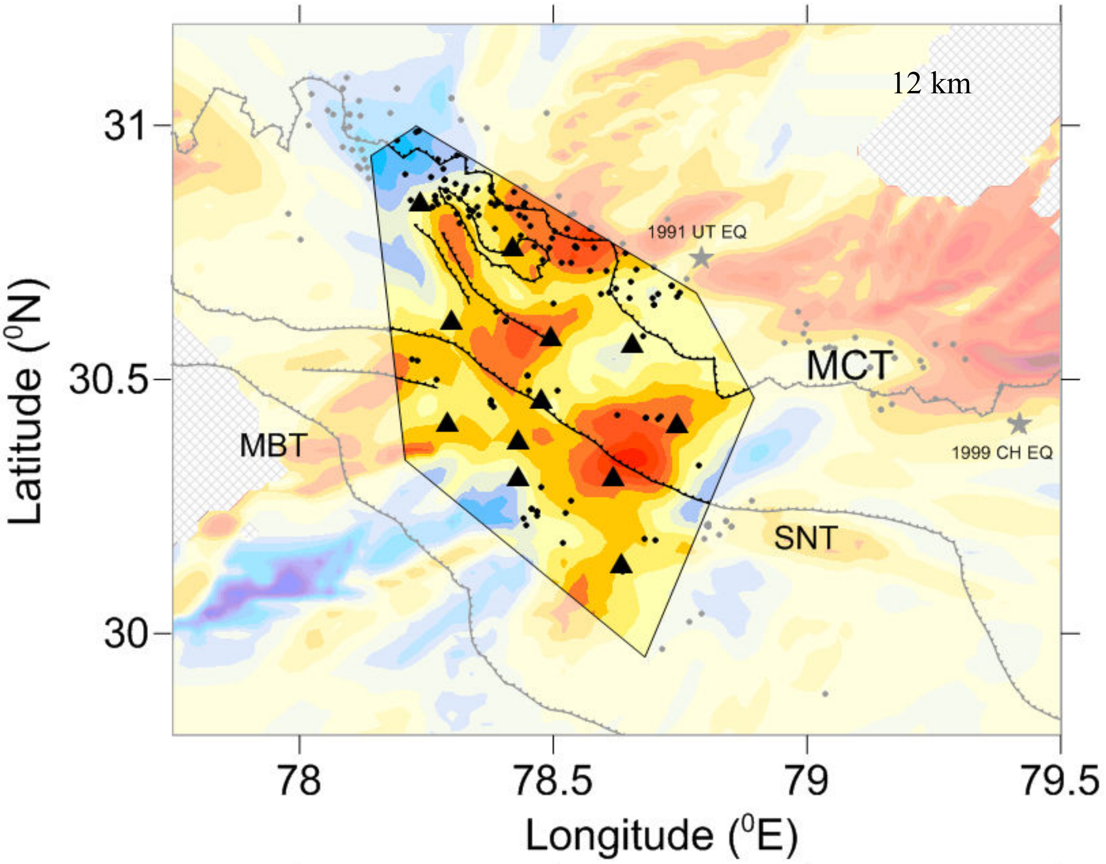
12 km
1991 UT EQ
MCT
MBT
SNT
1999 CH EQ
31
30.5
30
78
78.5
79
79.5
Latitude ($^0$N)
Longitude ($^0$E)

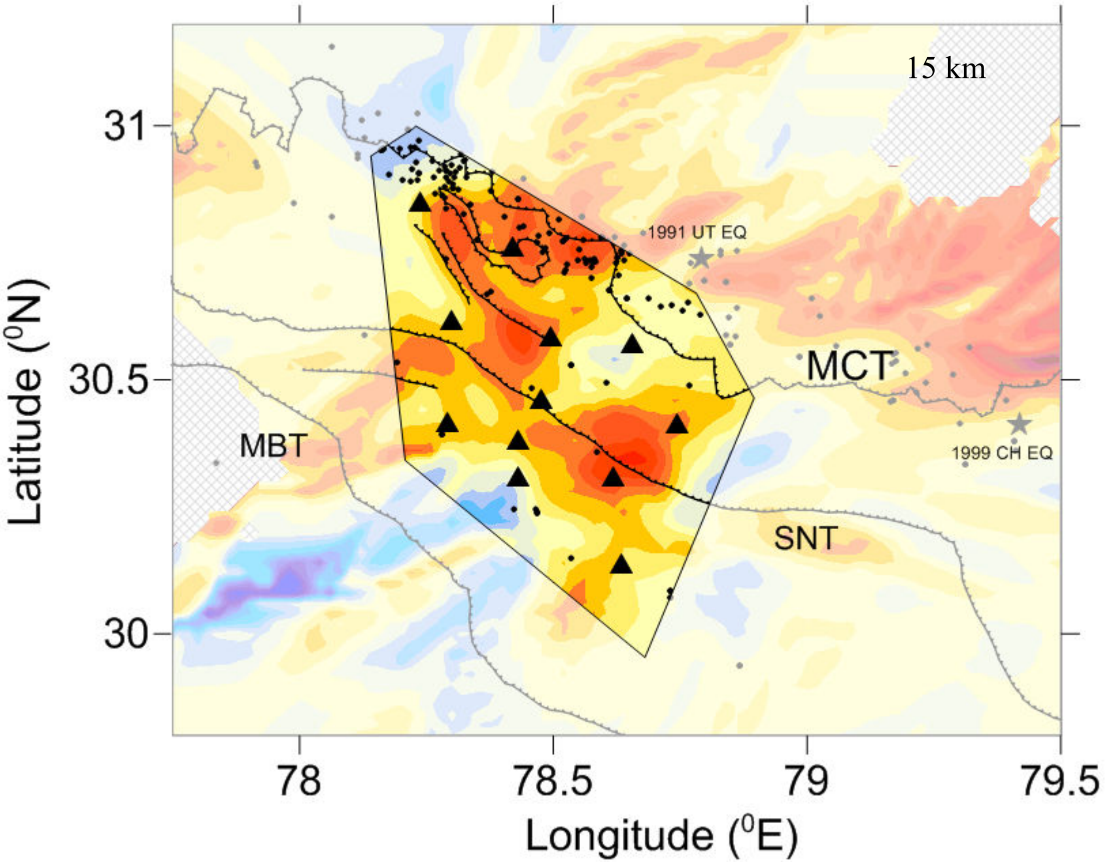
15 km
1991 UT EQ
MCT
MBT
SNT
1999 CH EQ
31
30.5
30
78
78.5
79
79.5
Latitude ($^0$N)
Longitude ($^0$E)

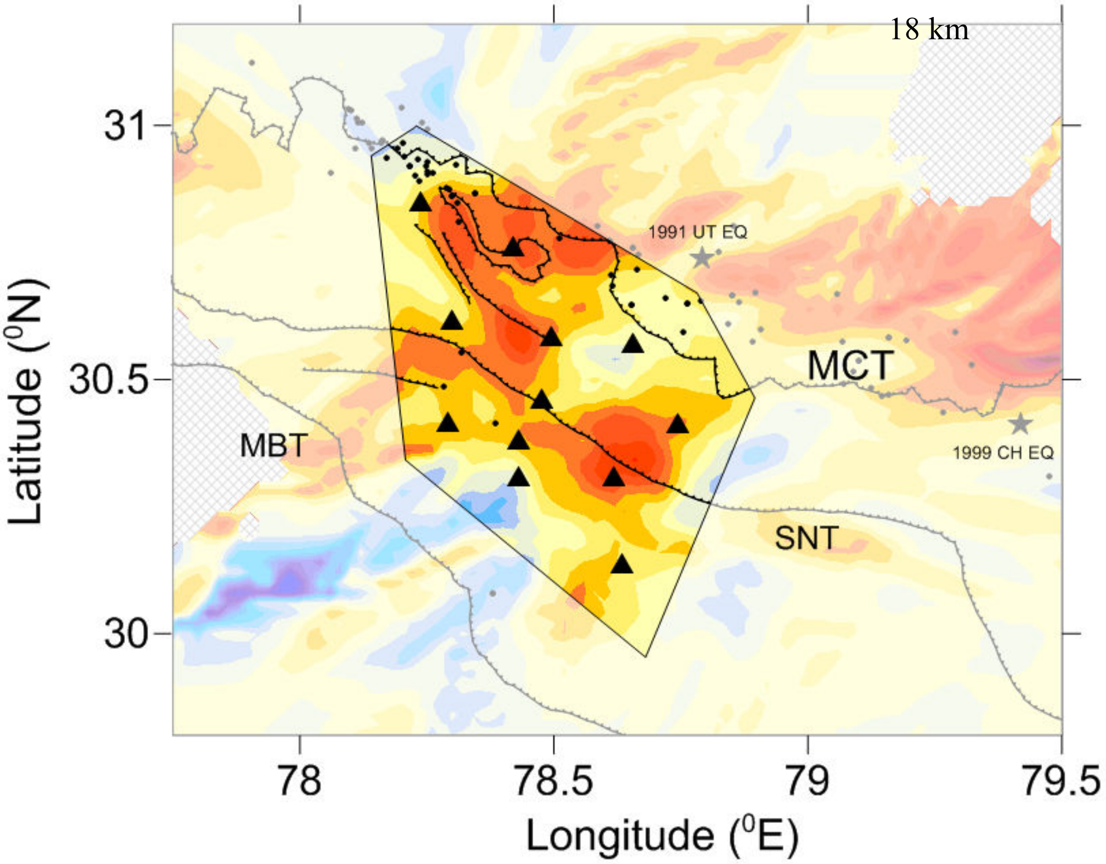

Enlarge view of Vs tomograms with distributed seismicity upto each depth level

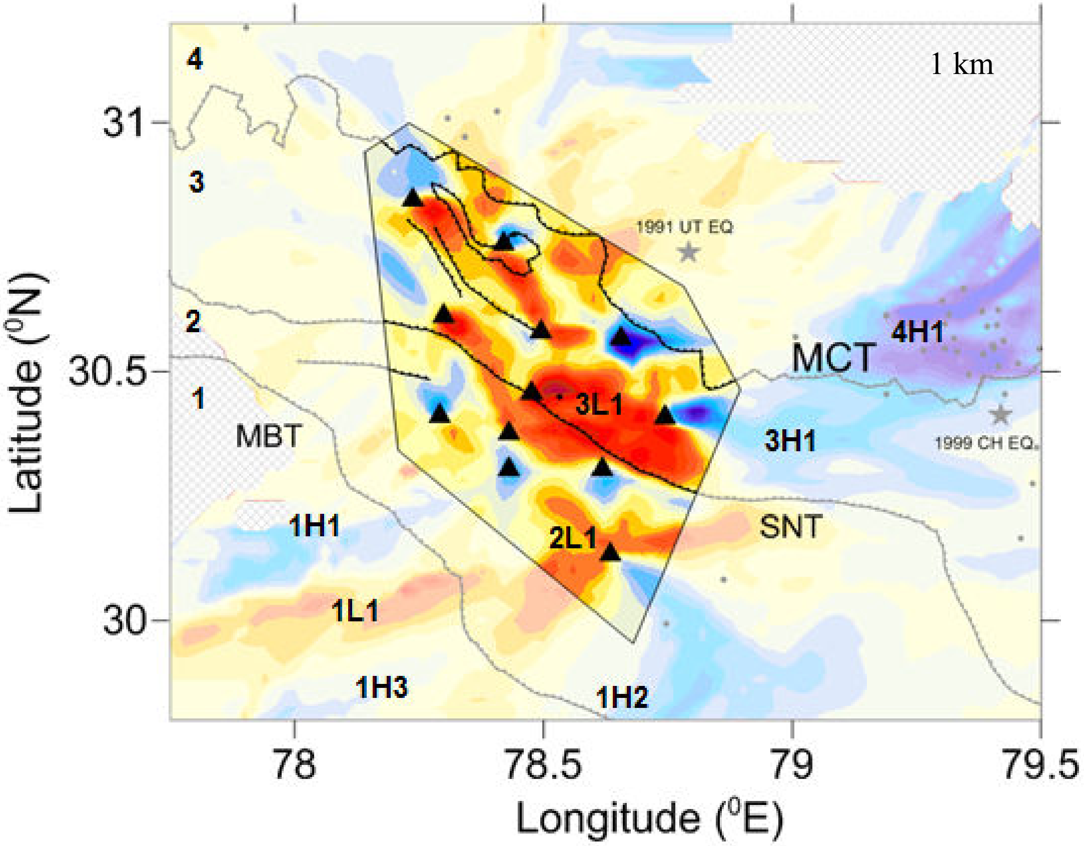

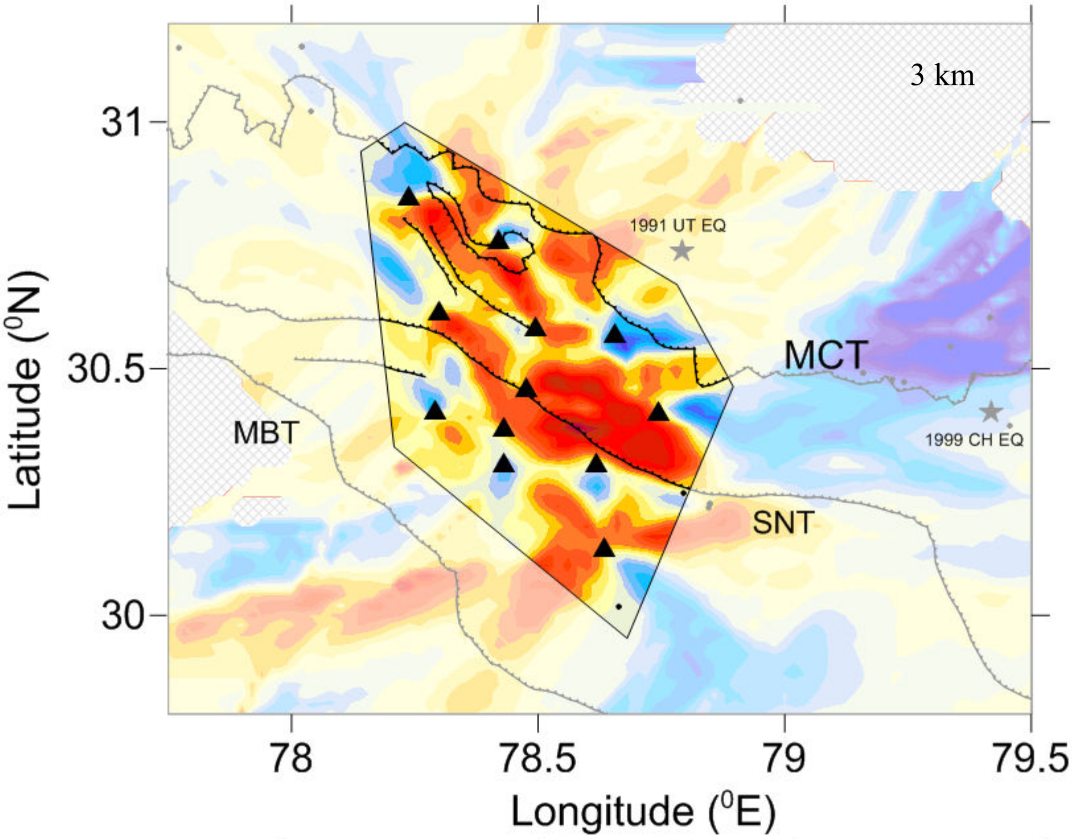
3 km
1991 UT EQ
MCT
1999 CH EQ
MBT
SNT
31
30.5
30
78
78.5
79
79.5
Latitude ($^0$N)
Longitude ($^0$E)

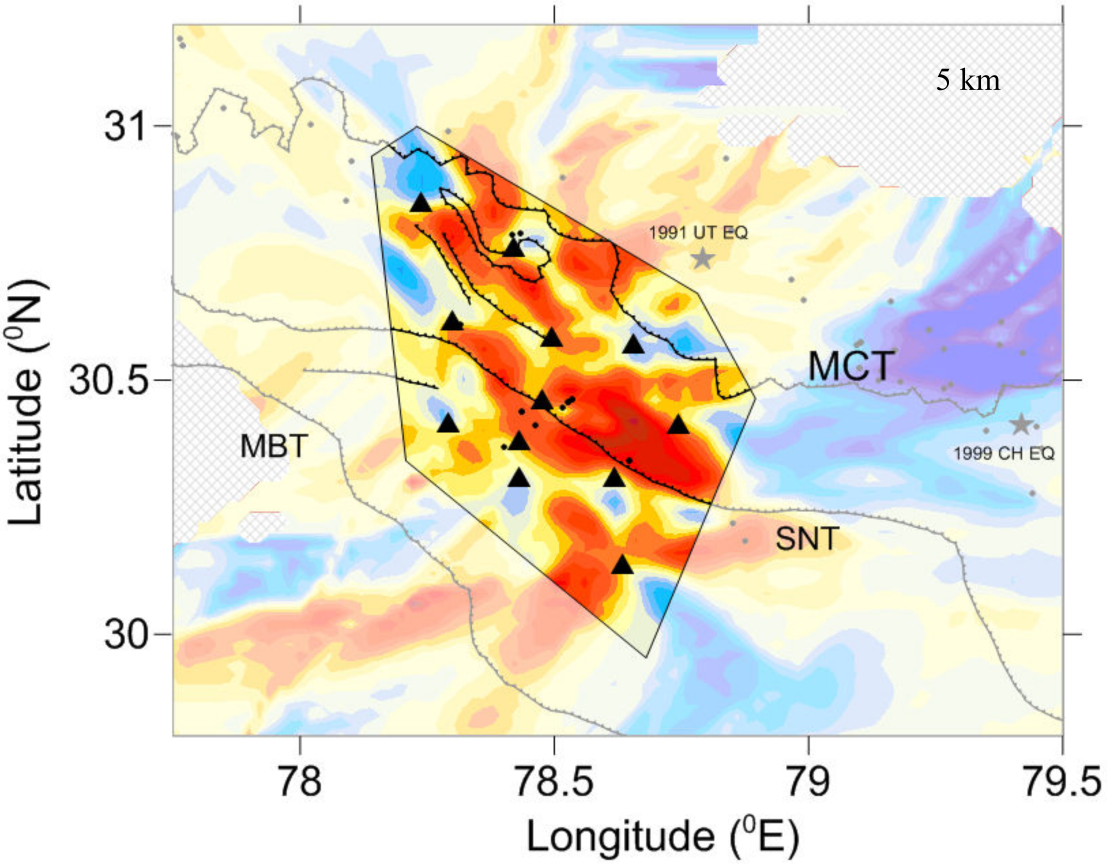
5 km
1991 UT EQ
MCT
1999 CH EQ
MBT
SNT
31
30.5
30
78
78.5
79
79.5
Latitude ($^0$N)
Longitude ($^0$E)

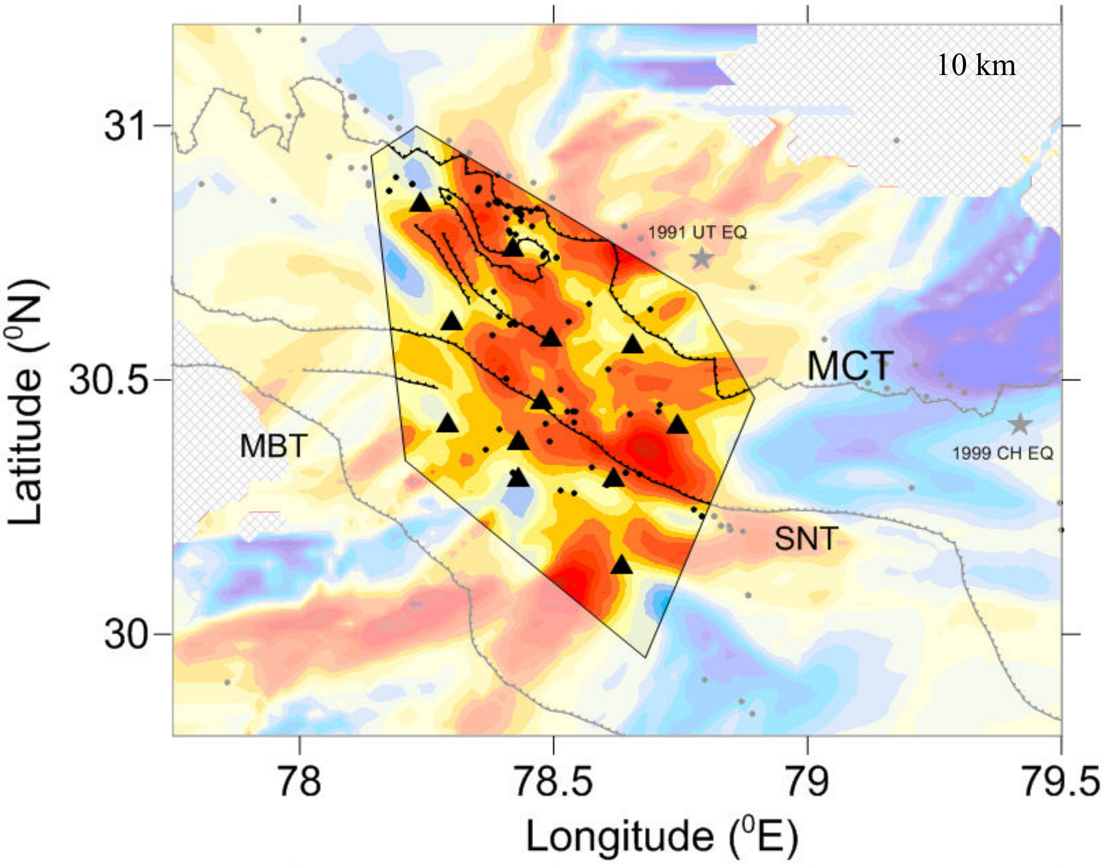
10 km
31
30.5
30
Latitude (⁰N)
78
78.5
79
79.5
Longitude (⁰E)
1991 UT EQ
MCT
1999 CH EQ
MBT
SNT

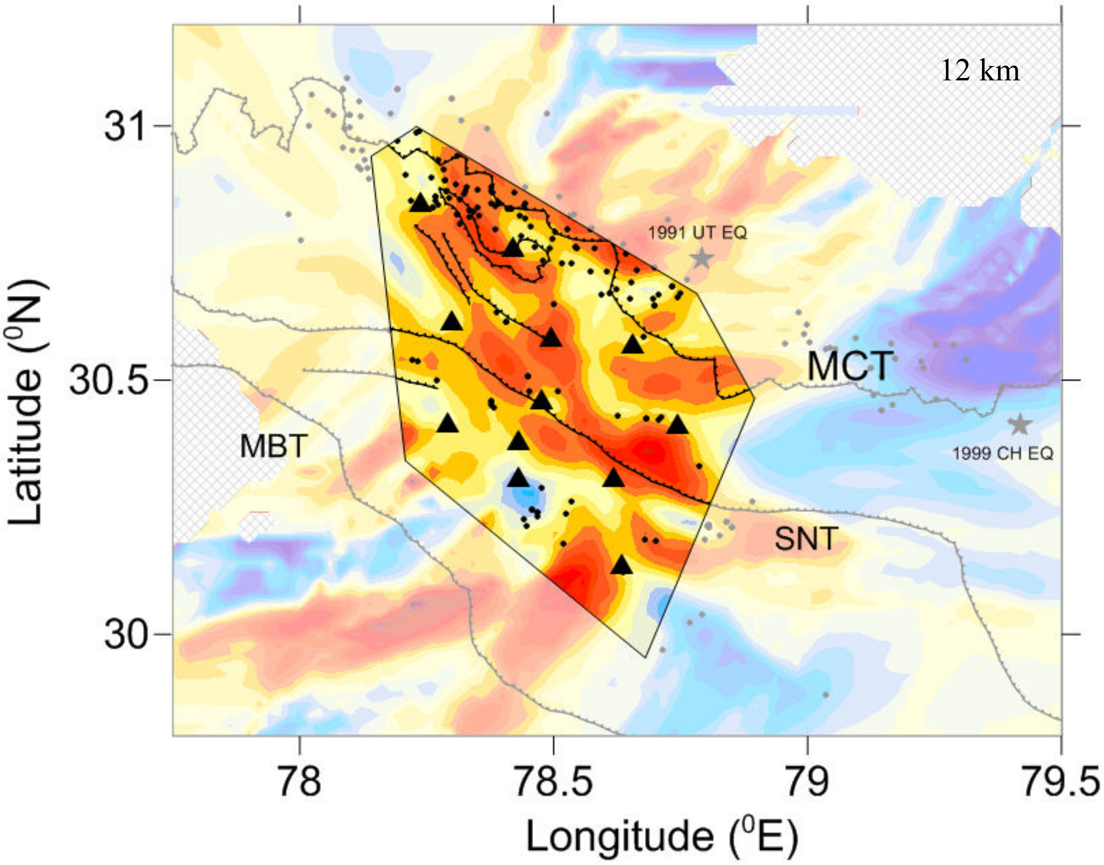
12 km
31
30.5
30
Latitude (⁰N)
78
78.5
79
79.5
Longitude (⁰E)
1991 UT EQ
MCT
1999 CH EQ
MBT
SNT

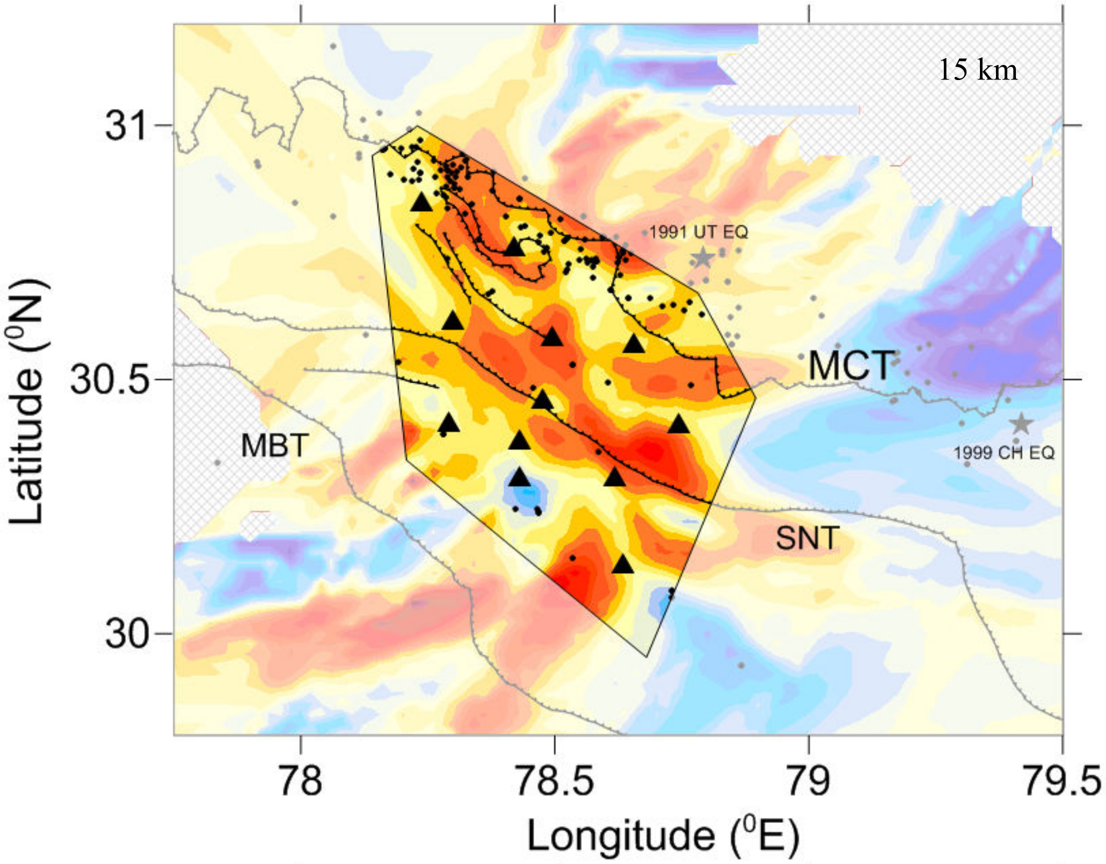
15 km
1991 UT EQ
MCT
MBT
SNT
1999 CH EQ
31
30.5
30
Latitude ($^0$N)
78
78.5
79
79.5
Longitude ($^0$E)

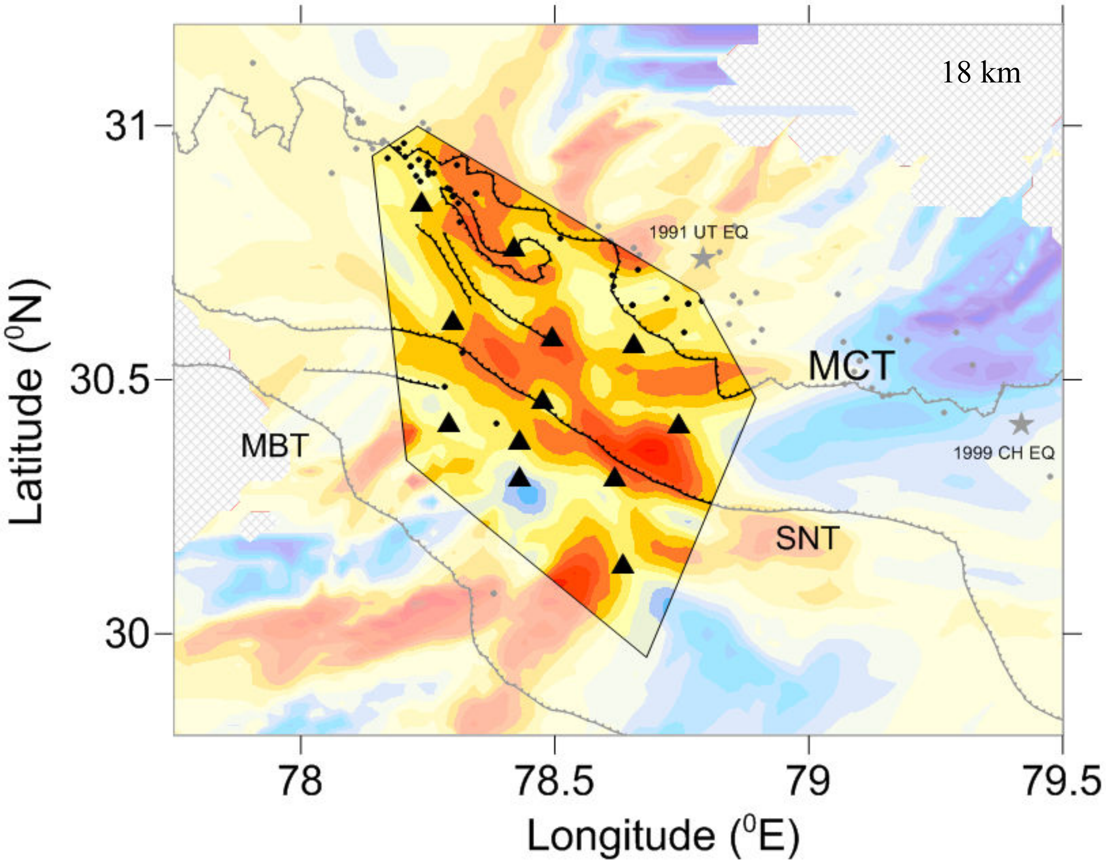
18 km
1991 UT EQ
MCT
MBT
SNT
1999 CH EQ
31
30.5
30
Latitude ($^0$N)
78
78.5
79
79.5
Longitude ($^0$E)

# APPENDIX II

Table: List of events used for the estimation of minimum 1-D model

| Date | Origin time (hhmm:sec) | | Lat (°N) | Lon (°E) | Depth | mag | Gap | Rms |
|---|---|---|---|---|---|---|---|---|
| 80105 | 1651 | 49.37 | 30.609 | 78.454 | 8 | 2.6 | 115 | 0.18 |
| 80119 | 2328 | 19.28 | 30.46067 | 78.66367 | 11.2 | 2.1 | 132 | 0.55 |
| 80208 | 1617 | 30.72 | 30.58667 | 78.44183 | 31.6 | 3.2 | 102 | 2.19 |
| 80209 | 842 | 49.11 | 30.2585 | 78.77217 | 19.3 | 2.7 | 232 | 0.21 |
| 80211 | 1607 | 19.16 | 30.60983 | 78.40217 | 11.5 | 3.1 | 95 | 0.34 |
| 80211 | 2246 | 25.5 | 30.44067 | 78.4335 | 8.1 | 3.4 | 106 | 0.27 |
| 80306 | 1819 | 7.63 | 30.3985 | 78.4935 | 11.2 | 3.2 | 54 | 0.34 |
| 80307 | 2036 | 45.31 | 30.6495 | 78.28183 | 51.3 | 1.3 | 171 | 0.66 |
| 80315 | 825 | 30.94 | 30.261 | 78.63983 | 15.7 | 2.7 | 151 | 0.4 |
| 80401 | 2143 | 20.04 | 30.36283 | 78.42517 | 11.5 | 1.9 | 117 | 0.53 |
| 80416 | 1928 | 9.34 | 30.55267 | 78.6225 | 33 | 0.7 | 113 | 0.2 |
| 80515 | 258 | 3.69 | 30.61617 | 78.39383 | 11.7 | 2.2 | 133 | 0.42 |
| 80524 | 2131 | 40.74 | 30.42817 | 78.682 | 5.3 | 2.7 | 118 | 0.76 |
| 80606 | 2209 | 31.26 | 30.26567 | 78.47983 | 14.3 | 3 | 176 | 0.38 |
| 80618 | 1909 | 44.14 | 30.45017 | 78.2945 | 25.5 | 2.1 | 175 | 0.31 |
| 80706 | 21 | 25.43 | 30.38217 | 78.59333 | 20.6 | 2.6 | 100 | 0.31 |
| 80724 | 938 | 10.51 | 30.45133 | 78.28667 | 23.6 | 1.7 | 178 | 0.49 |
| 80726 | 1043 | 19.92 | 30.61233 | 78.42167 | 10.5 | 1.5 | 103 | 0.38 |
| 80727 | 425 | 47.13 | 30.61033 | 78.41483 | 9.7 | 3.4 | 100 | 0.36 |
| 80727 | 426 | 2.24 | 30.60517 | 78.41817 | 10.1 | 2.2 | 100 | 0.35 |
| 80802 | 2354 | 8 | 30.7775 | 78.28633 | 20.9 | 2.2 | 155 | 0.49 |
| 80809 | 1705 | 11.96 | 30.62683 | 78.40167 | 8.4 | 4.1 | 106 | 0.18 |
| 80825 | 1637 | 23.42 | 30.52867 | 78.53533 | 13.6 | 2.8 | 109 | 0.32 |
| 80911 | 2140 | 11.73 | 30.30967 | 78.62233 | 11.2 | 2.7 | 130 | 0.64 |
| 80917 | 202 | 37.16 | 30.83467 | 78.2405 | 13.3 | 1.9 | 174 | 0.52 |
| 81123 | 722 | 29.16 | 30.47433 | 78.55083 | 7.7 | 3.2 | 69 | 0.34 |
| 81013 | 2121 | 4.08 | 30.48883 | 78.39933 | 12 | 2.7 | 94 | 0.34 |
| 81024 | 54 | 52.45 | 30.31683 | 78.42167 | 11.5 | 2.6 | 160 | 0.25 |
| 81024 | 1534 | 19.16 | 30.79567 | 78.32517 | 13 | 1.8 | 173 | 0.58 |
| 81024 | 2355 | 40.12 | 30.5065 | 78.45483 | 11.7 | 2.6 | 72 | 0.34 |
| 81102 | 1648 | 5.75 | 30.59133 | 78.3745 | 10.5 | 2.6 | 168 | 0.49 |
| 81110 | 756 | 57.57 | 30.31183 | 78.5955 | 24.1 | 2.3 | 125 | 0.72 |
| 81114 | 156 | 43.67 | 30.4625 | 78.52633 | 9.1 | 2.5 | 60 | 0.49 |
| 81114 | 516 | 36.72 | 30.45433 | 78.5235 | 8.1 | 3.2 | 58 | 0.4 |
| 81114 | 1353 | 13.88 | 30.42283 | 78.6465 | 20.7 | 3.1 | 139 | 0.35 |
| 81118 | 2038 | 33.53 | 30.33217 | 78.64267 | 9.9 | 3.3 | 133 | 0.35 |
| 81201 | 1515 | 51.79 | 30.31333 | 78.638 | 12 | 2.6 | 137 | 0.41 |
| 81203 | 1558 | 51.61 | 30.28083 | 78.59267 | 8.1 | 2.8 | 121 | 0.52 |

| | | | | | | | | |
|---|---|---|---|---|---|---|---|---|
| 81203 | 2034 | 42.04 | 30.2965 | 78.60367 | 10.4 | 2.8 | 114 | 0.43 |
| 81204 | 2017 | 47.83 | 30.42067 | 78.67983 | 11.7 | 2.8 | 109 | 0.28 |
| 81204 | 2240 | 27.23 | 30.288 | 78.56483 | 9.6 | 2.9 | 118 | 0.13 |
| 81205 | 52 | 37.2 | 30.29067 | 78.601 | 10.2 | 3.2 | 123 | 0.3 |
| 81205 | 2240 | 52.92 | 30.28717 | 78.548 | 7.1 | 2.8 | 125 | 0.38 |
| 90123 | 1444 | 27.48 | 30.27967 | 78.66967 | 20.8 | 2.6 | 165 | 1.68 |
| 90204 | 910 | 3.28 | 30.2635 | 78.57033 | 61.8 | 0.9 | 131 | 1.03 |
| 90205 | 1355 | 59.93 | 30.72783 | 78.442 | 14 | 2.8 | 174 | 1.1 |
| 90217 | 2224 | 55.51 | 30.26517 | 78.533 | 15.7 | 2.9 | 147 | 0.44 |
| 90218 | 2111 | 47.43 | 30.41267 | 78.49283 | 11.2 | 3.1 | 84 | 0.31 |
| 90224 | 18 | 43.27 | 30.5935 | 78.39633 | 9.6 | 3 | 176 | 0.4 |
| 90225 | 1454 | 32.06 | 30.43633 | 78.59817 | 27.1 | 2.4 | 180 | 2.02 |
| 90301 | 1947 | 24.02 | 30.41117 | 78.45767 | 7 | 3.4 | 101 | 0.19 |
| 90309 | 1030 | 49.15 | 30.427 | 78.43067 | 21.9 | 2.6 | 82 | 0.5 |
| 90309 | 1030 | 48.89 | 30.4045 | 78.4275 | 26.6 | 2.6 | 95 | 0.12 |
| 90310 | 2234 | 56.61 | 30.49533 | 78.32017 | 17.1 | 2.5 | 151 | 0.63 |
| 90321 | 1654 | 11.18 | 30.28817 | 78.64017 | 11.2 | 3.5 | 179 | 0.46 |
| 90322 | 1453 | 42.38 | 30.41583 | 78.62033 | 63.8 | 0.9 | 84 | 0.96 |
| 90401 | 1945 | 47.31 | 30.23833 | 78.5225 | 8.9 | 3.8 | 171 | 0.37 |
| 90501 | 1914 | 17.87 | 30.788 | 78.28983 | 8.5 | 2.7 | 144 | 0.4 |
| 90507 | 224 | 11.34 | 30.58733 | 78.38667 | 11.4 | 2.5 | 84 | 0.44 |
| 90508 | 2031 | 0.86 | 30.81333 | 78.28 | 10.1 | 2.9 | 165 | 0.37 |
| 90512 | 241 | 50.39 | 30.4465 | 78.6945 | 8.4 | 3 | 146 | 0.33 |
| 90512 | 2243 | 32.39 | 30.449 | 78.706 | 7.8 | 3.4 | 160 | 0.23 |
| 90530 | 44 | 45.73 | 30.47717 | 78.51233 | 5.6 | 3.1 | 63 | 0.32 |
| 90710 | 1741 | 27.68 | 30.80767 | 78.2865 | 6.8 | 2.5 | 163 | 0.67 |
| 90712 | 448 | 38.52 | 30.43083 | 78.61883 | 15.2 | 2.7 | 88 | 0.48 |
| 90718 | 1445 | 59.22 | 30.5675 | 78.40717 | 12.3 | 3.2 | 119 | 0.65 |
| 90718 | 2034 | 23.49 | 30.56383 | 78.40767 | 14 | 3.3 | 84 | 0.66 |
| 90811 | 1358 | 25.88 | 30.61367 | 78.50717 | 13 | 2 | 162 | 0.63 |
| 90820 | 807 | 31.79 | 30.74983 | 78.41433 | 3.7 | 2.6 | 102 | 0.37 |
| 90911 | 2021 | 51.95 | 30.29683 | 78.515 | 13.6 | 2.6 | 127 | 0.62 |
| 90916 | 1248 | 35.51 | 30.4115 | 78.3285 | 23.9 | 2.6 | 128 | 0.51 |
| 91004 | 2326 | 31.36 | 30.50333 | 78.286 | 12.8 | 2.5 | 175 | 0.41 |
| 91026 | 1708 | 22.6 | 30.793 | 78.31067 | 5.1 | 2.2 | 162 | 0.64 |
| 91026 | 1710 | 42.38 | 30.7905 | 78.31033 | 1.1 | 2.9 | 159 | 0.46 |
| 91104 | 648 | 56.31 | 30.48967 | 78.59767 | 16.2 | 2.1 | 89 | 0.34 |
| 91125 | 1338 | 5.39 | 30.50767 | 78.6665 | 7.3 | 2.3 | 155 | 0.62 |
| 91213 | 1403 | 29.37 | 30.30333 | 78.47733 | 13.1 | 1.8 | 128 | 0.49 |
| 91225 | 2146 | 26.86 | 30.48267 | 78.45667 | 13.9 | 2.3 | 70 | 0.33 |
| 91225 | 2149 | 57.22 | 30.481 | 78.45817 | 12.9 | 2.6 | 69 | 0.25 |
| 91225 | 2155 | 6.72 | 30.47383 | 78.45767 | 12.5 | 2.6 | 69 | 0.28 |
| 91227 | 2053 | 41.48 | 30.256 | 78.52167 | 13.7 | 2.5 | 159 | 0.44 |
| 100107 | 1558 | 46.83 | 30.36617 | 78.3985 | 9 | 3.5 | 139 | 0.4 |
| 100111 | 1505 | 39.87 | 30.47633 | 78.51017 | 7.8 | 2.8 | 62 | 0.33 |

| | | | | | | | | |
|---|---|---|---|---|---|---|---|---|
| 100115 | 701 | 54.57 | 30.69233 | 78.41333 | 7.5 | 2.5 | 142 | 0.3 |
| 100115 | 703 | 5.71 | 30.711 | 78.46883 | 8.1 | 2.5 | 175 | 0.28 |
| 100127 | 1210 | 9.9 | 30.366 | 78.57483 | 16.5 | 2 | 76 | 0.34 |
| 100129 | 412 | 41.9 | 30.40817 | 78.68417 | 10.6 | 2.6 | 101 | 0.47 |
| 100203 | 201 | 12.49 | 30.32917 | 78.5755 | 9.3 | 2.9 | 93 | 0.4 |
| 100211 | 1920 | 50.02 | 30.78117 | 78.33333 | 7.5 | 1.8 | 161 | 0.32 |
| 100211 | 2105 | 54.58 | 30.79533 | 78.32317 | 5.6 | 2 | 172 | 0.46 |
| 100213 | 1422 | 25.36 | 30.59567 | 78.5235 | 11.1 | 2.2 | 133 | 0.45 |
| 100215 | 937 | 37.5 | 30.786 | 78.33367 | 1.1 | 3.1 | 167 | 0.41 |
| 100215 | 2236 | 54.75 | 30.48933 | 78.33083 | 14.1 | 3 | 143 | 0.43 |
| 100219 | 1745 | 21.69 | 30.4695 | 78.62383 | 1.1 | 2.8 | 163 | 0.29 |
| 100222 | 1646 | 33.89 | 30.791 | 78.34767 | 8.5 | 1.4 | 180 | 0.42 |
| 100225 | 735 | 12.01 | 30.78767 | 78.34317 | 8.9 | 1.6 | 173 | 0.54 |
| 100303 | 710 | 18.26 | 30.813 | 78.3005 | 11.3 | 1.8 | 179 | 0.48 |
| 100330 | 459 | 51.92 | 30.75567 | 78.398 | 6.7 | 1.9 | 147 | 0.63 |
| 100407 | 2311 | 13.12 | 30.493 | 78.6425 | 13 | 2.5 | 124 | 0.57 |
| 100410 | 2034 | 23.86 | 30.4815 | 78.632 | 9 | 2.5 | 149 | 0.16 |
| 100417 | 1629 | 31.35 | 30.32983 | 78.65117 | 10.7 | 2.1 | 139 | 0.41 |
| 100503 | 1715 | 7.6 | 30.401 | 78.3965 | 10.5 | 1.8 | 113 | 0.5 |
| 100507 | 1831 | 22.65 | 30.48117 | 78.63667 | 9.1 | 2.6 | 117 | 0.2 |
| 100519 | 1013 | 18.01 | 30.76183 | 78.38317 | 9.3 | 1.7 | 157 | 0.39 |
| 100612 | 1701 | 56.34 | 30.60433 | 78.32533 | 1.7 | 2.8 | 101 | 0.34 |
| 100617 | 1832 | 5.72 | 30.61533 | 78.30833 | 7.6 | 2.3 | 93 | 0.49 |
| 100705 | 2142 | 20.91 | 30.4655 | 78.69683 | 8.7 | 1.8 | 163 | 0.35 |
| 100708 | 1625 | 53.39 | 30.309 | 78.55733 | 10.1 | 1.2 | 107 | 0.54 |
| 100719 | 805 | 19.46 | 30.29 | 78.541 | 8.7 | 2.6 | 125 | 0.37 |
| 100720 | 256 | 32.87 | 30.4295 | 78.54317 | 8.4 | 2.9 | 84 | 0.36 |
| 100817 | 1152 | 23.37 | 30.60417 | 78.51433 | 5.6 | 2.9 | 135 | 0.21 |
| 100817 | 2332 | 48.8 | 30.13133 | 78.76683 | 11.3 | 2 | 274 | 0 |
| 100906 | 1805 | 21.5 | 30.5125 | 78.43083 | 3 | 2.7 | 123 | 0.45 |
| 100910 | 731 | 52.62 | 30.266 | 78.4985 | 5.2 | 4.3 | 164 | 0.14 |
| 100911 | 2330 | 15.52 | 30.45467 | 78.38567 | 13.8 | 3 | 181 | 0.32 |
| 100913 | 1611 | 59.95 | 30.47717 | 78.4235 | 23.2 | 2.5 | 159 | 0.6 |
| 100919 | 1849 | 27.77 | 30.8085 | 78.26233 | 13.3 | 2.3 | 168 | 0.6 |
| 100928 | 1630 | 50.3 | 30.43217 | 78.669 | 7.5 | 2.8 | 156 | 0.16 |
| 101019 | 905 | 59.71 | 30.7015 | 78.46433 | 8.8 | 2.6 | 164 | 0.62 |
| 101026 | 2110 | 47.39 | 30.811 | 78.29383 | 10.6 | 2.1 | 172 | 0.55 |
| 101109 | 1048 | 46.38 | 30.41133 | 78.6635 | 9 | 3.4 | 94 | 0.32 |
| 101126 | 1652 | 14.21 | 30.49017 | 78.689 | 6.7 | 2.1 | 170 | 0.33 |
| 101217 | 1622 | 22.02 | 30.693 | 78.47633 | 2.4 | 2 | 166 | 0.18 |
| 101224 | 2335 | 27.91 | 30.56267 | 78.49967 | 9.5 | 1.9 | 162 | 0.49 |
| 110110 | 1147 | 34.84 | 30.42483 | 78.41433 | 17.3 | 2.3 | 89 | 0.36 |
| 110111 | 2009 | 28.51 | 30.43983 | 78.39 | 22.5 | 2.6 | 170 | 0.45 |
| 110115 | 2046 | 21.8 | 30.50033 | 78.45933 | 8.3 | 2.5 | 70 | 0.72 |
| 110120 | 207 | 16.55 | 30.81283 | 78.253 | 6.9 | 2.6 | 162 | 0.34 |

| | | | | | | | | |
|---|---|---|---|---|---|---|---|---|
| 110120 | 2306 | 54.96 | 30.83267 | 78.2435 | 7.5 | 2.1 | 163 | 0.45 |
| 110207 | 216 | 2.77 | 30.7215 | 78.46083 | 9 | 2.9 | 178 | 0.31 |
| 110304 | 7 | 49.61 | 30.75217 | 78.3545 | 10.5 | 2.5 | 134 | 0.72 |
| 110314 | 415 | 56.47 | 30.44583 | 78.52733 | 9.8 | 2.4 | 58 | 0.5 |
| 110315 | 1420 | 19.26 | 30.4445 | 78.53933 | 8.2 | 2.5 | 70 | 0.18 |
| 110403 | 228 | 42.91 | 30.72233 | 78.29817 | 15 | 2.2 | 156 | 0.38 |
| 110404 | 1749 | 20.51 | 30.669 | 78.36317 | 11.2 | 3.3 | 141 | 0.29 |
| 110405 | 1756 | 57.62 | 30.2555 | 78.4895 | 12 | 2.8 | 177 | 0.24 |
| 110407 | 1718 | 33.33 | 30.67433 | 78.32283 | 14.1 | 2.4 | 138 | 0.48 |
| 110503 | 1642 | 10.58 | 30.569 | 78.3405 | 22.1 | 2.7 | 125 | 0.42 |
| 110505 | 2103 | 48.8 | 30.8075 | 78.3 | 14.7 | 1.3 | 172 | 0.44 |
| 110511 | 1249 | 8.66 | 30.45083 | 78.29867 | 28.1 | 2.6 | 162 | 0.33 |
| 110514 | 1746 | 38.91 | 30.51 | 78.41217 | 20.6 | 2.2 | 89 | 0.43 |
| 110519 | 221 | 44.41 | 30.55283 | 78.32017 | 18.9 | 2.4 | 152 | 0.36 |
| 110624 | 1656 | 58.58 | 30.41583 | 78.53817 | 11.5 | 2.8 | 86 | 0.34 |
| 110627 | 1647 | 39.21 | 30.29933 | 78.602 | 11 | 3.2 | 102 | 0.31 |